Eng. M.Eng. Misael Dalbosco

Multiscale computational modeling of arterial tissue in health and disease

DOCTORAL THESIS

to achieve the university degree of

Doktor der technischen Wissenschaften

submitted to

Graz University of Technology

Supervisor

Univ.-Prof. Dipl.-Ing. Dr.techn. Gerhard A. Holzapfel
Institute of Biomechanics

in co-tutelle with

Prof. Eduardo Alberto Fancello, D.Sc.
Universidade Federal de Santa Catarina, Brazil

Graz, April 2024

AFFIDAVIT

I declare that I have authored this thesis independently, that I have not used other than the declared sources/resources, and that I have explicitly indicated all material which has been quoted either literally or by content from the sources used. The text document uploaded to TUGRAZonline is identical to the present doctoral thesis.

Date

Signature

This thesis is dedicated to Cindy.

Preface

The end of my PhD represents for me the closing of a story that started almost a century and a half ago. Back then, when TU Graz was only 64 years old (remarkably, the exact same age that UFSC will complete in 2024), my ancestors left the Austrian Empire in search of a better life and emigrated to Brazil, where I was born and started my education, which ultimately brought me back to Austria. After having experienced the life of an immigrant in much more comfortable circumstances, I can only acknowledge their courage.

On a more recent time frame, this PhD thesis is the outcome of an intensive journey over two continents, with a carbon footprint much higher than I would like to admit, and during which I was accompanied by many persons I'd like to thank. I am grateful to both my advisors, Prof. Eduardo A. Fancello and Prof. Gerhard A. Holzapfel, for having guided me in my academic path. Each in his own way, they taught me about continuum mechanics, numerical methods, academic life, and life itself. I am also indebted to Prof. Rolf B. Schroeter for over a decade of mentoring and Dr. Denis Boing for motivating me to pursue this path. This co-tutelle thesis would not have been possible without the help of Mag. Sabine Prem, head of the International Office at TU Graz, to whom I am also very grateful.

Many thanks go to former and current colleagues in Austria and in Brazil: Anna, Bettina, Bruno, Clarissa, Daniel, Francesca, Gerhard, José, Malte, Manos, Markus, Masoud, Max, Michi, Saeideh, Sanne, Selda, Stephan, and last but not least Thiago, who was always there to help when simulations did not converge. Thank you for the many cups of coffee together; it was a pleasure working with you! I was also blessed with the company of many friends, in both countries, who were the source of countless pleasant moments, which were also much needed during this PhD.

I am also grateful, from the bottom of my heart, to my family. To my parents for motivating me to study since I was a child and for many drives to and from the airport. To my sister and brother for keeping an eye on them while I was abroad. To my wife's family for taking care of her and of our little boy when I had to travel alone to Austria. I'd like to apologize to Luca for not being around in many moments of his first years: I'll do my best to make it up to you in the next decades, and I hope one day you will be proud of your dad. Finally and most importantly, I'd like to thank my wife Cindy, who was a constant source of joy and encouragement throughout the way: thank you for joining me in this effort. For being strong when I couldn't, patient when I needed it, and loving at every moment. I couldn't have done it without you. Here's to many more successful journeys together.

Misa

Ex arduis perpetuum nomen.

Abstract

Multiscale computational models based on representative volume elements (RVEs) constitute a valuable tool for investigating the relationship between the mechanics of arteries and biophysical phenomena that occur at smaller length scales. The microstructure of arterial tissue results from the activity of vascular cells that can sense and respond to mechanical stimuli through their extracellular matrix. In healthy arteries, this mechanism is responsible for maintaining tissue integrity and functionality, whereas in pathological conditions it can induce microstructural changes in response to altered mechanics. In abdominal aortic aneurysms (AAA), the localized bulging of the aorta is known to be associated with elastin loss, smooth muscle cell apoptosis, and intense collagen fiber growth and remodeling (G&R) promoted by mechanosensing cells.

In the present work, a new class of multiscale RVE-based models of arterial tissue is proposed, based on a combination of computational homogenization and the embedded elements technique. These models are then used to shed light on the formation of a neo-adventitia on the abluminal side of AAAs, as demonstrated by recent experimental findings. This cumulative dissertation consists of four scientific papers. The first study reviews key aspects of vascular biomechanics at different length scales as well as previous RVE-based models of arterial tissue. In the second study, the use of the embedded elements technique in a multiscale setting is introduced and details of the corresponding numerical implementation are presented, including a discussion on the influence of RVE size and of different multiscale boundary conditions. In the third and fourth studies, RVEs of healthy and aneurysmatic abdominal aortas are constructed and simulated under different biaxial loading conditions to investigate how the formation of a neo-adventitia might be related to mechanotransduction and G&R by vascular cells. The results suggest a possible protective role of this new layer, especially in larger AAAs, and thus contribute to a better understanding of this serious disease, the pathogenesis of which is not yet fully understood.

Zusammenfassung

Numerische Mehrskalenmodelle basierend auf repräsentativen Volumenelementen (RVEs) stellen ein nützliches Hilfsmittel dar, um die Beziehung zwischen der Mechanik von Arterien und auf kleinen Längenskalen ablaufenden biophysikalischen Phänomenen zu untersuchen. Die Mikrostruktur des arteriellen Gewebes resultiert aus der Aktivität von Gefäßzellen, die in der Lage sind, mechanische Reize über ihre extrazelluläre Matrix wahrzunehmen und entsprechend zu reagieren. In gesunden Arterien ist dieser Mechanismus verantwortlich für die Aufrechterhaltung der Integrität und Funktionalität des Gewebes, kann jedoch unter pathologischen Zuständen als Reaktion auf eine veränderte Mechanik mikrostrukturelle Abwechslungen auslösen. Bei abdominalen Aortenaneurysmen (AAAs) ist bekannt, dass die lokalisierte Aussackung der Aorta z. B. mit dem Verlust von Elastin, der Apoptose glatter Muskelzellen und einer ausgeprägten Umstrukturierung (*growth and remodeling*, G&R) von Kollagenfasern einhergeht, die durch mechanosensorische Zellen vorangetrieben wird.

In der vorliegenden Arbeit wird eine neue Klasse von RVE-basierten Mehrskalenmodellen für arterielles Gewebe vorgeschlagen, welche auf einer Kombination von numerischer Homogenisierung und der Embedded-Element-Methode basieren. Diese Modelle werden dann verwendet, um die Bildung einer Neoadventitia an der abluminalen Seite von AAAs zu erhellen, wie dies in neuesten experimentellen Befunden nachgewiesen wurde. Diese Manteldissertation besteht aus vier wissenschaftlichen Arbeiten. Die erste Veröffentlichung gibt einen Überblick über die zentralen Aspekte der vaskulären Biomechanik auf verschiedenen Längenskalen sowie einen Rückblick auf vorangegangene RVE-basierte Modelle von arteriellem Gewebe. In der zweiten Studie wird die Anwendung der Embedded-Element-Methode für Mehrskalenberechnungen eingeführt, und es werden Details zur entsprechenden numerischen Implementierung präsentiert, einschließlich einer Diskussion über den Einfluss der RVE-Größe und verschiedener mehrskaliger Randbedingungen. In der dritten und vierten Veröffentlichung werden RVEs gesunder und aneurysmatischer Bauchaorten generiert und unter verschiedenen zweiachsigen Lastbedingungen simuliert, um zu untersuchen, wie die Bildung einer Neoadventitia mit der Mechanotransduktion und dem von Gefäßzellen kontrolliertem G&R zusammenhängen könnte. Die Ergebnisse deuten auf eine mögliche schützende Rolle dieser neuen Wandschicht hin, insbesondere bei größeren AAAs, und tragen somit zu einem besseren Verständnis dieser schweren Erkrankung bei, deren Pathogenese noch nicht vollständig verstanden ist.

Resumo

Os modelos computacionais multiescala baseados em elementos de volume representativos (EVRs) são uma ferramenta relevante para investigar a relação entre o comportamento mecânico das artérias e fenômenos biofísicos que ocorrem em menores escalas de comprimento. A microestrutura do tecido arterial resulta da atividade de células vasculares capazes de identificar e responder a estímulos mecânicos por meio de sua matriz extracelular. Em artérias saudáveis, esse mecanismo é responsável por manter a integridade e a funcionalidade do tecido, ao passo que, em condições patológicas, ele pode induzir mudanças microestruturais em resposta a alterações mecânicas. Nos aneurismas da aorta abdominal (AAAs), sabe-se que a expansão localizada da aorta está associada à perda de elastina, à apoptose das células musculares lisas e a uma intensa remodelagem das fibras de colágeno (*growth and remodeling*, G&R) promovida por células mecanossensoras.

O presente trabalho introduz uma nova classe de modelos multiescala do tecido arterial baseados em EVR, construídos com base em uma combinação de homogeneização computacional e a técnica de *embedded elements*. Esses modelos são usados para lançar luz sobre a formação de uma camada neo-adventícia no lado abluminal dos AAAs, conforme demonstrado por resultados experimentais recentes. Esta tese cumulativa consiste de quatro artigos científicos. O primeiro estudo traz uma revisão dos principais aspectos da biomecânica vascular em diferentes escalas de comprimento, bem como de modelos anteriores de tecido arterial baseados em EVRs. No segundo estudo, o uso da técnica de *embedded elements* em um contexto multiescala é apresentado, incluindo detalhes a respeito da correspondente implementação numérica e uma discussão sobre a influência do tamanho do EVR e de diferentes condições de contorno multiescala. No terceiro e quarto estudos, EVRs de aortas abdominais saudáveis e aneurismáticas são construídos e simulados sob diferentes carregamentos biaxiais a fim de investigar como a formação de uma camada neo-adventícia pode estar relacionada à mecanotransdução e ao G&R pelas células vasculares. Os resultados sugerem uma possível função protetora dessa nova camada, especialmente em AAAs maiores, contribuindo portanto para uma melhor compreensão dessa grave doença, cuja patogênese ainda não foi totalmente esclarecida.

CONTENTS

1 INTRODUCTION

Cardiovascular diseases (CVDs) remain the main cause of death worldwide [269], despite being known and treated since ancient times [74]. In many cases, CVDs are associated with or caused by diseased blood vessels: the buildup of atherosclerotic plaque in the luminal side of arteries, e.g., can disrupt the blood supply to vital organs such as the heart or the brain, leading to, respectively, ischemic heart disease and stroke [119], which together were responsible for more than a quarter of all deaths around the globe in 2019 [269].

The main function of arteries is mostly a (bio)mechanical one, i.e., to transport pressurized blood throughout the body. Thus, the mechanical behavior of arterial tissue is an essential element of vascular physiology and, as such, has been studied from the early days of solid mechanics: in particular, the strong correlation between the microstructure of arterial tissue and its mechanical behavior has been recognized at least since the 17th century [17]. Arteries are composed mainly of vascular cells (e.g., fibroblasts and smooth muscle cells) embedded in an extracellular matrix (ECM) of collagen, elastin and other proteins [43, 200]. Arising from this complex microstructure, the mechanical behavior of arterial tissue is, in general, nonlinear, anisotropic and marked by residual stresses [105, 119].

To preserve this behavior over time, vascular cells constantly sense the mechanics of the tissue via their surrounding ECM (*mechanotransduction*) [87, 122] and modulate their activity to preserve *homeostasis*, i.e, the set of physical and chemical conditions that ensure tissue integrity and functionality [23, 64]. Not surprisingly, then, persistent changes to arterial mechanics are commonly accompanied by microstructural modifications in the tissue: chronic elevations of blood pressure (hypertension), e.g., have been associated with cellular alterations [5], increased collagen deposition by cells [275] and thickening of the arterial wall [121]; the latter, in particular, could be interpreted as an attempt to drive wall stresses back to pre-hypertensive (homeostatic) levels [6, 125].

In view of the above, it is clear that the (patho)physiology of arteries is strongly dependent on the dynamic reciprocity [15, 140] between arterial mechanics and (mechano)biological phenomena taking place at smaller length scales. Multiscale models of arterial tissue can thus shed light on this interdependence and provide relevant insights to many aspects of vascular biomechanics. Of particular relevance to this purpose are computational models based on representative volume elements (RVEs), in which a geometric model of the microstructure of the tissue (the RVE) is constructed and its deformation is simulated with multiscale boundary conditions, usually by means of the finite element method (FEM) [16, 49, 172]. As opposed to standard macroscopic constitutive models of fibrous tissues, in which the kinematics at lower scales is, in general, postulated *a priori* [21], RVE-based models – despite their higher computational cost – offer much more flexibility to explore micromechanical phenomena such as cellular mechanotransduction, while still capturing the macroscopic behavior of the tissue via homogenization.

1.1 Motivation and objectives

An abdominal aortic aneurysm (AAA) is a pathological bulging of the infrarenal aorta to more than 50% of its normal diameter. Despite their relatively low prevalence (1.3 – 8.9% in men and 1.0 – 2.2% in women [211]), AAAs stand out among CVDs for being particularly deadly: if untreated, an AAA might progress to a rupture of the aortic wall, an event associated with mortality rates of 80 – 90% due to internal bleeding [122, 249]. Almost five centuries after the first description of an AAA by Vesalius [212], the mechanisms behind the initiation, progression and rupture of AAAs still remain elusive. An important contribution to shed more light on the pathogenesis of AAAs was recently made by Niestrawska et al. [185], who proposed a three-stage theory relating microstructural and mechanical alterations along the course of the disease.

The main goal of the present thesis is to introduce a new class of RVE-based models of abdominal aortic tissue, and use it to investigate a particular aspect of this mechanopathogenic theory, namely the formation of a neo-adventitial layer in the abluminal side of the aneurysm – which could have important implications to the stability of the wall [185]. To this end, RVEs resembling the aortic tissue in health and disease are constructed, and simulated via the FEM by combining a sound multiscale framework [16, 49] with the embedded elements technique [67, 83]. The geometrical and constitutive assumptions of the RVEs are solidly grounded in experimental observations, and particular attention is given to the choice of RVE size and boundary condition. By subjecting the RVEs to different biaxial loadings, macro- and micro-scale results are analyzed to explore a possible link between the formation of the neo-adventitia and cellular mechanotransduction, since this new layer originates from intense G&R promoted by cells that are known to respond to mechanical stimuli [126, 185].

1.2 Organization of the PhD thesis

This cumulative dissertation is composed of four scientific papers related to the aforementioned leitmotif:

1. M. Dalbosco, E.A. Fancello, G.A. Holzapfel
   Multiscale computational modeling of arterial micromechanics: a review, *Computer Methods in Applied Mechanics and Engineering*, in press.
   Serving as theoretical background to the thesis, this paper starts by reviewing key aspects of the arterial microstructure and its relation to mechanics and mechanobiology at different length scales. Subsequently, a number of RVE-based models of arteries is reviewed, with emphasis on RVE geometries and simulation results at the macro- and micro-scales. Finally, the paper discusses some directions for future research based on the drawbacks and limitations of previous works.

2. M. Dalbosco, T.A. Carniel, E.A. Fancello, G.A. Holzapfel
   Multiscale numerical analyses of arterial tissue with embedded elements in the finite strain regime, *Computer Methods in Applied Mechanics and Engineering*, 381:113844, 2021.
   In this study, a novel class of finite element (FE) RVE models for arterial tissue is proposed, consisting of one-dimensional truss elements (representing collagen fibers) reinforcing three-dimensional elements (representing the non-collagenous ground substance) by means of the embedded elements technique. The formal derivation and numerical implementation of this approach in a multiscale setting are detailed and, subsequently, applied to an RVE of the medial (intermediate) layer of a healthy abdominal aorta. By simulating an equibiaxial deformation, the influence of RVE size and multiscale boundary condition over the results at the macro- and micro-scales is investigated; results suggest that, among the four classical multiscale models, the assumption of periodic fluctuations on the boundary represents the best choice for the proposed RVE, a fact that is used in the subsequent papers.

3. M. Dalbosco, T.A. Carniel, E.A. Fancello, G.A. Holzapfel
   Multiscale simulations suggest a protective role of neo-adventitia in abdominal aortic aneurysms, *Acta Biomaterialia*, 146:248–58, 2022.
   This study investigates the mechano-pathogenic model of Niestrawska et al. [185] by constructing three types of RVEs, representing the adventitial (outermost) layer of a healthy abdominal aorta, the abluminal side of an early-stage AAA and the neo-adventitia of a late-stage AAA. As in the previous paper, the RVEs consist of one-dimensional collagen fibers embedded into a continuum ground substance, and the network of collagen is stochastically-generated to resemble experimental measurements for each of the three tissue stages. An equibiaxial deformation is simulated using periodic fluctuations on the boundary, and results are analyzed at the macro- and micro-scales. By interpreting the deformation fields in the RVEs as mechanotransduction cues, a possible protective role of the neo-adventitia in late-stage AAAs is proposed. More specifically, it is hypothesized that the formation of this new layer and the associated macroscopic stiffening of the tissue would drive the level of microscopic deformation sensed by fibroblasts (which was disrupted in early-stage AAAs) closer to the homeostatic target of the healthy adventitia.

4. M. Dalbosco, M. Terzano, T.A. Carniel, E.A. Fancello, G.A. Holzapfel
   A two-scale numerical study on the mechanobiology of abdominal aortic aneurysms, *Journal of the Royal Society Interface*, 20:20230472, 2023.
   A drawback of the previous study was the assumption that both the healthy and diseased RVEs were subjected to the same equibiaxial deformation gradient. Aiming to fill this gap, in this paper macro-scale FE models of a healthy aortic ring and of early and late AAAs of increasing size are constructed and simulated. The deformation

gradient at the abluminal side of each model is extracted and used to simulate the biaxial deformation of RVEs of each tissue stage, constructed in the same way as in the previous study. The deformation fields are evaluated qualitatively and quantitatively, and, in conjunction with the findings of the previous study, results suggest that the macroscopic mechanics and the microstructure of the tissue evolve symbiotically in the course of the disease to maintain an approximately constant level of microscopic deformation along disease progression and AAA expansion, even if, in this case, this level is higher than the healthy one.

Further contributions from the author

In addition to the papers cited above, the candidate also co-authored the following publications:

1. M. Dalbosco, C.R.M. Roesler, P.G. Silveira, E.A. Fancello.
   Numerical study on the effect of stent shape on suture forces in stent-grafts, *Journal of the Mechanical Behavior of Biomedical Materials*, 110:103852, 2020.

2. M. Dalbosco, G.S. Lopes, P.D. Schmitt, L. Pinotti, D. Boing.
   Improving fatigue life of cold forging dies by finite element analysis: A case study, *Journal of Manufacturing Processes*, 64:349–355, 2021.

3. E. Klimstein, M. Dalbosco, G.A. Holzapfel.
   Effects of disease progression on mechanical stresses in human abdominal aortic aneurysms, in: G.R. Müller-Putz and C. Baumgartner (eds.), *Proc. Annual Meeting of the Austrian Society for Biomedical Engineering 2021*, Verlag der Technischen Universität Graz, Graz (2021), pp. 25–29.

4. M. Dalbosco, D.C. Haspinger, K. Li, S.-I. Murtada, A. Pukaluk, M. Rolf-Pissarczyk, S. Sherifova and G. Sommer.
   Multiscale experimental characterization and computational modeling of the human aorta, in: G. Sommer, K. Li, D.C. Haspinger and R.W. Ogden (eds.), *Solid (Bio)mechanics: Challenges of the Next Decade*, Springer, Cham (2022), pp. 3–52.

5. S. Saeidi, M.P. Kainz, M. Dalbosco, M. Terzano and G.A. Holzapfel.
   Histology-informed multiscale modeling of human brain white matter, *Scientific Reports*, 13:19641, 2023.

Finally, the author also contributed to the following conference presentations:

1. M. Dalbosco, T.A. Carniel, E.A. Fancello and G.A. Holzapfel.
Numerical investigation on the mechanobiology of collagen growth and remodeling in abdominal aortic aneurysms, in: *XVI International Conference on Computational Plasticity. Fundamentals and Applications (COMPLAS 2021)*, Barcelona, 2021.

2. M. Dalbosco, M. Terzano, T.A. Carniel, E.A. Fancello and G.A. Holzapfel.
Multiscale numerical study of the mechanobiology of abdominal aortic aneurysm growth, in: *11th European Solid Mechanics Conference (ESMC 2022)*, Galway, 2022.

3. M. Terzano, M. Dalbosco, S. Sherifova and G.A. Holzapfel.
A poro-viscoelastic numerical investigation of dissipative effects in muscular arteries under cyclic loading, in: *11th European Solid Mechanics Conference (ESMC 2022)*, Galway, 2022.

4. M. Terzano, S. Saeidi, M.P. Kainz, M. Dalbosco and G.A. Holzapfel.
A microstructure-informed model of the white matter of human brain, in: *7th ECCOMAS Young Investigators Conference (YIC2023)*, Porto, 2023.

5. M. Terzano, M. Dalbosco and G.A. Holzapfel.
Macro and microscale mechanics of abdominal aortic aneurysms, in: *XVII International Conference on Computational Plasticity. Fundamentals and Applications (COMPLAS 2023)*, Barcelona, 2023.

2 MULTISCALE COMPUTATIONAL MODELING OF ARTERIAL MICROMECHANICS: A REVIEW

Abstract. The mechanical properties of arterial tissue play a central role in healthy human physiology and have therefore been extensively studied and modeled in recent decades. These properties are closely related to the microstructural features of the tissue and at the same time can have a significant influence on them, because the arterial microstructure is maintained (and in some cases remodeled) at the microscopic level by vascular cells that can sense and respond to mechanical stimuli. This review addresses multiscale computational models based on representative volume elements (RVEs), which constitute an excellent tool for studying this micro-macro relationship. First, a comprehensive discussion on arterial biomechanics with emphasis on microstructural aspects is presented to underpin the subsequent discussion of RVE-based models and examine their geometrical, constitutive and kinematic assumptions. Second, a series of selected results is then presented to highlight the predictive and descriptive capabilities of the models. Finally, some directions for future work are suggested.

2.1 Introduction

The mechanical behavior of blood vessels has been a subject of interest since the beginnings of solid mechanics. Giovanni Borelli, a contemporary of Galileo, already wrote about the contractility of arteries due to the presence of 'circular fibers' (*fibris circularibus*) [17]. This constitutes an early example of a core principle of arterial biomechanics, in which the microstructure of the tissue is strongly correlated with its mechanical behavior. In fact, during his time as Chair of Mathematics at the University of Pisa (a position previously held by Galileo [246]), Borelli worked closely with the physician Malpighi [18], a pioneer of medical microscopy [190], which may have given him the necessary knowledge about the microstructure of arteries.

Healthy arteries consist of three clearly distinguishable layers: tunica intima, tunica media and tunica adventitia – the innermost, middle and outermost layers, respectively. Each layer is characterized by a specific arrangement of numerous microconstituents such as collagen fibers, elastin sheets, elastic fibers and proteoglycans, which form the extracellular matrix (ECM) [43, 119, 200]. The ECM not only gives arteries their shape and specific mechanical properties, but also provides a scaffold for vascular cells such as fibroblasts and vascular smooth muscle cells (vSMCs). The latter are responsible for the active (contractile) behavior of the arterial wall, while the passive mechanical behavior of arteries is mainly dominated by two ECM components, namely collagen and elastin [105, 119]. In the context of their physiological function, arteries can be therefore be viewed as contractile tubes reinforced by collagen fibers, which represent the main load-bearing component of the arterial wall *in vivo* [82, 199, 272].

To fulfill their biomechanical role of conducting pressurized blood, arteries must be able to maintain their microstructure over time. To this end, vascular cells constantly produce and degrade ECM proteins, controlled by a combination of biochemical pathways and mechanical signaling phenomena (*mechanobiology*) [87, 122], through which cells sense the mechanical state of the tissue and respond accordingly by (re)shaping the ECM to preserve mechanical *homeostasis* – the steady state of physical and chemical conditions that ensure the integrity and functionality of the tissue [23, 64, 126]. Therefore, not only the microstructure of the tissue influences its mechanical behavior, as Borelli observed, but the opposite is also true. Not surprisingly, then, vascular disorders such as hypertension [5, 121, 214], atherosclerosis [168, 253, 262] and aneurysms [124, 185, 245], among others, have been associated with changes both on the tissue mechanics and on its microstructure.

In terms of constitutive modeling, this *multiscale* nature of arterial mechanics promoted the transition from early *phenomenological* models [75, 108, 139, 235, 247] to *structurally-motivated* models [60, 79, 109, 113, 123, 149, 191], which incorporate microstructural information into their formulation, thus providing clear physical and biological meaning to their constitutive parameters. This family of arterial tissue models has achieved considerable success over the past two decades due to their excellent descriptive capabilities [92, 114], helping to reveal how the microstructure of an artery affects its macroscopic mechanical behavior in health and disease [40, 134, 183, 217, 223, 226].

Conversely, using these models to investigate the influence of macroscopic arterial mechanics on microscopic phenomena (e.g., cell mechanotransduction) is more complicated [231]; although they are more computationally expensive, multiscale models based on *representative volume elements* (RVEs) are better suited for this. The RVE consists of a characteristic representation of the microstructure of the material to be modeled, whose (micro)mechanical behavior is simulated with multiscale boundary conditions, thus enabling analyses of countless phenomena on smaller length scales [42, 162, 239]. In this case the macroscopic mechanical behavior can still be determined from numerical homogenization of the microscopic fields, ensuring a consistent connection between the macro- and microscale mechanics [16, 100, 166].

Against this background, an overview of RVE-based models of arterial tissue is presented here. This manuscript is structured as follows: in Section 2.2, key aspects of vascular physiology are introduced, with an emphasis on microstructure (Section 2.2.1), mechanical behavior (Section 2.2.2) and mechanobiology (Section 2.2.3) of arteries to support the subsequent discussion. Different RVE-based models available in the literature are presented in Section 2.3, which briefly discusses the framework of multiscale computational analyses (Section 2.3.1), followed by a review of the model features (Section 2.3.2) and by some selected results on the macro- and micro-scales (Section 2.3.3). Finally, in Section 2.4 conclusions are drawn from the reviewed knowledge and some possible directions for future research are suggested.

2.2 Arterial biomechanics

Since the pioneering work of Roy [207] in the 19th century, much has been investigated about the biomechanical properties of arteries. To support the subsequent discussion of RVE-based models, this section discusses some generally accepted facts of arterial biomechanics (without being exhaustive), with an emphasis on microstructural features and their relationship to the macroscopic behavior of the tissue in health and disease.

2.2.1 Microstructure

The circulatory system of the human body consists of blood vessels with different diameters from 20-30 mm (aorta) to 5-10 µm (capillaries) [128]. Arteries can be classified as *elastic* (larger vessels, located closer to the heart) or *muscular* (smaller vessels, located more distally within the circulatory system) [109, 243]. Despite relevant microstructural differences between the two types [133, 200], the three-layered structure of arteries is generally maintained along the arterial tree down to the single-layered capillaries [119, 276]. Figure 2.1 shows a healthy elastic artery (right) with its three characteristic layers and illustrates the microstructure of each layer (left).

The *intima* consists of a single-layer of endothelial cells that lines the arterial lumen and is supported by a basal lamina reinforced by collagen fibers [119, 200, 276]. In young, healthy arteries the intima is quite thin. However, with increasing age, non-pathological intimal hyperplasia may develop due to cell migration and ECM turnover [177, 213, 230]. This thickening process can lead to the pathological formation of lipid-rich atheromatous plaques on the luminal side of the arterial wall (atherosclerosis) [111, 253], which is associated with a number of cardiovascular diseases – e.g., myocardial infarction, stroke and peripheral artery disease [119, 160].

The *media* is separated from the intima by the fenestrated internal elastic lamina, which is 70-90 µm thick [200]. It consists of concentric layers of spindle-shaped vSMCs with a length of about 60 µm and 5 µm in width [161], which control the contractile behavior of the arterial wall due to its ability to shrink and relax in response to chemomechanical stimuli [43, 86, 180]. These cells are embedded in an ECM composed of interlamellar elastic and collagen fibers as well as proteoglycans, organized into repeating *medial lamellar units* (MLUs) with a characteristic thickness of $\sim 15\,\mu m$ [57, 188, 273]. In elastic arteries, these layers are separated by thin ($\sim 2\,\mu m$), fenestrated elastin lamellae [57, 188]. Similar to collagen fibers, vSMCs exhibit a helical orientation in the axial-circumferential plane of the artery, with an additional radial tilt [161, 188]. However, in the course of some pathologies, significant disruptions in the microstructure of the media can occur: in aortic aneurysms, e.g., in the early stages of the disease there is a severe loss of elastin and smooth muscle cells [94, 122, 175, 185], up to the point that the three-layered structure of the vessel wall is largely lost [40, 183].

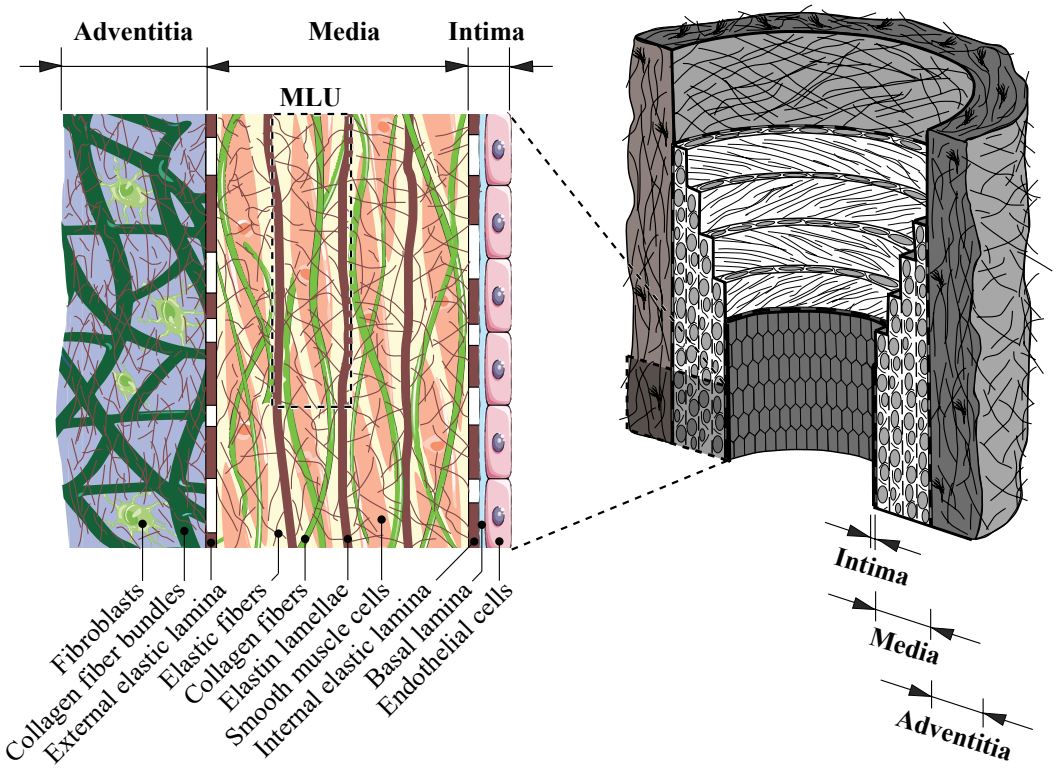

Figure 2.1: The characteristic three-layered structure of arteries (right, adapted from [109]) with a schematic representation of the microstructure of each layer (left): in the intima, a single layer of endothelial cells is supported by the basal lamina. The media is located between the internal and external elastic laminae and consists of medial lamellar units (MLUs) of smooth muscle separated by elastin lamellae and reinforced by elastic and collagen fibers. The adventitia consists of thick bundles of collagen fibers populated by fibroblasts. In muscular arteries, the external elastic lamina is sometimes missing and the elastin in the media is more fragmented [119, 276].

Compared to the (healthy) media, the *adventitia* has a rather simpler microstructure, consisting mainly of thick bundles of collagen fibers embedded in an elastin-rich ground substance populated by fibroblasts and fibrocytes [35, 176, 198]. In larger arteries it is separated from the media by the external elastic lamina, which is absent in more muscular arteries (e.g., cerebral arteries) [119, 200, 276]. While the adventitia was previously thought to play the passive role of protecting the arterial wall from overstretching [31, 109, 157], it is now known that it also plays an important role in arterial (patho)physiology [93, 213, 275]. In larger arteries such as the aorta, the adventitia and the outer media are supplied by their own network of blood vessels (*vasa vasorum*) [133, 176, 276].

In all three layers, collagen molecules (mainly types I and III) organize themselves into stiff fibrils with diameters of 10-500 nm, which in turn form fibers with diameters of 0.5-

3.0 µm and finally fiber bundles of up to 20 µm [126, 200]. The fiber arrangement within the wall depends on the layer, as exemplified in Fig. 2.2(a) for the abdominal aorta. In the intima, a carpet-like plexus of thin collagen fibers reinforces the basal lamina, as mentioned above. In the media, two fiber families alternate transmurally with a certain degree of dispersion around the circumferential direction of the vessel (represented by the 0° angle in the intensity plot, Fig. 2.2(b)), and in the adventitia, thicker bundles of collagen fibers are organized into two families dispersed around the axial direction (90° in Fig. 2.2(b)) of the artery. In the circumferential-radial plane, the fibers are tightly packed around the circumferential direction, with a low dispersion which can be higher under certain pathological conditions, e.g., in abdominal aortic aneurysms [183].

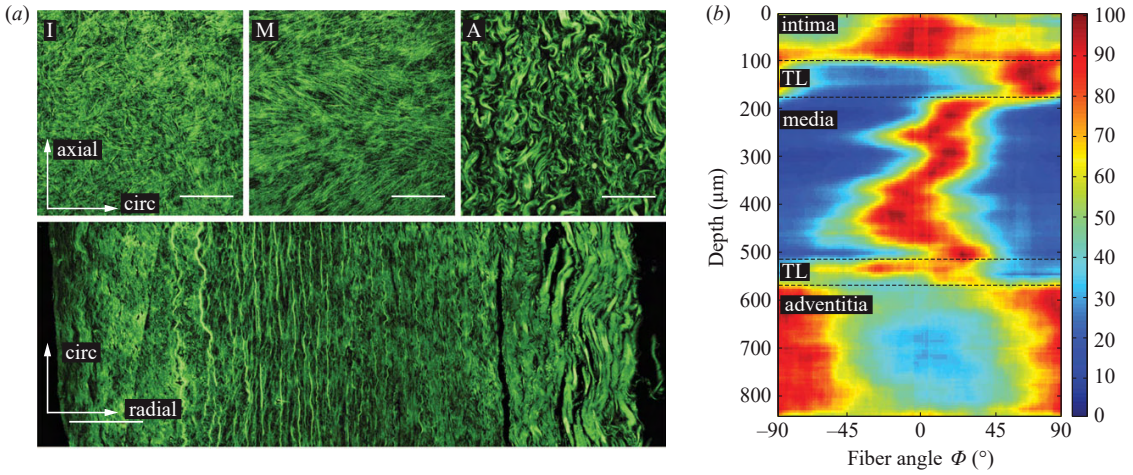

Figure 2.2: Characteristic distribution of collagen in the abdominal aorta: (a) second-harmonic generation images of collagen fibers in the intima (I), media (M) and adventitia (A) and a cross-sectional (circumferential-radial) view of all three layers. Scale bar = 100 µm; (b) intensity plot depicting the orientation of collagen fibers in the axial-circumferential plane; dark red indicates highly aligned fibers with respect to the in-plane angle Φ and dark blue denotes no fibers are aligned according to Φ. The angle values $\Phi = 0°$ and $\Phi = \pm 90°$ designate the circumferential and axial directions of the artery, respectively. Figure adapted from [183].

Notably, similar collagen organization has also been observed in other locations of the arterial tree, e.g. the subclavian, iliac [226], femoral [134] and femoropolipteal arteries [280], suggesting a special organization of collagen in these blood vessels.

2.2.2 Mechanical behavior

Collagen fibers, together with elastin, dominate the *passive* mechanical behavior of the arterial wall [82]. The contribution of each of these two ECM proteins to arterial mechanics is illustrated in Fig. 2.3(a), which shows data from the classical experiment on arterial ring inflation by Roach and Burton [199]: the collagen-digested sample shows a more compliant behavior characteristic of elastin, whereas the elastin-digested sample displays a highly nonlinear behavior with gradual stiffening. The nonlinearity arises from the waviness of the collagen fibers in the load-free tissue (as shown in Fig. 2.2), a configuration whereby these fibers are usually considered to be incapable of withstanding tension [149]. Hence, the mechanical behavior of the wall under small loads is dominated by elastin. As intraluminal pressure increases, the stiff collagen fibers gradually straighten and begin to bear load, resulting in the characteristic J-shaped response of the control tissue (Fig. 2.3(a)).

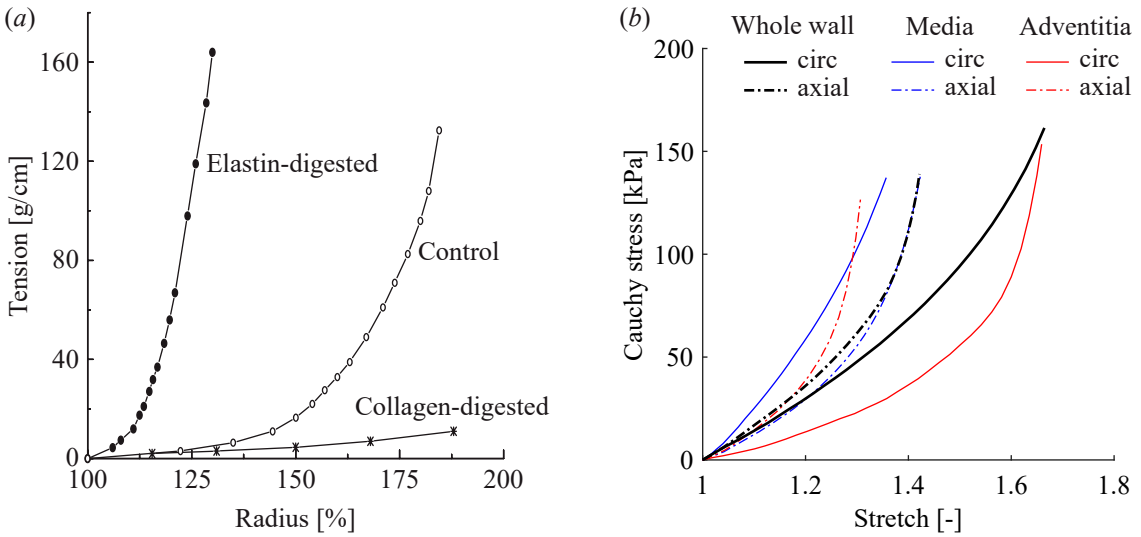

Figure 2.3: Passive mechanical behavior of arterial tissue: (a) inflation of elastin-digested, collagen-digested and control iliac arterial rings. The characteristic J-shaped response of the control tissue clearly arises from the combination of the highly compliant elastin (collagen-digested sample) and the gradually recruited collagen fibers (elastin-digested sample). Adapted from [103]; (b) uniaxial stress-stretch responses of thoracic aortic strips: the anisotropy of the isolated media and adventitia can be associated with the characteristic organization of the collagen fibers (Fig. 2.2), while the response of the whole wall results from the combination of the layers. Redrawn from [71].

This phenomenon of *fiber recruitment* is a central feature of the mechanical behavior of arteries and has therefore been extensively studied and modeled in the last decades [4, 31, 37, 70, 149, 194, 195, 215, 263, 267]. However, it is important to note that even at

zero intraluminal pressure, the arteries are never fully unloaded due to the presence of residual stresses that have a significant influence on the *in vivo* mechanics of blood vessels [105, 112, 116, 125, 168].

In the physiological loading range, recruited collagen fibers are the most important load-bearing component of arterial tissue [82, 199, 272] and therefore their organization within the wall is crucial for vascular mechanics. In particular, the specific organization of collagen (Fig. 2.2) results in a layer-specific anisotropic mechanical behavior, as illustrated in Fig. 2.3(b), which shows data from uniaxial tensile tests performed on circumferentially and axially oriented aortic samples, both from the entire wall and from the isolated media and adventitia [71]. In the latter case, axial samples show a stiffer response than circumferential samples, while the opposite is true for medial samples. This behavior agrees well with the collagen organization for each layer shown in Fig. 2.2. It is noteworthy that the anisotropic mechanical behavior of the entire wall in Fig. 2.3(b) is clearly due to the combination of the specific layers, which may be related to the fact that samples shown in the graph were received from the same donor [71].

Due to the pulsatile nature of blood flow, the arteries are subjected to cyclic loading. In large arteries such as the aorta, the energy dissipation in each cycle has been shown to be quite small [71, 72, 129, 236], hence their characterization as *elastic*. Towards the periphery of the vascular system, arteries become more viscoelastic, a fact often associated with their higher smooth muscle content [33, 110, 151, 280], which is why they are also referred to as *muscular*. In fact, micromechanical tests have demonstrated the viscoelastic behavior of the spindle-shaped vSMCs, which differs along their long and short axes [169, 206, 270]. This anisotropy can be explained by the architecture of their cytoskeleton, in which the contractile actomyosin units are preferentially aligned along the axial direction of the cell [55, 58, 181]. The actomyosin units consist of thick myosin filaments that slide like a ratchet against thin actin filaments. This movement is responsible for the contractility of VSCMs and thus for the *active* mechanical behavior of arterial tissue [43, 105, 180].

Another important inelastic feature of arteries is the stress softening that takes place in the supraphysiological loading range – e.g., during balloon angioplasty or arterial clamping. Experimental results [39, 167, 264, 265] suggest that damage to collagen fibers is the main reason for the softening, which seems reasonable given that they represent the main load-bearing component of arteries. Damage to arterial microconstituents can also occur through pathophysiological processes. For example, it is known that the elastic fiber degradation takes place with increasing age [132, 133, 138, 151] and also in connection with the development of an abdominal aortic aneurysm [175, 185, 210].

2.2.3 Mechanobiology

Given its central role in arterial mechanics, maintaining a (healthy) ECM is crucial to preserve *homeostasis*, i.e., tissue integrity and functionality [23, 64, 126]. While elastin, the major constituent of elastic fibers and lamellae, is remarkably stable (with a half-life of 40 to 70 years) and is rarely produced after maturity [6, 200, 249], collagen fibers in arteries that continually renovate by vascular cells have a half-life of weeks to months [103, 119, 200]. The activity of these cells in the arterial tissue is controlled by a cascade of biochemical signals (e.g., growth factors, cytokines and hormones, among others), which can also originate from biomechanical cues [87, 93, 122, 130]. For example, endothelial cells in the intima are constantly exposed to shear stress due to blood flow, which is *mechanotransduced* into biochemical signals that control a number of biological processes within the arterial wall [87, 165, 196, 244].

Likewise, vSMCs and fibroblasts are able to sense the mechanical state of the ECM in which they are embedded, which is also translated into biochemical signals that control many cellular processes, e.g., migration [130, 135, 159, 222, 274], phenotypic changes [61, 84, 86, 221] and turnover of ECM proteins [126, 155, 158, 187, 225]. Thus not only the mechanical behavior of the arterial tissue is affected by its microstructure, but the opposite is also the case. This *dynamic reciprocity* [15, 140] enables arteries, and soft tissues in general to adapt, at least to some extent, to changes in the loads to which they are exposed (a fact referred to as Davis' Law [45]), which is crucial for the long-term maintenance of tissue functionality. What is also important is that there appears to be a preferred mechanical state towards which the activity of vSMCs and fibroblasts is directed. Therefore, changes in the (micro)mechanics of the tissue are sensed by the cells, which might reorganize the ECM to return it to the homeostatic target [46, 63, 117, 126, 153].

Such changes can result from a number of pathophysiological conditions, e.g., atherosclerosis, hypertension or aneurysm formation. Given the above, it is hardly surprising that these diseases are associated with relevant microstructural changes [5, 121, 124, 168, 214, 245, 253, 262]. In some cases, the arterial microstructure can be permanently altered due to chronic changes to tissue mechanics: in abdominal aortic aneurysms (AAAs), e.g., the permanent dilatation of the aorta leads to significant changes in wall strains [44, 53] and as a result of intensive *growth and remodeling* (G&R) of the collagen network, the ECM configuration of the diseased tissue changes drastically [185]. Figure 2.4 summarizes a particular mechanopathogenic theory by Niestrawska et al. [185] that correlates mechanical and microstructural changes along AAA progression.

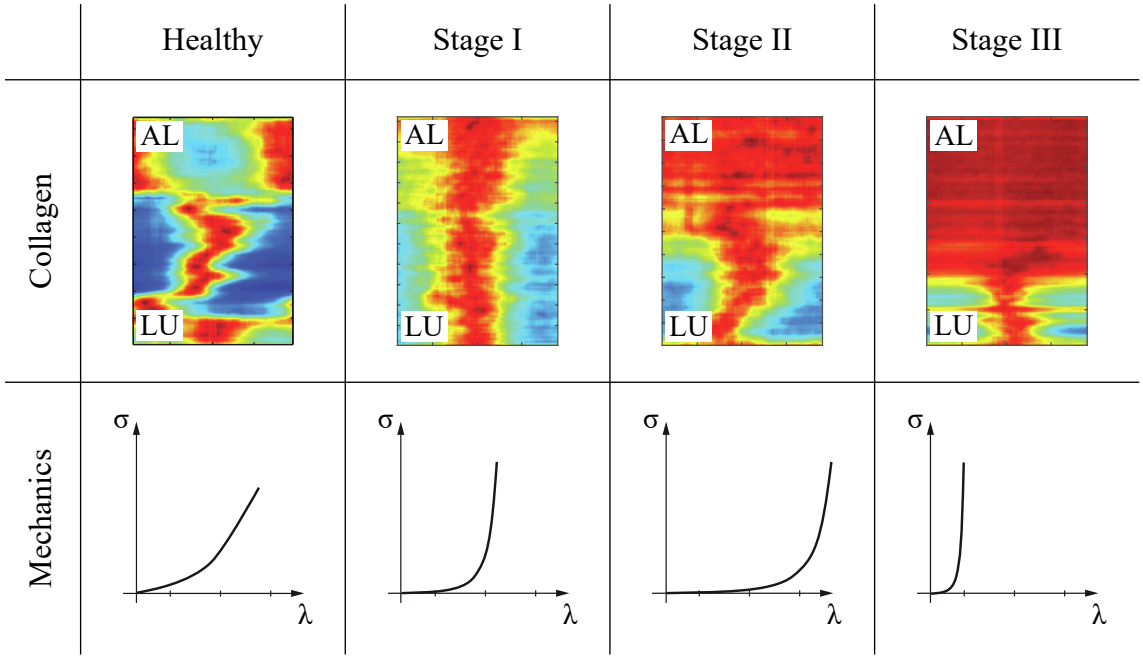

Figure 2.4: A three-stage model of AAA pathophysiology: in the healthy abdominal aorta, the three-layered organization of collagen (top, see also Fig. 2.2) leads to a macroscopic mechanical behavior (bottom) that is initially dominated by elastin, with a relatively moderate stiffening after a significant amount of collagen fibers has already been recruited (see also Fig. 2.3(a)). The loss of vSMCs, elastic fibers and elastic lamellae [94, 122, 175] at the onset of an AAA (Stage I) decreases the initial macroscopic stiffness (bottom) and an aneurysm starts to form. The bulging increases the circumferential load and the collagen fibers realign towards the circumferential direction (top), and thus the three-layered structure is lost. Due to the intense collagen G&R, a *neo-adventitia*, characterized by randomly oriented (isotropic) collagen fibers, starts to form on the abluminal side of the wall (Stage II, top). In Stage III, a thick neo-adventitia can be seen (top) and the tissue becomes very stiff (bottom), which is likely to be associated with a decrease in collagen waviness [186]. Adapted from [185].

2.3 RVE-based models of arterial tissue

In view of the above, it is clear that there is a strong and dynamic connection between the macroscopic mechanics of arterial tissue and the microscopic phenomena that take place at the cellular level. As discussed in the Introduction, RVE-based microstructural models provide an excellent tool for investigating this relationship. This section provides a review of such models, focusing on their multiscale capabilities.

2.3.1 Multiscale framework

Let $\Omega \subset \mathbb{R}^3$ be a deformable macroscopic continuum body in which every point $\mathbf{X} \in \Omega$ is associated with a microscopic *representative volume element* (RVE) $\Omega_\mu \subset \Omega$ (Fig. 2.5). The RVE is a representation of the microstructure of Ω, which might be composed of different material phases with dissimilar mechanical properties. While it is assumed that there is a clear scale separation between Ω and Ω_μ, the size of the RVE depends on the dimensional scale of the phenomena or microstructure being modeled. For arterial tissue, the macro-scale (artery) is usually measured in millimeters, while the micro-scale (RVE) is commonly placed at the level of cells and ECM components, i.e., in the micrometer range (see Section 2.2.1).

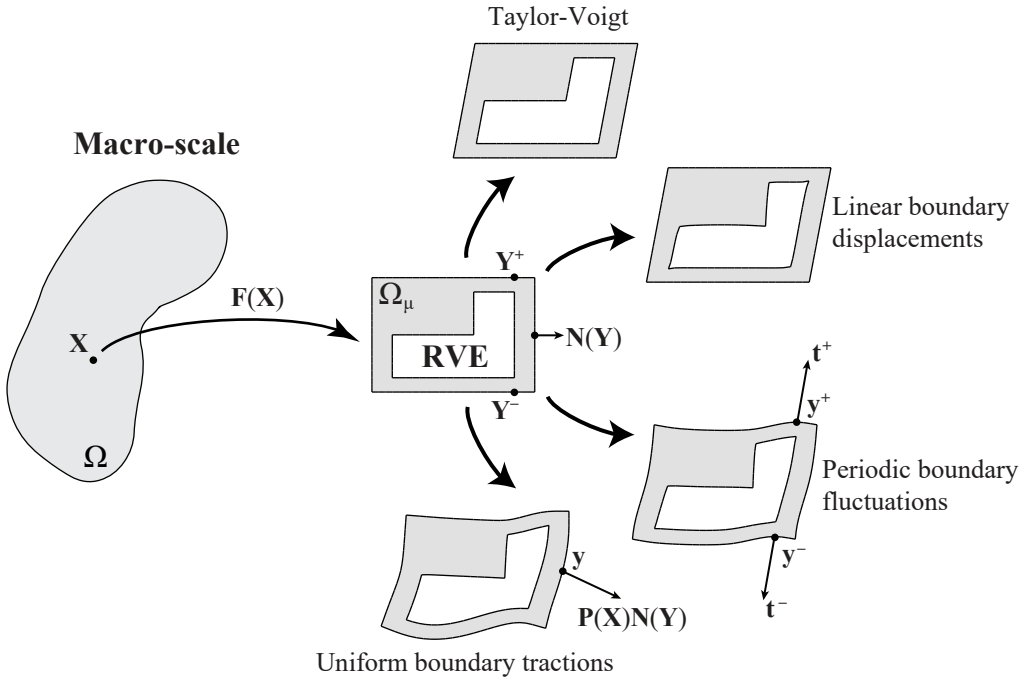

Figure 2.5: Macro-scale continuum body Ω and microscopic RVE Ω_μ at point $\mathbf{X} \in \Omega$, which is deformed by the action of the macroscopic deformation gradient $\mathbf{F}(\mathbf{X})$. The resulting deformation fields in the RVE strongly depend on the chosen multiscale boundary condition.

Let $\mathbf{F}(\mathbf{X})$ be the deformation gradient that describes the kinematics of the material point $\mathbf{X} \in \Omega$. To create a consistent mechanical multiscale model, a physically meaningful relationship must be established between the deformations at the macro-scale and the RVE (micro-scale) [16]. A robust way to do this is to apply the Hill-Mandel principle of macro-homogeneity: in short, it requires that the stress power at the macro-scale be equal to the volumetric average of the stress power at the micro-scale [49, 100, 166]. In the context of computational homogenization, adherence to the Hill-Mandel principle can be ensured

through a suitable choice of boundary conditions (BCs), i.e., of a specific multiscale model, of which there are four classical types in the literature:

1. *Taylor-Voigt*, also known as *uniform strain* or *rule of mixtures*: in this case, the deformation is postulated to be *affine* (Fig. 2.5); i.e., the displacements at each point $\mathbf{Y} \in \Omega_\mu$ of the micro-scale domain are uniquely determined by the macro-scale deformation gradient $\mathbf{F}(\mathbf{X})$.

2. *Linear boundary displacements* or *uniform boundary strain*: similar to the previous model, affine deformations are imposed, but only at the *boundary* $\partial\Omega_\mu$ of the micro-scale domain, while the displacements in the interior of Ω_μ are determined from the mechanical equilibrium (Fig. 2.5).

3. *Periodic boundary fluctuations* or *anti-periodic boundary tractions*: in this case there are also micro-scale displacements determined from mechanical equilibrium. However, at the boundary $\partial\Omega_\mu$ it is postulated that they consist of the sum of an affine part (as in the linear model) and of periodic *displacement fluctuations* that are equal in each pair of symmetric boundary points $(\mathbf{Y}^+, \mathbf{Y}^-) \in \partial\Omega_\mu$. This is equivalent (for periodic RVEs) to the application of anti-periodic tractions $(\mathbf{t}^+, \mathbf{t}^-)$ to the boundary (Fig. 2.5).

4. *Uniform boundary tractions*, also known as *minimally constrained*: this model assumes that uniform tractions $\mathbf{t}(\mathbf{Y}) = \mathbf{P}(\mathbf{X})\mathbf{N}(\mathbf{Y})$ are applied at each boundary point $\mathbf{Y} \in \partial\Omega_\mu$ (Fig. 2.5), where $\mathbf{N}(\mathbf{Y})$ is the normal vector at $\mathbf{Y}$ and $\mathbf{P}(\mathbf{X})$ is the first Piola-Kirchhoff stress tensor at the macro-scale point $\mathbf{X} \in \Omega$.

Some authors [208] also include the Reuss-Sachs assumption of constant stresses in the RVE among the classical multiscale models, although in this case the compatibility of the deformation field in the RVE may be violated. In addition to the cited models, other multiscale BCs (hereafter referred to as *mixed*) can also be adjusted to better reproduce the micro-macro kinematic transfer in certain materials, see [28] for a notable example.

Regardless of the model chosen, the displacement field in the RVE can then be uniquely determined for a given macroscopic deformation gradient $\mathbf{F}(\mathbf{X})$ while still complying with the Hill-Mandel principle. The displacements – and thus also the stresses and strains – are usually calculated by means of finite element (FE) simulations [16]. The macroscopic stress tensor $\mathbf{P}(\mathbf{X})$ can then be determined by calculating the volumetric average of the stresses in the RVE, or, equivalently, by integrating the boundary tractions. In a finite deformation setting, other macro-stress measures (e.g., the Cauchy stress) can also be calculated [49]. This allows the (local) macroscopic behavior to be assessed and, e.g., compared with experimental data while at the same time gaining important insights into micro-scale phenomena. Of course, RVE-based models can also be used as constitutive models in fully coupled micro-macro FE simulations. However, the applicability of this

approach (often referred to as FE^2) is often limited due to the high computational cost associated with running a full FE simulation for each iteration of each macro-scale integration point [76, 228].

A more detailed discussion of the constitutive and numerical aspects of RVE-based (mechanical) multiscale modeling is beyond the scope of this review. The interested reader is referred to the works of Miehe [172], de Souza Neto and Feijóo [49], Blanco et al. [16] and Saeb et al. [208]. As a final remark to this section, it is pointed out that under the Taylor-Voigt BC a numerical model of the RVE is actually not necessary, since the macroscopic stresses can be computed analytically. In fact, it can be shown that the hypothesis of homogeneous strains in the RVE provides a simple rule of mixtures at the macroscopic level [16, 49], on which many successful (macroscopic) constitutive models of arteries are based. Such models have already been extensively reviewed [43, 104, 150] and are therefore not discussed here. The following sections will focus exclusively on RVE models of arterial tissue based on computational homogenization and the finite element method, which are presented in Table 2.1.

2.3.2 Model features

Geometry and constitutive models

As discussed in Section 2.2.1, arteries have an intricate microstructure characterized by a complex arrangement of their many constituents, which can change with age or disease. Therefore, creating a characteristic representation of the arterial microstructure (a necessary condition for RVE-based models) is a non-trivial task. In fact, it is often necessary to characterize the microstructure of arteries using statistical distributions. A typical example is the use of the von Mises distribution to describe the dispersion of collagen fibers [113], which is crucial for arterial mechanics (see Section 2.2.2). As a result, RVEs of arterial tissue are often stochastically generated to match experimental observations [41, 42, 220, 238].

Given the above, it should come as no surprise that all RVE-based arterial models also simplify the tissue microstructure to a certain extent. To illustrate the different levels of simplification found in the literature, Fig. 2.6 presents some proposed geometries for the tunica media, the most commonly modeled layer (Table 2.1). It can be seen that models are often based on one-dimensional finite elements to simulate collagen fibers, aiming to reproduce the above-mentioned variability in the orientation and waviness of collagen with less computational effort. Speirs et al. [228] proposed an RVE consisting of a network of superimposed trusses (collagen fibers) on 2D plane stress elements, which represent an elastin-rich ground substance (Fig. 2.6(a)). The collagen fibers, that were oriented without dispersion, were modeled by a logarithmic strain-energy function with *recruitment stretch*. This is a common strategy to reproduce the gradual recruitment of fibers (see Section 2.2.2)

Table 2.1: Overview of published RVE-based models of arterial tissue: M = tunica media; A = tunica adventitia; M-A = media-adventitia composite; NA = neo-adventitia; H = healthy; D = diseased; Disp. = dispersion; IP = in-plane (circumferential-axial) dispersion; OP = out-of-plane dispersion; Exp = exponential; Log = logarithmic; RS = with recruitment stretch; Dam = with damage; Lin = linear; Poly = polynomial; Helix = helical model [73]; HGO = Holzapfel-Gasser-Ogden model [109]; GS = ground substance; EL = elastic lamella; IC = interlammelar connections, AF = actin fibers; B = biaxial; U = uniaxial; S = shear; L = linear boundary displacements model; T = Taylor-Voigt model; P = periodic boundary fluctuations model; Mix = mixed multiscale BC; Min = minimally constrained model.

			Collagen fibers			Boundary conditions	
Paper	Layer	State	Disp.	Model	Other comp.	Macro	MS Model
[232]	M	H	IP/OP*	Exp	GS***	FE^2	L
[228]	M	H	No	Log+RS	GS	B	T/P
[51]	M-A	H	No	Gent	GS	U/S	P
[220]	M	H	IP/OP*	Exp+Dam	GS***	FE^2	L
[238]	M	D	IP	Lin+RS	EL, GS	U	Mix
[271]	M	H	IP*	Exp+Dam	EL, IC, GS***	FE^2	L
[202]	A	H	IP/OP*	Poly	-	U	Min
[239]	M	H/D	IP	Lin+Dam+RS	EL, GS	U	Mix
[8]	A	H	IP*	Lin	-	U	Mix
[14]	M	H	IP**	Yeoh	GS	B	P
[143]	M	D	IP*	Exp+Dam	EL, IC, GS***	FE^2	L
[178]	M	H	IP/OP*	Lin+RS	EL, vSMC, GS	U	?
[164]	M	H/D	IP	Lin+Dam+RS	EL, GS	B	Mix
[162]	M	H/D	IP*	Helix	EL, AF	B/S	L
[41]	M	H	IP/OP	Lin+RS	GS	B	T/L/P/Min
[9]	A	H/D	IP*	Lin+Dam	GS***	U/B	Mix
[3]	M	H/D	No	HGO	GS	FE^2	P
[42]	A/NA	H/D	IP/OP	Lin+RS	GS	B	P
[76]	M/A	H/D	IP*	Helix	EL, AF	FE^2	L
[44]	A/NA	H/D	IP/OP	Lin+RS	GS	B	P
[10]	A	H	IP*	Lin+Dam	GS	U	Mix

* No study has been conducted on how representative the dispersion was compared to experimental data.
** The dispersion was accounted for at the macro-scale only by varying the orientation of the RVE.
*** The ground substance does not interact with the other microconstituents.

in the tissue if their waviness is not explicitly taken into account in the RVE (Table 2.1). A different value of recruitment stretch was assigned to each fiber (represented by the different colors in Fig 2.6(a)) that mimics the different degrees of waviness in the tissue (Fig. 2.2).

Another way to reproduce the characteristic J-shaped mechanical response of arterial tissue (Fig. 2.3) is to use the classical exponential function [75, 109] as done by Shah et al. [220], which modeled all fibrillar components of arterial tissue as a network of discrete, interconnected 1D truss elements (Fig. 2.6(b)). Their model, based on previous work by the same group [232], also took into account the possibility of fiber damage by excluding elements from the RVE that stretched beyond a certain point. This model was later

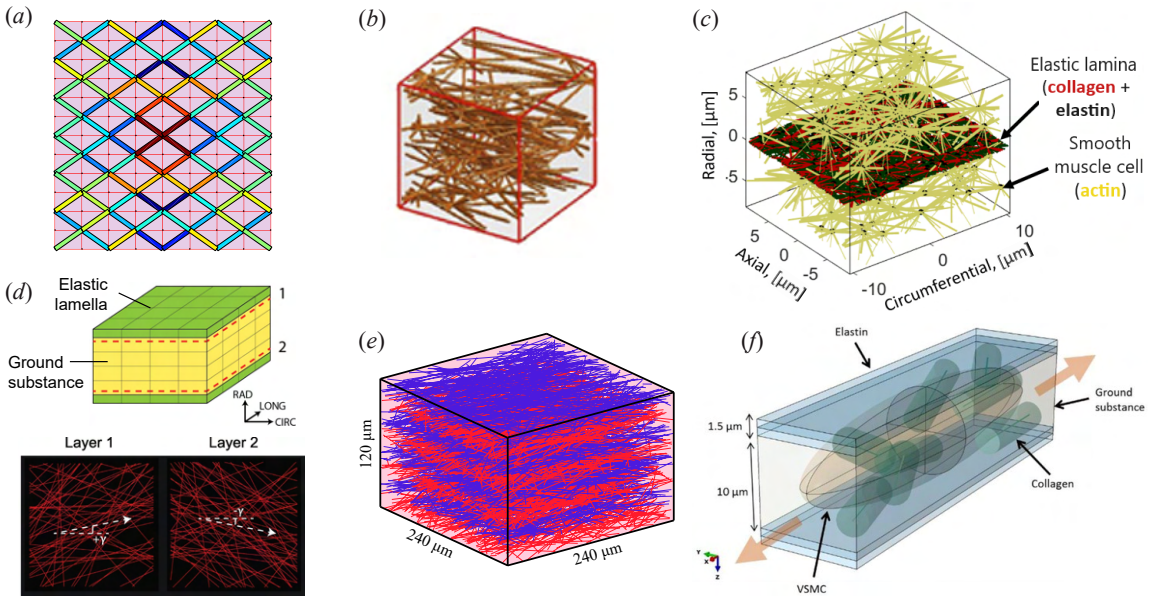

Figure 2.6: Different RVE geometries proposed for the tunica media: (a) a 2D RVE consisting of plane stress elements representing elastin superimposed by a network of trusses that represent collagen fibers. Reproduced from [228]; (b) a discrete network of trusses representing all fibrillar components of the arteries. Adapted from [220]; (c) a 2D network of trusses representing collagen and elastin is combined with a 3D truss network representing actin filaments (and, by extension, vSMCs). Adapted from [162]; (d) continuum (3D) elements representing the elastic lamellae (green) and an interlamellar ground substance (yellow), reinforced by two layers of collagen fibers, which reinforce the ground substance via the embedded elements technique. Adapted from [239]; (e) an elastin-rich ground substance (pink) reinforced by two families of collagen fibers (red and blue) alternating along the radial (vertical) direction. Adapted from [41]; (f) a 3D RVE consisting of two elastic lamellae and an interlamellar ground substance, reinforced by 1D collagen fibers and containing a ellipsoidal vSMC. Reproduced from [178]. The characteristic length of the RVEs ranges from $\sim 10\,\mu\text{m}$ (c) to $\sim 3\,\text{mm}$ (a).

refined to include additional microconstitutents, e.g., elastic fibers, interlamellar connections [143, 271] and actin fibers that represent smooth muscle cells [162] (Fig. 2.6(c)). The latter included passive and active contributions to fiber stress. Importantly, the possibility of growth and remodeling of actin and collagen within the network was also considered in [162] and complemented by modeling residual stresses within the network in a subsequent study [76].

A drawback of the study by Shah et al. [220], which is also shared by other discrete models [9, 143, 232, 271], is the assumption that non-fibrillar components that form a neo-

Hookean homogeneous ground substance do not interact with the fibers of the RVE. While this hypothesis works quite well for macro-scale arterial models [104], it is questionable whether this is actually the case at the microstructural level. In this context, DeBotton and Oren [51] modeled both collagen fibers and ground substance as 3D elements. However, the dispersion of fiber directions was not included. This issue was partially addressed in [14], which also did not include dispersion of the 3D fibers within the RVE, but varied the orientation of the RVE with respect to the macro-scale to account for different fiber orientations.

An intermediate solution was proposed in [164, 238, 239], which modeled 1D fibers reinforcing a 3D ground substance using the classical embedded element approach initially developed for concrete [83]. In their model of the medial aortic lamellar unit (Fig. 2.6(d)), the embedded fibers were placed closed to the elastic lamellae, organized into two fiber families (one for each lamella) and dispersed around two preferential angles, oriented symmetrically to the circumferential direction of the artery. However, only dispersion in the circumferential-axial plane was considered. The out-of-plane dispersion, which is small in healthy arteries but can be relevant, e.g., in aortic aneurysms [183, 223], was not modeled, although the authors also employed the proposed RVE to model aneurysmal aortas. Fibers were modeled as linear 1D elements with recruitment stretch, since fiber waviness was not explicitly accounted for in the geometry of the RVE. However, a single value of recruitment stretch was used for all fibers, whereas the fibers in the real tissue have varying degrees of waviness (see Section 2.2.1). The fibers were embedded as reinforcements to the neo-Hookean interlamellar ground substance, which contained other microconstituents (e.g, proteoglycans and cells) but did not include active behavior of vSMCs. These issues were partially addressed in [41], where the same embedded elements technique was used to model an RVE of the media, including the out-of-plane dispersion of two families of collagen fibers (red and blue in Fig. 2.6(e)). Different values of recruitment stretch, sampled from a beta distribution, were assigned to each (linear) fiber. However, the active part of arterial mechanics was also not modeled and, in contrast to [164, 238, 239], elastic lamellae were not considered as a separate phase, but were included in the neo-Hookean ground substance (pink in Fig. 2.6(e)).

In [178], a detailed model of a medial lamellar unit was proposed (Fig. 2.6(f)), which includes elastic lamellae, a 3D ellipsoid vSMC and an interlamellar ground substance reinforced by collagen fibers, which were modeled as 1D linear elastic reinforcements with recruitment stretch. Although different fiber orientations (both in-plane and out-of-plane) were considered, it is clear that such a small number of short fibers cannot properly reproduce the variability of collagen orientations within the tissue (Fig. 2.2). In this context, it is important to note that although most models take into account the in-plane and/or out-of-plane dispersion of collagen fibers (Table 2.1), only a handful of them [41, 42, 44, 164, 238, 239] provide a proper comparison between the statistical distribution of fiber orientations in the RVE and the modeled tissue, a topic that deserves more attention in future work.

Although less common (Table 2.1), some RVE-based models of arterial adventitia have also been proposed and are exemplified in Fig. 2.7. Ayyalasomayajula et al. [8] proposed a 3D RVE made of 1D fibers modeled as linear elastic beam elements with reduced bending stiffness. In the constitutive model of the fibers, no recruitment stretch was included because the (varying) waviness of the fibers was explicitly accounted for (Fig. 2.7(a)). However, only the in-plane dispersion of fibers was included and non-collagenous components of the adventitia were not modeled. Similarly, the model by Gacek et al. [76] consists of a network of 1D trusses (Fig. 2.7(b)), representing dispersed collagen fibers whose constitutive behavior follows the helical model of Freed and Doehring [73]. While the interesting possibility of collagen G&R was included, non-collagenous components were also not explicitly modeled. Instead, at the macro level, the collagen fiber network acts in parallel with an osmotic pressure component. Using the embedded element technique, Dalbosco et al. [42] proposed a model of the adventitia consisting of two families of linear elastic trusses (red and blue in Fig. 2.7(c)) with different values of recruitment stretch and embedded in a neo-Hookean ground substance (pink in Fig. 2.7(c)). A similar model with a more isotropic distribution of fibers was later used [44] to evaluate the micro-mechanical state of the neo-adventitia in AAAs (see Section 2.3.3).

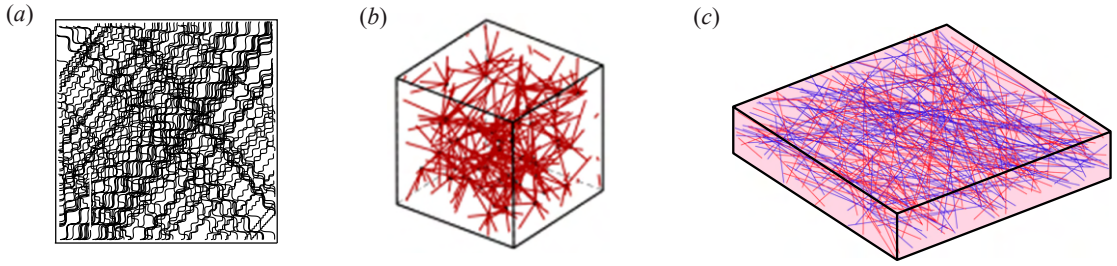

Figure 2.7: Different RVE geometries proposed for the tunica adventitia: (a) a 3D network of 2D wavy collagen fibers discretized with 1D beam elements. Adapted from [8]; (b) a discrete network of trusses representing collagen fibers. Adapted from [76]. An elastin-rich ground substance (pink) reinforced by two intertwined families of collagen fibers (red and blue). Adapted from [42].

Boundary conditions

In Table 2.1 it can be seen that all four classical multiscale BCs mentioned in the Section 2.3.1 along with some mixed BCs, were used in computational RVE-based models of arterial tissue. Despite the ongoing debate [144, 145, 231] about the degree of affinity at the micro-scale of arterial tissue, it can be seen from Fig. 2.5 that for the same macroscopic deformation gradient $\mathbf{F}(\mathbf{X})$ there is a significant influence of the boundary condition on the deformations observed in the RVE and consequently on the macroscopic (homogenized) response of the model.

In this context, Chandran and Barocas [32] investigated the influence of the chosen BC on a network of discrete trusses, but only compared the Taylor-Voigt model and linear boundary displacements. The authors argued for the superiority of the latter over the former and chose the linear model for their subsequent works [76, 143, 162, 220, 232, 271]. Other multiscale BCs were not considered, a gap recently addressed in [202], which formally defined the four classical models for discrete fiber networks using the principle of multiscale virtual power, a generalization of the Hill-Mandel principle proposed by Blanco et al. [16]. In a later work [203] they included the possibility of damage to the fibers within the network; the results are shown in Fig. 2.8. A band of weaker fibers (blue) was included in the undeformed configuration of the RVE (Fig. 2.8(a)) and macroscopic stretching in the horizontal direction was imposed by both linear boundary displacements (Fig. 2.8(b)) and uniform boundary tractions (Fig. 2.8(c)), with undamaged fibers shown in blue and fully damaged fibers shown in dark red. It is clear that the strong assumption of affine deformations at the boundary (Fig. 2.8(b)) leads to spurious boundary effects that result in damaged fibers outside the weaker central area at the top and bottom of the deformed RVE. In contrast, the minimally constrained model (Fig. 2.8(c)) provides a more realistic deformed boundary and the damage is concentrated in the central band of weaker fibers.

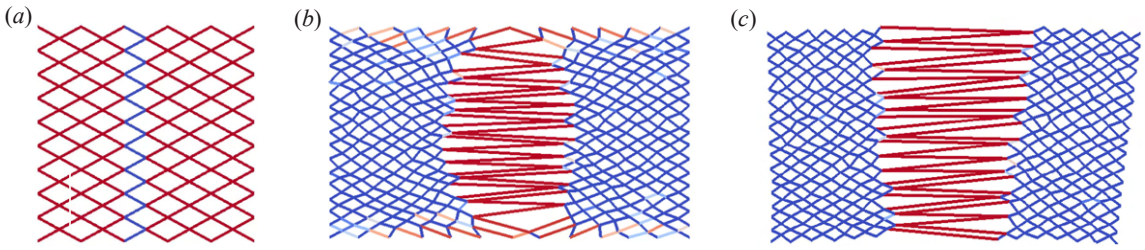

Figure 2.8: The influence of the chosen boundary condition on a 2D network of trusses, including the possibility of damage. The undeformed RVE (a) contains a central band of weaker fibers (blue). When uniaxial deformation is imposed in the horizontal direction, using a minimally constrained model (c) avoids spurious boundary effects that occur when linear displacements are applied on the boundary (b). Adapted from [203].

Dalbosco et al. [41] conducted a similar investigation on the influence of the chosen multiscale BC on RVEs simulated using the embedded elements technique. An equibiaxial deformation of the RVE shown in Fig. 2.6(e) was simulated with linear boundary displacements, periodic boundary fluctuations and uniform boundary tractions and the resulting fields of von Mises strains in the ground substance of the RVE are compared in Fig. 2.9, where the opposing effects of the affine boundary (Fig. 2.9(a)) and the minimally constrained models (Fig. 2.9(c)) can be seen. In the first case the strains tend to concentrate in the interior of the RVE, while in the second case the opposite is observed, i.e., strains concentrate on the boundary. Based on their results, Dalbosco et al. [41] argued for the superiority of the periodic boundary fluctuations model (Fig. 2.9(b)) over the other three

classical multiscale BCs (Section 2.3.1) and used this BC in subsequent micromechanical analyses [42, 44, 209].

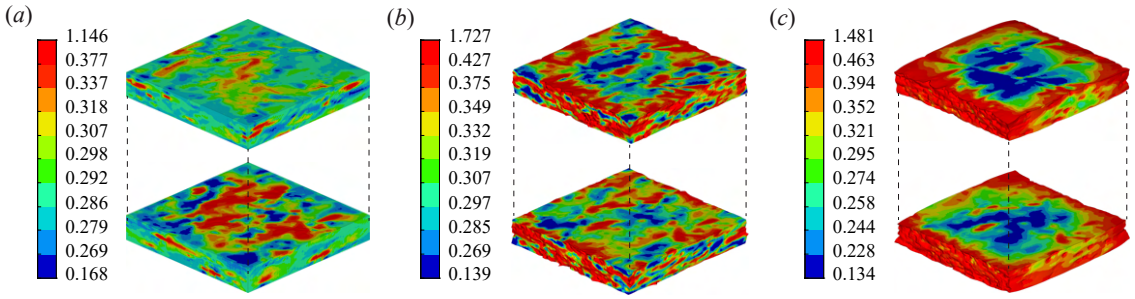

Figure 2.9: The influence of different boundary conditions on the microscopic deformations in the ground substance of the medial RVE shown in Fig. 2.6(e). The RVE domain was bisected to facilitate visualization of the strain fields. When (a) the linear boundary displacements model is used, the strains are concentrated in the interior of the RVE. The opposite is the case if (c) uniform tractions are applied. In the periodic boundary fluctuations model (b), the strains within the RVE are more evenly distributed (but still very inhomogeneous), indicating less intense boundary effects. Adapted from [41].

Given the above, it is clear that choosing an appropriate multiscale model for a given problem is not a trivial matter. However, the influence of the chosen BC is often overlooked in RVE-based simulations of arterial tissue, since most works do not provide a rational for the chosen multiscale BC. Furthermore, the mixed BCs used in a number of the models listed in Table 2.1 often result from a rather arbitrary application of forces and displacements to the boundary of the RVE, instead of being carefully designed with the aim of better representing the micro-macro kinematic transfer in the tissue [28, 30]. Importantly, in many cases [8–10, 14, 143, 164, 178, 220, 232, 238, 239, 271, 277] in which geometrical and constitutive parameters of the RVEs are adjusted to fit macroscopic mechanical data, the fact that the parameter values so obtained depend on the chosen multiscale BC and therefore could be different if another was used, is usually not discussed or even mentioned.

Regardless of the multiscale model chosen, RVEs can be used to simulate any type of macro-scale deformation. As shown in Table 2.1, the most common types of macroscopic BC are uniaxial and biaxial deformations, as well as some works using fully coupled micro-macro simulations (FE^2). Due to the high computational costs, the latter were either applied to discrete RVEs [76, 143, 220, 232, 271] or limited to a small part of the macro-scale dominion [3] (see Section 2.3.1). In the next section, some results from RVE-based simulations at both macro- and micro-scales (or tissue and RVE levels) will be presented and discussed to highlight the versatility of these models.

2.3.3 Selected results

Biaxial macroscopic behavior

As discussed above and summarized in Table 2.1, RVE-based models available in the literature adopt different strategies to reproduce the gradual recruitment of collagen fibers that characterizes arterial tissue (see Section 2.2.2). As shown in Fig. 2.10, these approaches are generally able to reproduce the typical J-shaped (passive) mechanical response of arteries on the macro-scale under equibiaxial loading (Fig. 2.10).

Witzenburg et al. [271] simulated equibiaxial tests on cruciform samples of the tunica media of porcine ascending aortic tissue using a fully coupled FE^2 model. The RVE, which acted in parallel (but did not interact) with a neo-Hookean ground substance, was similar to that in Fig. 2.6(c). However, in this case only the passive behavior of the interlamellar fibers (gold) was simulated and all fibrillar components were modeled with exponential functions. The model-predicted circumferential (C) and axial components (A) of the homogenized first Piola-Kirchhoff stress (red curves) are compared in Fig. 2.10(a) with experimental data (black dots). It can be seen that the model provided a good approximation of the mechanical response of the samples within the 95% confidence interval (error bars), although with a slight overprediction of the degree of anisotropy. However, it must be said that in [271] the same set of model parameters were used to fit different tests, namely, uniaxial, peel and shear lap tests in addition to the equibiaxial ones. The fit could probably be better if only the experimental data on Fig. 2.10(a) were taken into account.

Figure 2.10(b) shows the equibiaxial macroscopic response of the RVE model by Maiti et al. [164] (Fig. 2.6(d)), in which a ground substance of 3D elements is reinforced by 1D truss elements representing linear elastic collagen fibers with recruitment stretch, using the embedded elements technique. As in the previous case, the circumferential direction is stiffer than the longitudinal direction, as expected for the media (see Section 2.2.2). However, in this case, the stresses in both directions follow a bilinear curve with a steep increase at a stretch of about 1.25. This is because a constant value of recruitment stretch is used for all collagen fibers, while the fibers in real tissue have different degrees of waviness (Fig. 2.2); a similar effect was seen in [178]. Dalbosco et al. [41] also employed the embedded element technique in their model (Fig. 2.6e) to reinforce a neo-Hookean ground substance with linear collagen fibers, which in their case were assigned different values of recruitment stretch. As a result, the homogenized equibiaxial response (Fig. 2.10(c)) shows a more gradual, J-shaped stiffening in both circumferential and axial directions, similar to Fig. 2.3. Their results agree well with experimental data (shown in gray in Fig. 2.10(c)) and also illustrate the considerable effect of the chosen multiscale boundary condition on the predicted macroscopic response, as discussed in Section 2.3.2.

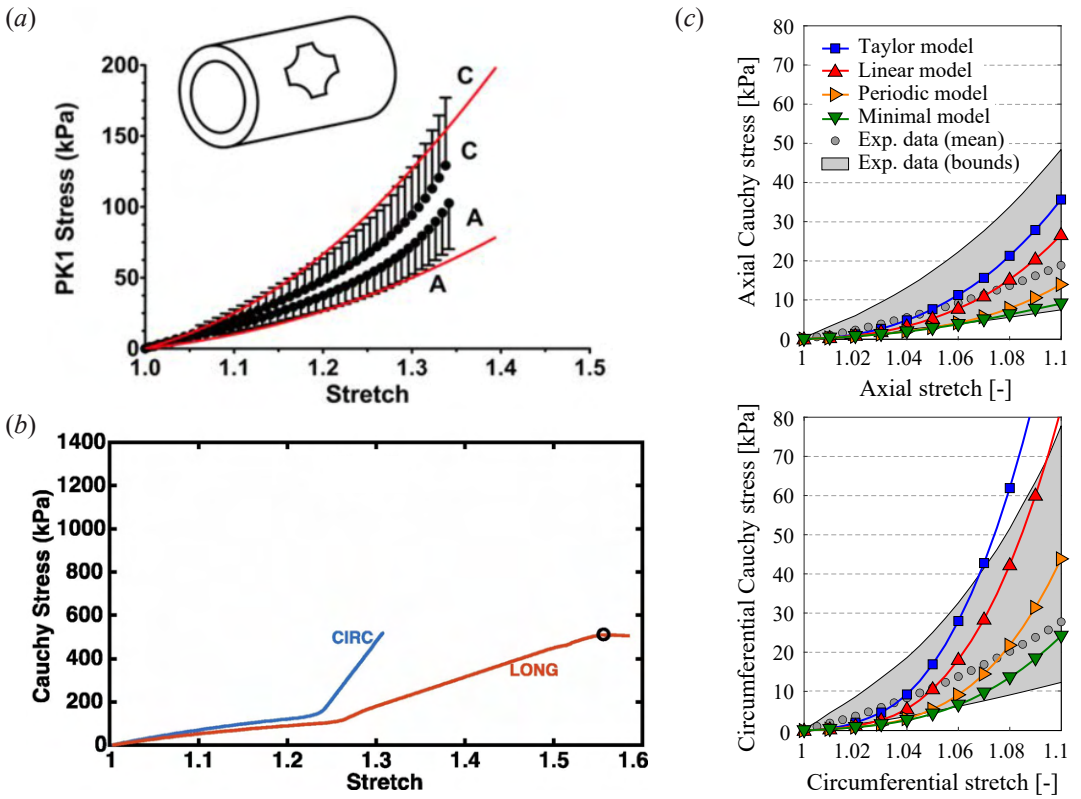

Figure 2.10: Some macro-scale (homogenized) equibiaxial stress-stretch responses of RVE-based models: (a) equibiaxial loading of cruciform samples of porcine aortic media. Experimental results (dots) in the circumferential direction (C) and axial direction (A) with a confidence interval of 95% (error bars) are compared to model predictions (red). Adapted from [271]; (b) equibiaxial response of the medial RVE shown in Fig. 2.6(d) in the circumferential direction (CIRC) and axial direction (LONG). Since the model also includes damage, the circle marks the peak stress. Adapted from [164]; (c) axial (top) and circumferential (bottom) homogenized stress-stretch curves for the RVE of Fig. 2.6(e) for different multiscale models plotted against experimental equibiaxial data of medial samples of the human aorta. Adapted from [41].

Fiber kinematics

In view of the above, one could say that RVE-based models have similar descriptive capabilities regarding the macro-mechanical behavior of arteries as purely macroscopic constitutive models. However, as explained in previous sections, they are generally better suited to studying the microscopic phenomena that lead to this behavior. Macroscopic constitutive models of fibrous materials are often based on the assumption of affine (Taylor-Voigt) deformations at the micro-scale, and even when this is not the case, the kinematic assump-

tions of these models are generally fixed [21]. RVE-based models, on the other hand, offer significantly more flexibility, as discussed in Section 2.3.2, since depending on the chosen multiscale BC, the same macro-deformation $\mathbf{F}(\mathbf{X})$ can lead to considerably different deformation fields in the RVE (see also Figs. 2.8 and 2.9).

In this context, Fig. 2.11 presents some interesting results from RVE-based models regarding the kinematics of fibrillar components (e.g., collagen and elastin) in arteries. Shah et al. [220] used a fully coupled FE^2 to simulate equibiaxial (Fig. 2.11(a)) and uniaxial (Fig. 2.11(b)) tests on dog bone and cruciform samples of the tunica media from porcine ascending aortic tissue. The constitutive behavior at each point of the tissue was determined by the (non-interacting) combination of a neo-Hookean ground substance and an RVE of discrete trusses that encompass all fibrillar components of the tissue (see Fig. 2.6(b)). For the equibiaxial loading case (Fig. 2.11(a)), the model predicted little to no reorientation of fibers within the RVE. This is consistent with the experimental results of Pukaluk et al. [194] using multi-photon images to investigate the kinematics of collagen and elastin in the media of human aortas deforming under equibiaxial loading.

For the uniaxial case (Fig. 2.11(b)), a study by Krasny et al. [144] using a similar experimental setting as Pukaluk et al. [194] found that the realignment of medial collagen and elastin under uniaxial loading was only moderate and, in general could be predicted by affine (Taylor-Voigt) deformations, whereas in Fig. 2.11(b) a stronger realignment of the fibers towards the loading direction was observed, which may also be related to the use of linear boundary displacements that allow non-affine deformations within the RVE. A possible reconciling explanation is provided by Yu and Zhang [277], who modeled a single layer of porcine aortic elastin fibers with a discrete network of beam elements. The authors found that the amount and stiffness of fiber cross-links strongly influences the degree of fiber reorientation within the RVE. Another possible explanation for the differences is provided by the RVE model of the media by Thunes et al. [238] (similar to Fig. 2.6(d)), in which the fibers are embedded in a ground substance of 3D finite elements. The model predicted a more moderate realignment of collagen fibers according to the loading direction (Fig. 2.11(c)). In this case, it can be hypothesized that the presence of other microconstituents (e.g., smooth muscle cells) could also hinder the reorientation of fibers. Finally, it is emphasized that Krasny et al. [144] used rabbit carotid arteries (as opposed to porcine aortas in [220]). Therefore, the differences between the results of the two works could be at least partly related to the different species and locations from which the arterial samples were harvested.

The adventitia model (Fig. 2.7(a)) by Ayyalasomayajula et al. [8] also predicted a strong realignment of fibers towards the circumferential direction (0° in Fig. 2.11(d)) of the load, in a very non-affine way. In contrast to the media, these results are consistent with those of Krasny et al. [144], in which the experimentally measured fiber reorientation angles in the adventitia were significantly higher than affine predictions.

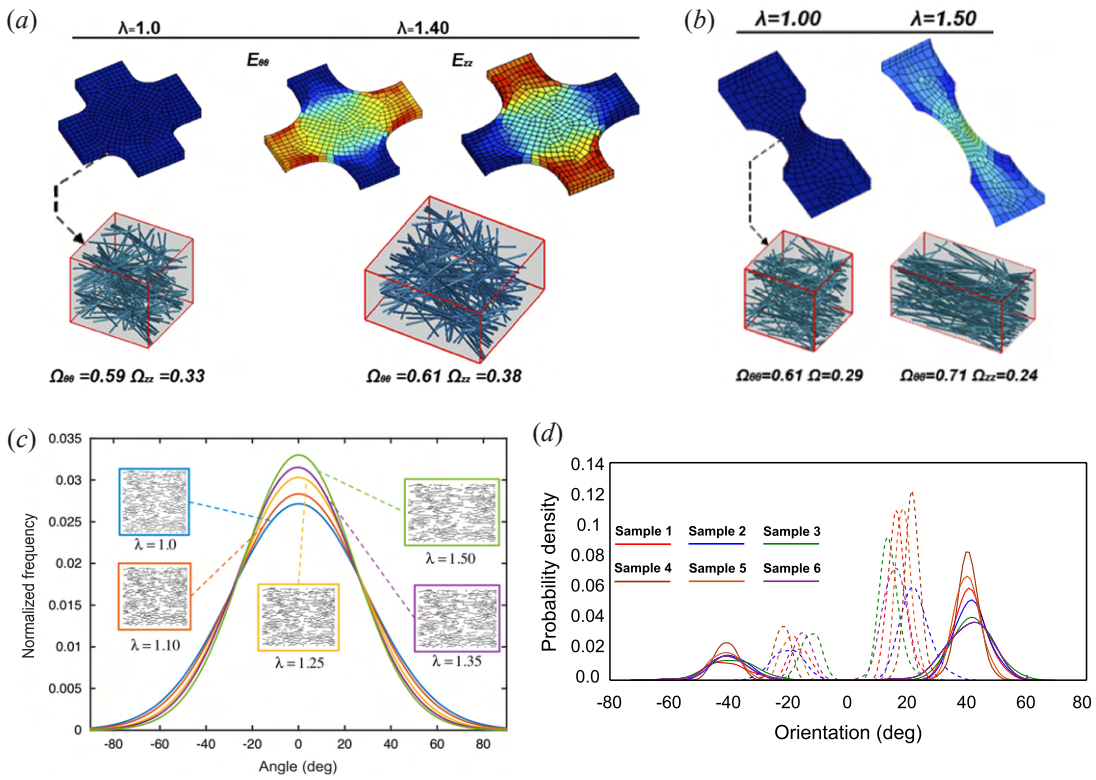

Figure 2.11: Model predictions of fiber reorientation at the tissue micro-scale: (a) the model by Shah et al. [220] predicts almost no reorientation under equibiaxial loading, but (b) a strong realignment under uniaxial loading. $\Omega_{\theta\theta}$ and Ω_{zz} are average orientation parameters of the network with respect to the circumferential and axial directions, respectively ($\Omega = 1$ means full alignment). Figures adapted from [220]; (c) the medial RVE by Thunes et al. [238] and (d) the adventitial RVE by Ayyalasomayajula et al. [8] also predict a considerable realignment of fibers towards the circumferential axis of the tissue (0°) due to uniaxial loading in this direction. The solid and dashed curves represent the orientation of the fibers before and after deformation, respectively. Figures adapted from [238] (c), and [8] (d).

Supraphysiological loadings

Another relevant aspect of arterial mechanics is stress softening that occurs due to supraphysiological loading (e.g., balloon angioplasty or arterial clamping), see also Section 2.2.2. Thunes et al. [239] modeled this interesting phenomenon by including in their medial RVE (Fig. 2.6(d)) a linear decrease in collagen stiffness after a critical fiber stretch was exceeded. The model was thus able to capture the softening behavior of the macroscopic mechanical response of healthy samples of human ascending thoracic aortas under uniaxial loading (Fig. 2.12(a)). At the micro-scale, the RVE showed several highly

stressed segments (red) and failed (white) fiber segments at the point of maximum macro-stress ($\lambda = 1.45$), especially in fibers more aligned towards the circumferential (loading) direction. Importantly, the stresses in the ground substance around the failed fibers were consistently higher (see detailed view in Fig. 2.12(a)), which suggests that after collagen failure, the more compliant ground substance in these regions took the load. In general, these findings are in agreement with experimental results [39, 167, 264, 265], which correlate stress softening of arterial tissue at the macro-scale with damage and failure of collagen at the micro-scale.

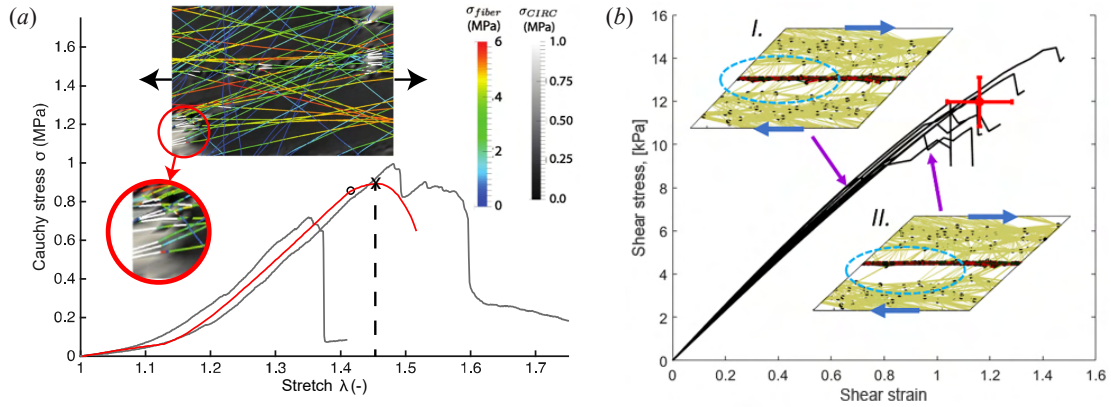

Figure 2.12: Micro-scale simulations of macroscopic stress softening due to fiber damage: (a) comparison between experimental results (gray curves) and model predictions (red curve) of uniaxial loading along the circumferential direction of medial samples. The circle represents the average experimental tissue strength and the x marks the stretch applied to the RVE shown right above the curve ($\lambda = 1.45$). Figures adapted from [239]; (b) shear loading of a medial RVE with delaminations due to failure of actin fibers. The red dot and error bars each represent the mean experimental failure behavior with a confidence interval of 95%. Adapted from [162].

Mahutga and Barocas [162] added a brittle damage model for actin, collagen and elastin fibers in their discrete RVE (Fig. 2.6(c)) assuming that they lose their load-bearing capacity immediately after a critical stretch value is exceeded (which varies depending on the fiber type). An interesting result can be seen in Fig. 2.12(b), which shows the homogenized mechanical response of different networks under shear along with a representative network before (I) and after (II) the onset of fiber failure. It can be seen that failure initiates in the network of actin fibers forming vSMCs and leads to local delamination (dashed ellipse in Fig. 2.12(b)), similar to what was observed experimentally in [91] for healthy bovine descending aortas and in [226] for diseased human thoracic aortas. Failure of actin fibers occurs near the elastic lamella, which may indicate vSMC detachment with possible negative effects on cell mechanotransduction [120]. Importantly, the macroscopic failure stresses predicted by the model are much lower for shear loads compared to uniaxial loads,

similar to what was measured in Sommer et al. [226] for aneurysmal and dissected aortic tissue, suggesting a central role of shear loads on aortic wall failure in the course of these diseases.

Growth and remodeling

A fairly common pathophysiological condition that leads to supraphysiological loading in arteries is chronic hypertension, i.e., a persistent elevation of blood pressure. As discussed in Section 2.2.3, vascular cells such as vSMCs and fibroblasts are able to sense the resulting alteration in tissue mechanics via their ECM and respond accordingly to bring it back to homeostatic values by promoting G&R of the arterial microstructure. In this context, another interesting study was performed by Mahutga and Barocas [162], whose RVE (Fig. 2.6(c)) included the possibility of growth and remodeling of actin and collagen fibers with the effect of hypertension in a mouse aorta in an FE^2 setting. At the macro-scale, the model employed the theory of kinematic growth, which assumes a multiplicative split of the macroscopic deformation gradient [2].

The results are shown in Fig. 2.13(a), where the RVE is shown immediately before (time = 135 days) and after (time = 300 days) the mean blood pressure was increased from 100 to 150 mmHg. After the increase, a considerable volumetric growth of the RVE is observed, which is reflected on the macro-scale as the *reference configuration* (0 mmHg intraluminal pressure) of the artery increases in diameter and thickness to restore baseline stress levels, as observed in experimental studies [121]. This effect can be seen in Fig. 2.13(b), where it is shown that after the increase in blood pressure, the G&R within the wall drives the macroscopic stress in the circumferential direction (blue curve) back to homeostatic levels. In particular, the stress level after the onset of hypertension is slightly higher than before, which highlights the choice of the Greek prefix *homeo* ('similar') as opposed to *homo* ('same') by Cannon when he introduced the concept of homeostasis in 1929 [23].

Figure 2.13(b) also shows that after the increase in blood pressure, the stiff collagen fibers initially bear most of the additional load, but after intensive G&R the actin fibers increase their share. This suggests that vSMCs play a central role in restoring homeostasis. In this context, Fig. 2.13(c) shows the lateral view of a remodeled RVE, in which thick actin fibers can be seen in the circumferential (horizontal) direction. It should be noted that the remodeling process in the model does not account for deposition of new fibers, i.e., fibers are only remodeled by altering their length and diameter. This drawback is discussed by the authors [162] and could potentially lead to different results if the possibility of adding new fibers to the network over the course of G&R was included in the model.

Another drawback of the model is that the artery was assumed to be formed only by the media at the macro-scale. To investigate the role of the adventitia in hypertension, Gacek et al. [76] created an FE^2 model in which the macro-scale consisted of three layers of finite

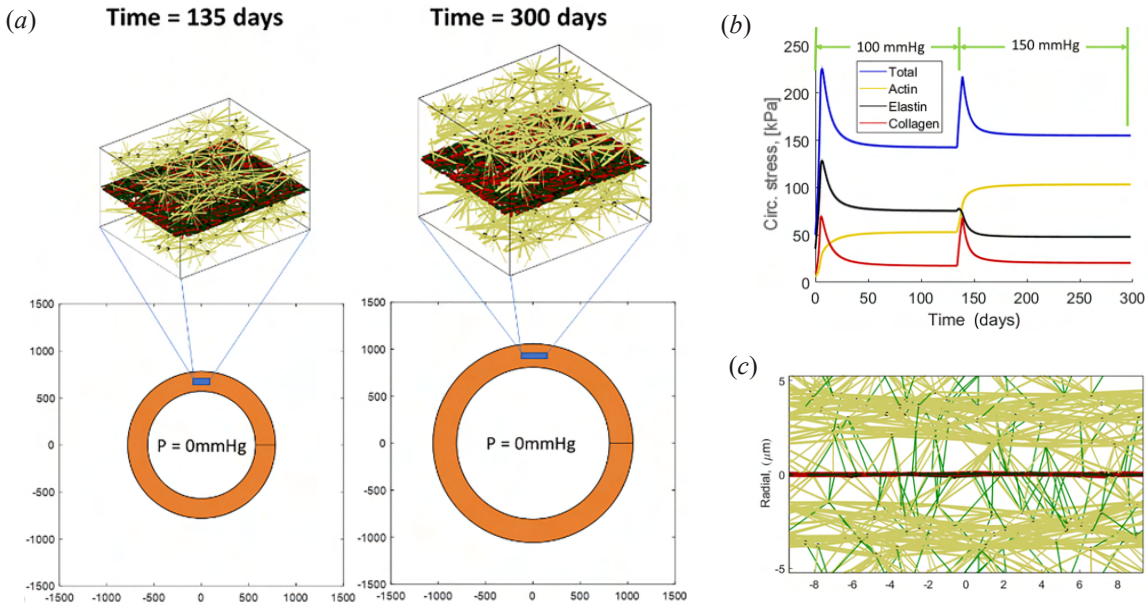

Figure 2.13: Predictions of tunica media growth and remodeling due to chronic hypertension: (a) RVE state before (time = 135 days) and after (time = 300 days) the increase of intraluminal blood pressure showing pronounced volumetric growth reflected in the reference geometry of the artery, which thickens and increases in diameter; (b) contributions of each fiber type to total stress; after the onset of hypertension, the microstructure remodels and the homogenized stress returns to a homeostatic level; (c) lateral view of a remodeled network with thick actin struts aligned along the circumferential direction. Figures adapted from [162].

elements representing the media, the micro-scale of which was modeled with a similar RVE as in [162] (Fig. 2.6(c)) and an outer layer representing the adventitia, the RVE of which consisted of trusses representing collagen fibers (Fig. 2.7(b)). In this case, the remodeling of the medial RVEs was more moderate and the adventitial layer absorbed much of the additional load, consistent with the much discussed protective role of the adventitia against overstretching [31, 109, 157].

Mechanobiology of AAAs

Another disease known to result in intense G&R of the arterial ECM is the formation and progression of abdominal aortic aneurysms, as discussed in Section 2.2.3. In this context, Dalbosco et al. [44] employed RVEs that consist of two families of collagen fibers embedded in an elastin-rich ground substance (Fig. 2.7(c)), to evaluate the theory of AAA pathogenesis proposed by Niestrawska et al. [185] (Fig. 2.4), with particular emphasis on the formation of the neo-adventitia on the abluminal side of the aortic wall. The orientation

of the collagen fibers was varied to match different stages of the disease, namely healthy adventitia and stages I and III (Fig. 2.4), which represent, respectively, the tissue stage before and after the development of the neo-adventitia due to the intense G&R of collagen in the tissue. Five stochastic RVEs were generated for each microstructure. To ensure realistic loading conditions during disease progression, the macroscopic deformation gradient $\mathbf{F}(\mathbf{X})$ (see Section 2.3.1) imposed on each RVE was determined from macro-scale tissue simulations of a healthy aorta (for the adventitial RVEs) and AAAs of increasing size (for stages I and III).

Figure 2.14(a) shows the resulting fields of maximum principal stretches λ_1 in representative RVEs of the healthy adventitia and of the aneurysm tissue. The values of λ_1 were interpreted as possible mechanotransduction cues sensed by vascular cells – particularly fibroblasts – since vSMCs are largely absent in AAA tissue [94, 122, 175, 185].

Qualitatively, it can be said that while strain levels in the diseased RVEs were consistently higher than in the healthy tissue, they were remarkably similar between the early and late microstructural stages of the disease (respectively, I and III), being only slightly higher for the latter. Furthermore, only negligible changes were observed with increasing diameter. This similarity is remarkable considering that both the geometry of the RVEs and the macroscopic deformation gradient $\mathbf{F}(\mathbf{X})$ applied to them were different for each case.

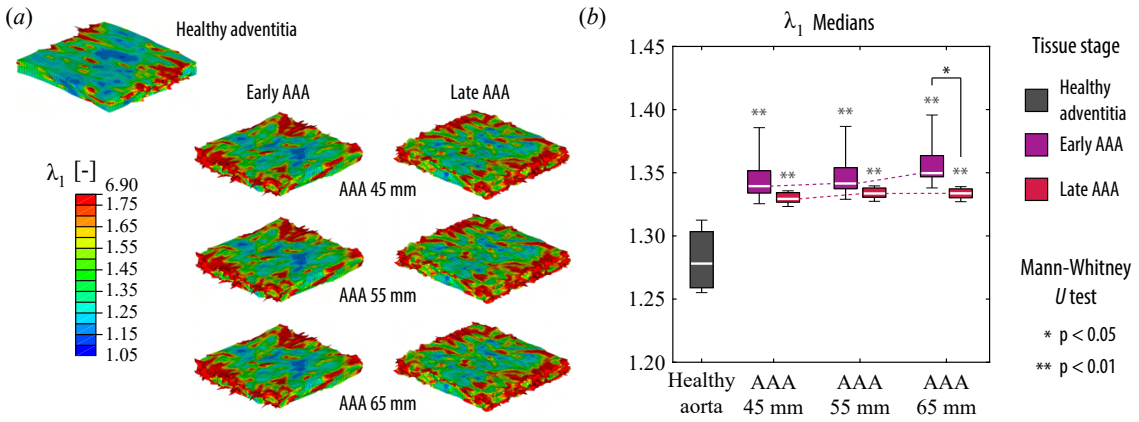

Figure 2.14: Prediction of micromechanical alterations in arterial tissue due to AAA pathogenesis (λ_1 = maximum principal stretch): (a) micro-scale AAAs of different sizes are stretched more with respect to the healthy adventitia, both for early (I) and late (III) microstructural stages, that are very similar as diameter increases; (b) boxplots of the median values of λ_1 for the seven groups of five RVE simulations. The level of deformation of diseased tissue is significantly higher than in the healthy RVEs, but remarkably stable along the AAA growth. Gray asterisks indicate the results of the Mann–Whitney U test for differences between each diseased group and the healthy group. Figures adapted from [44].

To better quantify the above differences, the median value of λ_1 from each RVE was calculated and summarized in the boxplot shown in Fig. 2.14(b). The Mann-Whitney U-test was used to examine differences between groups. It can be seen that the extent of deformation in the diseased RVEs is actually significantly higher than in the healthy adventitia, as in Fig. 2.14(a). Furthermore, there are no significant differences in the level of λ_1 between early and late microstructures, except for AAAs of 65 mm. These results suggest that as the disease progresses, both the macroscopic mechanics of the tissue and its microstructure change symbiotically due to the collagen G&R promoted by cells, with the aim of achieving an apparently new level of homeostatic mechanical state of their ECM. The significant difference in the level of λ_1 for the larger AAA diameter further suggests that the thick neo-adventitia forming in the abluminal size of the tissue may have a stabilizing effect on larger aneurysms, as the authors had suggested in a previous work [42].

2.4 Conclusions and future perspectives

As with most soft tissues, the mechanical behavior of arteries, which play a central role in vertebrate physiology, is strongly related to their microstructure. This microstructure is maintained – or adapted – by vascular cells, whose activity is controlled in part by mechanobiology. In this context, the results discussed in the previous section highlight the potential of RVE-based multiscale computational models in simulating the micromechanics of arteries while maintaining (via homogenization) good descriptive capabilities at the macro-scale (tissue level). Thus, despite their higher computational cost, such models can simulate microscopic phenomena (and their consequences at the macro-scale) that basically cannot be captured by macroscopic models, e.g., the delamination of the medial layer at cellular level due to shear (Fig. 2.12(b)). Nevertheless, there are some key aspects that could be considered in future experimental and computational studies to further improve RVE models of arteries:

- While histological and microscopy images have been paramount in establishing our current knowledge of the arterial microstructure, available 3D information is still limited. In this regard, advances in 3D imaging techniques and reconstructions [31, 188, 198] shall be crucial for the development of more realistic RVE geometries.
- In the same context, recent studies [31, 35, 36, 144, 145, 194, 195, 215] have provided detailed information on the kinematics of arterial microconstituents (particularly collagen fibers and elastin) under load, but appropriate multiscale boundary conditions that could reproduce these experimental results are still missing. In any case, as discussed in Section 2.3.2, future RVE-based simulations should always take into account the considerable influence of the chosen boundary condition on the predicted results.

- As already mentioned in Section 2.3.1, the computational cost of RVE-based models is much higher than purely macroscopic constitutive models, and for this reason a fully coupled simulation (FE^2) can easily become impractical due to the high number of degrees of freedom. Recently, some hybrid approaches [44, 76] have been proposed to lower the computational cost of coupled multiscale simulations, but improving the efficiency of such models – e.g., by using reduced order modeling techniques [95, 279] – is certainly a crucial area for future studies.
- To the best of the authors' knowledge, no RVE models of the tunica intima have been proposed to date. Although it is mechanically irrelevant in young, healthy arteries (see Section 2.2.1), the intimal layer of endothelial cells controls countless biological processes within the arterial wall [87, 165, 196, 244]. RVE-based models of the intima therefore have the potential to elucidate how arterial micromechanics influences these processes.

Although cardiovascular diseases have been diagnosed and treated since ancient times [74], they are still the leading cause of death worldwide [269]. The biological function of arteries is intrinsically mechanical (i.e., the conduction of pressurized blood). Therefore, the use of simulations has the potential of revolutionize cardiovascular healthcare [7]. In this context, RVE-based models in combination with patient-specific simulations [143] may provide a unique opportunity to visualize micro-mechanical phenomena that simply cannot be assessed experimentally using current techniques. The development of this interesting field of computational biomechanics therefore has the potential to foster a better understanding and treatment of cardiovascular diseases for the benefit of patients and physicians.

3 MULTISCALE NUMERICAL ANALYSES OF ARTERIAL TISSUE WITH EMBEDDED ELEMENTS IN THE FINITE STRAIN REGIME

Abstract. Multiscale models based on representative volume elements (RVEs) might help unraveling the ways in which macroscopic loadings affect the microstructure of tissues reinforced by collagen fibers, and vice versa. Tissues such as arteries, however, are characterized by a significant collagen dispersion. Therefore, many fibers have to be included in the RVE to achieve a representative geometrical model of the microstructure. For this reason, when the finite element method is employed in the numerical homogenization, fibers are commonly modeled as 1D elements, either by considering a network of trusses or the embedded elements technique. With regard to the latter, there has been little attention in previous works concerning the influence of the chosen multiscale boundary conditions and RVE size. In order to address this issue, the present work combines a sound multiscale framework with the classical embedded elements technique to simulate four increasingly larger RVEs, which resemble the microstructure of the medial layer of the arterial wall. Each RVE is modeled as a ground substance with embedded collagen fibers and subjected to a macroscopic isochoric equibiaxial stretch up to 10%, according to four classical multiscale boundary conditions: Taylor-Voigt, linear boundary displacements, periodic boundary fluctuations and minimally constrained model. Results are evaluated both at the macroscopic level (homogenized response) and the microscopic level (strains in the ground substance and fiber stretches). At the macroscopic level, the homogenized response for the periodic boundary condition seems to converge faster than the other three with increasing RVE size. At the microscopic level, the periodic model is also less prone to concentrated effects at the boundaries of the RVE. Therefore, among the four classical multiscale boundary conditions, the periodic model seems to be better suited to simulate the microstructure of fibrous tissues employing the embedded elements technique. Importantly, the resulting microscopic strain fields are characterized by a considerable degree of inhomogeneity and some values are significantly larger than the macroscopic (imposed) strain. That could help to shed more light on relevant mechanotransduction mechanisms, e.g., cell signaling, that are known to happen in the arterial media and are linked to biological processes such as growth and remodeling. Therefore, the framework herein proposed may serve as a valuable tool for the investigation of microstructural phenomena that happen in arteries, or even other fibrous tissues.

3.1 Introduction

Among the different types of biological tissues that may be regarded as composite materials, connective tissues stand out as a broad category that encompasses, e.g., skin,

tendons, cartilage and blood vessels [78, 149, 276]. Their mechanical behavior is usually anisotropic due to position, size, distribution and mechanical properties of reinforcing collagen fibers embedded in a soft ground substance that comprises other microconstituents [149]. The (healthy) arterial tissue, e.g., is composed of three clearly distinguishable layers – tunica intima, tunica media and tunica adventitia. Each one of them is characterized by different collagen fiber arrangements, resulting in a complex layered composite [105, 113, 183]. Due to their small size, the collagen fibers are not distinguishable from a macroscopic point of view. Therefore, a common modeling strategy involves accounting only for the *effect* of the reinforcing fibers, by suitably modifying the constitutive model in terms of invariants [102]. In the last few decades, this approach has been extensively employed in the modeling of arteries and other fibrous tissues; for a recent review see Holzapfel et al. [114] and references therein.

The mechanical behavior of the tissue under loading results from complex interactions between its microscopic constituents (e.g., collagen fibers, elastin layers and smooth muscle cells in the arterial wall), which also trigger important mechanotransduction mechanisms that might induce microstructural changes, pathological processes and, ultimately, alter the macroscopic response [11, 34, 122, 126, 185]. These relevant microscopic phenomena are more easily accounted for by means of multiscale models based on *representative volume elements* (RVEs) of the tissue [14, 26, 27, 29, 51, 202, 220, 228, 232, 238, 239, 271], in which a geometric model of the microstructure is built and simulated, and the macroscopic response is obtained through homogenization of the microscopic fields; this approach has the advantage of allowing not only for the comparison of the macroscopic response of the tissue with experimental data, but also for the evaluation of, e.g., the mechanical interaction between different microstructural material phases [27, 51, 228].

In this direction, a number of multiscale models were developed for a myriad of biological tissues, e.g., tendons [26, 27, 29], bones [170, 254, 278] and arteries [14, 202, 220, 228, 232, 238, 239, 271]. With specific regard to the latter, the dispersion observed in the collagen network of the tissue means that a large number of fibers must be included in the RVE order to achieve a representative microstructure. Therefore, when the finite element method (FEM) is employed, a common strategy involves modeling the collagen reinforcement as 1D elements. Following this approach, Stylianopoulos and Barocas [232] employed a two-scale approach to simulate the classical problem of 'closing' a stress-free arterial segment, and then subjecting it to an axial stretch followed by intraluminal pressurization [109]. At each integration point of the macroscopic, continuum mesh, the stress was calculated as the sum of a nearly-incompressible neo-Hookean ground substance and the volumetric average of a set of exponential collagen fibers. This average was obtained, via numerical homogenization, from an RVE made of a network of truss elements with certain preferential directions (which are characteristic of arteries [113]). The results at the macroscopic level were then compared with an experimental curve of pressure and mean diameter.

In subsequent works, the model was further specialized to include fiber damage [220] and also the effect of elastin layers and interlamellar connections [271]. However, as pointed out by Rocha et al. [202], none of these studies provide a detailed discussion on the kinematic relation between the macro- and micro-scales for the fiber network, and only the multiscale linear boundary displacements model (addressed in Section 3.2.2) was considered. From a biomechanical point of view, the strong assumption that the fiber network and the ground substance deform independently does not allow for a proper evaluation of the interaction between the two at the microscopic level. It is also worth mentioning that the computational costs involved in this kind of two-scale simulations tend to be considerably high: all the numerical analyses of the cited studies were run on clusters [220, 232, 271].

Speirs et al. [228] constructed an RVE composed of an elastin sheet (discretized with plane stress elements) overlaid with truss elements representing collagen fibers. The elastin was modeled as an incompressible neo-Hookean material, while a tensile-only logarithmic strain-energy with recruitment stretch (different for each fiber) was assumed for the collagen fibers. The trusses were oriented along two preferential directions, but the characteristic fiber dispersion seen in arteries [113] was not taken into account. Employing a sound multiscale framework, based on kinematic admissibility and energy consistency between scales (see Section 3.2.2 for more details), the macroscopic stress was obtained by means of a volumetric average of the microscopic stresses when the RVE was subjected to biaxial isochoric deformations, considering boundary conditions of both Taylor and periodic types. Since in this approach only the micro-scale is simulated, this allows for much lower computational costs. Even so, the homogenized response still allowed for a macroscopic evaluation of the mechanical behavior, which was then compared with two different numerical models. However, experimental data was considered only indirectly in their work and no analysis was performed on the resulting microscopic fields.

Following a different approach, Thunes et al. [238] modeled an RVE of the medial layer of an artery using the classical embedded elements technique, in which a mesh of reinforcing truss elements (acting as elastin and collagen fibers) was embedded into a 3D mesh (representing the ground substance), whose deformation is affected by the reinforcement. The network of trusses was constructed based on experimental measurements of fiber dispersion in tricuspid and bicuspid ascending thoracic aortic aneurysms published in the literature. Nevertheless, the out-of-plane dispersion, which is considerably influential to the mechanical response of aortic aneurysms [183], was not considered. The ground substance was modeled as an incompressible neo-Hookean material, while collagen fibers were modeled as tensile-only linear trusses with recruitment stretch. Each RVE was then subjected to two numerical tests, corresponding to uniaxial stretches in the circumferential and longitudinal directions of the artery, respectively. However, no discussion was made on the kinematic relation between the (simulated) microstructure and the (averaged) macroscopic response, and the influence of different boundary conditions was not investigated. Moreover, the averaged stress response, which was compared with experimental data, was calculated from the reaction forces at the boundary nodes, as opposed to the more usual

approach of volumetric averaging. Further studies specialized the model to include, e.g., fiber damage [164, 239], but did not address these issues.

Motivated by the fact that most of the multiscale models employing 1D elements do not investigate the effect of different boundary conditions, as discussed above, Rocha et al. [202] developed a comprehensive framework based on kinematic admissibility and energy consistency between scales that may be used for multiscale simulation of a network of trusses. The minimally constrained space of admissible microscopic displacement fields was defined and several aspects of the theoretical framework, including RVE size convergence and the influence of multiscale boundary conditions over the macroscopic (homogenized) response, were investigated. However, the fact that no ground substance was included in the model hinders the evaluation of important interactions between the collagen fibers and other microscopic constituents, which are known to play a crucial role in several biological processes in fibrous tissues [11, 34, 122, 126, 185].

Based on the above considerations, the present work aims to investigate the effect of boundary conditions and size on multiscale simulations of RVEs with the embedded elements technique, which allows for the inclusion of the ground substance. To the best of the authors' knowledge, such issues have not been properly investigated in previous works. The goal is to obtain a reliable framework for the investigation of micromechanical phenomena (e.g. mechanotransduction mechanisms) in arteries, and possibly other fibrous tissues. To that end, the RVE-based multiscale theory detailed in [49] is suitably adapted in order to comply with the embedded elements formulation. The medial layer of the healthy arterial tissue is employed as a representative example, and numerical experiments are performed on RVEs constructed from a network of fibers resembling the characteristic fiber organization seen in the tunica media of the arterial wall [113]. The influence of RVE size and multiscale boundary conditions is then evaluated in terms of the macroscopic (homogenized) response, as well as the microscopic fields both at the ground substance and at the fibers.

This paper is organized as follows: Section 3.2 recalls some important aspects of the embedded elements technique [83], of the aforementioned multiscale theory [16, 50] and of the characteristic collagen fiber dispersion observed in arteries [113]. Section 3.3 proposes a series of numerical experiments on RVEs based in the medial layer of healthy arteries, which aim to investigate the aspects discussed above. The results of such experiments are presented and discussed in Section 3.4, and Section 3.5 summarizes the main conclusions of the present work. Additional details are presented in the Appendices.

3.2 Theoretical background

3.2.1 Embedded elements technique

As commented by Goudarzi and Simone [83], the embedded elements technique seems to have been introduced by Phillips and Zienkiewicz [193], originally developed for the simulation of reinforced concrete. Briefly, it consists in placing a 'reinforcement mesh' of (usually 1D) finite elements inside a 'host mesh' of (2D or 3D) finite elements. A kinematic bond is then imposed upon the reinforcement mesh by means of the shape functions of the elements of the host mesh, which therefore may be generated independently of the reinforcement layout [67, 77, 193].

This section recalls some main aspects of the method, which is implemented in most commercial finite element (FE) codes. In the present approach, a 'no-slip' condition is assumed between the reinforcement and the ground substance [90, 193]. Further details regarding the FE implementation in terms of isoparametric elements in a large strain setting are presented in Appendix A.

Kinematics

Let $\Omega_0 \subset \mathbb{R}^3$ be a continuum body which deforms to $\Omega \subset \mathbb{R}^3$ in a quasi-static manner (Fig. 3.1). Let $\chi : \Omega_0 \to \Omega$ be a smooth bijective map that describes the deformation of the body, such that the spatial position $\mathbf{x} \in \Omega$ is defined for all material points $\mathbf{X} \in \Omega_0$ by the relation $\mathbf{x} = \chi(\mathbf{X})$. The displacement field $\mathbf{u} : \Omega_0 \to \mathbb{R}^3$ is then defined as

$$\mathbf{u}(\mathbf{X}) = \chi(\mathbf{X}) - \mathbf{X}, \qquad \forall \mathbf{X} \in \Omega_0. \tag{3.1}$$

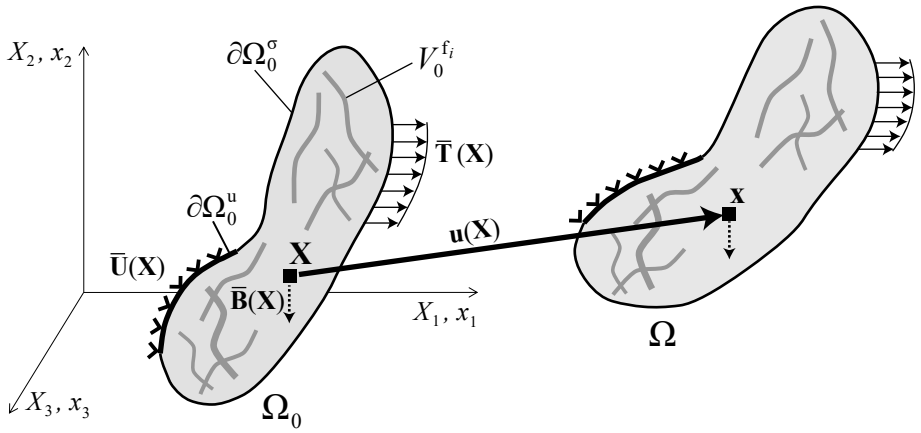

Figure 3.1: Quasi-static deformation of a continuum body Ω_0 with N_{f_T} embedded fibers, each one of them with initial volume $V_0^{f_i}$.

The deformation takes place due to the field $\overline{\mathbf{U}}: \partial\Omega_0^{\mathrm{u}} \to \mathbb{R}^3$ of displacements prescribed on the portion $\partial\Omega_0^{\mathrm{u}}$ of the boundary $\partial\Omega_0$, combined with both the body load field $\overline{\mathbf{B}}: \Omega_0 \to \mathbb{R}^3$, and the surface traction field $\overline{\mathbf{T}}: \partial\Omega_0^{\sigma} \to \mathbb{R}^3$ prescribed on the portion $\partial\Omega_0^{\sigma}$ of the boundary $\partial\Omega_0$ (where $\partial\Omega_0^{\mathrm{u}} \cup \partial\Omega_0^{\sigma} = \partial\Omega_0$ and $\partial\Omega_0^{\mathrm{u}} \cap \partial\Omega_0^{\sigma} = \varnothing$). Using Eq. (3.1), the deformation may be described at each point $\mathbf{X} \in \Omega_0$ in terms of the deformation gradient $\mathbf{F}(\mathbf{X})$, defined as

$$\mathbf{F}(\mathbf{X}) = \frac{\partial \chi(\mathbf{X})}{\partial \mathbf{X}} \equiv \mathbf{I} + \operatorname{Grad}\mathbf{u}(\mathbf{X}), \qquad \forall \mathbf{X} \in \Omega_0, \tag{3.2}$$

where $\mathbf{I}$ is the identity second-order tensor and $\operatorname{Grad}\mathbf{u}(\mathbf{X})$ is the gradient of the vector field $\mathbf{u}(\mathbf{X})$ at the reference configuration.

Principle of virtual work

We assume henceforth that the body Ω_0 consists of an hyperelastic ground substance g with $N_{\mathrm{f_T}}$ hyperelastic embedded fibers, each one of them with initial volume $V_0^{\mathrm{f}_i} \subset \Omega_0$ (Fig. 3.1). Let $\pi(\mathbf{u})$ be an energy functional such that

$$\pi(\mathbf{u}) = \pi_{\mathrm{int}}(\mathbf{u}) + \pi_{\mathrm{ext}}(\mathbf{u}), \tag{3.3}$$

where the external energy functional $\pi_{\mathrm{ext}}(\mathbf{u})$ is defined, as usual [102], by

$$\pi_{\mathrm{ext}}(\mathbf{u}) = -\int_{\Omega_0} \overline{\mathbf{B}} \cdot \mathbf{u}\, \mathrm{d}V - \int_{\partial\Omega_0^{\sigma}} \overline{\mathbf{T}} \cdot \mathbf{u}\, \mathrm{d}S, \tag{3.4}$$

and the herein proposed internal energy functional $\pi_{\mathrm{int}}(\mathbf{u})$ is defined by

$$\pi_{\mathrm{int}}(\mathbf{u}) = \int_{\Omega_0 \setminus V_0^{\mathrm{f_T}}} \psi_{\mathrm{g}}(\mathbf{F})\, \mathrm{d}V + \sum_{i=1}^{N_{\mathrm{f_T}}} \int_{V_0^{\mathrm{f}_i}} \psi_{\mathrm{f}_i}(\mathbf{F})\, \mathrm{d}V, \tag{3.5}$$

where $V_0^{\mathrm{f_T}} = \sum_{i=1}^{N_{\mathrm{f_T}}} V_0^{\mathrm{f}_i}$ is the total (initial) volume of fibers. In Eq. (3.5) an additive decomposition of the internal strain energy of the body is assumed, which means that it is divided between the ground substance g (i.e., ψ_{g}), and the $N_{\mathrm{f_T}}$ embedded fibers (i.e., ψ_{f_i}). Since

the deformation gradient $\mathbf{F}$ is continuous over Ω_0 ('no-slip' condition), Eq. (3.5) may be rewritten as

$$\pi_{\text{int}}(\mathbf{u}) = \int_{\Omega_0} \psi_{\text{g}}(\mathbf{F})\,\mathrm{d}V - \sum_{i=1}^{N_{\text{f}_\text{T}}} \int_{V_0^{\text{f}_i}} \psi_{\text{g}}(\mathbf{F})\,\mathrm{d}V + \sum_{i=1}^{N_{\text{f}_\text{T}}} \int_{V_0^{\text{f}_i}} \psi_{\text{f}_i}(\mathbf{F})\,\mathrm{d}V, \tag{3.6}$$

$$\pi_{\text{int}}(\mathbf{u}) = \int_{\Omega_0} \psi_{\text{g}}(\mathbf{F})\,\mathrm{d}V + \sum_{i=1}^{N_{\text{f}_\text{T}}} \int_{V_0^{\text{f}_i}} \psi_{\text{c}_i}(\mathbf{F})\,\mathrm{d}V, \tag{3.7}$$

where $\psi_{\text{c}_i}(\mathbf{F}) = \psi_{\text{f}_i}(\mathbf{F}) - \psi_{\text{g}}(\mathbf{F})$ may be seen as a 'correction' strain energy, which addresses the known issue of volume redundancy in models with embedded reinforcement (see, e.g., the discussion in Garimella et al. [77]). The principle of virtual work results from the stationary condition of the energy functional, such that, if the directional derivative

$$D_{\delta\mathbf{u}}\pi(\mathbf{u}) \equiv \delta\pi = \delta\pi_{\text{int}} + \delta\pi_{\text{ext}} = \delta W_{\text{int}} - \delta W_{\text{ext}} = 0, \qquad \forall\,\delta\mathbf{u} \in \mathbb{V}, \tag{3.8}$$

where $\mathbb{V} = \{\,\delta\mathbf{u} : \Omega_0 \to \mathbb{R}^3 \mid \delta\mathbf{u}(\mathbf{X}) = \mathbf{0},\ \forall\,\mathbf{X} \in \partial\Omega_0^{\text{u}}\,\}$ is the space of admissible virtual displacements $\delta\mathbf{u}$, then the displacement field $\mathbf{u}$ is the solution of the equilibrium problem. By employing the chain rule in Eq. (3.8) and recalling the hyperelasticity of the fibers and of the ground substance, we get

$$\int_{\Omega_0} \mathbf{P}_{\text{g}} : \delta\mathbf{F}\,\mathrm{d}V + \sum_{i=1}^{N_{\text{f}_\text{T}}} \int_{V_0^{\text{f}_i}} \mathbf{P}_{\text{c}_i} : \delta\mathbf{F}\,\mathrm{d}V - \int_{\Omega_0} \overline{\mathbf{B}} \cdot \delta\mathbf{u}\,\mathrm{d}V - \int_{\partial\Omega_0^{\sigma}} \overline{\mathbf{T}} \cdot \delta\mathbf{u}\,\mathrm{d}S = 0, \qquad \forall\,\delta\mathbf{u} \in \mathbb{V}, \tag{3.9}$$

which is the principle of virtual work. In Eq. (3.9), $\mathbf{P}_{\text{g}}$ and $\mathbf{P}_{\text{c}_i}$ are the first Piola-Kirchhoff stress tensors of the ground substance g and of the correction of the i-th fiber f_i, respectively, and $\delta\mathbf{F} = \operatorname{Grad}\delta\mathbf{u}$ is the first variation of the deformation gradient $\mathbf{F}$.

The task of finding the displacement field $\mathbf{u}$ that satisfies (3.9) is normally tackled by means of numerical methods such as the FEM. Implementation strategies with respect to the latter are available in the literature, but usually in a small strain setting (e.g., [83, 90]). Therefore, a FEM implementation suitable for finite strain simulations is presented in Appendix A.

3.2.2 RVE-based multiscale theory

The past decades have seen the development of several multiscale theories, which aim to relate the macroscopic behavior of continua to physical phenomena taking place at smaller scales. In the field of solid mechanics, the works of Hill [97–100] and Mandel [166], among others, have provided a robust framework for the estimation of the macroscopic mechanical response of heterogeneous materials. More recently, theories based on the concept of a *representative volume element* (RVE) have been developed within the context of computational mechanics, often combined with the FEM, in which the stresses and strains at the macro-scale result from the volumetric average (over the RVE) of their microscopic counterparts; for a comprehensive review, see Blanco et al. [16] and references therein.

This section recalls some main aspects of a particular RVE-based multiscale theory detailed in de Souza Neto and Feijóo [49], which will be employed in the present work. The underlying concepts of the theory, which is based on *kinematic admissibility* and *energy consistency* between scales, will be reviewed. The theory will then be specialized to the context of embedded elements by assuming the same decomposition of the strain energy between ground substance and fibers, as in the previous section, in order to obtain the *micro-scale equilibrium equation* and the *stress homogenization* relation.

Kinematics

Let $\Omega_0 \subset \mathbb{R}^3$ be the reference configuration of a macroscopic continuum body (with characteristic length l) that deforms to $\Omega \subset \mathbb{R}^3$ in a quasi-static manner (Fig. 3.2). We assume that each point $\mathbf{X} \in \Omega_0$ is associated with a representative volume element $\Omega_0^\mu \subset \Omega_0$ with characteristic length $l^\mu \ll l$, which deforms to $\Omega^\mu \subset \Omega$. The domains Ω_0, Ω and Ω_0^μ, Ω^μ are referred to as macro- and micro-scales, respectively. While the microscopic RVE Ω_0^μ is considered small enough in order to be representative of the local behavior of the material at the macroscopic level, it is assumed that it is large enough to still be regarded as a continuum body and to be representative enough of the microstructure of Ω_0.

We now define a macroscopic displacement field $\mathbf{u} : \Omega_0 \to \mathbb{R}^3$ as well as a microscopic displacement field $\mathbf{u}^\mu : \Omega_0^\mu \to \mathbb{R}^3$ in the same way as in Eq. (3.1). These fields are related by the kinematic averaging (homogenization) relationships [50]

$$\mathbf{u} = \frac{1}{V^\mu} \int_{\Omega_0^\mu} \mathbf{u}^\mu \, \mathrm{d}V^\mu \qquad \text{and} \qquad \mathbf{F} = \frac{1}{V^\mu} \int_{\Omega_0^\mu} \mathbf{F}^\mu \, \mathrm{d}V^\mu, \tag{3.10}$$

where $\mathbf{F}$ and $\mathbf{F}^\mu$ are, respectively, the macroscopic and microscopic deformation gradients, defined in the same way as in Eq. (3.2), and V^μ is the volume of the RVE. It may be

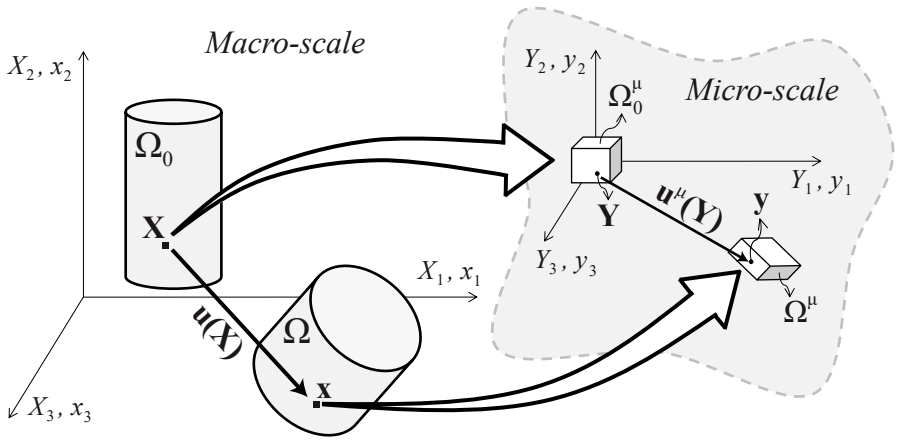

Figure 3.2: Deformation of a continuum body Ω_0 and of the microscopic RVE Ω_0^μ at point $\mathbf{X} \in \Omega_0$.

shown [50] that these kinematic averaging relationships represent constraints on the microscopic displacement field $\mathbf{u}^\mu$, preventing, respectively, rigid body translations (Eq. $(3.10)_1$) and rigid body rotations (Eq. $(3.10)_2$) of the RVE. Hence, only the microscopic displacement fields $\mathbf{u}^\mu$ that comply with Eq. (3.10) may be candidate solutions for the equilibrium of the RVE. This motivates the definition of the so-called *minimally constrained space of kinematically admissible microscopic displacements* as [16, 28, 50]

$$\mathcal{K}^{\min}_{\mathbf{u}^\mu} \equiv \left\{ \mathbf{u}^\mu \in H^1(\Omega_0^\mu) \;\middle|\; \mathbf{u} - \frac{1}{V^\mu}\int_{\Omega_0^\mu} \mathbf{u}^\mu \, \mathrm{d}V^\mu = \mathbf{0} \;\text{ and }\; \mathbf{F} - \frac{1}{V^\mu}\int_{\Omega_0^\mu} \mathbf{F}^\mu \, \mathrm{d}V^\mu = \mathbf{0} \right\}, \quad (3.11)$$

where $H^1(\Omega_0^\mu)$ is the first-order Sobolev space. The corresponding space of *virtual* kinematically admissible microscopic displacements is then defined as

$$\mathcal{V}^{\min}_{\mathbf{u}^\mu} \equiv \left\{ \mathbf{w} = \mathbf{w}_1 - \mathbf{w}_2 \;\middle|\; \mathbf{w}_1, \mathbf{w}_2 \in \mathcal{K}^{\min}_{\mathbf{u}^\mu} \right\}. \quad (3.12)$$

By assuming, without loss of generality, a linear expansion of the microscopic displacement field $\mathbf{u}^\mu$ in terms of the macroscopic deformation gradient $\mathbf{F}$, de Souza Neto et al. [50] have shown that $\mathcal{K}^{\min}_{\mathbf{u}^\mu}$ (Eq. (3.11)) may be rewritten as

$$\mathcal{K}^{\min}_{\mathbf{u}^\mu} \equiv \left\{ \mathbf{u}^\mu = \mathbf{u} + [\mathbf{F} - \mathbf{I}]\mathbf{Y} + \tilde{\mathbf{u}}^\mu, \forall \mathbf{Y} \in \Omega_0^\mu \;\middle|\; \tilde{\mathbf{u}}^\mu \in \mathcal{V}^{\min}_{\tilde{\mathbf{u}}^\mu} \right\}, \quad (3.13)$$

where the higher-order terms $\tilde{\mathbf{u}}^\mu$ are the so-called *displacement fluctuations*. As discussed by the authors, while the space $\mathcal{K}^{\min}_{\mathbf{u}^\mu}$ contains all the possible microscopic displacement

fields that comply with the kinematic postulates of the present theory, it is perfectly acceptable (and sometimes quite useful, as demonstrated, e.g., in [28, 29]) to *further* restrict this kinematic space, provided that the resulting set of admissible microscopic displacements is a subset of $\mathcal{K}^{\min}_{\mathbf{u}^\mu}$. While this implies that a large array of different kinematic models may be constructed, four classical multiscale boundary conditions [50] will be considered in the present work:

1. *Taylor-Voigt model*, also known as *uniform strain* or *rule of mixtures*: this model assumes that the deformation at every point of the microscopic domain Ω^μ_0 is defined by the macroscopic deformation gradient $\mathbf{F}$; this corresponds to postulating that the displacement fluctuations $\tilde{\mathbf{u}}^\mu$ vanish over all the RVE domain, or

$$\mathcal{K}^{\text{tay}}_{\mathbf{u}^\mu} \equiv \left\{ \mathbf{u}^\mu = \mathbf{u} + [\mathbf{F} - \mathbf{I}]\mathbf{Y}, \forall \mathbf{Y} \in \Omega^\mu_0 \right\}. \tag{3.14}$$

2. *Linear boundary displacements model*, also known as *uniform boundary strain*: in this case, it is assumed that the displacement fluctuations $\tilde{\mathbf{u}}^\mu$ vanish only over the *boundary* $\partial\Omega^\mu_0$ of the RVE, which is equivalent to postulating that the deformation at every point of $\partial\Omega^\mu_0$ is controlled by the macroscopic deformation gradient $\mathbf{F}$, or

$$\mathcal{K}^{\text{lin}}_{\mathbf{u}^\mu} \equiv \left\{ \mathbf{u}^\mu = \mathbf{u} + [\mathbf{F} - \mathbf{I}]\mathbf{Y} + \tilde{\mathbf{u}}^\mu, \forall \mathbf{Y} \in \Omega^\mu_0 \;\middle|\; \tilde{\mathbf{u}}^\mu(\mathbf{Y}) = \mathbf{0}, \forall \mathbf{Y} \in \partial\Omega^\mu_0 \right\}. \tag{3.15}$$

3. *Periodic boundary fluctuations model*: given an RVE with periodic boundaries $\partial\Omega^\mu_0$, the displacement fluctuations $\tilde{\mathbf{u}}^\mu$ are postulated to coincide in each pair of $(\mathbf{Y}^+, \mathbf{Y}^-)$ points, where $\mathbf{Y}^+$ is a point at one side (or surface) of the pair and $\mathbf{Y}^-$ is the corresponding, symmetric point at the other side (or surface). In mathematical terms, we may write

$$\mathcal{K}^{\text{per}}_{\mathbf{u}^\mu} \equiv \left\{ \mathbf{u}^\mu = \mathbf{u} + [\mathbf{F} - \mathbf{I}]\mathbf{Y} + \tilde{\mathbf{u}}^\mu, \forall \mathbf{Y} \in \Omega^\mu_0 \;\middle|\; \tilde{\mathbf{u}}^\mu(\mathbf{Y}^+) = \tilde{\mathbf{u}}^\mu(\mathbf{Y}^-), \right.$$
$$\left. \forall (\mathbf{Y}^+, \mathbf{Y}^-) \in \partial\Omega^\mu_0 \right\}. \tag{3.16}$$

4. *Minimally constrained model*, also known as *uniform traction on the boundaries*: in this case, no additional restriction is imposed and the space of admissible microscopic displacements equals the one defined in Eq. (3.13). Then it may be shown that this implies [49]

$$\mathbf{P}^\mu(\mathbf{Y})\hat{\mathbf{n}}(\mathbf{Y}) = \mathbf{P}\hat{\mathbf{n}}(\mathbf{Y}), \quad \forall \mathbf{Y} \in \partial\Omega^\mu_0, \tag{3.17}$$

where $\mathbf{P}^{\mu}$ and $\hat{\mathbf{n}}$ are, respectively, the microscopic first Piola-Kirchhoff stress tensor and the boundary normal vector at $\mathbf{Y}$. The macroscopic (homogenized) first Piola-Kirchhoff stress tensor $\mathbf{P}$ (at the point $\mathbf{X} \in \Omega_0$) is related to $\mathbf{P}^{\mu}$ by an averaging relationship similar to Eq. $(3.10)_2$.

Principle of multiscale virtual work

Starting from the original theory, we will henceforth assume a decomposition of the microscopic RVE domain Ω_0^{μ} into a ground substance g and $N_{\mathrm{f_T}}$ embedded fibers, analogously to what was done in Eq. (3.5). We emphasize that, since the displacement field $\mathbf{u}^{\mu}$ and the deformation gradient $\mathbf{F}^{\mu}$ are continuous over Ω_0^{μ} ('no-slip' condition), the integrals in Eq. (3.10) do not need to be decomposed and all the kinematic theory discussed in the previous section remains valid.

In order to ensure energy consistency between the macro- and microscopic scales, we start by considering the *principle of multiscale virtual work* derived by de Souza Neto et al. [50] from the well-known Hill-Mandel principle of macro-homogeneity. The principle states that the virtual work at the macro-scale coincides with the volumetric average of its counterpart on the micro-scale, such that

$$\mathbf{P} : \delta\mathbf{F} = \frac{1}{V^{\mu}} \int_{\Omega_0^{\mu}} \mathbf{P}^{\mu} : \delta\mathbf{F}^{\mu} \, \mathrm{d}V^{\mu}, \quad \forall\, \delta\mathbf{F}; \forall\, \delta\mathbf{u}^{\mu} \in \mathcal{V}_{\mathbf{u}^{\mu}}, \tag{3.18}$$

where $\delta\mathbf{F}^{\mu} = \mathrm{Grad}\, \delta\mathbf{u}^{\mu}$ and $\mathcal{V}_{\mathbf{u}^{\mu}} \subset \mathcal{V}_{\mathbf{u}^{\mu}}^{\min}$ is an admissible multiscale model. By means of the linear expansion of the microscopic displacement field $\mathbf{u}^{\mu}$ in terms of the macroscopic deformation gradient $\mathbf{F}$ (Eq. (3.13)), one can show that Eq. (3.18) may be rewritten as [50]

$$\mathbf{P} : \delta\mathbf{F} = \frac{1}{V^{\mu}} \int_{\Omega_0^{\mu}} \mathbf{P}^{\mu} : (\delta\mathbf{F} + \mathrm{Grad}\, \delta\tilde{\mathbf{u}}^{\mu}) \, \mathrm{d}V^{\mu}, \quad \forall\, \delta\mathbf{F}; \forall\, \delta\tilde{\mathbf{u}}^{\mu} \in \mathcal{V}_{\tilde{\mathbf{u}}^{\mu}}. \tag{3.19}$$

Now, by considering the same additive decomposition as in Eq. (3.5), we assume that the virtual work at the micro-scale is divided between the ground substance g and the $N_{\mathrm{f_T}}$ embedded fibers, such that

$$\mathbf{P} : \delta\mathbf{F} = \frac{1}{V^{\mu}} \left[\int_{\Omega_0^{\mu}} \mathbf{P}_{\mathrm{g}}^{\mu} : (\delta\mathbf{F} + \operatorname{Grad} \delta\tilde{\mathbf{u}}^{\mu}) \, \mathrm{d}V^{\mu} + \sum_{i=1}^{N_{\mathrm{f_T}}} \int_{V_0^{\mathrm{f}_i}} \mathbf{P}_{\mathrm{c}_i}^{\mu} : (\delta\mathbf{F} + \operatorname{Grad} \delta\tilde{\mathbf{u}}^{\mu}) \, \mathrm{d}V^{\mu} \right], \quad \forall \, \delta\mathbf{F}; \forall \, \delta\tilde{\mathbf{u}}^{\mu} \in \mathcal{V}_{\tilde{\mathbf{u}}^{\mu}}, \tag{3.20}$$

where $\mathbf{P}_{\mathrm{g}}^{\mu}$ and $\mathbf{P}_{\mathrm{c}_i}^{\mu}$ are the first Piola-Kirchhoff stress tensors of the ground substance and of the correction of the i-th fiber f_i, respectively, as defined in Eq. (3.9). Since the variations of the fluctuations are arbitrary, we choose $\delta\tilde{\mathbf{u}}^{\mu} \equiv \mathbf{0}$ and recall that the macroscopic deformation gradient $\mathbf{F}$ is constant in all the microscopic domain Ω_0^{μ} in order to write

$$\left[\mathbf{P} - \frac{1}{V^{\mu}} \left(\int_{\Omega_0^{\mu}} \mathbf{P}_{\mathrm{g}}^{\mu} \, \mathrm{d}V^{\mu} + \sum_{i=1}^{N_{\mathrm{f_T}}} \int_{V_0^{\mathrm{f}_i}} \mathbf{P}_{\mathrm{c}_i}^{\mu} \, \mathrm{d}V^{\mu} \right) \right] : \delta\mathbf{F} = 0, \, \forall \, \delta\mathbf{F}, \tag{3.21}$$

and since $\delta\mathbf{F}$ is also arbitrary, we get

$$\mathbf{P} = \frac{1}{V^{\mu}} \left(\int_{\Omega_0^{\mu}} \mathbf{P}_{\mathrm{g}}^{\mu} \, \mathrm{d}V^{\mu} + \sum_{i=1}^{N_{\mathrm{f_T}}} \int_{V_0^{\mathrm{f}_i}} \mathbf{P}_{\mathrm{c}_i}^{\mu} \, \mathrm{d}V^{\mu} \right), \tag{3.22}$$

which is the *stress homogenization* relation. Similarly, we now choose $\delta\mathbf{F} \equiv \mathbf{0}$ in Eq. (3.20) in order to get the *micro-scale equilibrium equation*

$$\int_{\Omega_0^{\mu}} \mathbf{P}_{\mathrm{g}}^{\mu} : \operatorname{Grad} \delta\tilde{\mathbf{u}}^{\mu} \, \mathrm{d}V^{\mu} + \sum_{i=1}^{N_{\mathrm{f_T}}} \int_{V_0^{\mathrm{f}_i}} \mathbf{P}_{\mathrm{c}_i}^{\mu} : \operatorname{Grad} \delta\tilde{\mathbf{u}}^{\mu} \, \mathrm{d}V^{\mu} = 0, \quad \forall \, \delta\tilde{\mathbf{u}}^{\mu} \in \mathcal{V}_{\tilde{\mathbf{u}}^{\mu}}. \tag{3.23}$$

By comparing Eq. (3.23) with Eq. (3.9) one can see that the embedded elements technique described in Section 3.2.1 may be directly applied to solve the equilibrium problem of the RVE using the FEM. We point out that since a 'no-slip' condition is assumed, no additional degrees of freedom associated with the reinforcement mesh are added to the system (see Appendix A for more details). Therefore, the implementation strategies available in the literature (e.g., [49, 172, 208]) for the four classical multiscale models may be readily employed.

3.2.3 Collagen fiber distribution in arterial tissue

The healthy arterial wall is composed of three clearly distinguishable layers: the *tunica intima* (innermost layer), *tunica media* (middle layer) and *tunica adventitia* (outermost layer). Each layer is characterized by an intricate microstructure, composed of vascular cells embedded in an *extracellular matrix*, a complex network of collagen fibers, elastic fibers, elastin layers and other components [102, 103, 113, 200].

The (passive) mechanical behavior of the arterial tissue is dominated by the extracellular matrix, particularly the elastin and collagen components [103, 149, 199]. At low stretches, the highly compliant elastin bears most of the load; at higher stretches, the collagen fibers – which are wavy in the unloaded state – get straightened up and start bearing load. This phenomenon, known as *fiber recruitment*, leads to the characteristic J-shaped mechanical response of the arterial tissue [176, 200, 234].

This response is usually anisotropic, since the distribution of collagen fibers is not uniform, but rather oriented (with some degree of dispersion) along two preferential directions in the circumferential-axial plane of the artery [113, 216]. These directions, which are usually different for each layer, are represented by the $\pm\alpha$ angles in Fig. 3.3(a). In the radial-axial plane, the collagen fibers show a comparatively small degree of dispersion, which, however, might get higher in diseased tissue (e.g., in aneurysms) [183].

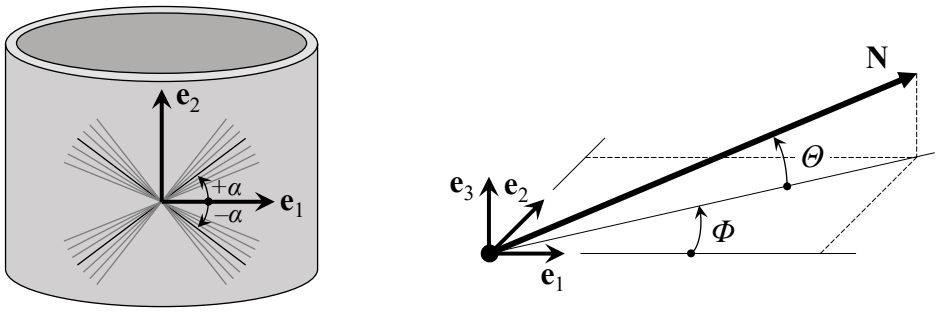

(a) (b)

Figure 3.3: Fiber families in the arterial media: (a) two symmetric fiber families in the circumferential-axial plane; (b) fiber **N** described in terms of azimuthal (Φ) and elevation (Θ) angles.

In order to properly capture the complex mechanical behavior of the arterial tissue, it is therefore crucial to suitably describe the collagen fiber distribution. To this end, we start by fixing a coordinate system described by the basis vectors $\{\mathbf{e}_1, \mathbf{e}_2, \mathbf{e}_3\}$, which are aligned, respectively, with the circumferential, axial and radial directions of an artery (Fig. 3.3(b)).

The unit vector $\mathbf{N}$ along a fiber direction may be expressed in terms of two angles Φ (azimuthal or in-plane angle) and Θ (elevation or out-of-plane angle), such that

$$\mathbf{N}(\Phi,\Theta) = \cos\Phi\cos\Theta\,\mathbf{e}_1 + \sin\Phi\cos\Theta\,\mathbf{e}_2 + \sin\Theta\,\mathbf{e}_3, \tag{3.24}$$

where $\Phi \in [0, 2\pi]$ and $\Theta \in [-\pi/2, +\pi/2]$. Aiming to describe the dispersion of the angles Φ and Θ, Holzapfel et al. [113] introduced a bivariate von Mises distribution by assuming independent probability distributions for each angle, given by

$$\rho(\Phi,\Theta) = \rho_{\text{ip}}(\Phi)\,\rho_{\text{op}}(\Theta). \tag{3.25}$$

The authors then proposed two different π-periodic von Mises distributions for $\rho_{\text{ip}}(\Phi)$ and $\rho_{\text{op}}(\Theta)$, namely

$$\rho_{\text{ip}}(\Phi) = \frac{\exp[a\cos 2(\Phi\pm\alpha)]}{I_0(a)} \qquad \text{and} \qquad \rho_{\text{op}}(\Theta) = 2\sqrt{\frac{2b}{\pi}}\frac{\exp[b(\cos 2\Theta - 1)]}{\text{erf}(\sqrt{2b})}, \tag{3.26}$$

where a and b are concentration parameters, α is the mean fiber in-plane angle, I_0 is the modified Bessel function of the first kind of order 0 and erf is the error function. Based on experimental evidence, the mean out-of-plane angle is taken to be zero [113].

The concentration parameters a and b were also used to introduce two scalar quantities

$$\kappa_{\text{ip}} = \frac{1}{2} - \frac{I_1(a)}{2I_0(a)} \qquad \text{and} \qquad \kappa_{\text{op}} = \frac{1}{2} - \frac{1}{8b} + \frac{1}{4}\sqrt{\frac{2}{\pi b}}\frac{\exp(-2b)}{\text{erf}(\sqrt{2b})}, \tag{3.27}$$

that describe the degree of in-plane and out-of-plane dispersion, respectively. For a more detailed discussion on the meaning of κ_{ip} and κ_{op}, see Holzapfel et al. [113] and Niestrawska et al. [183].

3.3 Numerical experiments

The embedded elements formulation and the multiscale framework described in Sections 3.2.1 and 3.2.2, respectively, were implemented in a Fortran code, which was used to run the numerical experiments described in the current section. Since the goal of the present study is to propose a suitable method to investigate microstructural phenomena in arteries, the tunica media is chosen as a representative example, as it constitutes the main load-bearing layer under physiological conditions and plays a crucial role in mechanobiological processes [105, 126]. We emphasize, however, that the method herein proposed could be easily extended to the intima and the adventitia, or even to other fibrous tissues.

3.3.1 RVE geometries

Starting from Wolinsky and Glagov [273], numerous authors have described the intricate microstructure of the media. Briefly, it might be seen as a complex layered structure composed of several *lamellar units*, which in turn are made up of collagen fibers, smooth muscle cells (SMCs), elastin sheets and other microstructural components [57, 120, 176, 188]. In the present work, however, we will assume that, at the investigated length scale, collagen fibers are the only distinguishable components, while all the other constituents form a homogeneous ground substance. For the sake of clarity, we emphasize that the word 'fiber' is herein employed to refer to a bundle of collagen fibrils (which, in turn, are formed by collagen molecules) [126, 200].

Based on this assumption, the characteristic microstructural geometry shown in Fig. 3.4 was created for the analyses. The black bounding box represents the ground substance, to be meshed with 3D elements, whereas the blue and red lines represent the centerlines of the collagen fibers, organized in two symmetric families, to be meshed with embedded truss elements.

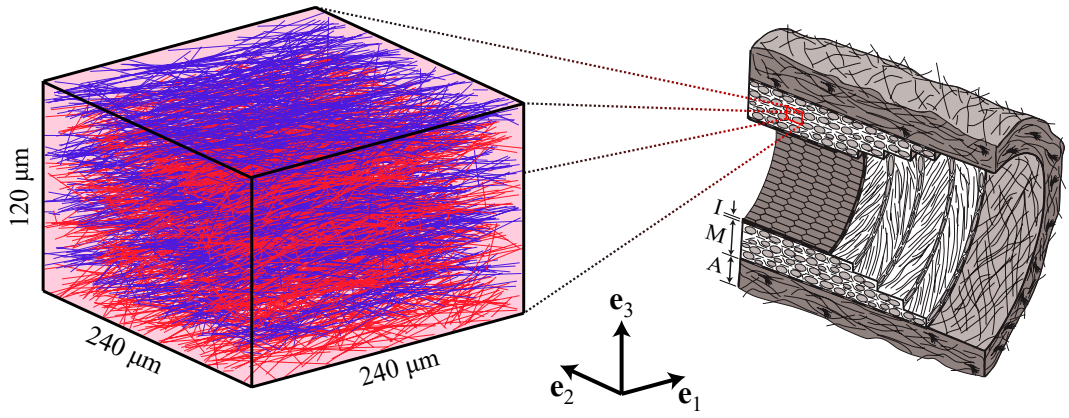

Figure 3.4: Right: illustration of the healthy arterial wall showing the tunica intima (I), tunica media (M) and tunica adventitia (A) (adapted from [109]). Left: representation of the microstructure of the medial layer, with two symmetric families of dispersed collagen fibers (blue and red) and a ground substance (pink).

Care was taken to resemble the layered organization observed in the media of healthy arteries, in which the fiber families are not intertwined, but rather alternate along the radial direction [183]. We point out that, in the present approach, no direct connection was considered between the collagen fibers, as opposed to models that employ networks of trusses [202, 220, 232, 271]. When the embedded elements technique is used, fibers actually interact with each other, by construction, via the elastin-rich ground substance. Experimental results do suggest that matrix-fiber interactions play an important role in the kinematics of collagen fibers within the arterial tissue [145], but most importantly, such

interactions are crucial for mechanobiology [105, 126]. As discussed in the Introduction, this was the main reason for choosing the embedded elements technique over the truss network approach.

The geometry shown in Fig. 3.4 was generated according to the stochastic procedure detailed in Appendix B. Briefly, values are chosen for the volume size, the fiber diameter d, the collagen volume fraction VF and the parameters α, κ_{ip} and κ_{op} of the bivariate von Mises distribution (Eq. (3.26)). Straight lines, representing the centerlines of collagen fibers, are then added to the network at different orientations by randomly sampling in- and out-of-plane angle values from the corresponding von Mises distributions, and the volume fraction VF is updated by assuming a cylindrical shape for the fibers. The procedure stops when the target volume fraction VF is reached.

Table 3.1 presents a characteristic set of parameters for the healthy media, which were employed to generate the fiber network shown in Fig. 3.4. The volume size of $240 \times 240 \times 120$ μm, on the other hand, was chosen in order to ensure that the network is representative of the desired von Mises distributions (i.e., that enough fiber directions are included); see Appendix B for more details.

Table 3.1: Characteristic values of microstructural features of the healthy arterial media.

Param.	Description	Value	Ref.
VF	Volume fraction	30%	[223]
d	Fiber diameter	3 μm	[200, 238]
α	Mean in-plane angle	6.91°	[183]
κ_{ip}	In-plane dispersion	0.208	[183]
κ_{op}	Out-of-plane dispersion	0.487	[183]

In this sense, Fig. 3.5(a) shows normalized histograms of the in-plane angle values Φ for the two symmetric fiber families (red and blue) of Fig. 3.4, whereas Fig. 3.5(b) presents a normalized histogram of the out-of-plane angle values Θ of all fiber directions. In both cases, a good approximation of the target von Mises distribution (thick curves) was achieved. The effective parameters of the fiber network, calculated by means of a maximum likelihood estimate (see Appendix B), were $\alpha^{\text{eff}} = 7.37°$, $\kappa_{ip}^{\text{eff}} = 0.211$ and $\kappa_{op}^{\text{eff}} = 0.486$; these are fairly close to the target values presented in Table 3.1 and lie well within the experimental limits reported by Niestrawska et al. [183] for the healthy arterial media.

In order to investigate the convergence of the macroscopic response for different multiscale models with regard to RVE size, as well as its influence over the microscopic fields, the fiber network of Fig. 3.4 was employed to construct four RVEs of increasing size, which are presented in Fig. 3.6. RVE 4 coincides with the whole network, while RVEs 1 to 3 are

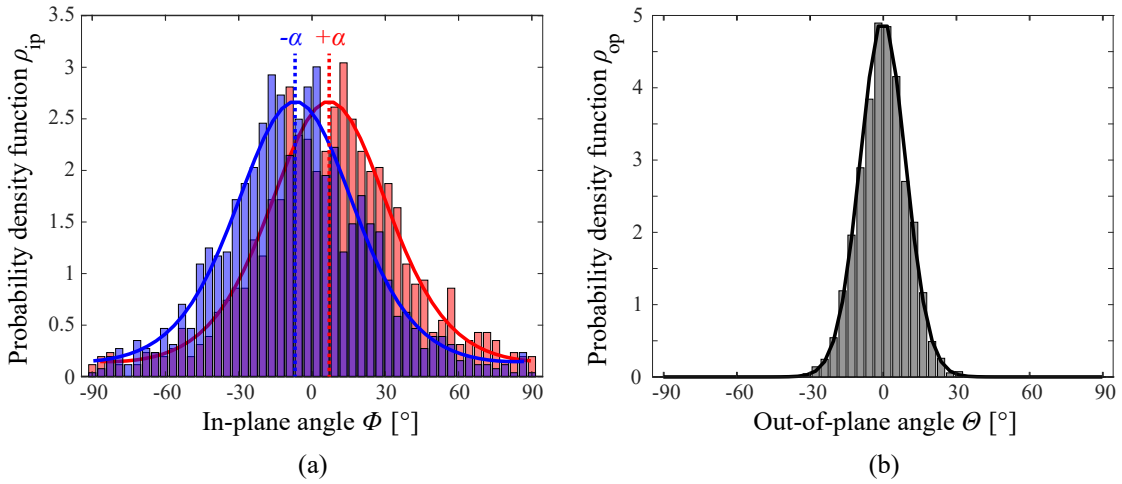

Figure 3.5: Dispersion of fiber angles of a representative collagen network: (a) target (thick curves) and effective (bars) PDF of the in-plane angle values for the two symmetric fiber families, dispersed around the angles $+7.37°$ (red) and $-7.37°$ (blue); (b) target (thick curve) and effective (bars) PDF of the out-of-plane angle values for all fibers.

'sliced' from RVE 4 around the center of the volume. In all RVEs, red fibers belong to the family dispersed around the mean in-plane angle $+7.37°$, and blue fibers are dispersed around $-7.37°$.

FE meshes

Second-order tetrahedrons were employed to mesh the ground substance (black bounding boxes in Fig. 3.6). After mesh convergence analyses (see Appendix C), the same characteristic element size of 5 µm was chosen for all RVEs, as illustrated in Fig. 3.7; this was done to ensure consistent microscopic fields between different RVE sizes. Mesh sizes ranged from 648 (RVE 1) to 331776 elements (RVE 4).

To mesh the fibers (red and blue lines in Fig. 3.6), second-order truss elements were used. Care was taken to obtain a compatible discretization, which means that each 1D element was completely contained within a 3D 'host' element, as required by Eq. (A.2). Mesh sizes ranged from 686 (RVE 1) to 235225 truss elements (RVE 4). We recall that since the 1D elements are embedded in the 3D elements and a 'no-slip' condition is assumed, the truss elements do not add extra degrees of freedom to the system (see Appendix A for more details).

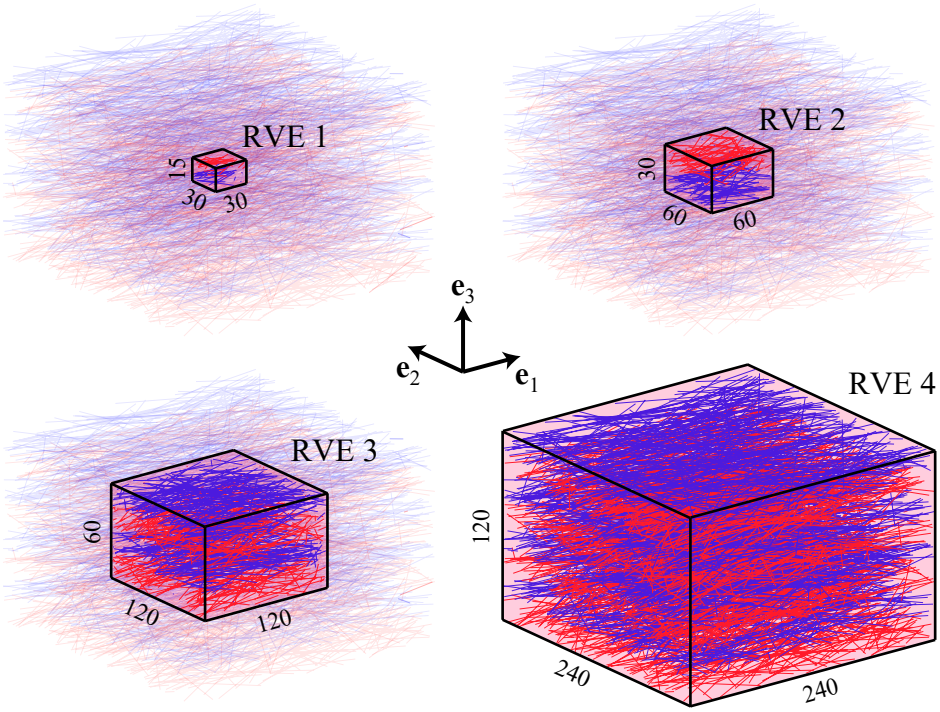

Figure 3.6: RVEs 1 (smallest) to 4 (largest) are constructed from the same microstructural geometry, shown in Fig. 3.4. Red fibers are dispersed around the in-plane angle $\alpha = +7.37°$ and blue fibers are dispersed around $\alpha = -7.37°$.

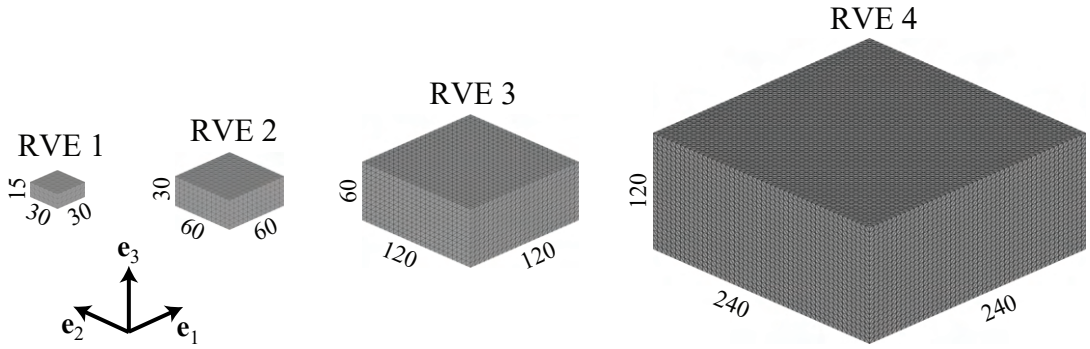

Figure 3.7: 3D 'host' meshes employed to model the ground substance. The same element size was used for all RVEs.

3.3.2 Constitutive models

Ground substance

Following a common modeling strategy [104, 109, 220, 232, 238], the ground substance was modeled as an isotropic nearly-incompressible neo-Hookean material, whose strain-energy function ψ_{g} (Eq. (3.7)) is given in the decoupled form

$$\psi_{\mathrm{g}}(\overline{\mathbf{C}}) = \frac{G_{\mathrm{g}}}{2}(\bar{I}_1 - 3) + \frac{K_{\mathrm{g}}}{2}(J-1)^2, \tag{3.28}$$

where $\overline{\mathbf{C}} = J^{-2/3}\mathbf{C}$ is the modified right Cauchy-Green tensor (with $\det\overline{\mathbf{C}} \equiv 1$), $J = \det\mathbf{F} > 0$ is the volume ratio, $\bar{I}_1 = \overline{\mathbf{C}} : \mathbf{I}$ is the first invariant of $\overline{\mathbf{C}}$, G_{g} is the shear modulus of the ground substance and K_{g} is a penalty (volumetric) parameter. In the present work, a value of $G_{\mathrm{g}} = 16.08$ kPa was used [183], whereas the penalty parameter was chosen as $K_{\mathrm{g}} = 100 G_{\mathrm{g}}$, which results in an apparent Poisson's ratio of 0.495.

Collagen fibers

Considering that the characteristic waviness of the collagen fibers is not taken into account in the RVE, the effect of fiber recruitment (as discussed in Section 3.2.3) was emulated by choosing, for each i-th fiber, a correction strain-energy function ψ_{c_i} (Eq. (3.7)) of the form

$$\psi_{\mathrm{c}_i}(\lambda) = \begin{cases} 0, & \text{if} \quad 0 < \lambda < \lambda_{\mathrm{r}}^i, \\ \dfrac{E_{\mathrm{f}}}{2}(\lambda - \lambda_{\mathrm{r}}^i)^2, & \text{if} \quad \lambda \geq \lambda_{\mathrm{r}}^i, \end{cases} \tag{3.29}$$

where $E_{\mathrm{f}} = 54.3$ MPa is the uniaxial stiffness of the fiber after recruitment [174], λ is the stretch in the fiber direction and λ_{r}^i is the *recruitment stretch* of the i-th fiber. We emphasize that this simple strain-energy function could be easily extended to account for other important microstructural characteristics, e.g., fiber damage [238, 239] and fibril cross-linking within fibers [106, 107].

Since the amount of waviness might be different between fibers, in Eq. (3.29) we assume each i-th fiber is characterized by a different value of λ_{r}^i. Following a common modeling approach [96, 127, 148, 267], we assume furthermore that the distribution of recruitment stretches in the tissue may be described by a beta distribution [267] of the form

$$\rho_{\mathrm{r}}(\lambda_{\mathrm{r}}) = \frac{(\lambda_{\mathrm{r}} - \lambda_1)^{a_1 - 1}(\lambda_2 - \lambda_{\mathrm{r}})^{a_2 - 1}}{\beta(a_1, a_2)(\lambda_2 - \lambda_1)^{a_1 + a_2 - 2}} \tag{3.30}$$

where a_1 and a_2 are shape parameters, with λ_1 and λ_2 being the limits of the distribution (respectively, the minimum and maximum recruitment stretches). The parameters λ_r^i were attributed to each i-th fiber by randomly sampling values from the beta distribution with $\lambda_1 = 1.00$, $\lambda_2 = 1.323$ and $a_1 = a_2 = 1.90$ [267]. An overview of the constitutive parameters used in the present work is given in Table 3.2.

Table 3.2: Constitutive parameters employed in the present work.

Param.	Description	Value	Ref.
G_g	Ground substance shear modulus	16.08 kPa	[183]
K_g	Penalty parameter	$100G_g$	[-]
E_f	Fiber Young modulus	54.3 MPa	[174]
$[\lambda_1, \lambda_2]$	Interval of recruitment stretches	[1.000,1.323]	[267]
$a_1 = a_2$	Shape parameters (beta dist.)	1.90	[267]

The normalized histogram of recruitment stretch values sampled for the whole network of Fig. 3.4 is displayed in Fig. 3.8(a), where the solid curve represents the target beta distribution (Eq. (3.30)). The dispersion of recruitment stretches inside an RVE is exemplified in Fig. 3.8(b), where an in-plane view of RVE 2 is shown. The circumferential and axial directions are aligned with the horizontal and vertical axes, respectively, and fiber diameters were scaled according to their depth within the volume. The color indicates the recruitment stretch λ_r^i assigned to each i-th fiber. We emphasize that these values are attributed to the fibers *before* the FE discretization, so that the distribution of recruitment stretches is independent of the mesh.

Multiscale boundary conditions

Each one of the four RVEs shown in Fig. 3.6 was subjected to numerical analyses simulating a macroscopic in-plane equibiaxial stretch up to 10%, according to the macroscopic deformation gradient $\mathbf{F}_{\text{macro}}$ given, in matrix form, as

$$[\mathbf{F}_{\text{macro}}] = \begin{bmatrix} \lambda_{\text{circ}} & 0 & 0 \\ 0 & \lambda_{\text{axial}} & 0 \\ 0 & 0 & \lambda_{\text{rad}} \end{bmatrix} = \begin{bmatrix} 1.10 & 0 & 0 \\ 0 & 1.10 & 0 \\ 0 & 0 & 0.826 \end{bmatrix}, \tag{3.31}$$

which was applied in 20 steps. We emphasize that, at each step, λ_{rad} was calculated so that $\det \mathbf{F}_{\text{macro}} \equiv 1$, which means an incompressible behavior from a macroscopic point of view, a common assumption in the mechanical modeling of arterial tissue (see, e.g., Holzapfel and Ogden [104] and references therein).

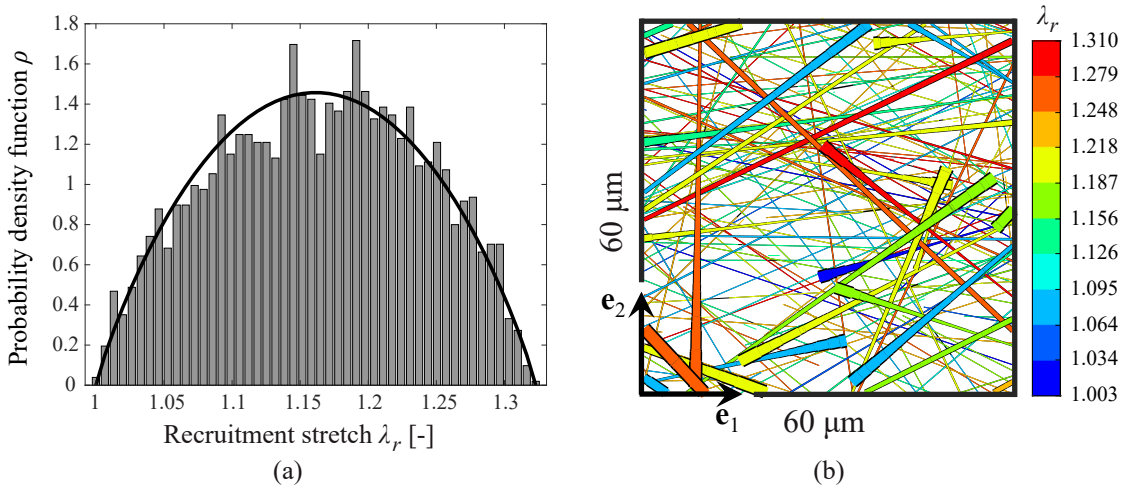

Figure 3.8: (a) Target (thick curve) and effective (bars) PDF of recruitment stretches for the whole fiber network shown in Fig. 3.4; (b) representative in-plane (circumferential-axial) view of recruitment stretches in RVE 2; the color indicates the recruitment stretch assigned to each fiber, according to the scale shown on the right. Fiber diameters were scaled according to their depth within the volume.

The numerical experiment was repeated for each of the four classical multiscale models described in Section 3.2.2, that is:

1. Taylor-Voigt model
2. Linear boundary displacements model
3. Periodic boundary fluctuations model
4. Minimally constrained model.

In total, 16 numerical experiments were performed. All simulations were run on a desktop computer (8-core Intel® i9-9900K with 128 GB of RAM). Runtimes ranged from a few minutes (for RVE 1) to 3-4 days (RVE 4).

3.4 Results and discussion

In this section, the results of the numerical experiments described above will be analyzed, both at the macroscopic (homogenized) and the microscopic level.

3.4.1 Homogenized results

In Fig. 3.9, the axial (top) and circumferential (bottom) components of the homogenized Cauchy stress, which is obtained by means of a *push-forward* operation [102] on the macroscopic first Piola-Kirchhoff stress calculated from Eq. (3.22), are plotted against the macroscopic axial and circumferential stretches, respectively. The numerical results (in color) are compared with experimental data (gray) from 13 samples of arterial media tested under in-plane equibiaxial stretch. The dark gray dots correspond to the mean curves for the 13 samples, whereas the gray shaded area represents the bounds of the data.

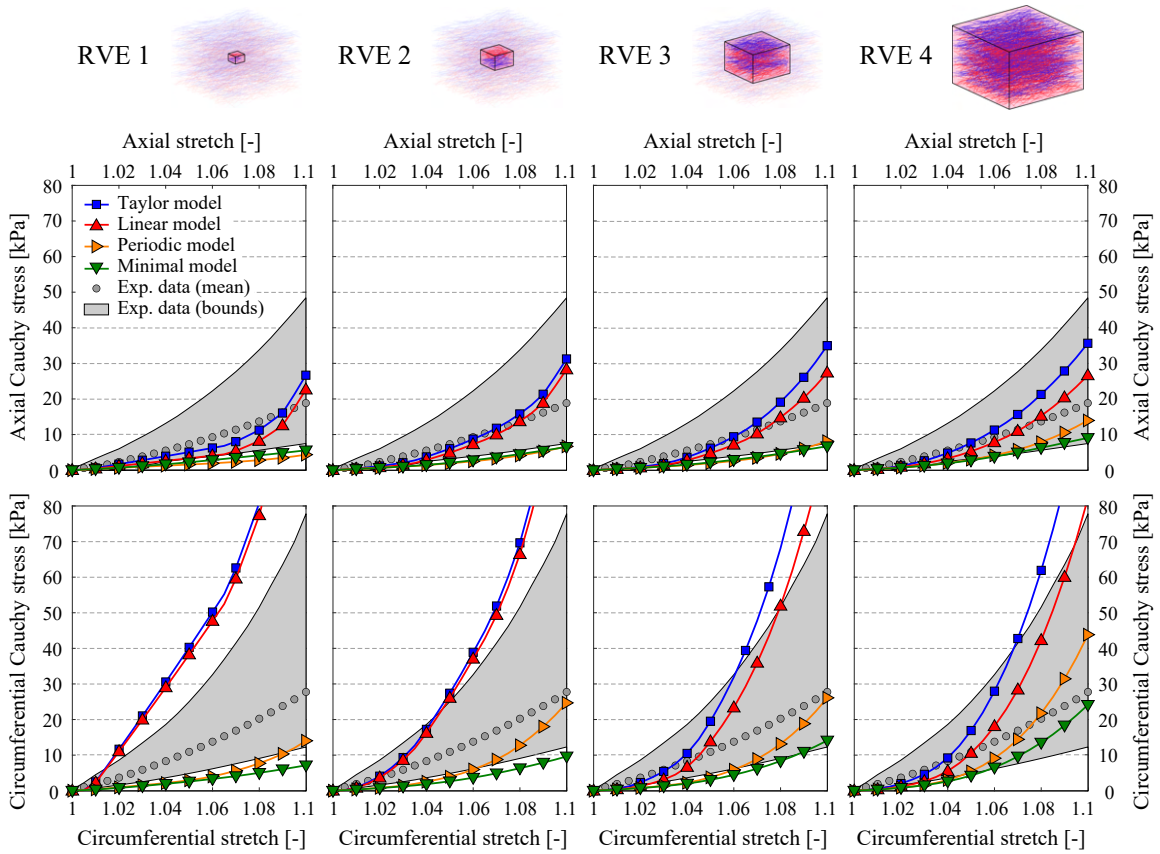

Figure 3.9: Homogenized (macroscopic) stress response at the axial (top) and circumferential (bottom) directions, for increasing RVE size (left to right) and the four multiscale models, is compared with experimental data. The curves obtained numerically exhibit a convergence-like behavior with increasing RVE size.

By looking at the numerical results, we notice that for all RVEs and multiscale models, the combination between the dispersed fiber directions and the (beta) distribution of recruitment stretches yields homogenized stress curves that reproduce the characteristic J-shaped mechanical response of the arterial tissue [176, 200, 234] both at the circumferential and

axial directions. This phenomenon will be further explored in Section 3.4.4. Moreover, for both directions, the Taylor model yields the stiffest homogenized response, whereas the minimally constrained model yields the softest response, which is a well-known characteristic of the multiscale theory discussed in Section 3.2.2 [49]. Furthermore, for all models and RVE sizes, the circumferential response is stiffer than the axial one, as expected, since collagen fibers in the media are preferentially aligned towards the circumferential direction.

In Fig. 3.9, the response of the four multiscale models shows a convergence-like pattern with increasing RVE size (from left to right), which is expected, since the larger the RVE, the more representative of the microstructure it is. Moreover, we point out that each model converges to axial and circumferential curves that clearly lie within the bounds of experimental data. Especially at the circumferential direction, we notice furthermore that the periodic boundary condition seems to be converging faster to a (hypothetical) limit homogenized curve.

In order to further investigate this convergence-like behavior, the total internal work was calculated, for each of the 16 experiments, by numerically integrating

$$W^k = \mathbf{P}^k_{\text{macro}} : \mathbf{F}^k_{\text{macro}} \tag{3.32}$$

along the (pseudo-)time, where $\mathbf{P}^k_{\text{macro}}$ and $\mathbf{F}^k_{\text{macro}}$ are, respectively, the homogenized first Piola-Kirchhoff stress tensor (Eq. (3.22)) and the macroscopic deformation gradient (Eq. (3.31)) at the k-th step. Results are plotted in Fig. 3.10 against RVE volume.

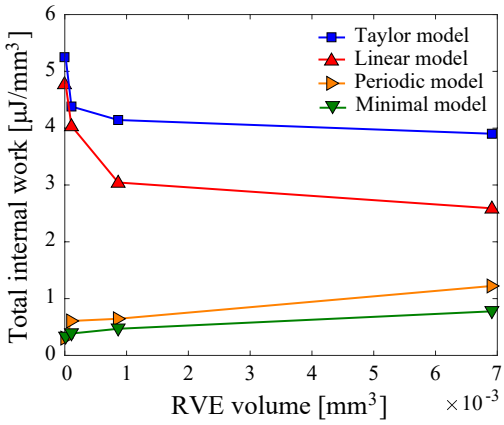

Figure 3.10: Total internal work plotted against RVE volume for the four multiscale models. The curves exhibit a convergence-like behavior with increasing RVE size.

The trend observed in Fig. 3.9 is repeated in Fig. 3.10: with increasing RVE size, there is a convergence-like pattern for all multiscale models. Reflecting the stiffer responses

observed in the macroscopic curves, the Taylor and linear models yield higher levels of strain energy when compared with the minimally constrained and periodic models. Once again, the periodic model seems to be converging faster to a (hypothetical) limit value.

3.4.2 Microscopic strains

As discussed in previous sections, the main advantage of the multiscale theory herein employed is the possibility of evaluating the microscopic deformation that is driving the macroscopic (homogenized) response shown in Fig. 3.9, as well as the relation between them. In the context of biological tissues, this evaluation might help unraveling the ways in which important mechanobiological processes take place. In the arterial wall, e.g., there are different microconstituents that act as biological sensors, continually evaluating environmental cues and triggering biological processes accordingly to promote homeostasis (biological equilibrium) [105, 126]. Smooth muscle cells (SMCs) in the media relax or contract to regulate, e.g., arterial diameter, blood pressure and blood flow distribution [200]. They are also responsible for producing extracellular matrix components (collagen and elastin), and, therefore, might induce medium and long-term changes to the microstructural architecture in response to mechanical stimuli (e.g., cyclic stretches) or pathological processes (e.g., aneurysm formation), a process known in the literature as *growth and remodeling* [87, 103, 122, 150, 200].

To evaluate the influence of RVE size and multiscale model over the microscopic deformation field, the equivalent (von Mises) measure of the logarithmic (Hencky) strain ε_{eq} will be employed. Since in the present model SMCs are included within the ground substance, these strain fields might also indicate mechanical stimuli being captured by the cells.

For the Taylor model, the microscopic strain field is uniform by hypothesis (see Eq. (3.14)), i.e., at 1.10 equibiaxial stretch the equivalent logarithmic strain equals 0.286 (macroscopic value, calculated from Eq. (3.31)) all over the RVE, independently of the size. Therefore, this trivial case won't be addressed here.

The middle part of Fig. 3.11 shows the strain fields for the linear boundary displacements model at 1.10 equibiaxial stretch. Each of the four RVEs was sliced halfway through the thickness (i.e., in the radial direction) and the top and bottom parts are displayed. Moreover, in order to enhance visualization, a nonlinear color scale is employed, in which each color represents 10% of the elements of each RVE. These deciles are also pictured in the histograms shown in the bottom part of Fig. 3.11, which were plotted from the set of equivalent logarithmic strains of all elements. Since each RVE has a different number of same-sized elements, the histogram bars were normalized to yield an area equal to one, resulting in an estimation of the probability density function (PDF) of strain values, for each RVE. Finally, the macroscopic equivalent logarithmic strain is identified by an arrow under the horizontal axis of each PDF.

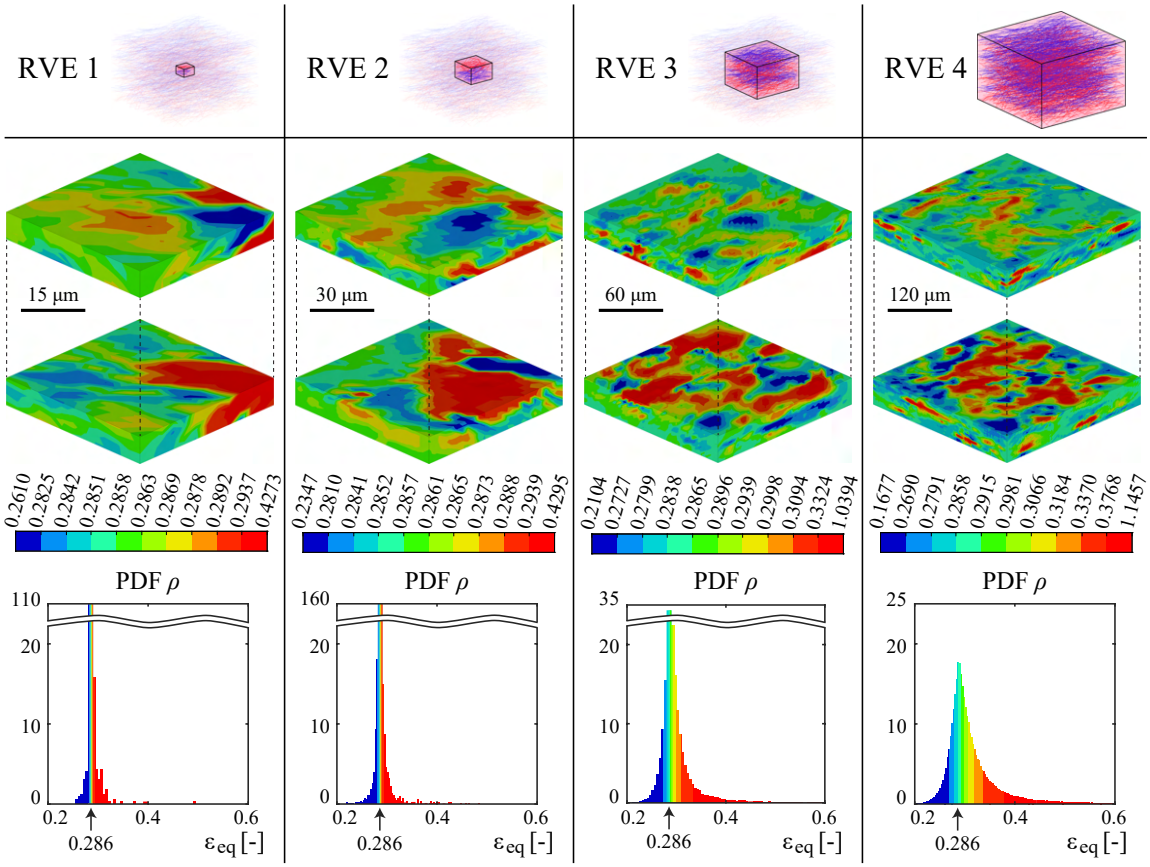

Figure 3.11: Distribution of equivalent logarithmic strains (middle) and corresponding PDF histograms (bottom) for the linear boundary displacements model. RVE size increases from left to right.

It can be seen that, for the two smallest RVEs, 80% of the elements is experiencing equivalent strains within less than 3% of the imposed (macroscopic) value. This indicates a Taylor-like behavior, which is also represented by the narrow PDFs. With increasing RVE size, the histogram becomes wider and a clear tendency arises, namely, that the higher strains concentrate in the interior of the domain. Both effects result from the imposed displacements on the boundary: since the same element size was used for all simulations, in RVEs 1 and 2 there is a larger proportion of boundary nodes with regard to the whole mesh, meaning that a larger part of the domain has prescribed displacements, resulting in an almost uniform strain field. On the other hand, in RVEs 3 and 4, the larger amount of elements away from the boundary allows for higher strains (up to more than 100%) to develop in the interior of the volumes, which also yields a broader PDF.

Figure 3.12 shows the logarithmic strain fields and corresponding PDFs for the periodic boundary fluctuations model. One can see that the nonzero fluctuations on the boundary allow for a considerably wide range of equivalent strain values, even for the smallest

RVEs. This behavior may also be seen in the broader PDF graphs at the bottom of the figure, which, furthermore, exhibit a convergence-like behavior: for increasing RVE size, the PDFs seemingly tend to the same distribution of equivalent strains. Moreover, as opposed to the linear model, no clear boundary effect is seen: for all RVE sizes, large and small strains – arising from the presence of the collagen fibers – are inhomogeneously distributed throughout the volumes, both at the interior and the boundaries. Considering that the microscopic fields should resemble a piece of microstructure being deformed by the surrounding material, this boundary-independent behavior is desirable. Furthermore, we notice that in all RVEs, at least 70% of the elements is experiencing strains above the macroscopic (imposed) values; this highlights the relevance of this type of multiscale analyses when micromechanical phenomena (e.g., mechanotransduction) are to be investigated and simulated.

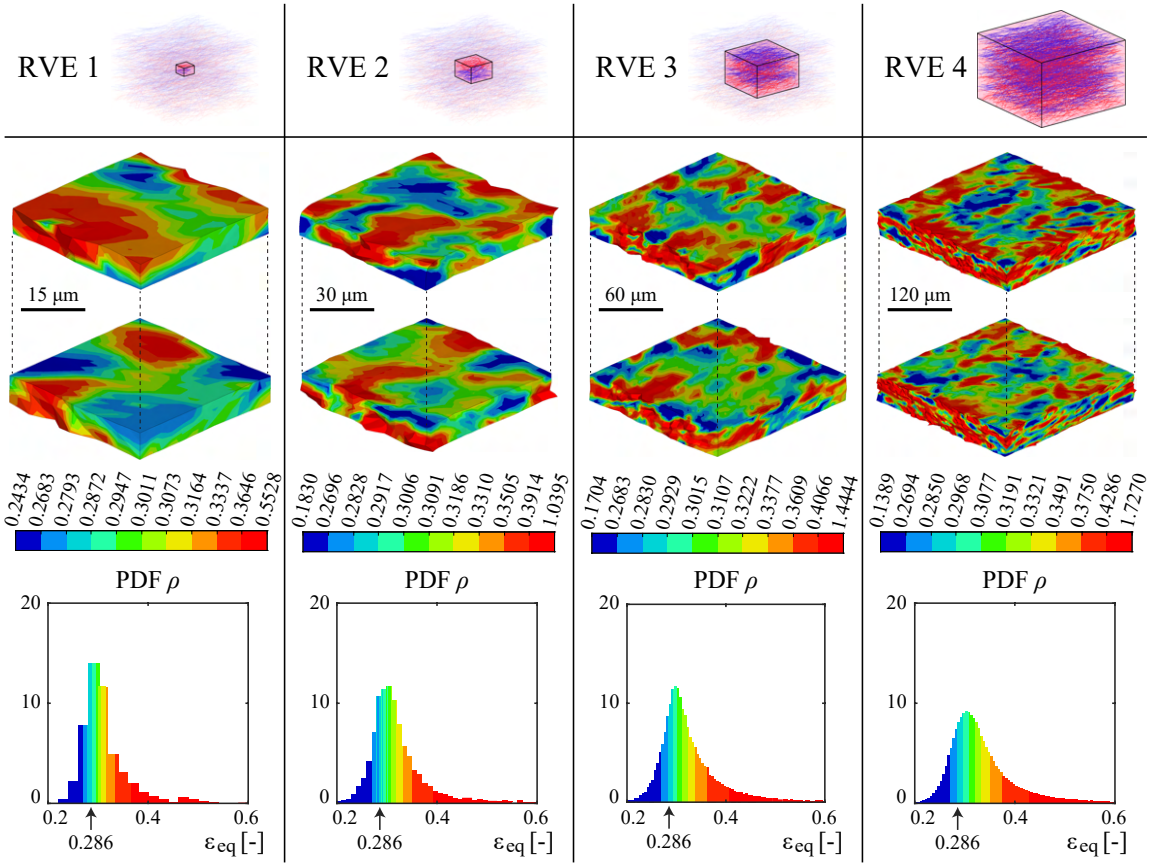

Figure 3.12: Distribution of equivalent logarithmic strains (middle) and corresponding PDF histograms (bottom) for the periodic boundary fluctuations model. RVE size increases from left to right.

The logarithmic strain fields and PDFs for the minimally constrained model are presented in Fig. 3.13. Contrarily to the linear model, higher strains tend to arise at the

circumferential-axial boundary of the volumes, while lower strains concentrate in the middle of the RVEs. The reason behind this behavior are the uniform tractions on the boundary (see Eq. (3.17)) that characterize the minimal model, which are known to yield physically unfeasible results at the boundaries of RVEs, especially when phases with strongly dissimilar mechanical properties are present [29]. The same effect is also responsible for the lack of a clear convergence trend in the PDFs: while for RVEs 1 and 2 the PDF is more or less centered around the macroscopic value, for RVEs 3 and 4 the distribution is shifted to the left, due to the higher proportion of elements away from the boundary, where higher strains are concentrated.

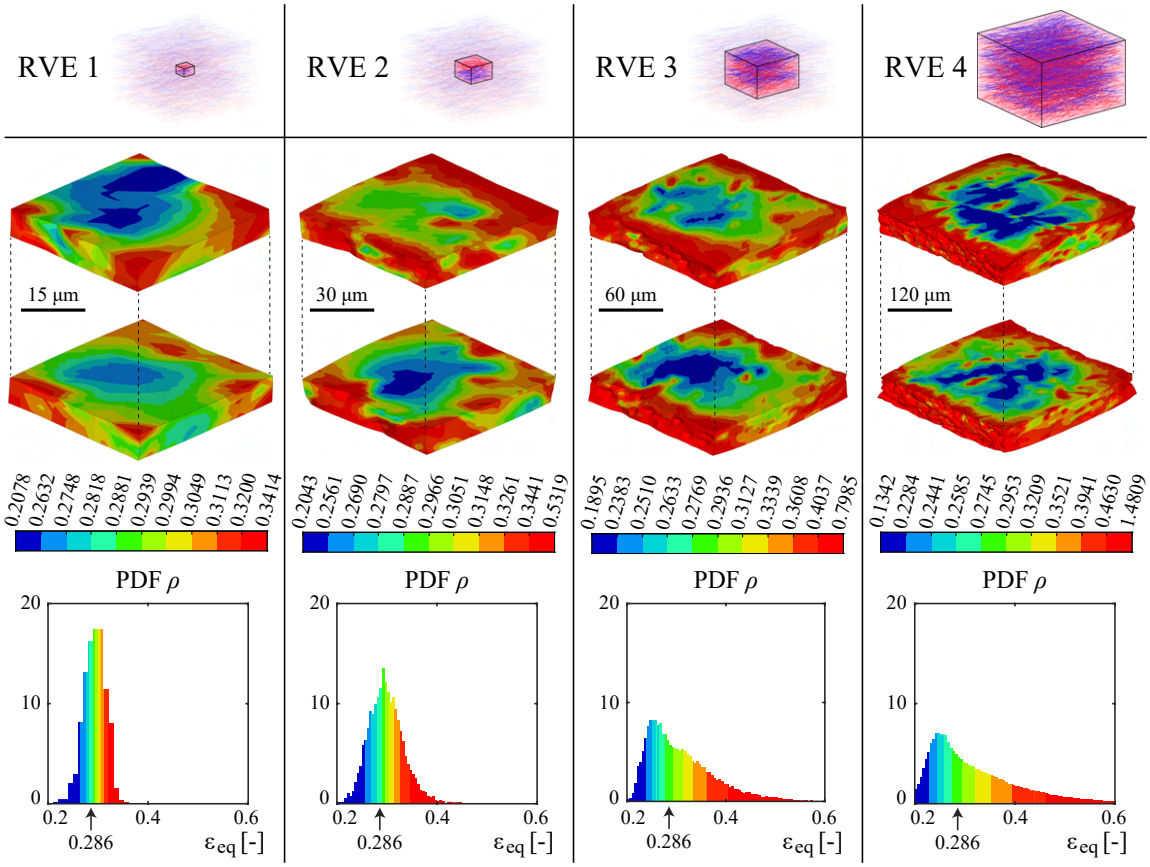

Figure 3.13: Distribution of equivalent logarithmic strains (middle) and corresponding PDF histograms (bottom) for the minimally constrained model. RVE size increases from left to right.

As a final remark to this section, we emphasize that the microscopic strain fields might be quite different even when the macroscopic response is similar: compare, e.g., the similarity of the macroscopic response for RVE 3 in Fig. 3.9 for the periodic and minimal models with the differences in the corresponding microscopic strain fields shown in Figs. 3.12 and 3.13. This stresses the importance of suitably choosing the boundary condition and

RVE size if meaningful results are to be obtained at the microscopic level: it is not enough to simply compare the homogenized response with experimental data. With specific regard to the four models analyzed, the lack of a strong boundary effect indicates that, among the four classical models, the periodic boundary condition is likely the best option for multiscale simulations of fibrous tissues employing the embedded elements technique. As for the RVE size, if the periodic model is employed, the strain field of RVE 3 seems to be already representative enough.

3.4.3 Fiber stretches

Since the ground substance is isotropic, the strain fields observed in Figs. 3.11-3.13 are driven by the effect of the reinforcing collagen fibers, i.e., of the embedded truss elements. In order to illustrate this relation, we choose RVE 3 as a representative example and present (Fig. 3.14) the in-plane view of the distribution of stretches of the fiber segments, for the four multiscale models studied. The circumferential and axial directions are aligned with the horizontal and vertical axes of the figure, respectively. Fiber diameters were scaled according to their depth within the RVE, and, once again, a nonlinear color scale was employed, where each color represents 10% of the (truss) elements. These deciles are also pictured in the PDF histograms shown in the bottom part of the figure. Aiming to enhance visualization of the minimum and maximum values, transparency was added to fibers according to their stretch: the closer to the median, the more transparent the fiber.

Given the homogeneous displacement field throughout the RVE, for the Taylor model, the stretch of the fiber depends solely on its direction inside the volume; since fibers in the media are oriented more towards the circumferential direction, it can be seen that almost all fibers are subjected to stretches around the imposed macroscopic value of 1.10. For the linear model, the PDF still shows a high number of fibers being subjected to stretches close to the prescribed macroscopic value of 10%, albeit with a higher dispersion when compared with the Taylor model. For the periodic and minimal models, the distributions are similar and considerably broader than the ones observed for the Taylor and linear models; for the minimal model, in particular, the PDF is slightly shifted to the left, and there is also a clear tendency of higher stretches concentrating closer to the boundaries. Overall, we notice that the same tendencies observed for the strain fields of the ground substance (3D mesh) are also present in Fig. 3.14, as expected, since ground substance and fibers deform together.

3.4.4 Fiber recruitment

As briefly discussed in Section 3.2.3, the (passive) mechanical response of most connective tissues is characterized by a phenomenon known as *fiber recruitment*, which arises from the waviness of collagen fibers in the unloaded state. With specific regard to arteries, this

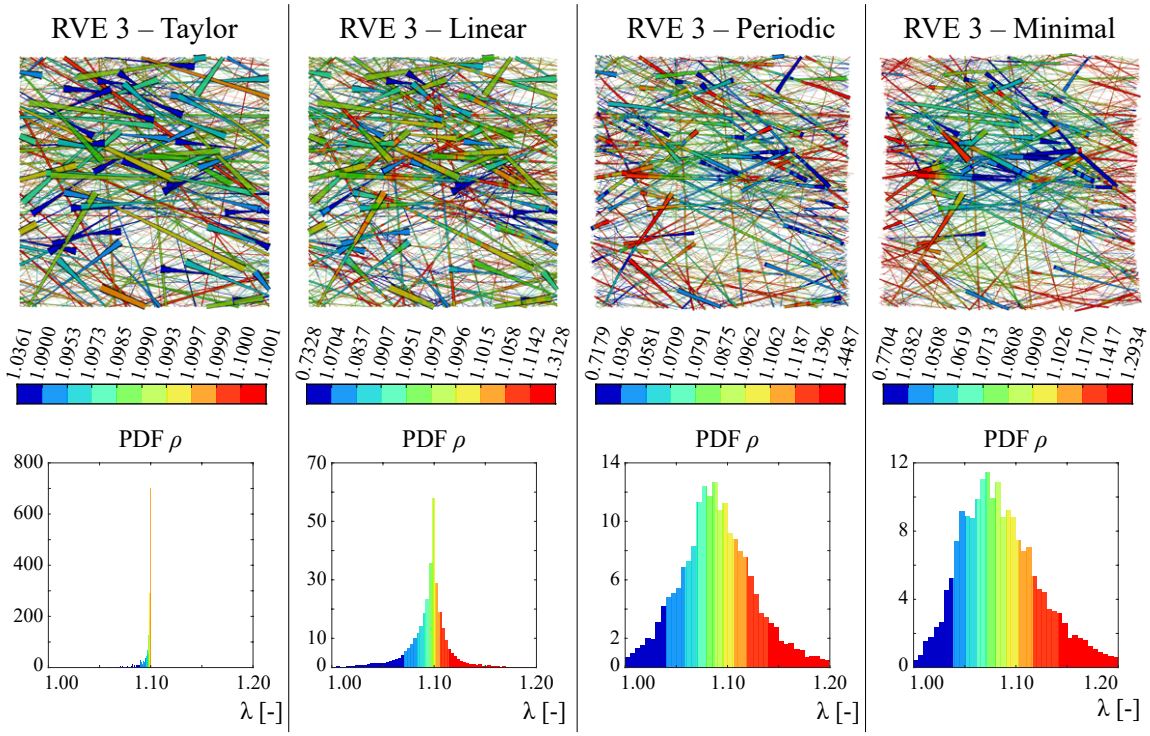

Figure 3.14: In-plane (circumferential-axial) view of the distribution of fiber stretches in RVE 3 for the four multiscale models (middle) and corresponding PDF histograms (bottom).

behavior has been extensively studied and described both in experimental and numerical settings [37, 96, 199, 234, 239, 267]. In the present study, the recruitment was simulated by choosing a suitable strain-energy function (Eq. (3.29)) and assigning a different value of recruitment stretch λ_r^i to each i-th fiber.

In order to highlight the potential of the herein proposed multiscale technique as a means to describe and investigate microstructural phenomena in arteries (and, potentially, other fibrous tissues), Fig. 3.15 illustrates the fiber recruitment evolution in RVE 3 subjected to periodic multiscale boundary conditions. In the graph of Fig. 3.15(a), the homogenized mechanical response in the circumferential direction (thick black curve) is plotted against the fiber (dashed curve) and ground substance (dotted curve) contributions, calculated by homogenizing the stresses, respectively, only at the truss mesh (second term of Eq. (3.22)) and only at the 3D mesh (first term of Eq. (3.22)). The thick curve can be obtained from the other two by considering the collagen volume fraction of 30%, and we notice that the characteristic J-shaped response arises indeed from the effect of the fiber recruitment.

We emphasize the striking similarity with the inflation curves presented in the classical experimental work by Roach and Burton [199] for fresh, elastin-digested and collagen-digested arterial samples. Even so, it must be said that in the curves of Fig. 3.15(a) we

merely separated the response of each phase, whereas eliminating one of the microstructural components like in [199] would surely change the microscopic strain fields, and, potentially, influence the macroscopic response.

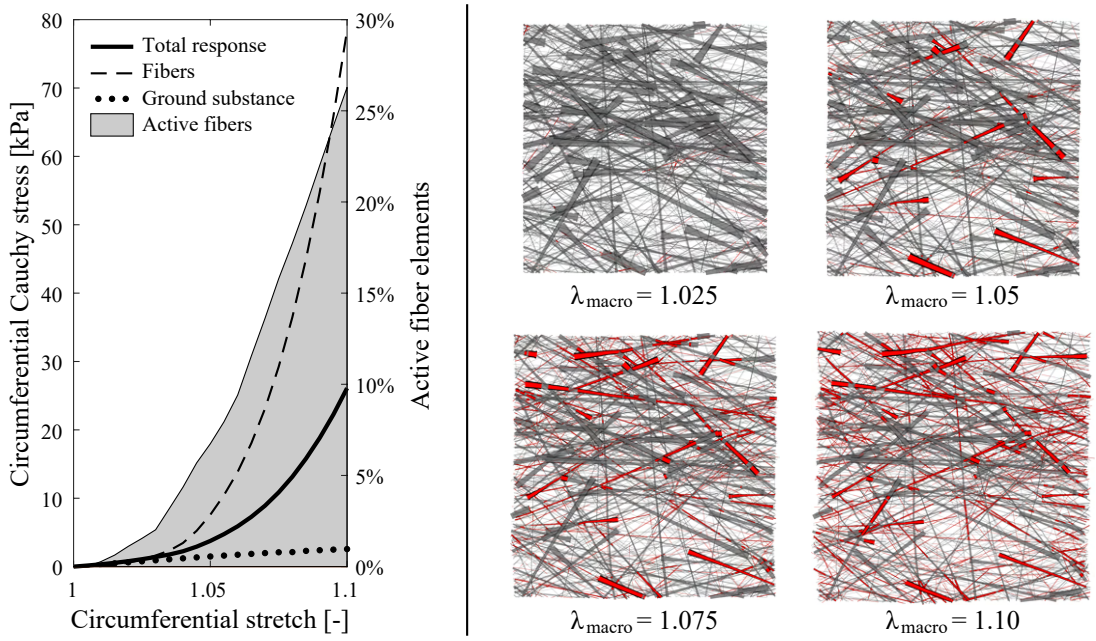

Figure 3.15: Illustration of the effect of fiber recruitment over the macroscopic response: (a) circumferential response (thick black curve) of RVE 3 combined with the periodic model, emphasizing the ground substance (dotted curve) and fiber (dashed curve) contributions; (b) active fibers (red) at 2.5, 5.0, 7.5 and 10% of equibiaxial macroscopic stretch.

The shaded gray area in Fig. 3.15(a) represents the amount of truss elements that have being *recruited* (i.e., whose recruitment stretch λ_r^i was surpassed), whereas Fig. 3.15(b) illustrates the gradual increase of recruited fibers (shown in red) for four stretch levels. At an equibiaxial stretch level of 10%, about 25% of the fiber segments is bearing load. This is in line with the results of the experimental work by Chow et al. [37], which reported that collagen fibers in the medial layer are recruited up to 20% of applied (macroscopic) stretch.

3.5 Concluding remarks

Multiscale models based on RVEs allow for the evaluation of microscopic phenomena which, in general, are not accounted for in phenomenological models. In certain fibrous

tissues such as arteries, however, there is a considerable amount of dispersion in the orientations of the collagen fiber network, meaning that it might be necessary to include a large number of fiber directions in order to achieve a representative microstructure. For that reason, when the FEM is employed for the numerical homogenization, collagen fibers are commonly modeled using 1D elements [164, 202, 220, 228, 232, 238, 239, 271]. This might be accomplished either by simply considering a network of trusses [202, 220, 232, 271] or by using the embedded elements technique [164, 238, 239]. The advantage of the latter with respect to the former is that the inclusion of a ground substance in which the fibers are embedded may provide additional insights on the important interaction between the collagen network and other microstructural components, such as mechanosensing cells. We point out, however, that the kinematic bond imposed between 1D and 3D elements by the use of the same shape functions might overshadow some of these interactions, especially at the fiber interfaces. Moreover, the use of truss elements implies that bending and torsion of the fibers are neglected.

To the best of the authors' knowledge, the influence of multiscale boundary conditions and RVE size in the context of the embedded elements technique was not properly addressed before. Motivated by this fact, in the present study, the multiscale framework (Section 3.2.2) introduced by de Souza Neto and Feijóo [49], based on *kinematic admissibility* and *energy consistency* between scales, was combined with the embedded elements technique to model the microstructure of the medial layer of the arterial tissue. Four RVE sizes, obtained from the same characteristic microstructure, were subjected to a macroscopic isochoric equibiaxial stretch up to 10%; this deformation was applied according to the four classical multiscale models: Taylor-Voigt, linear boundary displacements, periodic boundary fluctuations and minimally constrained.

By employing a fiber recruitment strain-energy function for the fibers, it was possible to capture the characteristic J-shaped mechanical response at the macroscopic (homogenized) level for all RVE sizes and models, with a stiffer response in the circumferential direction, as expected for the media. Moreover, a convergence-like behavior with increasing RVE size is observed for all the four classical models analyzed and, among them, the periodic boundary fluctuations model seems to converge faster to a (hypothetical) limit macroscopic response (see Figs. 3.9 and 3.10).

At the microscopic level, on the other hand, the resulting strain fields in the ground substance show a strong dependency on the chosen multiscale boundary conditions. Importantly, even when two models yield similar macroscopic responses, the microscopic strain fields might be quite different; this stresses the importance of properly choosing the multiscale boundary conditions if meaningful results are to be obtained at the microscopic level. Of the four models analyzed, the periodic model seems to be less sensitive to changes in RVE size and it is also less prone to localized effects at the RVE boundaries than the linear and minimal models.

Based on the above considerations, the periodic model seems to be the most suitable for investigating microstructural phenomena in arteries (or even other fibrous tissues) by means of the embedded elements technique, at least among the four classical multiscale models. The biomechanical relevance of such analyses is illustrated, e.g., in Fig. 3.12, where the strain amplification (with regard to the macroscopic value) and the inhomogeneity observed in the strain fields of the ground substance might shed light on relevant mechanotransduction mechanisms (e.g., cell signaling). It is also exemplified in Fig. 3.15, which provides a very simple demonstration of the gradual fiber recruitment and its influence over the macroscopic response.

In the present work, a 'no-slip' condition was assumed between the collagen fibers and the ground substance. Alternative formulations of the embedded elements technique that include the possibility of relative sliding between fibers and matrix are available in the literature [83, 90], and could be used to extend the current work, albeit at a higher computational cost (since, in this case, additional degrees of freedom associated with the 1D mesh must be included in the problem). However, the analyses herein presented would probably need to be redone, since adding slip would likely lead to changes in the results (especially at the microscopic level), and possibly in the multiscale formulation itself. Nevertheless, by incorporating this feature, other interesting phenomena could be investigated, e.g., frictional sliding of collagen fibers.

Other future studies employing the approach herein presented could focus, e.g., on the mechanobiological effects of structural changes in the collagen network, which are associated with pathological processes and growth and remodeling mechanisms in arteries [185]. The impact of supraphysiological loads (e.g., in stenting procedures) could also be investigated, by suitably modifying the fiber strain-energy function to add damage mechanisms. These and other possibilities might help unraveling the ways in which various cardiovascular diseases develop, to the benefit of patients and physicians.

Appendices

A FE implementation of the embedded elements technique

This section presents a suitable implementation for solving the principle of virtual work for the embedded elements technique (Eq. (3.9)) in the finite strain regime, employing the FEM, in a total Lagrangian setting. For the sake of brevity, we will henceforth restrict our attention to the case in which the body Ω_0 deforms to Ω (Fig. 3.1) only due to the action

of prescribed displacements $\overline{\mathbf{U}}$, i.e., there are no body forces $\overline{\mathbf{B}}$ or surface forces $\overline{\mathbf{T}}$, which means that Eq. (3.9) reduces to

$$\delta W_{\text{int}} = \int_{\Omega_0} \mathbf{P}_{\text{g}} : \delta\mathbf{F}\,\mathrm{d}V + \sum_{i=1}^{N_{\text{f}_\text{T}}} \int_{V_0^{\text{f}_i}} \mathbf{P}_{\text{c}_i} : \delta\mathbf{F}\,\mathrm{d}V = 0, \qquad \forall\,\delta\mathbf{u} \in \mathbb{V}. \tag{A.1}$$

FE discretization

We start by subdividing the body Ω_0 into N_{el} continuum finite elements, so that the principle of virtual work (Eq. (3.9)) may be rewritten as

$$\delta W_{\text{int}} = \mathop{\mathcal{A}}_{e=1}^{N_{\text{el}}} \left[\int_{\Omega_0^{(e)}} \mathbf{P}_{\text{g}} : \delta\mathbf{F}\,\mathrm{d}V + \sum_{i=1}^{N_{\text{f}(e)}} \int_{V_0^{\text{f}_i(e)}} \mathbf{P}_{\text{c}_i} : \delta\mathbf{F}\,\mathrm{d}V \right] = 0, \qquad \forall\,\delta\mathbf{u} \in \mathbb{V}, \tag{A.2}$$

where $\Omega_0^{(e)}$ is the (initial) domain of the e-th 'host' element, $\mathcal{A}$ is a suitable assembly operator and $N_{\text{f}(e)}$ is the number of fiber (centerline) segments *completely contained* within the e-th host element. It is therefore assumed that each embedded fiber f_i may be subdivided into smaller segments such that

$$V_0^{\text{f}_\text{T}} = \sum_{e=1}^{N_{\text{el}}} V_0^{\text{f}_\text{T}(e)} = \sum_{e=1}^{N_{\text{el}}} \sum_{i=1}^{N_{\text{f}(e)}} \int_{V_0^{\text{f}_i(e)}} \mathrm{d}V, \tag{A.3}$$

where $V_0^{\text{f}_\text{T}(e)} \subseteq \Omega_0^{(e)}$ is the total (initial) fiber volume contained within the e-th host element and $V_0^{\text{f}_\text{T}}$ is the total fiber volume embedded in the ground substance g. By fixing the coordinate system $\{\mathbf{e}_1, \mathbf{e}_2, \mathbf{e}_3\}$, Eq. (A.2) may be rewritten in matrix form as

$$\delta W_{\text{int}} = \mathop{\mathcal{A}}_{e=1}^{N_{\text{el}}} \left[\int_{\Omega_0^{(e)}} [\delta\mathbf{F}^{(e)}]^{\text{T}} [\mathbf{P}_{\text{g}}^{(e)}]\,\mathrm{d}V + \sum_{i=1}^{N_{\text{f}(e)}} \int_{V_0^{\text{f}_i(e)}} [\delta\mathbf{F}^{(e)}]^{\text{T}} [\mathbf{P}_{\text{c}_i}^{(e)}]\,\mathrm{d}V \right] = 0, \qquad \forall\,\delta\mathbf{u} \in \mathbb{V}. \tag{A.4}$$

In order to approximate $[\delta\mathbf{F}^{(e)}]$, we recall that $\delta\mathbf{F} = \mathrm{Grad}\,\delta\mathbf{u}$ and approximate the field of virtual displacements $\delta\mathbf{u}$ within the e-th host element $\Omega_0^{(e)}$ by means of suitable shape functions defined in terms of its nodes. After standard manipulations, we obtain

$$[\mathbf{f}_{\mathrm{int}}] = \mathop{\mathcal{A}}_{e=1}^{N_{\mathrm{el}}} [\mathbf{f}_{\mathrm{int}}^{(e)}] = \mathop{\mathcal{A}}_{e=1}^{N_{\mathrm{el}}} \left[\int_{\Omega_0^{(e)}} [\mathbf{B}^{(e)}]^{\mathrm{T}} [\mathbf{P}_{\mathrm{g}}^{(e)}]\, \mathrm{d}V + \sum_{i=1}^{N_{\mathrm{f}(e)}} \int_{V_0^{\mathrm{f}_i(e)}} [\mathbf{B}^{(e)}]^{\mathrm{T}} [\mathbf{P}_{\mathrm{c}_i}^{(e)}]\, \mathrm{d}V \right] \approx [\mathbf{0}], \qquad \forall\, \delta\mathbf{u} \in \mathbb{V} \tag{A.5}$$

where $[\mathbf{f}_{\mathrm{int}}]$ is the global internal force vector and $[\mathbf{B}^{(e)}]$ is the matrix of derivatives of the shape functions of the e-th host element $\Omega_0^{(e)}$; see, e.g., Belytschko et al. [13] for more details on the derivation of the FEM.

Integration employing isoparametric elements

The integrals in Eq. (A.5) are more easily solved in terms of isoparametric elements; to this end, for each e-th host element $\Omega_0^{(e)}$ we make use of a map $\mathbf{X}_{(e)}(\xi)$, where $[\xi] = [\xi_1\ \xi_2\ \xi_3]^{\mathrm{T}}$ are the coordinates of the isoparametric domain, as illustrated (for the 2D case) in Fig. A.1

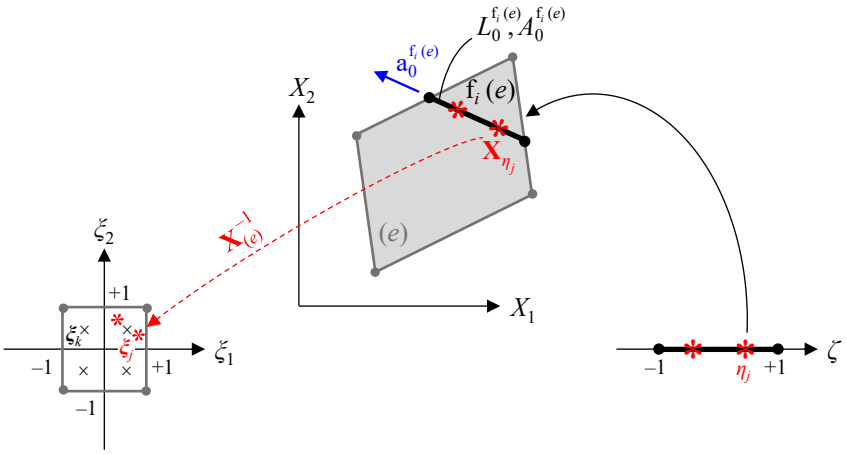

Figure A.1: Illustration (for the 2D case) of the embedded elements technique. The effect of the truss reinforcement is accounted for by means of suitably placed integration points at the isoparametric domain of the 'host' element e.

Integration of the first term inside the brackets in Eq. (A.5) is performed in terms of NQ_ξ Gaussian integration points ξ_k [13], from which we obtain

$$\int_{\Omega_0^{(e)}} [\mathbf{B}^{(e)}]^{\mathrm{T}} [\mathbf{P}_{\mathrm{g}}^{(e)}] \, \mathrm{d}V \approx \sum_{k=1}^{NQ_\xi} [\mathbf{B}^{(\xi_k)}]^{\mathrm{T}} [\mathbf{P}_{\mathrm{g}}^{(\xi_k)}] \det([J^{(\xi_k)}]) \omega_k, \tag{A.6}$$

where $[\mathbf{B}^{(\xi_k)}]$ are the derivatives of the shape functions of the isoparametric 3D element, evaluated at each of the NQ_ξ Gaussian quadrature points ξ_k, $[\mathbf{P}_{\mathrm{g}}^{(\xi_k)}]$ are the first Piola-Kirchhoff stresses of the ground substance at the material point $\mathbf{X}_{(e)}(\xi_k)$, $[J^{(\xi_k)}]$ is the Jacobian matrix of the map $\mathbf{X}_{(e)}(\xi_k)$ and ω_k is the weight of the k-th integration point ξ_k.

On the other hand, in order to integrate the second term inside the brackets in Eq. (A.5), we first make use of the isoparametric truss element in order to write

$$\int_{V_0^{\mathrm{f_i(e)}}} [\mathbf{B}^{(e)}]^{\mathrm{T}} [\mathbf{P}_{\mathrm{c}_i}^{(e)}] \, \mathrm{d}V \approx A_0^{\mathrm{f}_i(e)} \sum_{j=1}^{NQ_{\mathrm{f}_i(e)}} [\mathbf{B}^{(\mathrm{X}_{\eta_j})}]^{\mathrm{T}} [\mathbf{P}_{\mathrm{c}_i}^{(\mathrm{X}_{\eta_j})}] L_{0_j} \omega_j. \tag{A.7}$$

In Eq. (A.7), $A_0^{\mathrm{f}_i(e)}$ is the initial cross-sectional area of the i-th fiber segment inside the e-th element and $[\mathbf{B}^{(\mathrm{X}_{\eta_j})}]$ are the derivatives of the shape functions of the *physical* e-th host element $\Omega_0^{(e)}$, evaluated at the corresponding material points $\mathbf{X}_{\eta_j}$ of the $NQ_{\mathrm{f}_i(e)}$ Gaussian integration points η_j, each one associated with an (initial) fiber length L_{0_j} and weight ω_j. Finally, $[\mathbf{P}_{\mathrm{c}_i}^{(\mathrm{X}_{\eta_j})}]$ are the first Piola-Kirchhoff stresses of the fiber correction at the material point $\mathbf{X}_{\eta_j}$.

In order to evaluate the derivatives of the shape functions at the isoparametric domain (similarly to what was done in Eq. (A.6)), it is necessary to invert the map $\mathbf{X}_{(e)}(\xi)$ in order to find the points $\xi_j = \mathbf{X}_{(e)}^{-1}(\mathbf{X}_{\eta_j})$, as shown in Fig. A.1. Elwi and Hrudey [67] proposed at least two numerical ways of doing so; in the present work we have employed the Newton-Raphson iterative method.

Finally, by substituting Eqs. (A.6) and (A.7) into Eq. (A.5) we recall the finite strain version of the classical equation for the internal force vector of a continuum mesh with embedded truss elements [90], that is

$$[\mathbf{f}_{\mathrm{int}}] = \mathop{\mathcal{A}}_{e=1}^{N_{\mathrm{el}}} \left[\sum_{k=1}^{NQ_\xi} [\mathbf{B}^{(\xi_k)}]^{\mathrm{T}} [\mathbf{P}_{\mathrm{g}}^{(\xi_k)}] \det([J^{(\xi_k)}]) \omega_k + \sum_{i=1}^{N_{\mathrm{f}(e)}} A_0^{\mathrm{f}_i(e)} \sum_{j=1}^{NQ_{\mathrm{f}_i(e)}} [\mathbf{B}^{(\xi_j)}]^{\mathrm{T}} [\mathbf{P}_{\mathrm{c}_i}^{(\xi_j)}] L_{0_j} \omega_j \right], \tag{A.8}$$

where the derivative of the shape functions $[\mathbf{B}^{(\xi_j)}]$ are now evaluated at the isoparametric host element. This means that the truss elements do not add extra degrees of freedom to the system, but only additional integration points at the elements of the host mesh.

As a final remark to this section, we point out that since a global coordinate system $\{\mathbf{e}_1, \mathbf{e}_2, \mathbf{e}_3\}$ was fixed in order to write Eq. (A.4), the correction stress components $[\mathbf{P}_{\mathrm{c}_i}^{(\xi_k)}]$, which are usually evaluated in the truss coordinate system, have to be rotated; this is normally achieved by means of rotation matrices [77, 83, 193]. In the present work, an equivalent approach is employed, in which it is assumed that the material is *transversely isotropic* at each volume $V_0^{\mathrm{f}_i(e)}$, due to the strong directional properties arising from the difference between the stiffer fiber material and the softer ground substance. In mathematical terms, this means that [102]

$$\psi_{\mathrm{c}_i} \equiv \psi_{\mathrm{c}_i}(\mathbf{C}, \mathbf{a}_0^{\mathrm{f}_i(e)} \otimes \mathbf{a}_0^{\mathrm{f}_i(e)}), \tag{A.9}$$

where $\mathbf{C}$ is the right Cauchy-Green tensor and $\mathbf{a}_0^{\mathrm{f}_i(e)}$ is the unit direction vector of the i-th fiber in the material configuration (blue arrow in Fig. A.1). In this case, if ψ_{c_i} is written in terms of the fiber stretch λ, the second Piola-Kirchhoff stress tensor $\mathbf{S}_{\mathrm{c}_i}$ will be given by [102]

$$\mathbf{S}_{\mathrm{c}_i} = 2\frac{\partial \psi_{\mathrm{c}_i}}{\partial I_4}\mathbf{a}_0^{\mathrm{f}_i(e)} \otimes \mathbf{a}_0^{\mathrm{f}_i(e)}, \tag{A.10}$$

where $I_4 = \lambda^2 = \mathbf{a}_0^{\mathrm{f}_i(e)} \cdot \mathbf{C}\mathbf{a}_0^{\mathrm{f}_i(e)}$. Note that since $\mathbf{P}_{\mathrm{c}_i} = \mathbf{F}\mathbf{S}_{\mathrm{c}_i}$, we may see that, if the vector $\mathbf{a}_0^{\mathrm{f}_i(e)}$ is described in terms of the basis $\{\mathbf{e}_1, \mathbf{e}_2, \mathbf{e}_3\}$, calculating and writing the stresses $\mathbf{P}_{\mathrm{c}_i}$ in this coordinate system is a trivial task. It might be shown that this approach is equivalent to the one that employs rotation matrices; however, in a large strain setting it has the advantage of avoiding the recalculation of such matrices (due to changes in fiber orientation) at each iteration; this rotation is accounted for by means of the deformation gradient $\mathbf{F}$.

Linearization of the principle of virtual work

Under finite strains, the problem of finding the displacement field that satisfies the principle of virtual work is always of nonlinear nature. In order to solve it, an incremental/iterative

solution method of Newton-Raphson type is usually employed, to which a consistent linearization of the governing equation is required. To this end, we calculate the directional derivative of Eq. (A.1), which results in

$$D_{\Delta\mathbf{u}}\delta W_{\text{int}}(\mathbf{u},\delta\mathbf{u}) = \int_{\Omega_0} D_{\Delta\mathbf{u}}\mathbf{P}_{\text{g}} : \delta\mathbf{F}\,\mathrm{d}V + \sum_{i=1}^{N_{\text{f}_\text{T}}} \int_{V_0^{\text{f}_i}} D_{\Delta\mathbf{u}}\mathbf{P}_{\text{c}_i} : \delta\mathbf{F}\,\mathrm{d}V, \qquad \forall\,\delta\mathbf{u}\in\mathbb{V}, \quad \text{(A.11)}$$

where $\Delta\mathbf{u}$ is an increment of the displacement field $\mathbf{u}$. Applying the chain rule to Eq. (A.11) yields

$$D_{\Delta\mathbf{u}}\delta W_{\text{int}}(\mathbf{u},\delta\mathbf{u}) = \int_{\Omega_0} \Delta\mathbf{F} : \mathbb{A}_{\text{g}} : \delta\mathbf{F}\,\mathrm{d}V + \sum_{i=1}^{N_{\text{f}_\text{T}}} \int_{V_0^{\text{f}_i}} \Delta\mathbf{F} : \mathbb{A}_{\text{c}_i} : \delta\mathbf{F}\,\mathrm{d}V, \qquad \forall\,\delta\mathbf{u}\in\mathbb{V}, \quad \text{(A.12)}$$

where $D_{\Delta\mathbf{u}}\mathbf{F}(\mathbf{u}) = \Delta\mathbf{F} = \mathrm{Grad}\,\Delta\mathbf{u}$, and

$$\mathbb{A}_{\text{g}} = \frac{\partial\mathbf{P}_{\text{g}}(\mathbf{F})}{\partial\mathbf{F}} \quad \text{and} \quad \mathbb{A}_{\text{c}_i} = \frac{\partial\mathbf{P}_{\text{c}_i}(\mathbf{F})}{\partial\mathbf{F}}, \qquad \text{(A.13)}$$

are the first elasticity (fourth-order) tensors of the ground substance and of the correction of the i-th fiber f_i, respectively.

By employing the same FE mesh, the same interpolation functions and the same integration points as in the previous case, one can show that Eq. (A.12) reduces to the finite strain version of the classical expression for the stiffness matrix $[\mathbf{K}_\text{T}]$ of a continuum mesh with embedded truss elements [90], i.e.

$$[\mathbf{K}_\text{T}] = \mathop{\mathcal{A}}_{e=1}^{N_{\text{el}}} \Bigg[\sum_{k=1}^{NQ_\xi} [\mathbf{B}^{(\xi_k)}]^\text{T} [\mathbb{A}_{\text{g}}] [\mathbf{B}^{(\xi_k)}] \det([J^{(\xi_k)}])\,\omega_k + \sum_{i=1}^{N_{\text{f}(e)}} A_0^{\text{f}_i(e)} \sum_{j=1}^{NQ_{\text{f}_i(e)}} [\mathbf{B}^{(\xi_j)}]^\text{T} [\mathbb{A}_{\text{c}_i}] [\mathbf{B}^{(\xi_j)}] L_{0_j}\omega_j \Bigg]. \quad \text{(A.14)}$$

B Generation of fiber networks

In order to employ the embedded elements technique, whose implementation was detailed in the previous section, two geometries are needed: a solid geometry (to be meshed with 3D elements) and a description of the spatial position and orientation of the reinforcements (to be meshed with 1D elements) within the solid. Therefore, aiming to represent a piece of the microstructure of the arterial wall, we start by defining a right square prism with sides L_C, L_A, L_R, taken to be aligned with the circumferential, axial and radial directions of an artery, respectively. This solid represents the isotropic ground substance, that encompasses all the microstructural components, except for the collagen fibers. A random network of lines is generated within the solid to represent the collagen fiber reinforcement, resembling the distribution in the healthy arterial wall: two fiber families oriented (with some degree of dispersion) along two preferential directions, which are taken to be symmetric with respect to the circumferential axis [113, 216] – see Fig. 3.3(a). The stochastic generation scheme is illustrated in Fig. B.1.

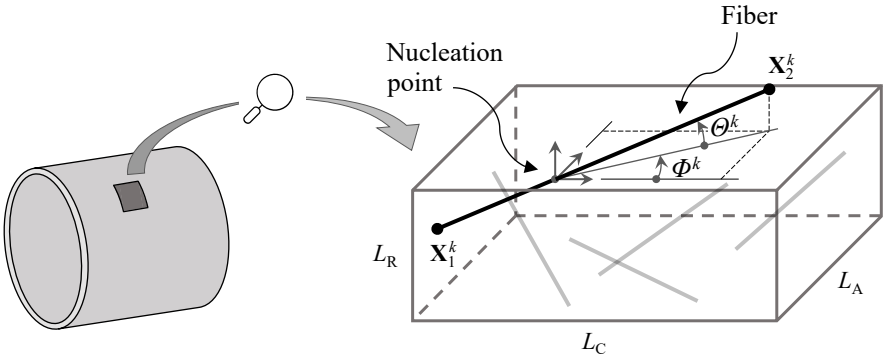

Figure B.1: Illustration of the fiber network generation algorithm. A random point is chosen inside the defined volume and the fiber direction is defined by sampling one in-plane angle Φ^k and one out-of-plane angle Θ^k from the bivariate von Mises distribution (Eq. (3.26)).

The procedure starts by fixing a fiber diameter d, a collagen volume fraction VF and the parameters α, κ_{ip} and κ_{op} of the bivariate von Mises distribution (Eq. (3.26)). Subsequently, a random nucleation point inside the volume is chosen, and a fiber direction $\mathbf{N}(\Phi^k, \Theta^k)$ (Eq. (3.24)) is defined by randomly sampling one in-plane angle Φ and one out-of-plane angle Θ from the von Mises distribution; the in-plane angle sampling alternates between the two symmetric fiber families (dispersed around $+\alpha$ and $-\alpha$, respectively). The k-th fiber centerline is then extended along the generated direction until it crosses the boundaries of the prism, and the so defined start and endpoints ($\mathbf{X}_1^k$ and $\mathbf{X}_2^k$, respectively) of the fiber are then stored. By assuming a cylindrical shape with diameter d, the total fiber volume is updated and the process is repeated until the target volume fraction VF is reached. The sampled in- and out-of-plane angle values are then used to calculate the effective pa-

rameters α^{eff}, $\kappa_{\text{ip}}^{\text{eff}}$ and $\kappa_{\text{op}}^{\text{eff}}$ of the network by using a maximum likelihood estimate, in order to allow for a comparison with the target values.

Algorithm 1: Generation of random fiber networks

Input: $L_{\text{C}}, L_{\text{A}}, L_{\text{R}}, VF, d, \alpha, \kappa_{\text{ip}}, \kappa_{\text{op}}, \text{dt}$

Output: $\mathbf{X}_1^k, \mathbf{X}_2^k, \Phi^k, \Theta^k, \forall k = 1, \ldots, N_{\text{fibers}}$
$\alpha^{\text{eff}}, \kappa_{\text{ip}}^{\text{eff}}, \kappa_{\text{op}}^{\text{eff}}$

$V_{\text{fiber}} = 0$
$VF_{\text{curr}} = 0$
$k = 1$
$N_{\text{L}} = L_{\text{R}}/15$
while $VF_{\text{curr}} < VF$ **do**
  for $n = 1, \ldots, N_{\text{L}}$ **do**
    $z_n^{\min} = 15(n-1)$
    $z_n^{\max} = 15n$
    if n = *odd* **then**
      Sample in-plane angle value Φ^k from the von Mises distribution (Eq. $(3.26)_1$) centered around $+\alpha$
    else
      Sample in-plane angle value Φ^k from the von Mises distribution (Eq. $(3.26)_1$) centered around $-\alpha$
    Sample out-of-plane angle value Θ^k from the von Mises distribution (Eq. $(3.26)_2$)
    Calculate fiber direction $\mathbf{N}(\Phi^k, \Theta^k)$ (Eq. (3.24))
    Generate random nucleation point $\mathbf{x}^0 = [x_1^0, x_2^0, x_3^0]$ with $x_1^0 \in [0, L_{\text{C}}], x_2^0 \in [0, L_{\text{A}}], x_3^0 \in [z_n^{\min}, z_n^{\max}]$
    $\mathbf{x} = \mathbf{x}^0$
    while $x_1 \in [0, L_{\text{C}}], x_2 \in [0, L_{\text{A}}], x_3 \in [z_n^{\min}, z_n^{\max}]$ **do**
      $\mathbf{x} = \mathbf{x}^0 - \text{dt}\,\mathbf{N}$
    $\mathbf{X}_1^k = \mathbf{x}$
    $\mathbf{x} = \mathbf{x}^0$
    while $x_1 \in [0, L_{\text{C}}], x_2 \in [0, L_{\text{A}}], x_3 \in [z_n^{\min}, z_n^{\max}]$ **do**
      $\mathbf{x} = \mathbf{x}^0 + \text{dt}\,\mathbf{N}$
    $\mathbf{X}_2^k = \mathbf{x}$
    $L_{\text{f}}^k = ||\mathbf{X}_2^k - \mathbf{X}_1^k||$
    $V_{\text{fiber}} = V_{\text{fiber}} + L_{\text{f}}^k (\pi/4) d^2$
  $VF_{\text{curr}} = V_{\text{fiber}}/(L_{\text{C}} L_{\text{A}} L_{\text{R}})$
Calculate $\alpha^{\text{eff}}, \kappa_{\text{ip}}^{\text{eff}}$ from the set of Φ^k values by maximum likelihood estimate
Calculate $\kappa_{\text{op}}^{\text{eff}}$ from the set of Θ^k values by maximum likelihood estimate

In the media, which is the arterial layer being considered in the current study, the two fiber families are not intertwined, but rather alternate along the radial direction [183]. Thus, the volume is sliced along the radial dimension L_R in N_L layers 15 µm thick (which is a characteristic value for the thickness of a medial lamellar unit [57, 188, 273]), and generation algorithm described above was applied to each layer separately. The procedure described above, which was implemented in MATLAB® (The MathWorks Inc., Natwick, US), is summarized in Algorithm 1.

In order to investigate which dimensions should be used for L_C, L_A, L_R to obtain a representative fiber network (i.e., how many fibers are needed), a stochastic numerical experiment was devised. To this end, a set of values representative for the healthy arterial media (shown in Table 3.1) was chosen for the parameters VF, d, α, κ_{ip} and κ_{op} and five volume sizes $L_C \times L_A \times L_R$ were investigated, namely:

V1: $30 \times 30 \times 15\,\mu m$

V2: $60 \times 60 \times 30\,\mu m$

V3: $120 \times 120 \times 60\,\mu m$

V4: $240 \times 240 \times 120\,\mu m$

V5: $480 \times 480 \times 240\,\mu m$

Seventeen random networks were then generated for each size and the effective parameters α^{eff}, κ_{ip}^{eff} and κ_{op}^{eff} were calculated. The median and the first and third quartiles for the 17 realizations were then compared with the experimental values reported by Niestrawska et al. [183] for 17 samples of healthy arterial media. The results are shown in Fig. B.2.

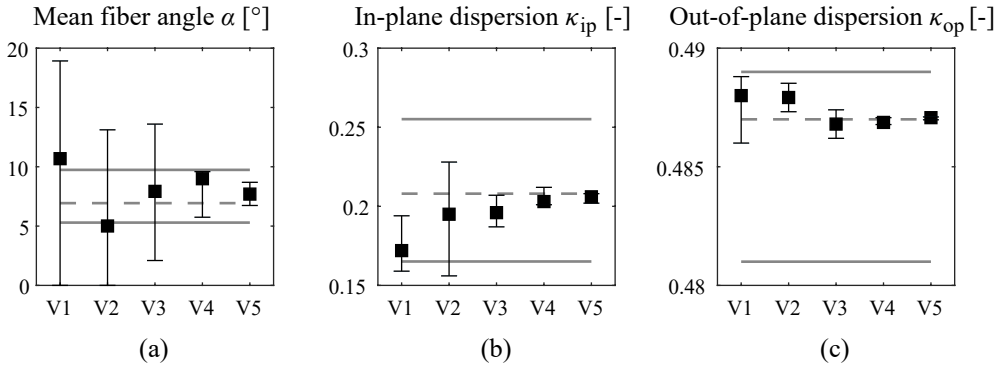

Figure B.2: Median (black squares), first and third quartiles (error bars) of the effective parameters (a) α^{eff}, (b) κ_{ip}^{eff} and (c) κ_{op}^{eff} calculated from 17 random networks generated according to Algorithm 1 are compared with the median (dashed gray line), first and third quartiles (solid gray lines) of the same parameters obtained from 17 samples of healthy arterial media by Niestrawska et al. [183].

The gray lines represent the experimental median (dashed) and first and third quartiles (solid). The black data points are the median values obtained for the numerical experiments, for each of the five sizes, and the error bars represent the first and third quartiles.

It may be seen that for the out-of-plane dispersion (Fig. B.2(c)), which is usually quite low in the healthy arterial wall (i.e., most fibers are aligned with the circumferential-axial plane), even the smallest volume V1 contains enough fibers to reproduce the experimental variation of the parameter κ_{op}. For the considerably higher in-plane dispersion κ_{ip} (Fig. B.2(b)), the volume V3 seems to be large enough to achieve a representative distribution, whereas for the mean fiber angle α (Fig. B.2(c)), a volume of size V4 is needed. Based on the above results, a single network of size V4 was generated and employed in the construction of the four RVEs studied in the present work, as detailed in Section 3.3.1.

C Mesh convergence

As detailed in Section 3.2.1 and Appendix A, the embedded element technique employs a 'host' mesh of 3D elements, in which 1D elements are embedded by means of a kinematic bond imposed via the shape functions of the continuum mesh. In the present work, second-order tetrahedrons were used to discretize the matrix material (ground substance); in order to choose a suitable element size, a mesh convergence analysis was performed for RVE 3, whose size is $120 \times 120 \times 60\,\mu\text{m}$ (see Fig. 3.6).

Four meshes were constructed employing characteristic element sizes of 7.5, 6.0, 5.0 and $4.0\,\mu\text{m}$; as a result, meshes 1 to 4 had, respectively, 18513, 35301, 60025 and 115351 nodes – resulting in a factor of approximately 2 between the mesh sizes. We recall the fact that a compatible discretization of the fiber network must be done for each mesh (see Eq. (A.2)). Therefore, the corresponding truss meshes had, respectively, 20311, 25494, 30478 and 38223 elements – which, however, do not add extra degrees of freedom to the problem, see the discussion in Appendix A.

An equibiaxial isochoric stretch of 10% (see Eq. (3.31)) was then simulated for each mesh with the periodic model. Similarly to Section 3.4.2, the equivalent (von Mises) measure of the logarithmic (micro-)strain ε_{eq} was chosen to be analyzed. Results are shown in Fig. C.1.

The resulting microscopic strain fields for the four meshes are shown in the middle part of the figure. The meshes were sliced halfway through the thickness (radial direction) in order to show also the inside of the RVE. As done in Figs. 3.11-3.13, each color of the (nonlinear) contour scales was chosen to represent 10% of the elements of each mesh. In the bottom part of Fig. C.1, normalized histograms show the distribution of equivalent logarithmic strains for each mesh, and the contour colors representing the deciles are also depicted. Finally, the arrow under the horizontal axis of each histogram identifies the value of the macroscopic equivalent logarithmic strain.

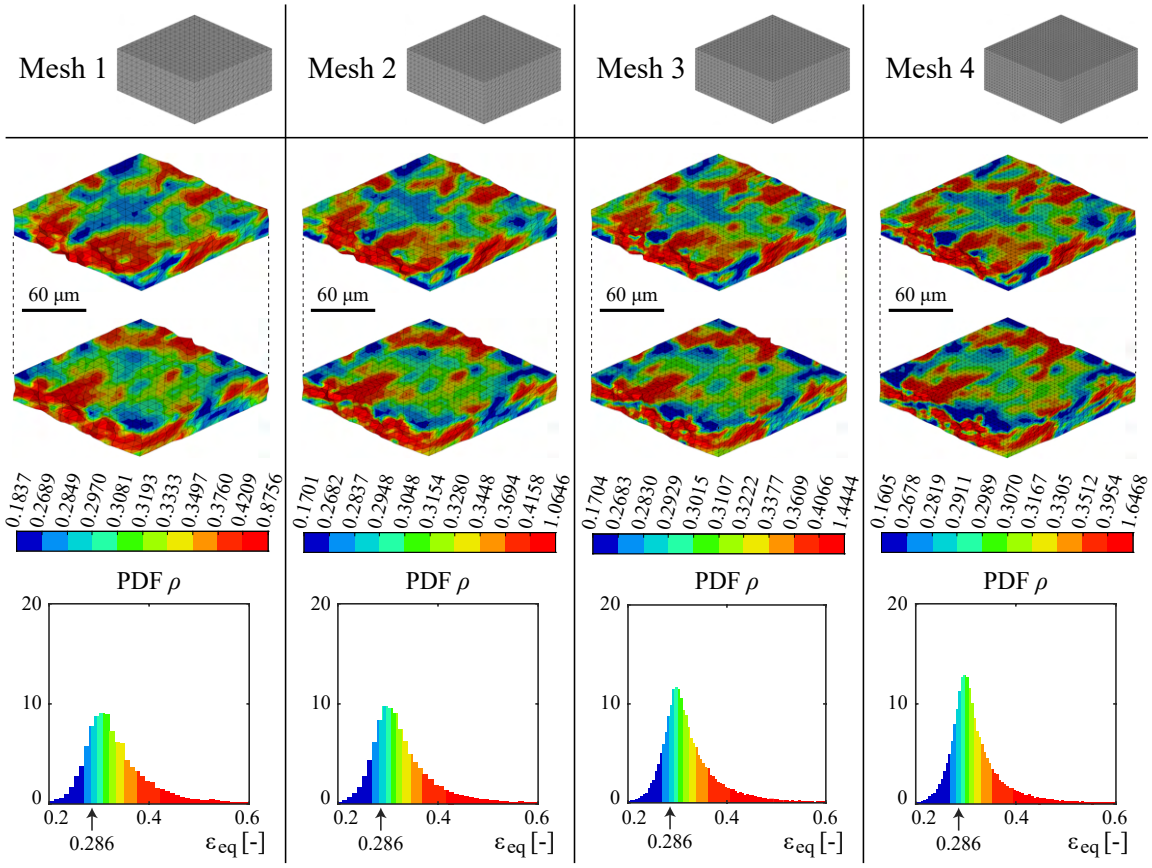

Figure C.1: Distribution of equivalent logarithmic strains (middle) and corresponding PDF distribution (bottom) for RVE 3 simulated with different element sizes and the periodic boundary fluctuations model. Mesh size increases from left to right.

From the results in Fig. C.1, we may see that the areas of higher and lower strains are similarly distributed in the meshes 1 to 4, since they arise from the embedded fiber network (which is the same for all meshes, albeit with different discretizations). The values of the strain deciles are remarkably consistent between different meshes, with variations lower than 3%, except for the minimum and maximum values. The larger variations observed for the extremes of the distribution are likely due to local singularities arising from the changes in the fiber network discretization. However, such local effects would probably have a limited influence on the overall mechanobiological state of the tissue, which is our main point of interest. Finally, we notice that only minimum changes can be seen in the normalized histograms of equivalent strains when refining the element size from 5.0 (mesh 3) to 4.0 µm (mesh 4). Therefore, a characteristic element size of 5.0 µm was employed to generate the 'host' meshes of RVEs 1 to 4 (Fig. 3.7).

4 MULTISCALE SIMULATIONS SUGGEST A PROTECTIVE ROLE OF NEO-ADVENTITIA IN ABDOMINAL AORTIC ANEURYSMS

Abstract. Abdominal aortic aneurysms (AAAs) are a dangerous cardiovascular disease, the pathogenesis of which is not yet fully understood. In the present work a recent mechano-pathological theory, which correlates AAA progression with microstructural and mechanical alterations in the tissue, is investigated using multiscale models. The goal is to combine these changes, within the framework of mechanobiology, with possible mechanical cues that are sensed by vascular cells along the AAA pathogenesis. Particular attention is paid to the formation of a 'neo-adventitia' on the abluminal side of the aortic wall, which is characterized by a highly random (isotropic) distribution of collagen fibers. Macro- and micro-scale results suggest that the formation of an AAA, as expected, perturbs the micromechanical state of the aortic tissue and triggers a growth and remodeling (G&R) reaction by mechanosensing cells such as fibroblasts. This G&R then leads to the formation of a thick neo-adventitia that appears to bring the micromechanical state of the tissue closer to the original homeostatic level. In this context, this new layer could act like a protective sheath, similar to the tunica adventitia in healthy aortas. This potential 'attempt at healing' by vascular cells would have important implications on the stability of the AAA wall and thus on the risk of rupture.

4.1 Introduction

Abdominal aortic aneurysms (AAAs) are a life-threatening medical condition characterized by a localized pathological bulging of the infrarenal aorta, which is usually diagnosed when the vessel diameter exceeds 30 mm [189, 249]. Among the cardiovascular diseases, AAAs stand out as being particularly dangerous: blood pressure can drive a constant and in many cases silent growth of the aneurysm sac up to rupture, with mortality rates of up to 90% being reported [189, 240].

The risk of rupture can be reduced by elective surgery, especially in the case of larger aneurysms [189, 211]. In view of the advanced age of most patients, however, the risk of the surgical procedure itself (even with minimally invasive techniques [131]) must be taken into account [68, 249]. To assess the need for intervention, medical criteria of an empirical nature were developed, which are mainly based on the size of the aneurysm: as a rule, intervention is typically advocated if the maximum diameter of the lesion reaches 5.0 cm in women or 5.5 cm in men, or if the diameter increases more than 0.5–1 cm in one year [85, 89, 101, 152, 189]. However, reports of ruptured AAAs that are smaller than this threshold, as well as larger AAAs that remain stable, have raised questions about the suitability of such rough guidelines [122, 227, 256, 258]. The complex pathogenesis of the

disease suggests that a better understanding of AAA evolution is needed to facilitate the development of better surgical criteria.

Soft tissues such as the aortic wall are a remarkable example of the *'form follows function'* principle in nature, since the arrangement of their microconstituents is generally closely related to their biological function. In tendons and ligaments, e.g., the stiff collagen fibers are strongly aligned with the load-bearing direction [25, 137, 229]. The healthy aorta, in turn, is characterized by three well-defined layers: tunica intima, tunica media and tunica adventitia – or the innermost, middle and outermost layers [109]. Each of the three contains vascular cells embedded in a highly organized extracellular matrix (ECM), which consists mainly of elastin and collagen. The result is a thick-walled tube, reinforced by a layered fibrous helix, a configuration that is clearly related to the (bio)mechanical function of the vessel [109, 215, 272].

The specific configuration of the ECM in soft tissues is maintained by cells that are able to probe their mechanical environment and react accordingly by degrading and producing ECM proteins – a characteristic example of mechanobiology [201, 233, 248]. The goal of this physiological mechanism is to preserve mechanical homeostasis, i.e., to maintain tissue integrity and functionality [23, 64, 126]. In the healthy aorta, smooth muscle cells (SMCs) in the media and fibroblasts in the adventitia play this role [105]; in fact, several *in vitro* studies with these cells have demonstrated their ability to sense changes in their mechanical environment and react accordingly in order to (re)organize the ECM [12, 22, 63, 86, 142, 153, 155].

The concept of mechanobiology is directly related to the fact that soft tissues are able to (re)model their structure (at least in part) according to the loads they are exposed to – or changes thereof, e.g., during somatic growth or in case of an injury (e.g., a skin cut or a torn ligament) [2, 179, 204, 237]. As summarized in the 19th century by Davis, *'ligaments, or any soft tissue, when put under even a moderate degree of tension, if that tension is unremitting, will elongate by the addition of new material; on the contrary, when ligaments, or other soft tissues, remain uninterruptedly in a loose or lax state, they will gradually shorten, as the effete material is removed, until they come to maintain the same relation to the bony structure with which they are united that they did before their shortening'* [45].

In this context, Niestrawska et al. [185] identified significant changes in both the microstructure and mechanical behavior of AAA tissue compared to healthy aortas. The authors then proposed a three-stage model to describe the pathogenesis of the disease: briefly, after an early loss of elastin and SMCs at the AAA site, the localized bulge starts to form; this leads to a remodeling of the collagen fibers in the circumferential direction and the healthy three-layer structure of the wall is lost. The expanding AAA also pushes against the surrounding adipose tissue, triggering an inflammatory process on the abluminal side of the wall. Inflammatory cells and fibroblasts promote fibrotic, scar-like growth and remodeling (G&R) of the collagen network, which stiffens the tissue considerably

and leads to the formation of a 'neo-adventitia', characterized by a random orientation (isotropy) of the collagen fibers on the abluminal side of the wall. For further details on their findings, the interested reader is referred to the work by Niestrawska et al. [185].

On the basis of the above considerations one could ask whether the remodeling of the collagen network in the AAA wall identified by Niestrawska et al. [185] is related to changes in mechanical loads sensed by vascular cells in the course of the disease. In view of the microscopic size of such cells, the present work aims to shed light on this possible connection by means of multiscale simulations, using a finite element (FE) model recently presented in [41]. Representative volume elements (RVEs) consisting of collagen fibers embedded in a ground substance are constructed based on the microstructure of healthy abdominal aortas [183], and various stages of AAAs identified by Niestrawska et al. [185]. A macroscopic equibiaxial stretch is simulated for each RVE. Then, the resulting microscale deformation fields are analyzed to correlate changes in the microscopic mechanical state of the tissue with possible cues sensed by cells that might drive G&R of the collagen network along the AAA pathogenesis in the framework of mechanobiology.

4.2 Methods

This section describes the geometries, constitutive models and boundary conditions that are used in the multiscale FE simulations.

4.2.1 RVE geometries

Fifteen RVEs were constructed, each representing a *point* of a healthy or diseased (aneurysmal) abdominal aorta. Each RVE geometry consists of a network of lines representing two collagen fiber families (red and blue), roughly symmetrical with respect to the circumferential direction of the artery and embedded into a ground substance (pink), see Fig. 4.1. The latter includes all non-collagenous constituents of the wall, e.g., elastin, proteoglycans and, above all, mechanosensing cells such as fibroblasts. Each of the three sets of five RVEs shown in Fig. 4.1 represent the abluminal side of the wall:

- of a healthy aorta (tunica adventitia), the fibers of which are preferably aligned in the axial direction of the vessel;
- of an AAA in the early stage, characterized by a reorientation of the fibers towards the circumferential direction;
- of an AAA at a late stage, in which a strongly isotropic fiber distribution (neo-adventitia) has developed as a result of the intense G&R promoted by inflammation and fibroblasts.

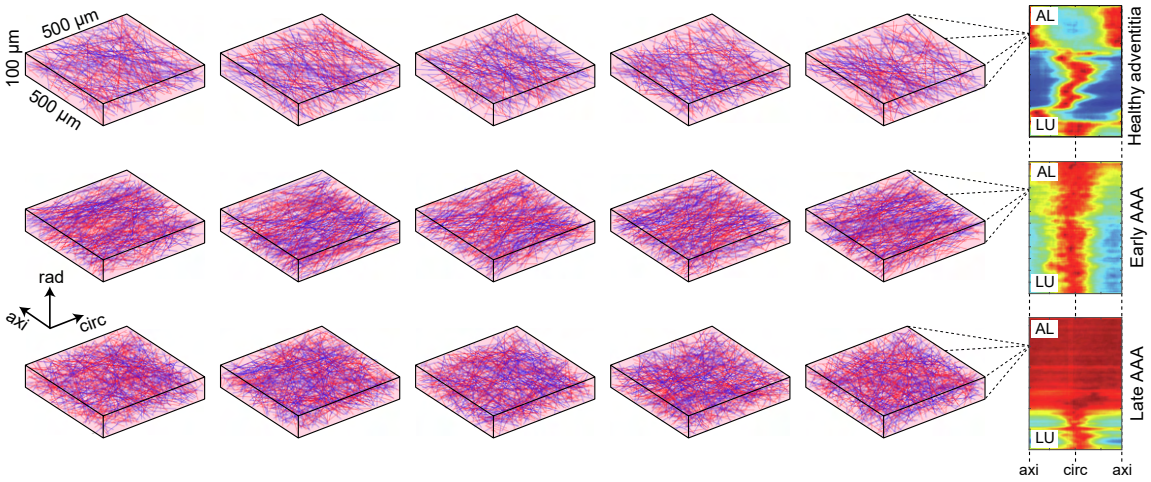

Figure 4.1: The fifteen RVEs considered in the present study. Each RVE represents a point of a healthy adventitia (top), an early AAA (middle) and a late AAA (bottom). The heatmaps (right) illustrate the experimentally measured orientation of collagen fibers in the circumferential-axial plane of the artery: red and blue colors indicate, respectively, high and low concentrations of fibers oriented in a certain direction. In this regard, the center and edges of the heatmap correspond to the circumferential and axial directions of the artery, respectively. AL = abluminal; LU = luminal. Heatmaps adapted from [185].

The RVEs shown in Fig. 4.1 were generated by adapting a stochastic algorithm that was previously used in [41]; further details can be found in the Supplementary Material. In short, after fixing the RVE size, fibers are added to the network until a collagen volume fraction F_T is achieved. The target values of F_T are 40%, 60% and 60% for healthy adventitia, early AAA and late AAA, respectively [8, 183, 185]. The RVE size of $500 \times 500 \times 100\,\mu m$ was chosen to ensure a representative network of fiber directions, i.e., so that there are enough fibers for the selected collagen fractions.

Each fiber direction is described in spherical coordinates by two angle values Φ and Θ, respectively, the azimuthal angle, measured in the circumferential-axial plane of the artery, and the elevation angle with respect to the same plane. Individual values for Φ and Θ are sampled for each fiber from a bivariate von Mises distribution, which is defined by the parameters α, κ_{ip} and κ_{op}, each denoting, respectively, the mean azimuthal angle, the amount of dispersion of the azimuthal angles around α and the amount of dispersion of the elevation angles, the mean value of which is assumed to be zero. For further information on the characterization of the collagen distribution in arterial tissues using the bivariate von Mises distribution, the reader is referred to the Supplementary Material and the work of Holzapfel et al. [113].

Table 4.1 shows the target (experimental) and effective (numerical) parameters α, κ_{ip} and κ_{op} for the three stages of the tissue. All values are given as median and interquartile ranges (IQR). The good agreement between experimental and numerical values indicates that the fiber networks are sufficiently representative for each microstructure, as required.

Table 4.1: Parameters of the bivariate von Mises distribution for healthy adventitia (left), early AAAs (middle), and late AAAs (right). All values are given in terms of medians and interquartile ranges. Experimental (target) values were taken from the literature [183, 185], while the numerical parameters were calculated from the fiber networks in Fig. 4.1; see the Supplementary Material for more details.

	Healthy adventitia		Early AAA		Late AAA	
	Exp. [183] ($n = 16$)	Num. ($n = 5$)	Exp. [185] ($n = 6$)	Num. ($n = 5$)	Exp. [185] ($n = 6$)	Num. ($n = 5$)
α	77.53° [67.04°-84.02°]	72.23° [71.91°-73.99°]	6.55° [5.19°-11.62°]	7.04° [5.76°-9.75°]	0.00° *	0.00 [0.00°-0.00°]
κ_{ip}	0.232 [0.192-0.182]	0.217 [0.200-0.225]	0.242 [0.234-0.260]	0.236 [0.232-0.236]	0.500 *	0.500 [0.493-0.500]
κ_{op}	0.466 [0.459-0.479]	0.466 [0.466-0.467]	0.433 [0.425-0.441]	0.433 [0.433-0.435]	0.402 [0.379-0.421]	0.396 [0.396-0.395]

* For a perfect in-plane isotropic distribution, $\kappa_{ip} = 0.5$ and the mean in-plane angle α becomes superfluous.

The changes in collagen arrangement identified by Niestrawska et al. [185] and mentioned at the beginning of this section are reflected in the values of Table 4.1, where the in-plane distribution of collagen fibers, described by α and κ_{ip}, shifts its preferential alignment from the axial direction in the healthy adventitia to the circumferential direction in the early AAAs, and subsequently remodels into a highly random (isotropic) distribution around the circumferential-axial plane in late AAAs. It can also be seen that the out-of-plane dispersion of healthy adventitia increases until late AAA, since $\kappa_{op} = 0.5$ denotes a perfectly planar distribution [113].

Constitutive models

As generally assumed in the literature [104, 109, 220, 232, 238], the ground substance was modeled as a nearly incompressible neo-Hookean material whose strain-energy function Ψ_g is given by

$$\Psi_g(\overline{\mathbf{C}}) = \frac{G_g}{2}(\bar{I}_1 - 3) + \frac{K_g}{2}(J-1)^2, \tag{4.1}$$

where $J > 0$ is the volume ratio, $\mathbf{C}$ is the right Cauchy-Green tensor, $\overline{\mathbf{C}} = J^{-2/3}\mathbf{C}$ is the modified right Cauchy-Green tensor (with $\det\overline{\mathbf{C}} \equiv 1$), G_g is the shear modulus of the

ground substance, $\bar{I}_1 = \overline{\mathbf{C}} : \mathbf{I}$ is the first invariant of $\overline{\mathbf{C}}$, and K_g is a penalty (volumetric) parameter, which was chosen to be $K_\mathrm{g} = 100 G_\mathrm{g}$ to ensure nearly incompressible behavior. The value of the shear modulus G_g depends on the state of the tissue and is set to 3.77 kPa [183], 0.59 kPa and 3.78 kPa [185] for the healthy adventitia, the early AAA and the late AAA, respectively.

As the characteristic waviness of the collagen fibers is not taken into account in the RVEs shown in Fig. 4.1, a strain-energy function Ψ_{f_i} of the form [41]

$$\Psi_{\mathrm{f}_i}(\lambda) = \begin{cases} 0, & \text{if} \quad 0 < \lambda < \lambda_\mathrm{r}^i, \\ \dfrac{E_\mathrm{f}^i}{2}(\lambda - \lambda_\mathrm{r}^i)^2, & \text{if} \quad \lambda \geq \lambda_\mathrm{r}^i \end{cases} \tag{4.2}$$

was assigned to each i-th fiber, where E_f^i is the fiber stiffness, λ is the stretch applied to the fiber and λ_r^i is the recruitment stretch of the fiber. In Eq. (4.2) it is assumed that fibers only bear load if they are recruited, i.e., if the applied stretch λ surpasses λ_r^i. This gradual fiber recruitment phenomenon is responsible for the characteristic J-shaped mechanical response of the arterial tissue, as discussed in detail in the literature [103, 149, 199, 215, 234].

It is worth noting that the fibers are assigned different values of E_f^i and λ_r^i to account for the stiffness and waviness variability between them. For the first parameter, Miyazaki and Hayashi [174] reported a mean value of 54.3 MPa with a standard deviation of 25.1 MPa. Assuming a normal distribution, a value for E_f^i is sampled for every i-th fiber. In turn, the fiber recruitment stretch λ_r^i is assigned to each i-th fiber by sampling a value of the fiber waviness parameter P_s^i (see Fig. 4.2(a)) from a beta distribution of the form [186, 198]

$$\rho_\mathrm{r}(P_\mathrm{s}) = \frac{{P_\mathrm{s}}^{a-1}(1-P_\mathrm{s})^{b-1}}{B(a,b)}, \tag{4.3}$$

where $B(a,b)$ is the beta function. The recruitment stretch of the fiber is then calculated as $\lambda_\mathrm{r}^i = L_\mathrm{f}/L_0 = 1/P_\mathrm{s}^i$.

It is assumed that the parameters a and b in Eq. (4.3) change according to the state of the tissue; from image analysis, Niestrawska et al. [186] found $\{a,b\} = \{4.84, 1.54\}$ for the healthy adventitia and $\{a,b\} = \{3.29, 0.635\}$ for the abluminal side of AAA samples. Since the authors did not differentiate between the stages of AAA when measuring P_s, it was assumed that these parameters apply to late AAAs, and that the distribution of the fiber waviness for early AAAs lies between the other two states, with $\{a,b\} = \{4.0, 1.1\}$. In the Figs. 4.2(b)-(d) the target distributions are compared with the normalized histograms of the P_s values attributed to the fibers of each of the three RVE sets shown in Fig. 4.1. Bearing in mind that a value of $P_\mathrm{s} = 1$ indicates a perfectly straight fiber, it might be seen that the fibers in the healthy adventitia (Fig. 4.2(b)) are, in general, much more wavy than those found in AAAs (Fig. 4.2(d)).

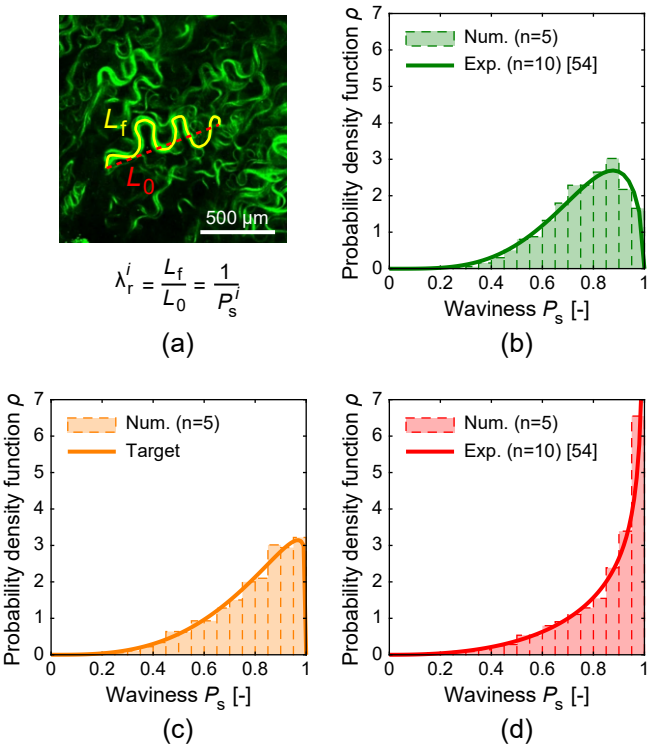

Figure 4.2: Second-harmonic generation image of a healthy abdominal aortic adventitia showing the collagen fibers in green (adapted from [8]); for the fiber highlighted in yellow, $P_s = 0.474$ (a). Normalized histograms of P_s values for the RVEs representing the healthy adventitia (b), the early AAA (c) and the late AAA (d) are compared with the respective target beta distribution (Eq. (4.3)) obtained from experiments [186].

Mesh and boundary conditions

The ground substance of each RVE was meshed using second-order hexahedrons with a characteristic size of 12.5 µm, defined after a mesh convergence analysis (see Supplementary Material), for a total of 12 800 elements per RVE. Fibers were meshed with second-order trusses, so that each 1D element is completely included within a certain hexahedron [41]. A kinematic bond (no-slip condition) is imposed between each 3D element and the reinforcing truss elements that it contains. The effect of this kinematic bond, combined with the recruitment stretch property of the fiber model (Eq. (4.2)), is illustrated in Fig. 4.3.

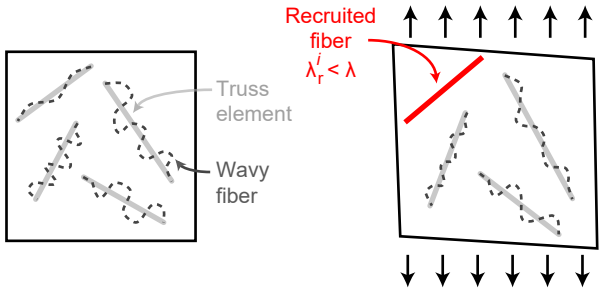

Figure 4.3: Illustration of the recruitment stretch fiber model combined with the embedded elements technique. Each truss FE (light gray) represents a fiber with a certain waviness (dark gray), embedded in the ground substance (continuum FE, black). Both phases deform together, and when the stretch applied to a particular truss element exceeds the recruitment stretch, the fiber is recruited and begins to bear load (red), which gives directional stiffness to the 3D domain. Further details can be found in [41].

It is assumed that the (macroscopic) point of the tissue at which each RVE is located experiences an incompressible equibiaxial stretch of 10% in the circumferential-axial plane, i.e., that the deformation gradient $\mathbf{F}$ at this point is given, in matrix form, by

$$[\mathbf{F}] = \begin{bmatrix} \lambda_{\text{circ}} & 0 & 0 \\ 0 & \lambda_{\text{axial}} & 0 \\ 0 & 0 & \lambda_{\text{rad}} \end{bmatrix} = \begin{bmatrix} 1.10 & 0 & 0 \\ 0 & 1.10 & 0 \\ 0 & 0 & 0.826 \end{bmatrix}. \tag{4.4}$$

A volume-averaging multiscale theory is used to simulate the corresponding microscopic deformation of each RVE; details on this can be found elsewhere [16, 49, 50]. Periodic displacement fluctuations are assumed at the boundary of the RVEs, as suggested in [41] for multiscale simulations used in combination with the embedded element technique.

The 15 simulations were carried out with a custom FE code on a desktop computer (8-core Intel® i9-9900K with 128 GB of RAM) [41]. Each simulation ran for about 4 hours.

4.2.2 Statistical analyses

In order to shed light on mechanobiological phenomena at the cellular level, relevant mechanical quantities were calculated at the micro-scale for each RVE and grouped according to the three sets from Fig. 4.1. In general, a normal distribution of these quantities within each group could not be assumed, therefore all results are given in terms of medians and interquartile ranges (IQR), unless otherwise stated. Consequently, statistical differences between the three groups were checked with the Mann-Whitney U test.

4.3 Results

In this section, the results of the simulations are presented both at the macroscopic (tissue) and microscopic (cellular) level.

4.3.1 Macroscopic results

For each RVE, the macroscopic (homogenized) Cauchy stress response was determined by computing the volumetric average of the stresses in the deformed RVE domain; see [41] for details. The homogenized stresses describe the mechanical response of the tissue at the (macroscopic) point at which each RVE is located when, as explained above, it is subjected to an equibiaxial stretch up to 10%.

The mean value (solid curves, red) and the bounds (dashed curves, red) of the circumferential (left) and axial (right) components of the macroscopic Cauchy stress were calculated for the three RVE sets in Fig. 4.1, and are plotted in Fig. 4.4 against the imposed stretch for (a) the healthy adventitia, (b) early AAAs and (c) late AAAs. For each of these three stages, the numerical responses are compared with experimental data (gray) obtained from equibiaxial tests on tissue samples in previous works [183, 185].

In Fig. 4.4(a) it can be seen that in the healthy adventitia the axial response (right) of the RVEs is stiffer than the circumferential (left), which is related to the preferred alignment of the collagen fibers in the axial direction, as shown in Fig. 4.1. The same anisotropy is observed in the bounds (gray shaded area) of the experimental data, while the mean response (gray dots) shows almost no anisotropy, at least up to 10% of equibiaxial stretch.

The opposite trend is present in Fig. 4.4(b): for the early AAA tissue, the circumferential direction (left) is stiffer, which corresponds to the fact that the collagen fibers are preferably oriented in this direction (Fig. 4.1). Here, too, this anisotropic behavior is more pronounced in the numerical data (red) and in the bounds of the experimental data (shaded gray area) compared to the mean experimental response (gray dots).

The anisotropy observed in the previous two stages has largely disappeared for the late AAA tissue, since in the curves of Fig. 4.4(c), the differences between the circumferential (left) and axial (right) responses are generally absent. This agrees with the random (isotropic) organization of the collagen fibers, which is shown in Fig. 4.1. It is emphasized that the late AAA is significantly stiffer than the other two states: for the numerical response, e.g., the stress in both directions at 10% stretch is approximately an order of magnitude higher.

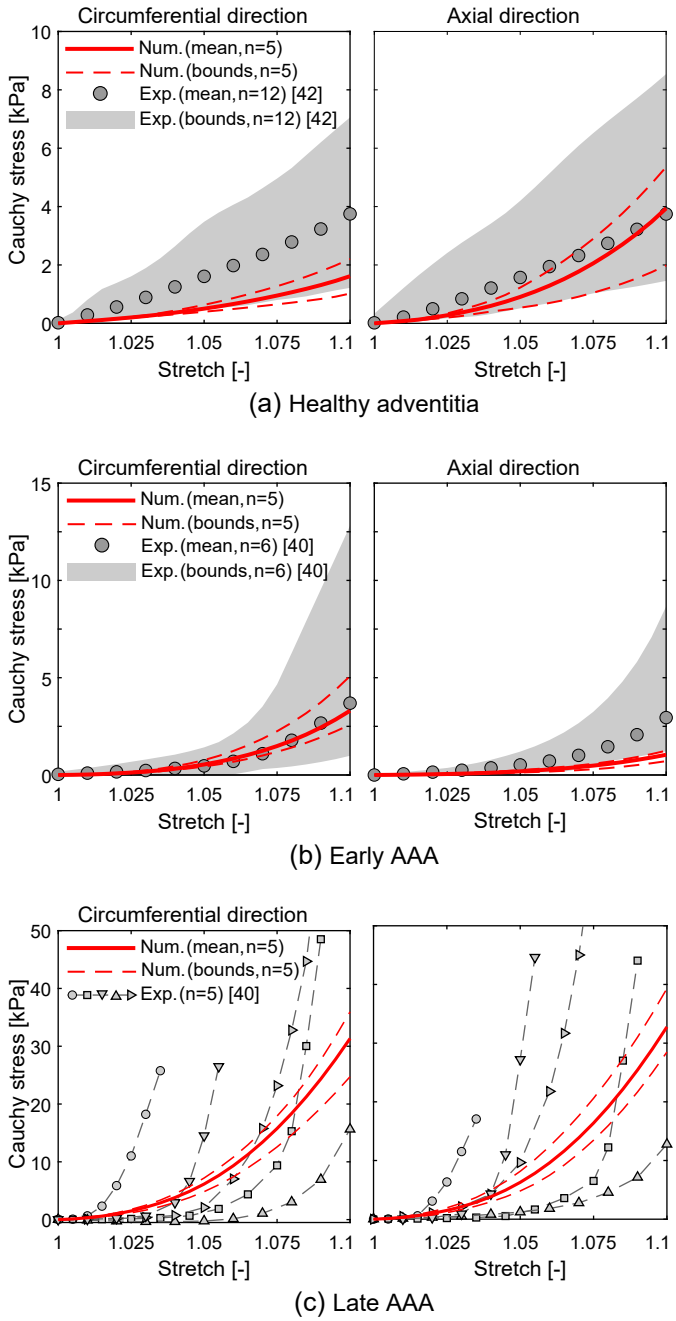

Figure 4.4: Comparison between experimental [183, 185] (gray) and numerical (red) Cauchy stress-stretch responses for (a) the healthy adventitia, (b) the early AAA and (c) the late AAA. For the last stage (c), individual curves (in gray) were plotted instead of the experimental mean and the bounds, since some samples did not reach a stretch of 10% before failing.

4.3.2 Microscopic results

So far there is no consensus on the mechanical quantity cells sense in the course of a mechanobiological process [65]. However, as argued by Humphrey [118], continuum metrics such as stress and strain can be a useful tool to correlate cellular responses to mechanical stimuli. In the present work the maximum principal stretch[a] λ_1 is used to evaluate possible mechanical cues sensed by cells at the focal adhesions connecting them to the collagen network, which are about one micrometer [88]. For all RVEs, this amount was calculated at each integration point of the (continuum) ground substance, which, as discussed above, comprises all the non-collagenous microconstituents of the tissue, including mechanotransducing cells such as fibroblasts. Therefore, it is assumed that changes in the overall levels of λ_1 between the three RVE groups might indicate micromechanical alterations sensed by such cells through their focal adhesions during AAA pathogenesis.

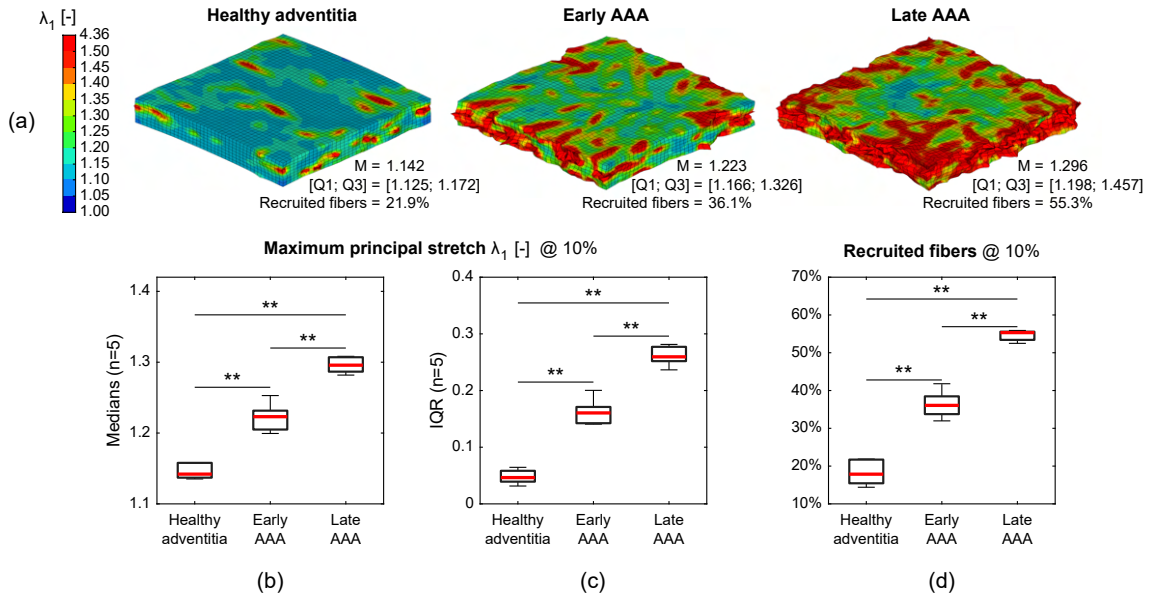

Figure 4.5: Distribution of the maximum principal stretches λ_1 (a) for RVEs of the healthy adventitia (left), the early AAA (center) and the late AAA (right) under a macroscopic equibiaxial stretch of 10%; the median (M) and quartiles (Q1; Q3) of the λ_1 values and the percentage of fibers recruited are given below each RVE. Boxplots showing the distribution of the medians (b) and the interquartile ranges (c) of the λ_1 values as well as the percentages of fibers recruited (d) for all RVEs (grouped according to the three sets of Fig. 4.1) under a macroscopic equibiaxial stretch of 10%. Mann-Whitney U test: ** corresponds to $p < 0.01$.

[a] For a deforming continuum medium the maximum principal stretch at one point is defined as the largest eigenvalue of the stretch tensors at this point; see [102] for further details.

Figure 4.5(a) shows the distribution of λ_1 in three examples of RVEs, one for each tissue state, under a macroscopic equibiaxial stretch of 10%. The median (M) and the interquartile range (IQR) of λ_1 values were calculated for each RVE from all integration points of the continuum mesh. In addition, the percentage of fibers recruited was calculated by dividing the number of load-bearing truss elements (i.e., whose recruitment stretch λ_r^i was exceeded, see Fig. 4.3) by the total number of elements.

The 15 median and IQR values of λ_1 as well as the percentages of recruited fibers were grouped according to the the three RVE sets from Fig. 4.1 and are shown in the boxplots of Figs. 4.5(b)-(d), which indicate that the values are generally not normally distributed. Therefore the Mann-Whitney U test was used to check for statistically significant changes between the groups. The results are also depicted in Figs. 4.5(b)-(d), where significant increases from the healthy adventitia to the late AAA are evident for all three metrics under the same level of macroscopic stretch (10%).

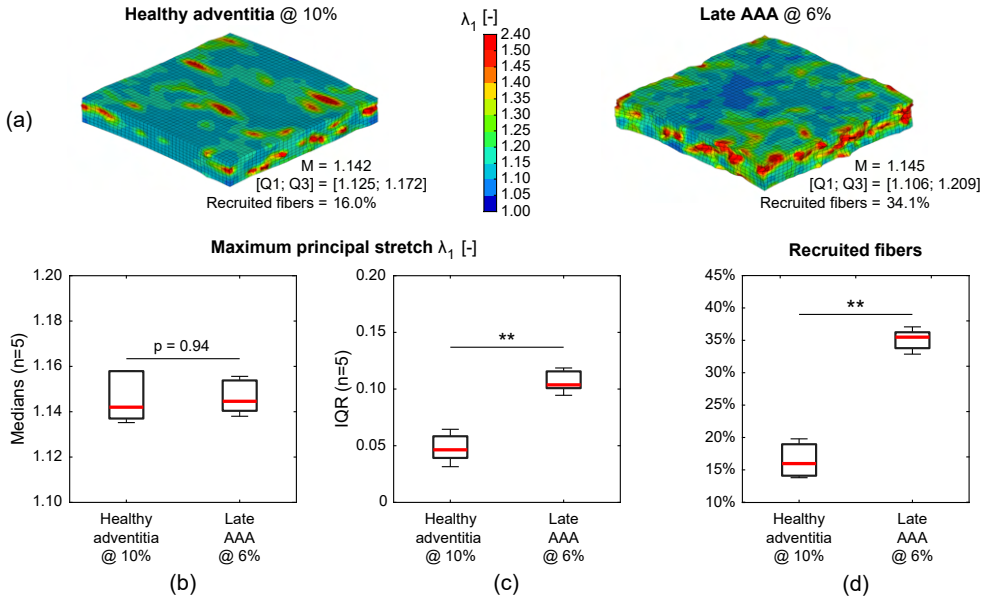

Figure 4.6: Distribution of the maximum principal stretches λ_1 for RVEs of the healthy adventitia (left) and the late AAA (right), (a), under macroscopic equibiaxial stretches of 10% and 6%, respectively; the median (M) and quartiles (Q1; Q3) of the λ_1 values and the percentage of fibers recruited are given below each RVE. Boxplots showing the distribution of the medians (b) and the interquartile ranges (c) of the λ_1 values as well as the percentages of fibers recruited (d) for RVEs of the healthy adventitia and the late AAA tissue under macroscopic equibiaxial stretches of 10% and 6%, respectively. Mann-Whitney U test: ** corresponds to $p < 0.01$.

However, considering that the late AAA tissue is substantially stiffer than the healthy adventitia (see Fig. 4.4), it is hypothesized that under similar blood pressure levels the stretches at the macroscopic (tissue) level would be higher in the healthy adventitia than in the late AAA tissue. On that basis, in Fig. 4.6 the analyses of Fig. 4.5 were repeated, now comparing the RVEs of the healthy adventitia and the late AAA under macroscopic equibiaxial stretches of 10% and 6%, respectively. In this case, Figs. 4.6(a)-(b) indicate that the overall level of deformation between the two groups is similar; in particular there is no statistically significant difference between the median values of λ_1 ($p = 0.94$), even if the late AAA tissue contains a higher number of recruited fibers (Fig. 4.6(d)). The latter seems to be related to the higher scatter of λ_1 (measured by the IQR, Fig. 4.6(c)) within the RVE domains of this group, which is also reflected in the higher heterogeneity of the λ_1 values in the example of a late AAA RVE (Fig. 4.6(a), right) compared to a healthy one (left).

As a final remark to this section it should be emphasized that the choice of the maximum principal stretch λ_1 as a measure for the deformation on the micro-scale is not completely arbitrary, since fibroblasts are known to react to tensile stimuli [22, 63, 153]. However, it was verified that other deformation measures, e.g., the von Mises strain, give similar patterns (results not shown here). Since a hyperelastic behavior is assumed for both material phases, the use of a stress measure would certainly lead to the same results. As discussed at the beginning of this section, the chosen continuum measure is used here just to compare the micromechanical state of different RVEs.

4.4 Discussion

The aim of the present work is to elucidate mechanobiological mechanisms that could drive changes in the microstructure of the aortic tissue along the pathogenesis of AAAs, as identified by Niestrawska et al. [185]. Particular attention is paid to G&R of the collagen network, which leads to the formation of a ‘neo-adventitia’, the fibers of which are more randomly aligned in the circumferential-axial plane, which leads to a high in-plane isotropy of the fiber directions. This G&R on the abluminal side of the aorta is mainly promoted by fibroblasts in a scar-like, fibrotic inflammatory process [185].

Given the microscopic size of such cells, multiscale models are used; therefore, RVEs were constructed and simulated, which represent the microstructure of the aorta in different disease stages, see Fig. 4.1. It is pointed out that while the FE models only refer to the micro-scale, the macroscopic response of the tissue (at a point represented by the RVE) could still be assessed by numerical homogenization [41].

Overall, the obtained numerical Cauchy stress-stretch response agrees fairly well with the experimental data for all stages, as shown in Figs. 4.4(a)-(c). The differences observed can be explained, firstly, by the fact that both the constitutive parameters and the arrangement

of the collagen network were obtained from micromechanical tests and imaging techniques instead of being fitted to the macroscopic experimental data. Secondly, by recalling that a wide range of values is reported in the literature for some of these parameters, e.g., for the stiffness of the collagen fibers [176]. However, it is emphasized that adjusting the constitutive parameters to achieve better fits could jeopardize the micro-scale results on which this work is focused. Therefore, the reasonable agreement between numerical and experimental (macroscopic) mechanical responses in Fig. 4.4 is considered sufficient for the subsequent discussion of the microscopic results.

Under this premise, Fig. 4.5 indicates an important 'multiplicative effect' that occurs between the macroscopic (tissue) and the microscopic (cellular) level, since the median value of the maximum principal stretch λ_1 (Fig. 4.5(b)) within each RVE is consistently higher than the macroscopic (imposed) value of 1.1 (Eq. (4.4)). This effect is directly related to the (gradual) recruitment of collagen reinforcement: if no fibers were bearing load, λ_1 would correspond to 1.1 everywhere. These results agree with recent experimental studies [136, 144, 145] on collagenous soft tissues, in which different kinematics were observed on the macro and micro-scale.

Figure4.5(b) also suggests that under the same macroscopic mechanics, the degree of microscopic deformation increases significantly from one state of the tissue to another; this seems to be associated with a higher amount of recruited fibers (Fig. 4.5(d)), which is to be expected since the fibers in the AAA tissue are less wavy than in the healthy adventitia [186], see Fig. 4.2. The higher proportion of recruited fibers also seems to be associated with an increased scatter of λ_1 values within the RVEs, as measured by the interquartile ranges (IQR) in Fig. 4.5(c).

All of the above changes to the extent and distribution of deformations on the micro-scale would have important effects on the mechanobiology of vascular cells – especially fibroblasts, since the amount of smooth muscle cells in AAAs decreases significantly [94, 175, 185]. In this context, many *in vitro* studies [12, 46, 84, 117, 153, 154] have demonstrated the ability of fibroblasts to probe the mechanical state of their ECM and to (re)model it accordingly; in particular, these cells seem to have a homeostatic target [22, 63, 126] that promotes tissue maintenance in health and triggers G&R reactions changes in loading due to injury or disease. In the current work it is assumed that the (micro)mechanical state of the healthy, fibroblast-rich adventitia represents the homeostatic target towards which the mechanobiological activity of these cells would be directed.

Based on that premise, several conclusions can be drawn from the results. First, it can be seen that more fibers are recruited (Fig. 4.5(d)) along the transition from the healthy adventitia to the early AAA in combination with the shift in the preferred alignment of the collagen fibers from the axial to the circumferential direction (Fig. 4.1). Both effects are probably related to the increase in circumferential loads arising from the formation of the AAA [185]. However, these microstructural changes do not lead to a pronounced change in tissue stiffness (at the macro-scale) between these two stages, at least for the 10%

equibiaxial stretch considered here (compare with Figs. 4.4(a) and (b)). Assuming that the blood pressure does not change in the course of the disease, it is therefore hypothesized that the macroscopic stretches on the tissue in both stages are likely to be similar. In this case, the level of microscopic deformation (measured by the maximum principal stretch λ_1) would be higher for the early AAA compared to the healthy adventitia, as shown in Figs. 4.5(a)-(c). As a result, fibroblasts in the early AAA would likely experience a disturbed mechanical state and consequently promote G&R of their ECM aiming to bring it back to the homeostatic level of the healthy adventitia. This could then explain the subsequent changes in the microstructure of the aortic wall in the course of the disease, as suggested by the mechanopathological model of Niestrawska et al. [185].

According to their theory, this G&R promoted by fibroblasts leads to the formation of a thick neo-adventitia on the abluminal side of late AAAs, which is characterized by a highly isotropic (random) distribution of the fiber directions in the circumferential-axial plane [185]. Assuming that the rather fusiform shape of most AAAs [224] can be approximated locally by a pressurized sphere, where the in-plane loads are the same in all directions, this G&R towards an isotropic fiber distribution makes sense from a mechanobiological point of view. The results from Fig. 4.5 seem to point in the opposite direction, however, as the RVEs of the late AAA tissue show the highest levels of deformation on the micro-scale, which means that the cells would be even further away from their homeostatic target.

This apparent contradiction could be reconciled by assuming that in this case the same blood pressure would lead to lower stretch levels compared to the healthy adventitia, due to the considerable stiffening of the late AAA tissue at the macro-scale level (compare Figs. 4.4(a),(b) with (c)). On this basis, the RVEs of the healthy adventitia and the late AAA tissue were compared with macroscopic stretch levels of 10% and 6%, respectively (Fig. 4.6). In this case there is a striking similarity between the distribution of the maximum principal stretches λ_1 in the two RVE examples from Fig. 4.6(a), which is reflected in the similar distribution of medians in both groups (Fig. 4.6(b)), albeit with a higher scatter in the late AAA group (Fig. 4.6(c)). It is emphasized that since more fibers are recruited in the late AAA tissue at 6% when compared to the healthy adventitia at 10% (Fig. 4.6(d)), the similar deformation levels in Fig. 4.6 must be at least partially related to the differences in the fiber arrangement.

Based on the above considerations, it seems safe to argue that, in our model, the micromechanical state of late AAA RVEs under a macroscopic equibiaxial stretch of 6% is closer to that of the healthy adventitia under 10% than that of early AAA RVEs under 10%, which seems to point to a potential mechanics-driven 'healing' effort within the aneurysm wall in the course of the disease, a hypothesis that is illustrated in Fig. 4.7.

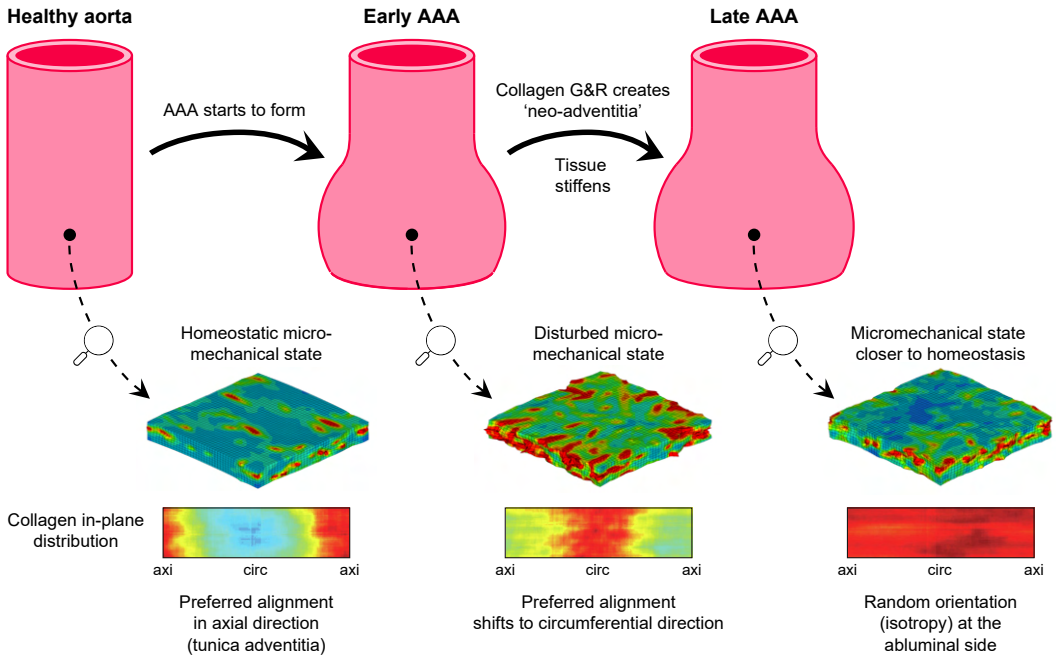

Figure 4.7: A hypothetical 'healing' mechanism of AAAs: after the aneurysm has formed, the fibroblast-rich tunica adventitia undergoes a remodeling of the collagenous fiber network, the preferred orientation of which shifts from the axial to the circumferential direction of the aorta as the loads in this direction increase. However, since the resulting micromechanical state is still disturbed in relation to the homeostatic target of the (healthy) aorta, collagen G&R continues. Subsequently, a neo-adventitia with a strongly isotropic collagen fiber distribution forms on the abluminal side of the wall and the tissue stiffens. Both effects seem to drive the micromechanical state of the tissue closer to homeostatic levels, which could suggest that the stability of the wall is related to the success of collagen G&R and the associated formation of a neo-adventitia. Heatmaps adapted from [185].

In short, the mechanical state of the healthy aorta is initially disturbed by the formation of the aneurysm. Subsequently, in the course of an inflammatory, fibrotic G&R of the collagen reinforcement, the preferred orientation of the fibers in the tunica adventitia shifts from the axial to the circumferential direction (Fig. 4.1), which is probably related to increasing circumferential loads. However, this change is not sufficient to bring the micromechanical state of the ECM back into homeostasis (Fig. 4.5), and, therefore, fibroblasts continue to remodel the collagen network, which leads to the formation of a strongly isotropic neo-adventitia and to a considerable stiffening of the tissue. The combination of both effects then brings the micromechanical state of the ECM closer to the healthy, homeostatic values of the tunica adventitia (Fig. 4.6). According to this hypothesis, the neo-adventitia could play the role of a protective sheath, similar to the tunica adventitia in healthy arter-

ies [119, 218]. It is important to note that Niestrawska et al. [185] observed that on some of the late AAA samples, the thick neo-adventitia appeared fairly 'healthy' with virtually no signs of inflammation, which could mean that the wall had actually reached a 'stable' configuration.

Along with recent clinical studies [1, 182] that identified a significant correlation between inflammation and the rupture risk of AAAs, these results suggest an important relationship between the ultimate fate of an AAA and mechanobiology: it is hypothesized that increased inflammation suggests that intense G&R is taking place within the AAA wall, which means that fibroblasts are still actively remodeling the ECM with the aim of bringing its mechanical state back to homeostasis. This in turn would mean that a stable configuration has not (yet) been achieved and thus the risk of rupture is higher. Interestingly, Niestrawska et al. [185] found no correlation between aneurysm diameter and stage of the disease. Some large aneurysms still had the microstructure of an early AAA, while some small AAAs had significant neo-adventitia and an increase in stiffness. Combined with the previous hypothesis, this could help explain why some large aneurysms do not rupture while some smaller ones do.

As a final note to this section, it is emphasized that while the computational results discussed herein provide important insights that would be difficult to observe *in vivo*, further experimental and clinical studies are needed to support the hypothesis of a 'healing' mechanism (Fig. 4.7). Besides looking for additional evidence of neo-adventitia development in AAA samples, it would be relevant to identify what happens to it on the long term, e.g., whether the isotropic fiber distribution stabilizes or evolves to yet another arrangement as the disease progresses. It would also be important to compare the microstructure of ruptured and unruptured AAAs to correlate relevant changes with the likelihood of a rupture event. In addition, it would be interesting to investigate such alterations also in the context of other regions prone to aneurysm development, e.g., in the thoracic aorta or in the brain. In this regard, the present study will hopefully serve as a motivation for future experimental and clinical studies in these directions.

4.5 Limitations and outlook

Despite the important insights on the mechanobiology of AAA pathogenesis, some limitations of the present study should be mentioned. First of all, it is emphasized that the macroscopic stretches imposed to the RVEs may not be representative of the *in vivo* loading conditions. In particular, the deformation at a point of the healthy adventitia is unlikely to be equibiaxial. Since the shape of the aorta changes as the disease progresses (bulging), the effects of tissue stiffening on macroscopic deformations must also be better investigated. Nevertheless, the equibiaxial stretch of 10% depicted in Eq. (4.4) was chosen, on the one hand, to enable a comparison with the macromechanical data from Niestrawska

et al. [185] and, on the other hand, to separate the effect of different macroscopic mechanics over the microscopic fields.

Future work will focus on re-evaluating the micromechanical state of the various disease stages under more (patho-)physiological macroscopic stretch values. More specifically, it shall be possible to examine the microscopic changes arising also from alterations to the macroscopic stretches caused by, e.g., disease progression and AAA growth. Such studies could also include the effects of other pathological phenomena associated with AAAs, e.g., arterial wall thickening, thrombus formation and the presence of calcium deposits, which also affect the macroscopic mechanical behavior of the tissue.

It should also be noted that the geometry of the RVEs, consisting of a network of collagen fibers and a ground substance comprising all other tissue components, clearly represents a simplification of the true microstructure of the tissue. However, since the model is purely mechanical, it seems reasonable to separate the stiff collagen fibers from the other microstructural phases (e.g., elastin and cells), which are much more compliant. Nevertheless, additional data on the microstructure of arterial tissue – e.g., the quantification of changes in collagen waviness during AAA progression and the distribution of collagen fiber stiffness in healthy and diseased tissue – would certainly contribute to improve the model.

Finally, while the mechanopathological model of Niestrawska et al. [185] describes a multitude of histological changes, this study focused on the formation of a neo-adventitia on the abluminal side of the AAA. It is worth noting that this new layer is about 2/3 of the wall thickness of late AAAs [185], indicating its central role in the G&R process along the pathogenesis of AAAs. While this study addressed the strongly different collagen arrangements along the AAA progression identified in [185], short-term microstructural changes due to collagen turnover could also be investigated, e.g., by deleting and adding specific fibers to the RVEs according to an appropriate evolution law.

4.6 Conclusions

In this paper, a mechanopathological theory of AAA progression proposed by Niestrawska et al. [185] was evaluated using multiscale simulations. In particular, changes in the collagen configuration on the abluminal side of the aortic wall were modeled and possible mechanical cues sensed by vascular cells were evaluated by looking at the deformation levels of the simulated RVEs on the micro-scale. The results highlight the central role of mechanobiology in the G&R of the aortic wall in the course of the disease. In particular, the changes in the collagen network could be attributed to a possible healing effort (Fig. 4.7), in which the formation of a protective neo-adventitia drives the (micro)mechanical state of the tissue back to a homeostatic level. The results of the present

study can contribute to a better understanding of AAA pathogenesis, in particular the dubious role of inflammation.

Supplementary material

Abstract. This Supplementary Material provides additional information to the paper *'Multiscale simulations suggest a protective role of neo-adventitia in abdominal aortic aneurysms'*, with an emphasis on generating the RVE geometries used in the multiscale analyses and on the selection of the finite element sizes (mesh convergence analysis).

S.1 Bivariate von Mises distribution

As discussed in the main text of the paper, the RVEs considered in the present study for both the healthy adventitia and the AAA tissue consist of a ground substance that is reinforced by two collagen fiber families. It is assumed that in the circumferential-axial plane of the artery the fibers of each family are dispersed around two symmetric directions, which are characterized by the mean fiber angle α, as illustrated in Fig. S.1.

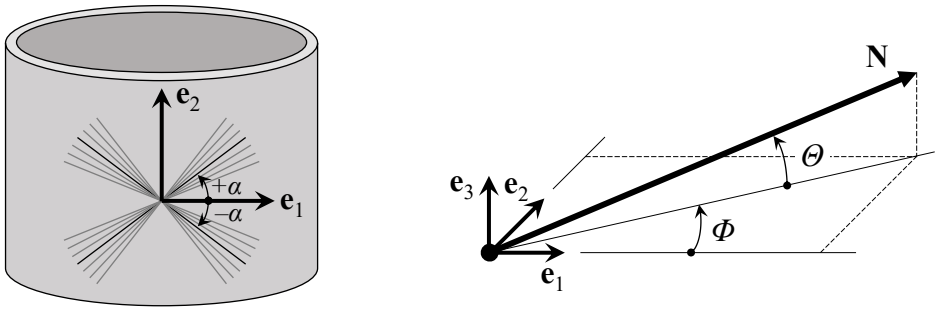

Figure S.1: Fiber families in arterial tissue: (a) two symmetric fiber families in the circumferential-axial plane, dispersed with respect to a preferred direction and characterized by the mean fiber angle $\pm\alpha$; (b) fiber direction $\mathbf{N}$, described in terms of azimuthal (Φ) and elevation (Θ) angles.

In Fig. S.1(b) the unit vector $\mathbf{N}$ of a collagen fiber direction is described by the angles Φ (azimuthal or in-plane) and Θ (elevation or out-of-plane), measured with respect to a coordinate system aligned with the circumferential ($\mathbf{e}_1$), axial ($\mathbf{e}_2$) and radial ($\mathbf{e}_3$) directions of the aorta. Hence,

$$\mathbf{N}(\Phi,\Theta) = \cos\Phi\cos\Theta\,\mathbf{e}_1 + \sin\Phi\cos\Theta\,\mathbf{e}_2 + \sin\Theta\,\mathbf{e}_3, \tag{S.1}$$

where $\Phi \in [0, 2\pi]$ and $\Theta \in [-\pi/2, +\pi/2]$. As proposed by Holzapfel et al. [113], it is postulated that the distribution of the collagen fiber directions in an artery follows a bivariate von Mises probability function, so that

$$\rho(\Phi, \Theta) = \rho_{\text{ip}}(\Phi)\, \rho_{\text{op}}(\Theta), \tag{S.2}$$

where the in- and out-of-plane probability distributions ρ_{ip} and ρ_{op} are assumed to be independent. In the same paper the authors suggested two particular π-periodic von Mises distributions to describe ρ_{ip} and ρ_{op}, namely

$$\rho_{\text{ip}}(\Phi) = \frac{\exp[a \cos 2(\Phi \pm \alpha)]}{I_0(a)} \qquad \text{and} \qquad \rho_{\text{op}}(\Theta) = 2\sqrt{\frac{2b}{\pi}}\frac{\exp[b(\cos 2\Theta - 1)]}{\text{erf}(\sqrt{2b})}, \tag{S.3}$$

where a and b are concentration parameters, I_0 is the modified Bessel function of the first kind of order 0 and erf is the error function. In Eq. $(S.3)_2$, the mean out-of-plane angle is taken to be zero, a hypothesis based on experimental evidence [113].

Two scalar quantities κ_{ip} and κ_{op} were proposed in the same work to characterize the degree of in-plane and out-of-plane dispersion; these refer to the parameters a and b by

$$\kappa_{\text{ip}} = \frac{1}{2} - \frac{I_1(a)}{2I_0(a)} \qquad \text{and} \qquad \kappa_{\text{op}} = \frac{1}{2} - \frac{1}{8b} + \frac{1}{4}\sqrt{\frac{2}{\pi b}}\frac{\exp(-2b)}{\text{erf}(\sqrt{2b})}. \tag{S.4}$$

For a more detailed discussion on the meaning of κ_{ip} and κ_{op}, the interested reader is referred to the paper of Holzapfel et al. [113].

S.2 Generation of fiber networks

For each RVE it is assumed that the ground substance has the shape of a right-angled prism with the side lengths L_{C}, L_{A}, L_{R}, aligned, respectively, with the circumferential, axial and radial direction of the aorta, see also Fig. S.1. The collagen reinforcement is represented by a network of straight lines, which is generated according to a stochastic process, illustrated in Fig. S.2.

The stochastic procedure, analogous to the one used in [41], starts with the definition of the volume $L_{\text{C}} \times L_{\text{A}} \times L_{\text{R}}$ of the RVE, the volume fraction of collagen F_{T}, the fiber diameter d and the tissue-specific values of the parameters α, κ_{ip} and κ_{op} (Table 1 of the main text). A nucleation point is then randomly selected within the RVE and a fiber direction $\mathbf{N}$ (Eq. (S.1)) is determined by sampling one in-plane angle Φ^k and one out-of-plane angle Θ^k from the bivariate von Mises distribution. The procedure alternates between $+\alpha$ and $-\alpha$ in order to consider both fiber families, see Fig. S.1. Starting from the nucleation point, the k-th fiber centerline is extended along $\mathbf{N}$ until it crosses the boundary of the RVE.

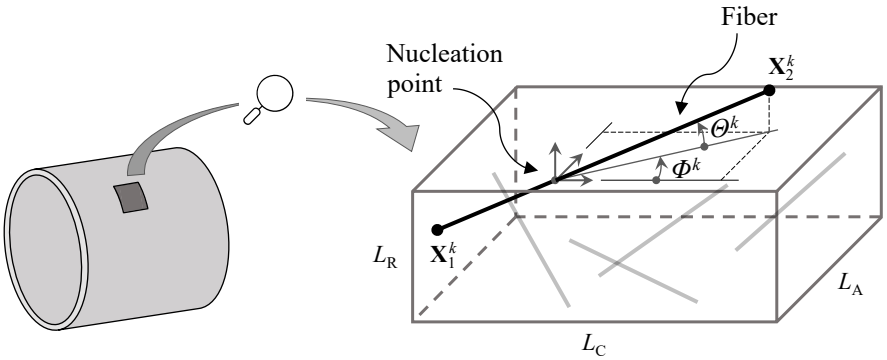

Figure S.2: Generation of fiber networks. A fiber direction $\mathbf{N}$ is defined by sampling one in-plane angle Φ^k and one out-of-plane angle Θ^k from the bivariate von Mises distribution (Eq. (S.3)); the start and end points $\mathbf{X}_1^k$ and $\mathbf{X}_2^k$ of the fiber are defined by extending the fiber centerline along $\mathbf{N}$ from a randomly selected nucleation point within the volume.

The intersection points $\mathbf{X}_1^k$ and $\mathbf{X}_2^k$ defined in this way are stored and the fiber end-to-end distance L_0^k is calculated. The constitutive parameters (see Eq. (2) in the main text) of the k-th fiber are then defined by sampling one stiffness value E_f^k from a normal distribution and a waviness value P_f^k from a beta distribution (Eq. (3) in the main text) with appropriate parameters. Finally, the arc length value L_f^k is calculated (see also Fig. 2(a) in the main text) and the fiber volume is computed assuming a perfectly circular cross-section. After updating the volume fraction of collagen, another nucleation point is selected and the process is repeated until the target volume fraction F_T is reached. After the fiber network generation is completed, the set of Φ^k and Θ^k angle values is used to fit the bivariate von Mises distribution of Eq. (S.3) by a maximum likelihood estimate, which leads to the effective parameters α^eff, $\kappa_\mathrm{ip}^\mathrm{eff}$ and $\kappa_\mathrm{op}^\mathrm{eff}$ of the network.

The procedure described above is summarized in the Algorithm 2 and was implemented in MATLAB® (The MathWorks Inc., Natwick, US).

Algorithm 2: Generation of RVE fiber networks

Input: $L_C, L_A, L_R, F_T, d, \alpha, \kappa_{ip}, \kappa_{op}, \mathrm{dt}$

Output: $\mathbf{X}_1^k, \mathbf{X}_2^k, \Phi^k, \Theta^k, E_f^k, P_f^k, \forall k = 1, \ldots, N_{\text{fibers}}$
$\alpha^{\text{eff}}, \kappa_{ip}^{\text{eff}}, \kappa_{op}^{\text{eff}}$

$V_{\text{fiber}} = 0$
$F_{\text{curr}} = 0$
$k = 1$
while $F_{\text{curr}} < F_T$ **do**
  if k = *odd* **then**
    Sample in-plane angle value Φ^k from the von Mises distribution (Eq. $(S.3)_1$) centered around $+\alpha$
  else
    Sample in-plane angle value Φ^k from the von Mises distribution (Eq. $(S.3)_1$) centered around $-\alpha$
  Sample out-of-plane angle value Θ^k from the von Mises distribution (Eq. $(S.3)_2$)
  Calculate fiber direction $\mathbf{N}(\Phi^k, \Theta^k)$, Eq. (S.1).
  Generate random nucleation point $\mathbf{x}^0 = [x_1^0, x_2^0, x_3^0]$ with $x_1^0 \in [0, L_C], x_2^0 \in [0, L_A], x_3^0 \in [0, L_R]$
  $\mathbf{x} = \mathbf{x}^0$
  while $x_1 \in [0, L_C], x_2 \in [0, L_A], x_3 \in [0, L_R]$ **do**
    $\mathbf{x} = \mathbf{x}^0 - \mathrm{dt}\,\mathbf{N}$
  $\mathbf{X}_1^k = \mathbf{x}$
  $\mathbf{x} = \mathbf{x}^0$
  while $x_1 \in [0, L_C], x_2 \in [0, L_A], x_3 \in [0, L_R]$ **do**
    $\mathbf{x} = \mathbf{x}^0 + \mathrm{dt}\,\mathbf{N}$
  $\mathbf{X}_2^k = \mathbf{x}$
  Sample stiffness parameter E_f^k from a normal distribution (Eq. (2) in the main text)
  Sample waviness parameter P_f^k from the beta distribution (Eq. (3) in the main text)
  $L_0^k = ||\mathbf{X}_2^k - \mathbf{X}_1^k||$
  $L_f^k = L_0^k / P_f^k$
  $V_{\text{fiber}} = V_{\text{fiber}} + (\pi/4)\, d^2\, L_f^k$
  $F_{\text{curr}} = V_{\text{fiber}} / (L_C\, L_A\, L_R)$
  $k = k + 1$
Calculate $\alpha^{\text{eff}}, \kappa_{ip}^{\text{eff}}$ from the set of Φ^k values by maximum likelihood estimate
Calculate κ_{op}^{eff} from the set of Θ^k values by maximum likelihood estimate

S.3 Representative volume size

A central requirement of the mutiscale theory used in the present work is that the RVE must be small enough to be considered a point on the macro-scale, but still large enough to be considered as a continuum body, and, more importantly, to be representative of the microstructure of the material [16, 50]. This requires a careful definition of the RVE size.

In particular, the stochastic generation of fiber directions described in the previous section includes the sampling of angle values from a bivariate von Mises distribution, which is described by specific (target) values of the parameters α, κ_{ip} and κ_{op}. On the one hand, it is clear that enough fiber directions must be included in the network so that it is representative of the desired microstructure. On the other hand, the number of fibers is directly related to the total volume of the RVE, the collagen volume fraction F_{T} and the fiber diameter d, as they control the termination criterion of the algorithm. In the present work, F_{T} and d were selected based on histological and microstructural evidence. As discussed in the main text, F_{T} is taken as 40% , 60% and 60% for healthy adventitia, early AAA and late AAA, respectively [8, 183, 185]. For the sake of simplicity it was further assumed that all fibers have a diameter of $d = 10\,\mu\text{m}$ [8].

Since these parameters are fixed, a suitable RVE volume $L_{\text{C}} \times L_{\text{A}} \times L_{\text{R}}$ must be selected to ensure a representative network. For this purpose a stochastic experiment was developed. Five increasing volume sizes were defined, namely

V1: $175 \times 175 \times 35\,\mu\text{m}$

V2: $250 \times 250 \times 50\,\mu\text{m}$

V3: $350 \times 350 \times 70\,\mu\text{m}$

V4: $500 \times 500 \times 100\,\mu\text{m}$

V5: $750 \times 750 \times 150\,\mu\text{m}$

with a ratio of approximately three between them. For each of the volume sizes V1-V5 given above, sixteen RVEs were generated with the target values $\alpha = 77.53^\circ$, $\kappa_{\text{ip}} = 0.232$ and $\kappa_{\text{op}} = 0.466$, which are the median values determined experimentally by Niestrawska et al. [183] from 16 samples of healthy aortic adventitias, see also Table 1 of the main text. For each RVE the effective parameters α^{eff}, $\kappa_{\text{ip}}^{\text{eff}}$ and $\kappa_{\text{op}}^{\text{eff}}$ were calculated as discussed in the previous section, and the median and interquartile ranges were determined for the set of 16 numerical samples, for each of the 5 volume sizes. In Fig. S.3 the results are shown and compared with the experimental values published by Niestrawska et al. [183].

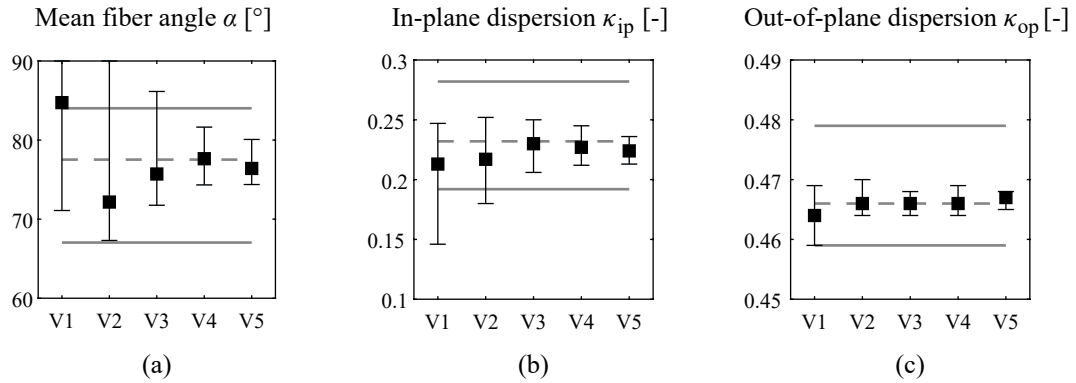

Figure S.3: Median (black squares) and interquartile ranges (error bars) of the effective parameters (a) α^{eff}, (b) $\kappa_{\text{ip}}^{\text{eff}}$ and (c) $\kappa_{\text{op}}^{\text{eff}}$ computed from 16 random networks with volumes V1-V5 are compared with the median (dashed gray lines) and the interquartile ranges (solid gray lines) of the same parameters, obtained experimentally from 16 samples of healthy adventitias by Niestrawska et al. [183].

It can be seen that an RVE with the dimensions $500 \times 500 \times 100\,\mu\text{m}$ (V4) is large enough to ensure that all three parameters are within the experimental bounds. It is pointed out that this size was also verified to be representative enough of the von Mises distributions of the early and late AAAs (results not shown here). Therefore this size was used for all RVEs in this work.

S.4 Mesh convergence analysis

The volume-averaged multiscale theory mentioned above was combined with the finite element method to calculate the microscopic deformation fields within each RVE. For this purpose, the (continuum) ground substance was meshed with second-order hexahedrons and the embedded collagen reinforcement was modeled with second-order trusses. Care was taken to ensure that each truss element was completely contained in a hexahedron [41].

A mesh convergence analysis was performed to select an appropriate size for the hexaedrons. For this purpose, the ground substance of the same (late AAA) RVE was meshed with element sizes of 25, 16.67, 12.5 and 10 µm. The four meshes constructed in this manner consisted of 1 600, 5 400, 12 800 and 25 000 hexaedrons, respectively, while the compatible meshes of fiber reinforcements had 8 179, 12 257, 16 373 and 20 443 truss elements. An equibiaxial macroscopic stretch of 10% was simulated for each mesh, whereby periodic fluctuations were assumed on the boundary. The results are shown in Fig. S.4, where the maximum principal stretches λ_1 within each mesh were plotted.

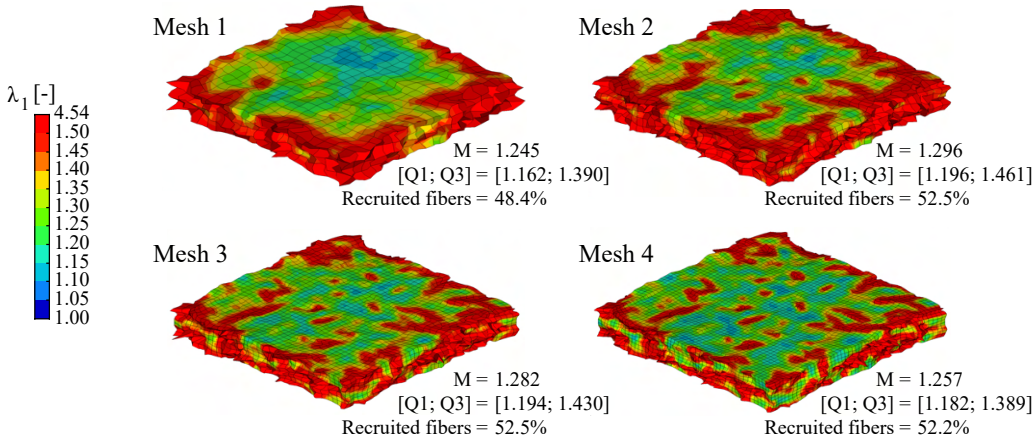

Figure S.4: Distribution of the maximum principal stretches λ_1 for different meshes of the same (late AAA) RVE. Element size decreases from Mesh 1 to Mesh 4. The median (M) and quartiles (Q1; Q3) of λ_1 values and the percentage of fibers recruited are given below each mesh.

The median (M) and quartiles (Q1; Q3) of λ_1 values and the percentage of fibers recruited are given below each mesh. The convergence threshold was defined as 5% for all quantities, whereby one may conclude that Mesh 3, with an element size of 12.5 µm, already satisfies the convergence criterion. Since the late AAA RVEs are the ones exhibiting the highest level of microscopic deformations (see Fig. 5 in the main text), it was assumed that an element size of 12.5 µm would also be sufficient to interpolate the deformation fields in the RVEs of early AAAs and of the healthy adventitia. Therefore, in the present work, this element size was used to perform all multiscale simulations, in combination with a compatible embedded truss mesh for each of the RVEs.

5 A TWO-SCALE NUMERICAL STUDY ON THE MECHANOBIOLOGY OF ABDOMINAL AORTIC ANEURYSMS

Abstract. Abdominal aortic aneurysms (AAAs) are a serious condition whose pathophysiology is related to phenomena occurring at different length scales. To gain a better understanding of the disease, this work presents a multiscale computational study that correlates AAA progression with microstructural and mechanical alterations in the tissue. Macro-scale geometries of a healthy aorta and idealized aneurysms with increasing diameter are developed on the basis of existing experimental data and subjected to physiological boundary conditions. Subsequently, microscopic representative volume elements of the abluminal side of each macro-model are employed to analyze the local kinematics at the cellular scale. The results suggest that the formation of the aneurysm disrupts the micromechanics of healthy tissue, which could trigger collagen growth and remodeling by mechanosensing cells. The resulting changes to the macro-mechanics and microstructure of the tissue seem to establish a new homeostatic state at the cellular scale, at least for the diameter range investigated.

5.1 Introduction

An abdominal aortic aneurysm (AAA) is a condition in which the shape of the abdominal aorta is permanently altered. It is typically characterized by a local and irreversible bulging of the vessel wall, which is recognized in clinical practice when the infrarenal aortic diameter exceeds 30 mm [122, 249]. It is a life-threatening cardiovascular pathology that can go unnoticed for years and has a high mortality rate if it progresses to rupture [189, 211]. Current treatment is based on surgical intervention, either with a traditional open abdominal procedure or with endovascular repair by deploying a stent-graft into the aneurysmal vessel [48, 212]. In any case, the risks associated with the procedure, which are often amplified by factors such as advanced age and concomitant cardiovascular pathologies, require specific medical criteria to evaluate the need for an intervention [258]. The most commonly used criterion is based on a correlation between the probability of rupture and the size of the aneurysm. In general, current guidelines recommend surgery when the maximum diameter of the aneurysm reaches 55 mm in men or 50 mm in women, or when it increases by more than 5-10 mm within a year [85, 89, 101]. However, autopsy studies and clinical reports have shown that small AAAs can still rupture [171, 173], while some large ones do not [62, 146], suggesting that alternative approaches should be pursued [227, 256, 258].

Various prospective studies have explored biomechanics-based indicators such as maximum wall stress and rupture potential index and, based on the analysis of large patient

cohorts, have argued their superiority in relation to the diameter criterion [59, 69, 163, 251, 255]. Despite promising achievements, the reliability of these indicators depends on the accuracy of the computational biomechanical simulations used to calculate them, which are closely linked to the modeling framework. Significant advances have been made over early models based on Laplace's law, including the use of advanced constitutive laws, three-dimensional patient-specific geometry, and fluid-structure interaction simulations [38, 56, 205, 250, 257, 261]. Nevertheless, the complex pathogenesis of the disease requires a more thorough examination of the mechanical behavior of the aortic wall. A detailed study of the aortic wall microstructure and its components and how these evolve during aneurysm growth can lead to the development of structure-based, multiscale constitutive models with improved predictive abilities [197, 202, 228, 271].

The healthy human aorta can be described as a thick-walled tube composed of three layers (intima, media and adventitia), each of which has a specific hierarchical arrangement of components at different scales ranging from molecules to cells, fibrils and fibers to tissue [43, 105, 200]. As with other soft tissues, it is the extracellular matrix (ECM) that maintains tissue integrity and provides the structural and biochemical environment in which cells are embedded. The ECM of vascular tissues appears as a network of collagen fibers, elastic fibers, elastin layers and proteoglycans [43, 194]. Their specific organization is maintained by the mechanotransduction activity of smooth muscle cells and fibroblasts, which can sense and respond to mechanical stimuli to maintain mechanical homeostasis [64, 126]. More relevant to the present study is the disruption of this equilibrium and the resulting changes in ECM structure and composition, as they may provide insights into disease progression [268]. In the context of AAA pathogenesis, recent work by Niestrawska et al. [183, 185, 186] identified significant differences in the microstructure and mechanical behavior of aneurysmal tissue compared to healthy aortas. The authors then proposed a three-stage model for describing disease development [185], based on a widely accepted pathophysiological theory of aneurysm formation and growth [122, 147]. In summary, loss of elastic fibers and smooth muscle cells initiates dilatation, followed by extensive growth and remodeling (G&R) of the collagen fibers and inflammation. The later stage of AAAs is characterized by the presence of a thick neo-adventitial layer at the abluminal side of the wall, which stiffens the tissue and shows a highly isotropic orientation of collagen fibers [185].

Given these recent findings, it seems obvious that an answer to the evolution of aneurysms, and in particular to the mechanobiological aspects involved, suggests a multiscale modeling approach, where simulation and experiment go hand in hand. In this direction, Dalbosco et al. [42] recently evaluated the mechano-pathological theory of Niestrawska et al. [185] by simulating the equibiaxial loading of representative volume elements (RVEs) of the arterial microstructure in the healthy tissue and in different stages of AAA, with a special focus on the changes in collagen arrangement. However, a major limitation of [42] is that only the micro-scale of the tissue subjected to an equibiaxial, macroscopic deformation of 10% was modeled. In reality, given the bulging of the wall as the disease progresses

and a thrombus is built up – observed in approximately 75% of AAAs [241, 252] – it is to be expected that the macroscopic mechanics of the wall will also change, affecting the microscopic mechanical state of the tissue.

To fill this gap, we propose here a two-scale computational finite element (FE) model that describes the passive behavior of the abdominal aorta. The macro-scale is located at the tissue level, and the micro-scale consists of RVEs in which a network of collagen fibers is embedded in a ground substance identified as the non-collagenous part of the tissue [41, 42]. First, the healthy abdominal aorta is simulated as a three-layered cylindrical segment under *in vivo* loading conditions. The deformation of points at the abluminal side of the vessel is then applied to (microscopic) RVEs whose geometry is based on the collagen configuration of the healthy adventitia [42, 183]. The resulting deformation fields in the RVEs are then interpreted as the homeostatic mechanical state experienced by vascular cells, particularly fibroblasts, in the healthy non-aneurysmal tissue.

Subsequently, models of the aneurysms are created with an idealized fusiform geometry [66], including the presence of an intraluminal thrombus (ILT), for different disease stages [42, 185] and varying diameters. As in the previous case, the deformation from the abluminal side of each AAA is then applied to RVEs representing the microstructural configuration of the corresponding disease stage. The resulting deformation fields at the micro-scale are then compared to the healthy case and evaluated along AAA (stage) progression and diameter increase. The goal is to correlate changes in the micro-mechanical state of the tissue with possible mechanobiological cues that might drive G&R through vascular cells, with a focus on the formation of the neo-adventitia.

5.2 Methods

5.2.1 Macroscopic simulations

This section describes geometries, boundary conditions, and constitutive models employed in the macroscopic simulations at the tissue scale. In such models, a distinction is made between an unknown stress-free reference configuration Ω_{ref}, a load-free but residually stressed configuration Ω_0 which represents the *ex vivo* state of the vessel, and finally the loaded current configuration Ω, which, e.g., can be observed through medical imaging [109]. While inverse design analyses have been proposed to identify the reference configuration of the FE model [80, 266], we instead chose a simplified approach combining experimental observations and simulations. All macroscopic analyses were performed with the commercial FE software Abaqus/Standard 2018 (Dassault Systèmes Simulia Corp, Providence, RI, USA) using the implicit static solver, custom Python scripts and a user material definition.

Healthy abdominal aorta

The healthy aorta in the load-free configuration Ω_0 is modeled as a thick-walled cylindrical segment with inner radius R_0, thickness T_0 and unit length in the axial direction [184]. A three-layered structure including the intimal layer is adopted, which is thought to be representative of elderly individuals – who are more prone to developing AAA [147, 189, 211] – with non-atherosclerotic intimal thickening [47, 112]. The intima, media and adventitia correspond, respectively, to 20%, 50% and 30% of the wall thickness [112]. Only a quarter of the aortic segment is simulated with appropriate boundary conditions to enforce symmetry. The geometry is meshed using linear hexahedral elements with a mixed stress-displacement formulation for material incompressibility and an appropriate mesh refinement in the wall thickness to resolve the layer-specific stress fields.

The configuration Ω_0 is characterized by the presence of unknown residual stresses. Therefore, the finite element simulations consist of two different stages. First, residual stresses are computed based on the concept of the opening angle, which can be measured *ex vivo* on excised rings of the aorta [112]. From a biomechanical perspective, the role of residual stresses is to reduce the stress gradient within each layer of the arterial wall in the physiologically loaded configuration. In the absence of consistent information on the opening angle for the layer properties of the aortic wall adopted in this work [183], we have identified an optimal value $2\theta_{\text{ref}}$ that minimizes the intramural layer-specific stress gradients in the final deformed configuration [92]. In the unknown reference configuration, the healthy aortic wall is described as an open circular segment with an inner radius R_{ref}, thickness T_{ref} and unit length in the axial direction (Fig. 5.1a). Closing is simulated by specifying displacements on a free edge of the ring, so that the load-free radius R_0 corresponds to the measured *ex vivo* value [112]. The stress field obtained defines the initial residual state, i.e. a self-equilibrated stress state in the undeformed, load-free configuration Ω_0 [24].

In the second stage, *in vivo* loading is simulated by applying an axial stretch and an internal pressure with the load-free configuration Ω_0 serving as a reference (Fig. 5.1b). The *in vivo* axial prestretch λ_{ax} contributes significantly to mechanical homeostasis as it allows the axial force in the artery to remain unchanged during the cardiac cycle [125]. Importantly, this value is generally larger than the *in situ* stretch $\lambda_{\text{ax},0}$, which was determined experimentally from the length of excised aortic segments [116]. Therefore, an iterative procedure was adopted to identify the axial *in vivo* prestretch as the optimal stretch at which the reduced axial force [109] remains approximately constant, in the range of physiological pressures [92]. A summary of the quantities of interest employed in the FE simulations is provided in Table 5.1.

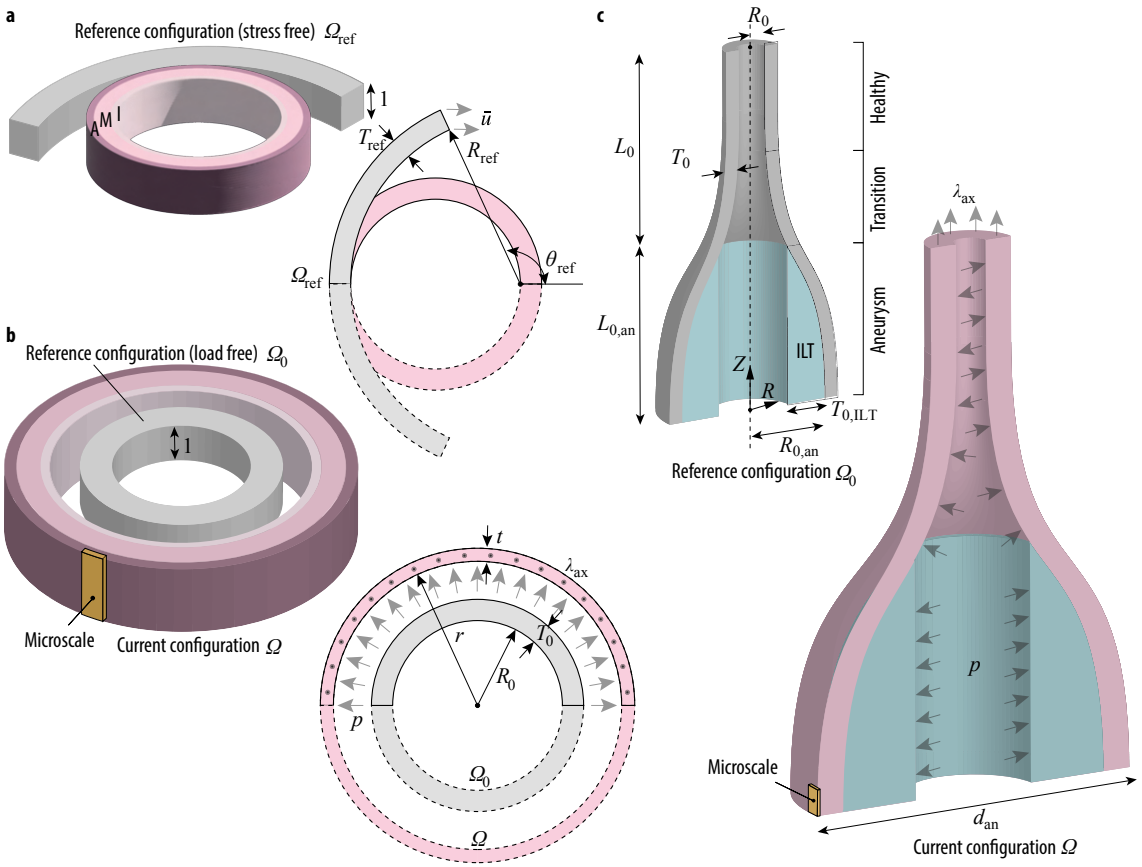

Figure 5.1: (a) Sketch of closure simulation on a healthy aortic segment with referential inner radius R_{ref}, thickness T_{ref} and opening angle θ_{ref} using a displacement $\bar{u}$, to calculate residual stresses with the three-layered arrangement of intima, media and adventitia; (b) sketch of the main simulation on the residually stressed, healthy aortic segment with initial inner radius R_0 and thickness T_0, which deforms to a final radius r and thickness t due to the effect of axial stretch λ_{ax} and intraluminal pressure p; (c) sketch of the simulation on the model with the abdominal aneurysm consisting of three regions: the aneurysm sac, with initial length $L_{0,an}$ and inner radius $R_{0,an}$, a transition zone (neck) and a healthy cylindrical part with inner radius R_0; the initial combined length of both is given by L_0 and the wall thickness T_0 is assumed to be constant. The model also contains an axisymmetric intraluminal thrombus (ILT) with initial thickness $T_{0,ILT}$ at the luminal side of the aneurysm sac. The aneurysm is subject to the same axial stretch λ_{ax} and intraluminal pressure p as the healthy aorta, resulting in a deformed outer diameter d_{an}. In (b) and (c), the solid elements shown in yellow are representative regions whose final deformation state is passed to the RVE as input for the micro-scale simulations. Symmetry along the longitudinal axis of the aorta is always assumed.

Table 5.1: Parameters employed in the FE element simulations of the healthy abdominal aorta. (Int = intima, Med = media, Adv = adventitia)

Geometry and loading				
Parameter	Description	Numerical value		Refs.
R_{ref} (mm)	Radius of the open segment	8.05		
T_{ref} (mm)	Thickness of the open segment	1.46		
$2\theta_{\text{ref}}$ (deg)	Opening angle	100.0		
R_0 (mm)	Radius of aortic wall *ex vivo*	5.61		[112]
T_0 (mm)	Thickness of aortic wall	1.46		[112]
$\lambda_{\text{ax},0}$ (-)	Axial prestretch *in situ*	1.07		[115]
λ_{ax} (-)	Axial prestretch *in vivo*	1.184		
p (mmHg)	Internal pressure	120.0		
Material parameters				
Parameter	Description	Int [183]	Med [183]	Adv [183]
μ_{A} (kPa)	Shear modulus of matrix	6.88	30.52	3.77
k_1 (kPa)	Shear modulus of fibers	4.90	22.81	0.36
k_2 (-)	Exponential parameter of fibers	41.95	22.78	45.88
κ_{ip} (-)	In-plane fiber dispersion	0.261	0.208	0.232
κ_{op} (-)	Out-of-plane fiber dispersion	0.484	0.487	0.466
α (deg)	In-plane fiber mean angle[a]	3.25	6.91	77.53

[a] With respect to the circumferential direction

Abdominal aortic aneurysm

The abdominal aneurysm is defined as an axisymmetric solid with a fusiform section in the axial-radial plane, described by

$$R(Z) = R_0 + \left(R_{0,\text{an}} - R_0 - c_3 \frac{Z^2}{R_0} \right) \exp\left(-c_2 \left| \frac{Z}{R_0}^{c_1} \right| \right), \tag{5.1}$$

where $R_{0,\text{an}}$ is the maximum radius of the aneurysm in the reference configuration, and c_1, c_2, c_3 are geometric coefficients [205].

The initial length of the aneurysm $L_{0,\text{an}} = f_1 R_{0,\text{an}}$ depends on the maximum radius by a geometric parameter f_1 [205] while the thickness T_0 is here assumed to correspond to the healthy aorta. Although aneurysms can lead to a thickening of the aortic wall, other studies have found that a thrombus-covered wall can be significantly thinner [141]. Moreover, Niestrawska et al. [185] reported that the intima and media of some of their AAA samples appeared to have split open and therefore, despite collagen accumulation and formation of the neo-adventitia on the abluminal side of some specimens, there was no significant difference in thickness between different tissue stages.

The geometry extends in the axial direction for an additional length $L_0 = L_{0,\mathrm{an}}$, which includes a portion of the healthy aortic wall and an intermediate transition zone (Fig. 5.1c). To the best of the authors' knowledge, there is no clear characterization of such a region in the literature. However, it appears reasonable to define a zone corresponding to the geometrical change from the healthy to the aneurysmal wall and include also here a transition in terms of mechanical response, see Section 5.2.1 and Appendix A.

The intraluminal thrombus is simplified as a hollow, axisymmetric solid adjacent the luminal side of the aneurysm sac. The reference thickness $T_{0,\mathrm{ILT}}$ is computed from Tong et al. [242] where experimental observations revealed an empirical correlation between the maximum thickness of the thrombus and the maximum *in vivo* diameter of the aneurysm d_{an}. Both the wall and the ILT are each described by a single material layer. Only a quarter of the model is simulated with appropriate boundary conditions to enforce symmetry. The geometry is meshed using linear hexahedral elements with a mixed stress-displacement formulation for material incompressibility. Preliminary studies of mesh convergence have been performed.

In contrast to the simulations of the healthy aorta, the current configuration Ω of the aneurysm under physiological loading is considered to be known, in particular the *in vivo* maximum outer diameter d_{an}, which is used in clinical practice to assess the risk of rupture of AAAs [101]. The unknown reference configuration is determined by an inverse procedure that finds the optimal value of the initial radius $R_{0,\mathrm{an}}$ of the aneurysm such that the deformed external diameter corresponds to d_{an}. To illustrate the changes along the AAA growth, three values of d_{an} (45, 55 and 65 mm) were simulated. In order to estimate the influence of mechanical and microstructural alterations along AAA pathogenesis, two different disease stages – the early and the late [42, 185] – were considered for each diameter (six simulations in total). Since no relationship between tissue stage and aneurysm size could be found [185], using the same diameters for different tissue stages was aimed at investigating the interplay between microstructural remodeling and AAA growth.

In vivo loading is simulated by applying axial stretch to the healthy portion of the aorta and internal pressure throughout the vessel (Fig. 5.1c). The *in vivo* axial prestretch λ_{ax} is taken from the previous simulation on the healthy wall, since no more detailed experimental characterization on AAAs is available. For the same reason, residual stresses in the circumferential direction of the aneurysm are neglected. A summary of the quantities of interest employed in the FE simulations can be found in Table 5.2.

Table 5.2: Parameters employed in the FE element simulations of abdominal aortic aneurysms. (EAAA = early abdominal aortic aneurysm, LAAA = late abdominal aortic aneurysm, ILT = intraluminal thrombus)

Geometry and loading				
Parameter	Description	Numerical value		Refs.
		EAAA	LAAA	
R_0 (mm)	Radius of healthy aortic wall	5.61		[112]
T_0 (mm)	Thickness of aortic wall	1.46		[112]
d_{an} (mm)	Maximum AAA diameter *in vivo*	45-55-65		
$R_{0,an}$ (mm)	Initial AAA radius (for each d_{an})	36.4-45.0-53.6	39.7-49.0-56.6	
f_1 (-)	Geometric parameter	4.0		
c_1 (-)	Geometric parameter	0.5		
λ_{ax} (-)	Axial prestretch *in vivo*	1.184		
p (mmHg)	Internal pressure	120.0		

Material parameters				
Parameter	Description	EAAA [185]	LAAA [185]	ILT [241]
μ_A (kPa)	Shear modulus of matrix	0.59	3.78	–
μ_I (kPa)	Stress-like parameter for ILT	–	–	9.26
b (-)	Non-dimensional parameter for ILT	–	–	1.62
k_1 (kPa)	Shear modulus of fibers	1.30	8.96	–
k_2 (-)	Exponential parameter of fibers	47.51	636.29	–
κ_{ip} (-)	In-plane fiber dispersion	0.242	0.224	–
κ_{op} (-)	Out-of-plane fiber dispersion	0.433	0.402	–
α (deg)	In-plane fiber angle [a]	6.55	22.90	–

[a] With respect to the local circumferential direction

Constitutive models

The mechanical behavior of both the healthy and aneurysmal aortic wall is described by the anisotropic strain-energy function Ψ_A proposed by Holzapfel et al. [113] (the subscript A stands for anisotropic), which contains two families of fibers with non-symmetric fiber dispersion. Assuming incompressible behavior, the strain-energy function reads

$$\Psi_A = \frac{\mu_A}{2}(I_1 - 3) + \sum_{i=4,6} \left\{ \frac{k_1}{2k_2} \exp\left[k_2(I_i^\star - 1)^2\right] - 1 \right\} - p(J-1), \tag{5.2}$$

where $\mu_A > 0$ and $k_1 > 0$ are stress-like material parameters, and $k_2 > 0$ is a dimensionless parameter. In (5.2), $I_1 = \mathbf{C} : \mathbf{I}$ is the first invariant of the right Cauchy-Green tensor $\mathbf{C}$, where $\mathbf{I}$ is the second-order identity tensor, $J = \sqrt{\det \mathbf{C}} > 0$ is the volume ratio and p is a

Lagrange multiplier that enforces material incompressibility. The invariant $I_i^\star$ with respect to the stretch of a single family of fibers is expressed by

$$I_i^\star = \mathbf{C} : \mathbf{H}_i\,, \quad \text{with} \quad \mathbf{H}_i = A\mathbf{I} + B\boldsymbol{M}_i \otimes \boldsymbol{M}_i + (1-3A-B)\boldsymbol{M}_\mathrm{n} \otimes \boldsymbol{M}_\mathrm{n}, \quad i = 4,6\,, \tag{5.3}$$

where $\mathbf{H}_i$ is a second-order symmetric structure tensor, $\boldsymbol{M}_i$ with $\|\boldsymbol{M}_i\| = 1$ represents the reference mean orientation of the i-th fiber family, $\boldsymbol{M}_\mathrm{n}$ is an out-of-plane unit vector, and A, B are coefficients related to the in-plane and out-of-plane dispersion of fibers κ_ip and κ_op [113].

The model described in (5.2) has been implemented as user material for the FE solver Abaqus/Standard, with an analytic derivation of the Cauchy stress tensor and of the spatial elasticity tensor. The material parameters adopted in the simulations of the three-layered healthy aorta can be found in Table 5.1. Two sets of parameters were employed for the aneurysmatic tissue to account for the different stages of the disease [42, 185], as shown in Table 5.2.

The healthy portion of the wall in the geometry with the aneurysm was modeled as a single layer with homogenized mechanical behavior, while in the intermediate region we assumed a continuous transition from the behavior of the homogenized healthy wall to the behavior of the aneurysm. We performed this homogenization process directly on the stress-strain response of the tissue under equibiaxial tension (Appendix A), not on the material properties, because of the nonlinear nature of (5.2).

Although a layered structure with an anisotropic luminal layer is observed in aged thrombi [241], for simplicity the ILT is modeled as a single layer of homogeneous material with isotropic properties. The layer-specific experimental data from biaxial tests reported in Tong et al. [241] were homogenized using the same procedure mentioned above and fitted with the exponential isotropic strain-energy function Ψ_I proposed by Demiray [52] (the subscript I stands for isotropic)

$$\Psi_\mathrm{I} = \frac{\mu_\mathrm{I}}{2}\left[\exp\left[b(I_1-3)\right]-1\right] - p(J-1)\,, \tag{5.4}$$

where $\mu_\mathrm{I} > 0$ is a stress-like material parameter and $b > 0$ is a non-dimensional parameter. The model described in (5.4) has been implemented as a hyperelastic user material for the FE solver Abaqus/Standard. The material parameters adopted in the simulations can be found in Table 5.2.

5.2.2 Microscopic simulations

In this section, geometries, boundary conditions, and constitutive models for the multiscale simulations of arterial tissue at the cellular level are described. The methods presented here were previously employed by Dalbosco et al. [42]; therefore, only the main features of the

multiscale model are presented. The goal of these simulations is to shed light on possible micro-mechanical cues sensed by vascular cells, especially fibroblasts, since smooth muscle cells are largely absent in AAAs [175, 185]. Such cells are responsible for collagen G&R during AAA pathogenesis and their activity is at least in partially driven by mechanotransduction [22, 63].

Geometry, mesh and boundary conditions

RVEs, which represent a tissue-level point (Fig. 5.2) and consist of two families of collagen fibers embedded in a ground substance of non-collagenous micro-constituents, were constructed for three different stages of AAA pathogenesis, namely:

- the fibroblast-rich adventitia of a healthy aorta, whose collagen fibers are preferentially aligned in an axial direction [42, 183] (Fig. 5.2a);
- the abluminal side of an early AAA [42, 185], in which there is a realignment of collagen fibers towards the circumferential direction (Fig. 5.2b);
- the abluminal side of a late AAA [42, 185], with a stiff neo-adventitia characterized by a highly isotropic distribution of collagen fibers in the circumferential-axial plane (Fig. 5.2c).

Five RVEs for each stage were generated using a stochastic algorithm described in [42], which gradually adds collagen fibers (red and blue lines in Fig. 5.2a-c) to the ground substance (shown in pink in Fig. 5.2a-c) by sampling the direction of the fiber from a specific von Mises distribution, characterized by a mean fiber angle α, an in-plane dispersion parameter κ_{ip} and an out-of-plane dispersion parameter κ_{op}. For each of the three stages, values for these parameters were taken from the literature [183, 185]; these are the same ones from our previous work [42] and in the macroscopic models (Section 5.2.1).

Each RVE measures $500 \times 500 \times 100$ μm along the circumferential, axial and radial directions of the arterial tissue. This size was chosen to ensure a representative network of collagen fibers, accounting for volume fractions of 40% for the healthy adventitia and 60% for the aneurysmatic tissue, see [42] for more details. After each RVE was generated, the set of fiber directions was fitted to the von Mises distribution to obtain the effective values of α, κ_{ip} and κ_{op} for that particular RVE. In general, there is good agreement between the microstructural parameters reported in the literature for each of the three stages and the corresponding (effective) parameters for the three sets of 5 RVEs (Table 5.3), suggesting that the fiber networks are sufficiently representative of each microstructure.

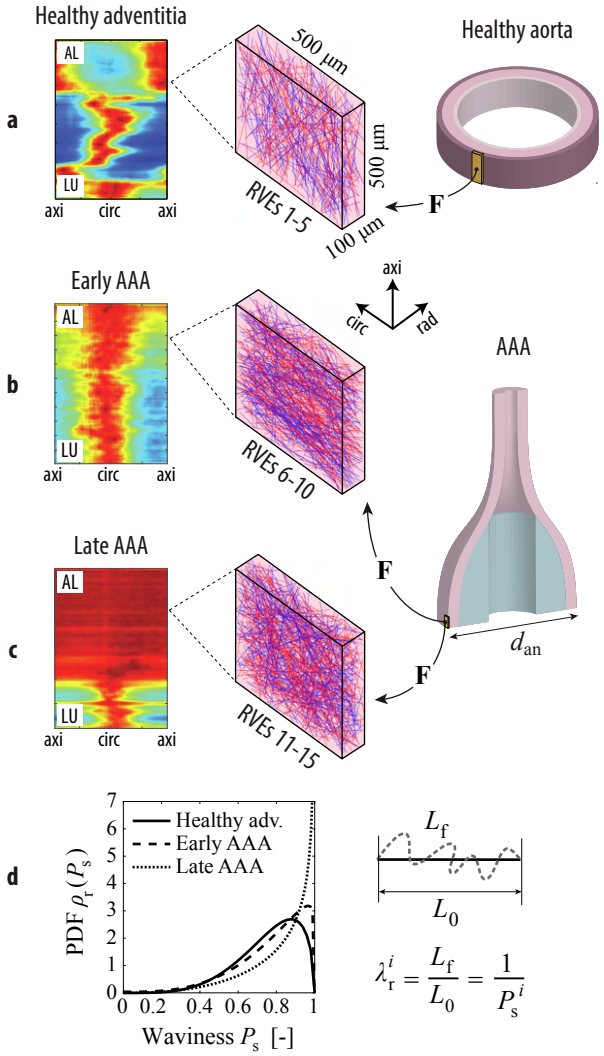

Figure 5.2: The micro-scale model consists of representative volume elements (RVEs) of (a) the tunica adventitia of a healthy aorta and AAAs at (b) an early and (c) late microstructural stage. For each stage, 5 realizations of the microstructure were created and simulated according to the deformation gradients $\mathbf{F}$ of the macro-scale models with different diameters d_{an}. The heatmaps in (a-c), reproduced from [183, 185], illustrate the characteristic arrangement of collagen fibers for each stage; the colors red and blue indicate high and low concentrations, respectively, of fibers aligned according to a specific in-plane angle between the circumferential (circ) and axial (axi) directions of the tissue for each radial (rad) layer between the luminal (LU) and the abluminal (AL) side of the vessel. (d) Since the two fiber families in the RVEs are represented as (red and blue) straight lines, the waviness of collagen in the real tissue is simulated by assigning a recruitment stretch λ_r^i to each i-th fiber by sampling a value P_s (ratio between the end-to-end distance L_0 and the arc length L_f of a wavy fiber) from a stage-specific beta distribution [42]; the probability density functions (PDFs) ρ_r for each stage can be seen in the graph.

Table 5.3: Experimental (target) and numerical (effective) parameters of the bivariate von Mises distributions for the three microstructural stages of the arterial tissue considered in the present study. Values are given as medians and interquartile ranges.

	Healthy adventitia		Early AAA		Late AAA	
	Exp. [183] ($n = 16$)	Num. ($n = 5$)	Exp. [185] ($n = 6$)	Num. ($n = 5$)	Exp. [185] ($n = 6$)	Num. ($n = 5$)
α (deg)	77.53 [67.04–84.02]	77.35 [73.46-79.92]	6.55 [5.19-11.62]	7.59 [5.88-8.41]	0.00[1]	0.00 [0.00–0.00]
κ_{ip} (-)	0.232 [0.192–0.282]	0.217 [0.205-0.239]	0.242 [0.234-0.260]	0.236 [0.231–0.259]	0.500[1]	0.500 [0.500-0.500]
κ_{op} (-)	0.466 [0.459–0.479]	0.468 [0.465–0.471]	0.433 [0.425-0.441]	0.432 [0.432-0.435]	0.402 [0.379-0.421]	0.401 [0.400-0.403]

[1] Assuming an isotropic in-plane fiber dispersion, $\kappa_{ip} = 0.5$ and the mean in-plane angle α becomes superfluous.

The ground substance of each RVE is meshed with second-order hexahedrons. The element size was defined as 12.5 μm after mesh convergence analyses [42]. The collagen fibers are meshed with second-order truss elements in such a way that each fiber element is fully contained in a particular hexahedron to which it is attached by a no-slip kinematic bond – the so-called embedded elements technique, see [41, 42] for more details.

Since they represent a tissue-level point, RVEs are assumed to undergo incompressible biaxial deformation in the circumferential-axial plane, characterized by the deformation gradient $[\mathbf{F}] = \mathrm{diag}(\lambda_{circ}, \lambda_{axial}, \lambda_{rad})$, in which the principal stretches λ_{circ}, λ_{axial} and λ_{rad} are obtained from the tissue-level simulations (Fig. 5.2).

A volume-averaging multiscale framework is used to simulate the biaxial deformation of the RVEs while ensuring energy consistency between the macro and micro-scales; details on this theory can be found elsewhere [16, 49]. As suggested in [41], periodic displacement fluctuations are enforced at the boundary of the RVEs.

Constitutive models

The ground substance of the RVEs is modeled as a nearly incompressible neo-Hookean material whose strain-energy function Ψ_g is given in the decoupled form

$$\Psi_g(\overline{\mathbf{C}}) = \frac{G_g}{2}(\bar{I}_1 - 3) + \frac{K_g}{2}(J-1)^2, \tag{5.5}$$

where $\overline{\mathbf{C}} = J^{-2/3}\mathbf{C}$ is the isochoric right Cauchy-Green tensor, with $\bar{I}_1 = \overline{\mathbf{C}} : \mathbf{I}$ its first principal invariant, G_g is the shear modulus of the ground substance and K_g is a penalty (volumetric) parameter, which was chosen to be $K_g = 100G_g$ to ensure nearly incompressible behavior. The values of the shear modulus for each of the three tissue stages are summarized in Table 5.4.

Table 5.4: Constitutive parameters employed in the RVE simulations.

Material parameters					
Parameter	Description	Numerical value			Refs.
		Healthy adventitia	Early AAA	Late AAA	
G_g (kPa)	Shear modulus of ground substance	3.77	0.59	3.78	[183, 185]
E_f^i (MPa)	Collagen fiber stiffness (normal distribution)	54.3 ± 25.1 (Mean $\pm$ Std)			[174]
a (-)	Waviness parameters	4.84	4.00	3.29	[42, 186]
b (-)	(beta distribution)	1.54	1.10	0.64	

Since collagen fibers in the unloaded arterial tissue are wavy [186, 198], a fact not taken into account in the geometry of the RVEs (Fig. 5.2a-c), each i-th fiber is assigned a strain-energy function Ψ_{f_i} of the form [41, 42]

$$\Psi_{f_i}(\lambda) = \begin{cases} 0 & \text{if} \quad 0 < \lambda < \lambda_r^i, \\ \dfrac{E_f^i}{2}(\lambda - \lambda_r^i)^2 & \text{if} \quad \lambda \geq \lambda_r^i, \end{cases} \tag{5.6}$$

where E_f^i is the fiber stiffness, λ is the stretch applied to the fiber, and λ_r^i is the recruitment stretch of the fiber. Therefore, it is assumed that fibers only bear load when they are recruited, i.e. when the stretch λ applied to the fiber is higher than λ_r^i. This simulates the well-known phenomenon of gradual fiber recruitment responsible for the characteristic nonlinear mechanical response of arterial tissue [105, 149, 199].

To account for variability of waviness and stiffness between the fibers, each i-th fiber is assigned to different values of E_f^i and λ_r^i. The former is taken from a normal distribution with a mean of 54.3 MPa and a standard deviation of 25.1 MPa (Table 5.4), while the latter is taken from a beta distribution with the form

$$\rho_r(P_s) = \frac{{P_s}^{a-1}(1-P_s)^{b-1}}{B(a,b)}, \tag{5.7}$$

where $B(a,b)$ is the beta function and P_s^i is a measure of the waviness of the i-th fiber with respect to its recruitment stretch $\lambda_r^i = 1/P_s^i$ (Fig. 5.2d). The parameters $\{a,b\}$, which

are different for each tissue stage, are given in Table 5.4. The beta distributions for each parameter set are shown in Fig. 5.2d, where it can be seen that fibers tend to be straighter ($P_s^i \to 1$) in diseased tissue as experimentally identified by Niestrawska et al. [186].

5.2.3 Statistical analyses

Simulation results were analyzed at the macro- and micro-scales; regarding the latter, results were organized in groups of 5 RVEs according to the three tissue stages (healthy, early AAA, and late AAA) and the maximum diameter of the aneurysms (45, 55 and 65 mm). Since normality of the data could not be assumed, the non-parametric Mann-Whitney U test was used to check for differences between groups.

5.3 Results and discussion

The results of the finite element simulations are summarized in Fig. 5.3, where the field of maximum principal stretches λ_1 is plotted (a) for the healthy aorta and (b-g) for AAAs with a maximum (deformed) diameter ranging from 45 to 65 mm. For the latter, results are shown for each size for (b-d) AAAs at an early stage and (e-g) at a late stage, after formation of the neo-adventitia ([42, 185], see also Fig. 5.2 and Table 5.2).

Macroscopic results show a fairly homogeneous deformation field in the healthy aorta (a), resulting in a hoop stress of about 100 kPa in the medial layer, which is widely accepted as the physiological stress value in a healthy abdominal aorta [119]. However, the AAA models (b-g) show important inhomogeneities in the deformation field due to the altered mechanical properties of the wall and its fusiform shape. In both early (b-d) and late (e-g) AAAs, the intraluminal thrombus, which is more compliant, deforms considerably more than the aortic wall. This could indicate a protective (mechanical) function of the thrombus, as previous works suggested [156, 261], although other concurrent effects (e.g., inflammatory processes [20] or hypoxia of the aortic wall due to isolation from blood flow [259, 260]) associated with the presence of an ILT are not captured by the present model.

Also in terms of the macro-models, the stretches in the aortic wall of early AAAs (b-d) are higher than their late counterparts (e-g), consistent with the observations in Niestrawska et al. [185], which reported a significant increase in the stiffness of the aortic tissue at a later stage. For early AAAs, stretches tend to be higher at the neck region of the wall, which has also been reported for real aneurysms [54]; on the other hand, the stretches in the late AAAs are lower in this region. In this context it has to be taken into account that the mechanical properties in the transition zone (i.e. the neck) are actually not derived from experiments but are interpolated from the parameters of the healthy and diseased tissue, see Section 5.2.1 and Appendix A. Moreover, the reference geometries for early

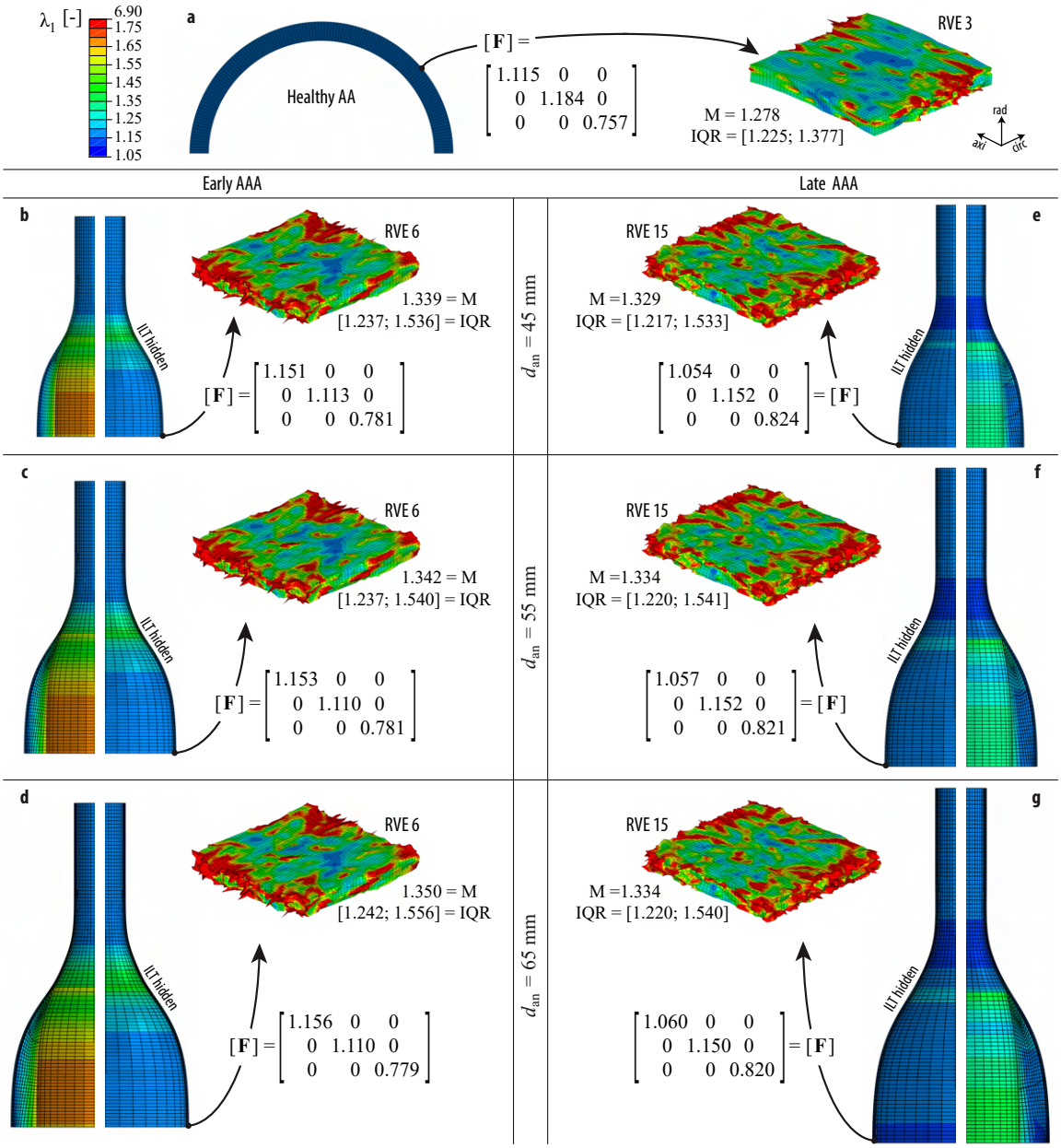

Figure 5.3: Maximum principal stretch λ_1 of the macro- and micro-scale models of (a) the healthy abdominal aorta (AA) and of AAAs with diameters ranging from 45 to 65 mm with (b-d) an early and (e-g) late microstructure. Half of the intraluminal thrombus (ILT) was hidden for each macro-scale model to better represent the stretches in the wall, and only one (of five) exemplary representative volume element (RVE), simulated according to the macro-deformation gradient $\mathbf{F}$, is shown. M and IQR refer to the median and interquartile range, respectively, of the λ_1 values for each RVE. The color scale applies to all models.

and late AAAs are different in order to have the same deformed diameter, as discussed in Section 5.2.1. Both assumptions of the model might also influence these contrasting results in the neck region, which however is not the region of interest in the present study.

The field of maximum principal stretches λ_1 in the ground substance of exemplary RVEs is shown at the micro-scale for each of the seven cases of Fig. 5.3. Since the ground substance encompasses all non-collagenous micro-constituents of the tissue, including mechanosensitive vascular cells such as fibroblasts, the microscopic deformations are interpreted here as possible mechanotransduction cues [22, 63] sensed by cells, see Dalbosco et al. [42] for a more detailed discussion on this particular choice. For the three exemplary RVEs shown in Fig. 5.3, important differences between the healthy (a) and diseased (b-g) states can be seen; on the other hand, these differences are much less pronounced in RVEs of early AAAs (b-d) and late AAAs (e-g) with the same diameter. Likewise, there are only negligible changes to the distribution of λ_1 with increasing diameter for each disease stage, at least qualitatively.

In order to quantitatively compare the seven cases from Fig. 5.3, the median (M) and interquartile range (IQR) of the maximum principal stretches λ_1 were calculated from all integration points of each individual RVE mesh. These quantities were then organized in groups of 5 RVEs according to the three tissue stages (healthy, early AAA, and late AAA) and the maximum diameter of the aneurysms (45, 55 and 65 mm). Boxplots of M and IQR values grouped according to the three tissue stages (healthy, early AAA, and late AAA) and the maximum diameter of the aneurysms (45, 55 and 65 mm) are presented in Fig. 5.4.

From Fig. 5.4 one can see that in general both the median (Fig. 5.4a) and the IQR (Fig. 5.4b) values of λ_1 are significantly higher in the diseased tissue compared to the healthy aorta, as indicated by the grey asterisks. This means that fibroblasts in AAAs would, on average, experience higher and more dispersed levels of deformation than the levels of deformation of the healthy adventitia, which could have mechanobiological implications. On the one hand, it is known from *in vitro* studies [12, 46, 63] that fibroblasts can sense their mechanical environment and respond accordingly – among other things, by promoting collagen G&R – when it deviates too far from healthy, homeostatic levels. In this respect, the differences predicted by the model between the micro-mechanics of healthy and diseased tissue could drive the changes in the collagen network in AAAs, as observed by Niestrawska et al. [185]. Importantly, this G&R process could be enhanced by the activation of fibroblasts to myofibroblasts (a cell phenotype often associated with pathological tissues), which is known to occur in response to altered mechanics at the cellular level [61, 126, 219].

On the other hand, it can be seen that for all aneurysm diameters that the median and IQR values of λ_1 for RVEs of early and late AAAs are remarkably similar, although the geometric and material properties of each disease stage, as well as the macroscopic deformation gradients applied to each of them (Fig. 5.3), are different. This motivates the hypothesis that both the macroscopic mechanics and the microstructure of the tissue – according to the mechano-pathogenic model of Niestrawska et al. [185] – change symbiotically in the

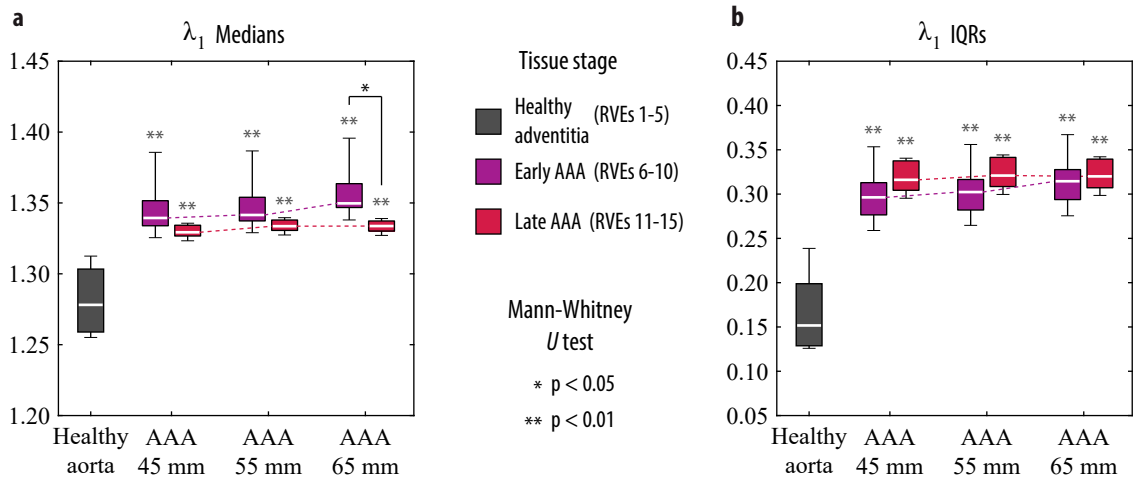

Figure 5.4: Boxplots of (a) the median and (b) the interquartile range (IQR) values of the maximum principal stretch λ_1 grouped by the three microstructural stages of the tissue and, in case of AAAs, also by maximum diameter. Each of the seven groups contains the results of five representative volume elements (RVEs). For both quantities, the grey asterisks indicate the results of the Mann-Whitney U test for differences between each diseased group and the healthy group. When comparing the AAA stages, the same test showed a significant difference only for λ_1 medians of an AAA with a diameter of 65 mm (black asterisk).

course of the disease in order to keep the level of deformation in the micro-scale approximately constant. In this case, the fact that this level is above the healthy one could mean that cells in the tissue have reached a new homeostatic state [64]. Importantly, a previous study using the same micro-scale model [42] showed significantly different levels of λ_1 when the same macroscopic deformation gradient is applied to RVEs of early and late AAAs. Therefore, changes at both scales are required for the model to provide similar deformation fields at the micro-scale.

Finally, one can see that for RVEs of early AAAs the levels of λ_1 tend to be slightly higher with larger diameters, although this increase is not significant (Kruskal-Wallis test: $p = 0.26$ for the medians, Fig. 5.4a, and $p = 0.44$ for the IQRs, Fig. 5.4b). Nevertheless, this trend, which is mostly absent in RVEs of late AAAs, leads to a significantly higher level of deformation in RVEs of early AAAs compared to their late counterparts for aneurysms with 65 mm of diameter (Fig. 5.4a). Since this is not the case for smaller diameters (for $p > 0.05$), it could mean that the microstructure of early AAAs is less effective in maintaining homeostasis at larger diameters than the late AAA microstructure with a thick abluminal neo-adventitia (Fig. 5.2c). This in turn could be a reason why the microstructure of the tissue continues to change from early to late as the aneurysm expands. It also underscores a hypothetical protective function of the neo-adventitia in late AAAs, as proposed in [42] – in this case especially for larger aneurysmal diameters. In fact, clinical evidence linking

faster AAA growth to an increased rupture risk [85] may indicate a failure of the tissue to adapt its microstructure to a rapidly changing geometry.

As a final remark to this section, it is emphasized that all seven models shown in Fig. 5.3 exhibit an important amplification effect from the macro to the micro-scale. For the healthy wall, e.g., the median value of the maximum principal stretch λ_1 of the exemplary RVE 3 shown in Fig. 5.3a is 80% higher than the value of λ_1 in the macroscopic model. In diseased tissue this difference is even more pronounced. This contrast between kinematics at macro and micro-scales (i.e., tissue and cell levels), which has been observed experimentally [144, 145] for arterial tissue, could have important consequences for microscopic phenomena, e.g., cell mechanotransduction. Therefore, this should be taken into account if meaningful results on the micro-scale are to be obtained [231].

5.4 Limitations and outlook

Despite the important insights into the mechanobiology of AAA pathogenesis provided by the model, some limitations to the present work can be mentioned. In the macroscopic simulations, an idealized geometry was used to model different AAA diameters, which did not take into account possible changes in the overall shape of a real aneurysm during its growth. Likewise, the thrombus was simplified into a homogeneous axisymmetric solid with isotropic mechanical behavior, while in real AAAs it usually has an asymmetric shape [89] and a three-layered structure with a certain degree of anisotropy [241]. In this context, applying the same modeling strategy to more complex, potentially patient-specific geometries of both the aneurysm and the thrombus could be the subject of future works. In particular, regional variations in curvature and wall thickness, which are common in real AAAs [59, 261], could have a significant influence on the local deformation gradient. This in turn would also change the results at the micro-scale, which could be related to mechanobiological phenomena, e.g., the transition from fibroblasts to myofibroblasts [61, 219]. Likewise, considering the external support of the perivascular tissues and spine [81, 192] could help to improve the fidelity of macro-scale models.

Another limitation is that the mechanical behavior in the transition zone between healthy and diseased tissue in AAAs had to be inferred from their respective material properties (Appendix A) due to the lack of specific experimental data. It is hoped that future studies on the spatial variability of mechanical properties of AAA tissues will provide better inputs to FE models like the present one.

Despite the intricate microstructure of arterial tissue [43, 105, 200], both in health and disease, the RVEs employed in the present work were simplified to a network of collagen fibers embedded in a ground substance, with all non-collagenous components of the tissue. While this is reasonable from a purely mechanical point of view (since collagen is much stiffer than the other micro-constituents), further refinements of the model could include,

e.g., proteoglycans and elastin [43, 194] as separate phases. In particular, the inclusion of elastin as a separate phase in the RVEs would make it possible, e.g., to investigate the consequences of elastin degradation (which is known to occur already in early stages of AAA formation [122, 185, 268]) on cell mechanobiology, which is also an interesting question for future studies.

Finally, it should be noted that in the present model, only the passive behavior of the wall was modeled at both scales. In this context, the active behavior of aortic tissue and chemo-mechanical phenomena, among others, could also have important implications for AAA pathogenesis and cell mechanotransduction. These concurring effects also represent an interesting field of study for future work.

5.5 Conclusions

In this study, a two-scale FE model of the aortic tissue in health and disease was presented. At the macro-scale (tissue level), the healthy aorta and AAAs of increasing size were modeled to simulate their passive mechanical behavior *in vivo*. At the micro-scale (cell level), the deformation gradient obtained from the macro-models was used as input to simulate RVEs of the healthy and diseased tissues.

In the context of mechanobiology, the microscopic deformations observed in the RVEs were interpreted as possible mechanotransduction cues sensed by vascular cells. The results suggest that the formation of an aneurysm disrupts the healthy micro-mechanical state of the tissue and thus represents a possible reason for the collagen G&R by mechanosensing cells (e.g., fibroblasts) along the AAA development [185]. After the formation of the aneurysm, an attempt seems to be made to keep the level of the microscopic deformations approximately constant with increasing diameter by altering both the microstructure and the macroscopic mechanics of the tissue, which could mean that a new homeostatic state was reached [64], at least for the diameter range investigated here.

Finally, it is emphasized that these conclusions are inextricably linked to the many hypotheses put forward to construct the model. However, since, to the best of the authors' knowledge, the micro-mechanical state of the aortic tissue simply cannot be visualized *in vivo* with current experimental techniques, the present numerical approach represents a valuable tool to improve our understanding of the multiscale pathogenesis of AAAs.

Appendix

A Mechanical properties of the transition zone

The geometries used in the macroscopic AAA simulations (Section 5.2.1) consist of a healthy aortic cylinder and a diseased aneurysm sac. Since these two regions are microstructurally and mechanically different, it is reasonable to assume that there is a transition zone between them, which here was taken to coincide with the aneurysm neck (Fig. 5.1c).

To the best of the authors' knowledge, the material properties of this hypothetical transition zone are not known from experiments. Therefore, they were derived from the equibiaxial response of the healthy and diseased parts, calculated from the parameters of Table 5.1 and Table 5.2, respectively, with the aim to model the transition zone as a mechanically graded material. Assuming a single material layer in such a zone, the mechanical parameters of the healthy wall were also averaged from the three different layers to obtain a consistent transition.

Considering an incompressible equibiaxial stretch λ in the circumferential-axial plane of the tissue, described by the deformation gradient $[\mathbf{F}] = \mathrm{diag}(\lambda_{\mathrm{circ}}, \lambda_{\mathrm{axial}}, \lambda_{\mathrm{rad}}) = \mathrm{diag}(\lambda, \lambda, 1/\lambda^2)$, the second Piola-Kirchhoff stress tensor $\mathbf{S}$ was calculated from (5.2) as [113]

$$\mathbf{S} = 2\frac{\partial \Psi_{\mathrm{A}}}{\partial \mathbf{C}} - p\mathbf{C}^{-1} = \mu_{\mathrm{A}}\mathbf{I} + \sum_{i=4,6} 2k_1(I_i^{\star} - 1)\exp\left[k_2(I_i^{\star} - 1)^2\right]\mathbf{H}_i - p\mathbf{C}^{-1}, \qquad \text{(A.1)}$$

where p is the Lagrange multiplier that enforces the incompressibility condition calculated here from the plane stress condition ($S_{33} = 0$). Finally, the Cauchy stress tensor was computed by a push-forward operation, i.e. $\sigma = \mathbf{F}\mathbf{S}\mathbf{F}^{\mathrm{T}}$. The resulting stress-stretch curves are shown in Fig. A.1 for the healthy aorta (grey), early AAA (purple) and late AAA (red).

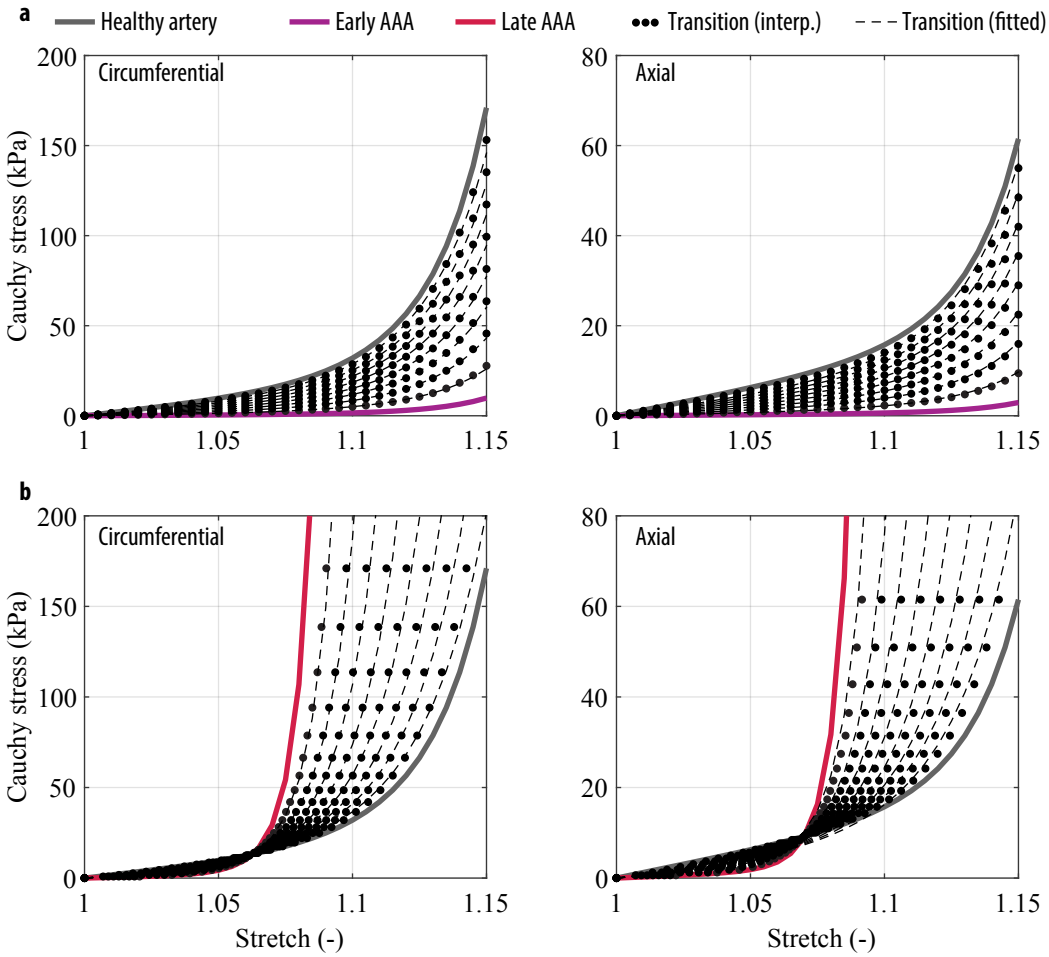

Figure A.1: Fitted equibiaxial mechanical response of the transition zone; (a) early AAAs and (b) late AAAs.

A series of fictitious stress-stretch responses (dotted curves in Fig. A.1) was then interpolated from the curves of healthy and diseased tissue. To get the constitutive parameters for each generated response, the structural parameters α, κ_{ip} and κ_{op} of the model (A.1) were fixed to values between the healthy and diseased stages (Table A.1) and the mechanical parameters μ_{A}, k_1 and k_2 were then fitted to each generated response. The results are shown in Fig. A.1 as dashed curves, where it can be seen that a good fit ($R^2 \geq 0.99$) could be achieved for all interpolated responses. The parameters obtained in this way for each curve of Fig. A.1 are presented in Table A.1.

Table A.1: Parameters of the interpolated curves shown in Fig. A.1.

Interpolated material parameters: Healthy aorta → Early AAA								
Parameter	Numerical value							
μ_A (kPa)	11.61	10.17	8.74	7.31	5.87	4.44	3.01	1.57
k_1 (kPa)	18.80	16.62	14.44	12.27	10.09	7.92	5.74	3.58
k_2 (-)	30.71	30.66	30.60	30.51	30.38	30.18	29.81	28.92
κ_{ip} (-)	0.240							
κ_{op} (-)	0.460							
α (deg)	15.0							
Interpolated material parameters: Healthy aorta → Late AAA								
Parameter	Numerical value							
μ_A (kPa)	5.61	5.87	6.10	6.30	6.49	6.66	6.79	6.88
k_1 (kPa)	40.24	38.06	35.24	31.65	27.17	21.77	15.56	9.02
k_2 (-)	36.70	44.76	55.33	69.51	89.11	117.2	159.6	228.5
κ_{ip} (-)	0.230							
κ_{op} (-)	0.440							
α (deg)	23.5							

The method described above was implemented in MATLAB (The MathWorks Inc., Natwick, US) to generate any desired number of interpolated curves. Based on the finite element mesh, each line of elements in the transition zone of macro-scale models is assigned a different set of parameters, considering equally spaced intervals along the longitudinal direction from healthy to diseased properties to ensure a smooth transition of deformation fields (Fig. 5.3) along the length of the AAA, as one would expect from a biological material.

6 CONCLUSIONS AND FUTURE PERSPECTIVES

In this thesis, a novel class of RVE-based models of arterial tissue in health and disease was proposed by combining a sound multiscale computational framework [16, 49] with the embedded elements technique [67, 83]. The geometry of the RVEs consists of a network of collagen fibers, discretized with truss elements, reinforcing a continuum ground substance encompassing all non-collagenous microconstituents of the tissue. While the assumption of a two-phase hyperelastic material is reasonable from a mechanical point of view [82], the RVE clearly simplifies the intricate microstructure of arteries [43, 119, 200]. Constructing more realistic geometries and including other physical phenomena, especially the active part of arterial mechanics due to smooth muscle cells, is an interesting area for future studies.

In Chapter 3, the influence of different multiscale BCs on the macro- and micro-scale results is investigated by submitting the proposed RVE to an equibiaxial loading. It is argued that the assumption of periodic fluctuations on the boundary yields more realistic results, with less boundary effects, when compared with the other three classical multiscale models, a fact that is used in the subsequent studies. It must be said, however, that the network of collagen fibers in the RVEs is not periodic, and, therefore, boundary effects should also be expected when using the periodic BC, even if with less intensity than in other multiscale models. To address this issue, future works could focus on constructing specialized BCs aiming to reduce boundary effects.

In Chapters 4 and 5, the model was used to shed more light on the mechano-pathogenic theory of AAA progression by Niestrawska et al. [185], focusing on the formation of a neo-adventitia layer at the abluminal side of the wall and its relation to the mechanobiology of vascular cells. RVEs were constructed for the fibroblast-rich adventitia of the abdominal aorta and for early and late stages of AAA tissue, each with its characteristic arrangement of collagen fibers as observed in experimental studies [183, 185, 186]. These RVEs were subjected, first, to equibiaxial loadings (Chapter 4) and then to various biaxial loadings obtained from suitable macro-scale FE simulations (Chapter 5). Taken together, the results pointed to a possible protective role of the neo-adventitia, whose formation could constitute an attempt by vascular cells to keep levels of microscopic deformation in check, especially for larger AAA diameters. This hypothesis, of course, merits further investigation by experimental studies, which hopefully can be motivated by the present thesis.

We conclude by recalling the aphorism by the British statistician George Box: *"All models are wrong, but some are useful."* [19]. Despite the many simplifications involved in the proposed RVE-based model, it provided a valid way to simulate micromechanical phenomena that might be involved in the pathogenesis of AAAs, and which cannot be observed *in vivo* with current techniques. The proposed model constitutes thus a valuable tool to help advancing our understanding of vascular pathophysiology.

REFERENCES

[1] L. C. Adams, J. Brangsch, C. Reimann, J. O. Kaufmann, R. Buchholz, U. Karst, R. M. Botnar, B. Hamm, and M. R. Makowski. Simultaneous molecular MRI of extracellular matrix collagen and inflammatory activity to predict abdominal aortic aneurysm rupture. *Scientific Reports*, 10:15206, 2020. doi: 10.1038/s41598-020-71817-x.

[2] D. Ambrosi, M. Ben Amar, C. J. Cyron, A. DeSimone, A. Goriely, J. D. Humphrey, and E. Kuhl. Growth and remodelling of living tissues: Perspectives, challenges and opportunities. *Journal of The Royal Society Interface*, 16:20190233, 2019. doi: 10.1098/rsif.2019.0233.

[3] S. H. Ardakani, P. F. Dehaghani, H. Moslemzadeh, and S. Mohammadi. 3D large strain hierarchical multiscale analysis of soft fiber-reinforced tissues: Application to a degraded arterial wall. *Engineering Computations*, 39:2108–2143, 2022. doi: 10.1108/EC-05-2021-0289.

[4] R. L. Armentano, J. Levenson, J. G. Barra, E. I.C. Fischer, G. J. Breitbart, R. H. Pichel, and A. Simon. Assessment of elastin and collagen contribution to aortic elasticity in conscious dogs. *American Journal of Physiology-Heart and Circulatory Physiology*, 260:H1870–H1877, 1991. doi: 10.1152/ajpheart.1991.260.6.H1870.

[5] S. M. Arribas, C. Hillier, C. González, S. McGrory, A. F. Dominiczak, and J. C. McGrath. Cellular aspects of vascular remodeling in hypertension revealed by confocal microscopy. *Hypertension*, 30:1455–1464, 1997. doi: 10.1161/01.HYP.30.6.1455.

[6] S. M. Arribas, A. Hinek, and M. C. González. Elastic fibres and vascular structure in hypertension. *Pharmacology and Therapeutics*, 111:771–791, 2006. doi: 10.1016/j.pharmthera.2005.12.003.

[7] S. Avril. Cardiovascular medtech: The grand challenge of computer simulations. *Frontiers in Medical Technology*, 5:1–3, 2023. doi: 10.3389/fmedt.2023.1304223.

[8] V. Ayyalasomayajula, B. Pierrat, and P. Badel. A computational model for understanding the micro-mechanics of collagen fiber network in the tunica adventitia. *Biomechanics and Modeling in Mechanobiology*, 18:1507–1528, 2019. doi: 10.1007/s10237-019-01161-1.

[9] V. Ayyalasomayajula, B. Pierrat, and P. Badel. An evaluation of fiber-based damage for assessing the failure of aortic tissue: Comparison between healthy and aneurysmal aortas. *Mechanics of Soft Materials*, 4:4, 2022. doi: 10.1007/s42558-022-00041-6.

[10] V. Ayyalasomayajula, B. Pierrat, and P. Badel. Evaluation of a multi-scale discrete fiber model for analyzing arterial failure. *Journal of Biomechanics*, 157:111700, 2023. doi: 10.1016/j.jbiomech.2023.111700.

[11] B. M. Baker, B. Trappmann, W. Y. Wang, M. S. Sakar, I. L. Kim, V. B. Shenoy, J. A. Burdick, and C. S. Chen. Cell-mediated fibre recruitment drives extracellular matrix mechanosensing in engineered fibrillar microenvironments. *Nature Materials*, 14: 1262–1268, 2015. doi: 10.1038/nmat4444.

[12] E. Bell, B. Ivarsson, and C. Merrill. Production of a tissue-like structure by contraction of collagen lattices by human fibroblasts of different proliferative potential in vitro. *Proceedings of the National Academy of Sciences*, 76:1274–1278, 1979. doi: 10.1073/pnas.76.3.1274.

[13] T. Belytschko, W. K. Liu, and B. Moran. *Nonlinear Finite Elements for Continua and Structures*. John Wiley & Sons, Chichester, UK, 2000. ISBN 978-0471987741.

[14] M. Ben-Or Frank, J. A. Niestrawska, G. A. Holzapfel, and G. DeBotton. Micromechanically-motivated analysis of fibrous tissue. *Journal of the Mechanical Behavior of Biomedical Materials*, 96:69–78, 2019. doi: 10.1016/j.jmbbm.2019.04.007.

[15] M. J. Bissell, H. G. Hall, and G. Parry. How does the extracellular matrix direct gene expression? *Journal of Theoretical Biology*, 99:31–68, 1982. doi: 10.1016/0022-5193(82)90388-5.

[16] P. J. Blanco, P. J. Sánchez, E. A. de Souza Neto, and R. A. Feijóo. Variational foundations and generalized unified theory of RVE-based multiscale models. *Archives of Computational Methods in Engineering*, 23:191–253, 2016. doi: 10.1007/s11831-014-9137-5.

[17] G. A. Borelli. *De Motu Animalium*. Typographia Angeli Bernabò, Rome, 1681.

[18] G. A. Borelli. *On the Movement of Animals*. Springer Berlin Heidelberg, Berlin, DE, 1989. doi: 10.1007/978-3-642-73812-8.

[19] G. E. P. Box. Robustness in the strategy of scientific model building. In R. L. Launer and G. N. Wilkinson, editors, *Robustness in Statistics*, pages 201–236. Academic Press, Cambridge, US, 1979. doi: 10.1016/B978-0-12-438150-6.50018-2.

[20] A. J. Boyd. Intraluminal thrombus: Innocent bystander or factor in abdominal aortic aneurysm pathogenesis? *JVS-Vascular Science*, 2:159–169, 2021. doi: 10.1016/j.jvssci.2021.02.001.

[21] B. R. Britt and A. E. Ehret. Constitutive modelling of fibre networks with stretch distributions. Part I: Theory and illustration. *Journal of the Mechanics and Physics of Solids*, 167:104960, 2022. doi: 10.1016/j.jmps.2022.104960.

[22] R. A. Brown, R. Prajapati, D. A. McGrouther, I. V. Yannas, and M. Eastwood. Tensional homeostasis in dermal fibroblasts: Mechanical responses to mechanical loading in three-dimensional substrates. *Journal of Cellular Physiology*, 175:323–332, 1998. doi: 10.1002/(SICI)1097-4652(199806)175:3<323::AID-JCP10>3.0.CO;2-6.

[23] W. B. Cannon. Organization for physiological homeostasis. *Physiological Reviews*, 9:399–431, 1929. doi: 10.1152/physrev.1929.9.3.399.

[24] L. Cardamone, A. Valentín, J. F. Eberth, and J. D. Humphrey. Origin of axial prestretch and residual stress in arteries. *Biomechanics and Modeling in Mechanobiology*, 8:431–446, 2009. doi: 10.1007/s10237-008-0146-x.

[25] T. A. Carniel and E. A. Fancello. A transversely isotropic coupled hyperelastic model for the mechanical behavior of tendons. *Journal of Biomechanics*, 54:49–57, 2017. doi: 10.1016/j.jbiomech.2017.01.042.

[26] T. A. Carniel and E. A. Fancello. A variational homogenization approach applied to the multiscale analysis of the viscoelastic behavior of tendon fascicles. *Continuum Mechanics and Thermodynamics*, 31:607–626, 2019. doi: 10.1007/s00161-018-0714-y.

[27] T. A. Carniel and E. A. Fancello. A numerical insight on the pericellular matrix and elastin fibers in the multiscale mechanics of tendon fascicles. *European Journal of Mechanics - A/Solids*, 76:146–154, 2019. doi: 10.1016/j.euromechsol.2019.04.001.

[28] T. A. Carniel, B. Klahr, and E. A. Fancello. A multiscale numerical approach for the finite strains analysis of materials reinforced with helical fibers. *Mechanics of Materials*, 126:75–85, 2018. doi: 10.1016/j.mechmat.2018.07.014.

[29] T. A. Carniel, B. Klahr, and E. A. Fancello. On multiscale boundary conditions in the computational homogenization of an RVE of tendon fascicles. *Journal of the Mechanical Behavior of Biomedical Materials*, 91:131–138, 2019. doi: 10.1016/j.jmbbm.2018.12.003.

[30] T. A. Carniel, M. Lazzari, B. Klahr, and E. A. Fancello. A computational homogenization approach for uniaxial stress state analyses of wavy fibrous materials. *Mechanics of Soft Materials*, 2:5, 2020. doi: 10.1007/s42558-020-00020-9.

[31] C. Cavinato, C. Helfenstein-Didier, T. Olivier, S. R. du Roscoat, N. Laroche, and P. Badel. Biaxial loading of arterial tissues with 3D in situ observations of adventitia fibrous microstructure: A method coupling multi-photon confocal microscopy and bulge inflation test. *Journal of the Mechanical Behavior of Biomedical Materials*, 74:488–498, 2017. doi: 10.1016/j.jmbbm.2017.07.022.

[32] P. L. Chandran and V. H. Barocas. Affine versus non-affine fibril kinematics in collagen networks: Theoretical studies of network behavior. *Journal of Biomechanical Engineering*, 128:259–270, 2006. doi: 10.1115/1.2165699.

[33] H. P. Charalambous, P. C. Roussis, and A. E. Giannakopoulos. Viscoelastic dynamic arterial response. *Computers in Biology and Medicine*, 89:337–354, 2017. doi: 10.1016/j.compbiomed.2017.07.028.

[34] C. S. Chen, M. Mrksich, S. Huang, G. M. Whitesides, and D. E. Ingber. Geometric control of cell life and death. *Science*, 276:1425–1428, 1997. doi: 10.1126/science.276.5317.1425.

[35] H. Chen, Y. Liu, M. N. Slipchenko, X. Zhao, J.-X. Cheng, and G. S. Kassab. The layered structure of coronary adventitia under mechanical load. *Biophysical Journal*, 101:2555–2562, 2011. doi: 10.1016/j.bpj.2011.10.043.

[36] H. Chen, M. N. Slipchenko, Y. Liu, X. Zhao, J.-X. Cheng, Y. Lanir, and G. S. Kassab. Biaxial deformation of collagen and elastin fibers in coronary adventitia. *Journal of Applied Physiology*, 115:1683–1693, 2013. doi: 10.1152/japplphysiol.00601.2013.

[37] M.-J. Chow, R. Turcotte, C. P. Lin, and Y. Zhang. Arterial extracellular matrix: A mechanobiological study of the contributions and interactions of elastin and collagen. *Biophysical Journal*, 106:2684–2692, 2014. doi: 10.1016/j.bpj.2014.05.014.

[38] T. K. Chung, N. L. Liang, and D. A. Vorp. Artificial intelligence framework to predict wall stress in abdominal aortic aneurysm. *Applications in Engineering Science*, 10:100104, 2022. doi: 10.1016/j.apples.2022.100104.

[39] M. I. Converse, R. G. Walther, J. T. Ingram, Y. Li, S. M. Yu, and K. L. Monson. Detection and characterization of molecular-level collagen damage in overstretched cerebral arteries. *Acta Biomaterialia*, 67:307–318, feb 2018. doi: 10.1016/j.actbio.2017.11.052.

[40] F. Cosentino, S. Sherifova, G. Sommer, G. Raffa, M. Pilato, S. Pasta, and G. A. Holzapfel. Regional biomechanical characterization of human ascending aortic aneurysms: Microstructure and biaxial mechanical response. *Acta Biomaterialia*, 169:107–117, 2023. doi: 10.1016/j.actbio.2023.08.016.

[41] M. Dalbosco, T. A. Carniel, E. A. Fancello, and G. A. Holzapfel. Multiscale numerical analyses of arterial tissue with embedded elements in the finite strain regime. *Computer Methods in Applied Mechanics and Engineering*, 381:113844, 2021. doi: 10.1016/j.cma.2021.113844.

[42] M. Dalbosco, T. A. Carniel, E. A. Fancello, and G. A. Holzapfel. Multiscale simulations suggest a protective role of neo-adventitia in abdominal aortic aneurysms. *Acta Biomaterialia*, 146:248–258, 2022. doi: 10.1016/j.actbio.2022.04.049.

[43] M. Dalbosco, D. C. Haspinger, K. Li, S.-I. Murtada, A. Pukaluk, M. Rolf-Pissarczyk, S. Sherifova, and G. Sommer. Multiscale experimental characterization and computational modeling of the human aorta. In G. Sommer, K. Li, D. Ch. Haspinger, and R. W. Ogden, editors, *Solid (Bio)mechanics: Challenges of the Next Decade. Studies in Mechanobiology, Tissue Engineering and Biomaterials.*, pages 3–52. Springer, Cham, CH, 2022. ISBN 978-3-030-92338-9. doi: 10.1007/978-3-030-92339-6_1.

[44] M. Dalbosco, M. Terzano, T. A. Carniel, E. A. Fancello, and G. A. Holzapfel. A two-scale numerical study on the mechanobiology of abdominal aortic aneurysms. *Journal of The Royal Society Interface*, 20:20230472, 2023. doi: 10.1098/rsif.2023.0472.

[45] H. G. Davis. *Conservative Surgery*. D. Appleton & Co., New York, US, 1867.

[46] N. de Jonge, F. M. W. Kanters, F. P. T. Baaijens, and C. V. C. Bouten. Strain-induced collagen organization at the micro-level in fibrin-based engineered tissue constructs. *Annals of Biomedical Engineering*, 41:763–774, 2013. doi: 10.1007/s10439-012-0704-3.

[47] M. de Lucio, M. F. García, J. D. García, L. E. R. Rodríguez, and F. A. Marcos. On the importance of tunica intima in the aging aorta: A three-layered in silico model for computing wall stresses in abdominal aortic aneurysms. *Computer Methods in Biomechanics and Biomedical Engineering*, 24:467–484, 2021. doi: 10.1080/10255842.2020.1836167.

[48] R. R. De Martino, B. W. Nolan, P. P. Goodney, C. K. Chang, A. Schanzer, R. Cambria, D. J. Bertges, and J. L. Cronenwett. Outcomes of symptomatic abdominal aortic aneurysm repair. *Journal of Vascular Surgery*, 52:5–12, 2010. doi: 10.1016/j.jvs.2010.01.095.

[49] E. A. de Souza Neto and R. A. Feijóo. Variational foundations of large strain multiscale solid constitutive models: Kinematical formulation. In M. Vaz, E. A. de Souza Neto, and P. A. Muñoz-Rojas, editors, *Advanced Computational Materials Modeling*, pages 341–378. Wiley-VCH Verlag, Weinheim, DE, 2010. ISBN 9783527324798.

[50] E. A. de Souza Neto, P. J. Blanco, P. J. Sánchez, and R. A. Feijóo. An RVE-based multiscale theory of solids with micro-scale inertia and body force effects. *Mechanics of Materials*, 80:136–144, 2015. doi: 10.1016/j.mechmat.2014.10.007.

[51] G. DeBotton and T. Oren. Analytical and numerical analyses of the micromechanics of soft fibrous connective tissues. *Biomechanics and Modeling in Mechanobiology*, 12:151–166, 2013. doi: 10.1007/s10237-012-0388-5.

[52] H. Demiray. A note on the elasticity of soft biological tissues. *Journal of Biomechanics*, 5:309–311, 1972. doi: 10.1016/0021-9290(72)90047-4.

[53] W. Derwich, A. Wittek, K. Pfister, K. Nelson, J. Bereiter-Hahn, C.-P. Fritzen, C. Blase, and T. Schmitz-Rixen. High resolution strain analysis comparing aorta and abdominal aortic aneurysm with real time three dimensional speckle tracking ultrasound. *European Journal of Vascular and Endovascular Surgery*, 51:187–193, 2016. doi: 10.1016/j.ejvs.2015.07.042.

[54] W. Derwich, A. Wittek, A. Hegner, C.-P. Fritzen, C. Blase, and T. Schmitz-Rixen. Comparison of abdominal aortic aneurysm sac and neck wall motion with 4D ultrasound imaging. *European Journal of Vascular and Endovascular Surgery*, 60: 539–547, 2020. doi: 10.1016/j.ejvs.2020.06.027.

[55] C. E. Devine and A. P. Somlyo. Thick filaments in vascular smooth muscle. *The Journal of Cell Biology*, 49:636–649, 1971. doi: 10.1083/jcb.49.3.636.

[56] E.S. Di Martino, G. Guadagni, A. Fumero, G. Ballerini, R. Spirito, P. Biglioli, and A. Redaelli. Fluid–structure interaction within realistic three-dimensional models of the aneurysmatic aorta as a guidance to assess the risk of rupture of the aneurysm. *Medical Engineering & Physics*, 23:647–655, 2001. doi: 10.1016/S1350-4533(01)00093-5.

[57] K. P. Dingemans, P. Teeling, J. H. Lagendijk, and A. E. Becker. Extracellular matrix of the human aortic media: An ultrastructural histochemical and immunohistochemical study of the adult aortic media. *The Anatomical Record*, 258:1–14, 2000. doi: 10.1002/(SICI)1097-0185(20000101)258:1<1::AID-AR1>3.0.CO;2-7.

[58] M. P. Dorta, I. V. de Brito, A. C. Pereira, and A. M. Alencar. Quantification of alignment of vascular smooth muscle cells. *Cytometry Part A*, 93:533–539, may 2018. doi: 10.1002/cyto.a.23355.

[59] B. J. Doyle, N. Bappoo, M. B. J. Syed, R. O. Forsythe, J. T. Powell, N. Conlisk, P. R. Hoskins, O. M. B. McBride, A. S. V. Shah, P. E. Norman, and D. E. Newby. Biomechanical assessment predicts aneurysm related events in patients with abdominal aortic aneurysm. *European Journal of Vascular and Endovascular Surgery*, 60: 365–373, 2020. doi: 10.1016/j.ejvs.2020.02.023.

[60] N. J. B. Driessen, C. V. C. Bouten, and F. P. T. Baaijens. A structural constitutive model for collagenous cardiovascular tissues incorporating the angular fiber distribution. *Journal of Biomechanical Engineering*, 127:494–503, 2005. doi: 10.1115/1.1894373.

[61] M. D'Urso and N. A. Kurniawan. Mechanical and physical regulation of fibroblast–myofibroblast transition: From cellular mechanoresponse to tissue pathology. *Frontiers in Bioengineering and Biotechnology*, 8:609653, 2020. doi: 10.3389/fbioe.2020.609653.

[62] J. L. Ebaugh and J. D. Raffetto. Giant abdominal aortic aneurysm. *New England Journal of Medicine*, 362:66–66, 2010. doi: 10.1056/NEJMicm0808225.

[63] J. F. Eichinger, D. Paukner, J. M. Szafron, R. C. Aydin, J. D. Humphrey, and C. J. Cyron. Computer-controlled biaxial bioreactor for investigating cell-mediated homeostasis in tissue equivalents. *Journal of Biomechanical Engineering*, 142:1–8, 2020. doi: 10.1115/1.4046201.

[64] J. F. Eichinger, L. J. Haeusel, D. Paukner, R. C. Aydin, J. D. Humphrey, and C. J. Cyron. Mechanical homeostasis in tissue equivalents: A review. *Biomechanics and Modeling in Mechanobiology*, 20:833–850, 2021. doi: 10.1007/s10237-021-01433-9.

[65] J. F. Eichinger, D. Paukner, R. C. Aydin, W. A. Wall, J. D. Humphrey, and C. J. Cyron. What do cells regulate in soft tissues on short time scales? *Acta Biomaterialia*, 134:348–356, 2021. doi: 10.1016/j.actbio.2021.07.054.

[66] D. F. Elger, D. M. Blackketter, R. S. Budwig, and K. H. Johansen. The influence of shape on the stresses in model abdominal aortic aneurysms. *Journal of Biomechanical Engineering*, 118:326–332, 1996. doi: 10.1115/1.2796014.

[67] A. E. Elwi and T. M. Hrudey. Finite element model for curved embedded reinforcement. *Journal of Engineering Mechanics*, 115:740–754, 1989. doi: 10.1061/(ASCE)0733-9399(1989)115:4(740).

[68] M. Fillinger. Who should we operate on and how do we decide: Predicting rupture and survival in patients with aortic aneurysm. *Seminars in Vascular Surgery*, 20:121–127, 2007. doi: 10.1053/j.semvascsurg.2007.04.001.

[69] M. F. Fillinger, S. P. Marra, M. L. Raghavan, and F. E. Kennedy. Prediction of rupture risk in abdominal aortic aneurysm during observation: Wall stress versus diameter. *Journal of Vascular Surgery*, 37:724–732, 2003. doi: 10.1067/mva.2003.213.

[70] E. Fonck, G. Prod'hom, S. Roy, L. Augsburger, D. A. Rüfenacht, and N. Stergiopulos. Effect of elastin degradation on carotid wall mechanics as assessed by a constituent-based biomechanical model. *American Journal of Physiology-Heart and Circulatory Physiology*, 292:H2754–H2763, 2007. doi: 10.1152/ajpheart.01108.2006.

[71] G. Franchini, I. D. Breslavsky, G. A. Holzapfel, and M. Amabili. Viscoelastic characterization of human descending thoracic aortas under cyclic load. *Acta Biomaterialia*, 130:291–307, 2021. doi: 10.1016/j.actbio.2021.05.025.

[72] G. Franchini, I. D. Breslavsky, F. Giovanniello, A. Kassab, G. A. Holzapfel, and M. Amabili. Role of smooth muscle activation in the static and dynamic mechanical characterization of human aortas. *Proceedings of the National Academy of Sciences*, 119(3), 2022. doi: 10.1073/pnas.2117232119.

[73] A. D. Freed and T. C. Doehring. Elastic model for crimped collagen fibrils. *Journal of Biomechanical Engineering*, 127:587–593, 2005. doi: 10.1115/1.1934145.

[74] S. G. Friedman. *A History of Vascular Surgery*. Blackwell Publishing, Malden, US, 2nd edition, 2005. doi: 10.1002/9780470750773.

[75] Y. C. Fung, K. Fronek, and P. Patitucci. Pseudoelasticity of arteries and the choice of its mathematical expression. *American Journal of Physiology-Heart and Circulatory Physiology*, 237:H620–H631, 1979. doi: 10.1152/ajpheart.1979.237.5.H620.

[76] E. Gacek, R. R. Mahutga, and V. H. Barocas. Hybrid discrete-continuum multiscale model of tissue growth and remodeling. *Acta Biomaterialia*, 163:7–24, 2023. doi: 10.1016/j.actbio.2022.09.040.

[77] H. T. Garimella, R. R. Menghani, J. I. Gerber, S. Sridhar, and R. H. Kraft. Embedded finite elements for modeling axonal injury. *Annals of Biomedical Engineering*, 47: 1889–1907, 2019. doi: 10.1007/s10439-018-02166-0.

[78] L. P. Gartner. *Textbook of Histology*. Elsevier, Philadelphia, US, 4th edition, 2017. ISBN 0323390684.

[79] T. C. Gasser, R. W. Ogden, and G. A. Holzapfel. Hyperelastic modelling of arterial layers with distributed collagen fibre orientations. *Journal of The Royal Society Interface*, 3:15–35, 2006. doi: 10.1098/rsif.2005.0073.

[80] M. W. Gee, C. Förster, and W. A. Wall. A computational strategy for prestressing patient-specific biomechanical problems under finite deformation. *International Journal for Numerical Methods in Biomedical Engineering*, 26:52–72, 2010. doi: 10.1002/cnm.1236.

[81] J. Gindre, A. Bel-Brunon, A. Kaladji, A. Duménil, M. Rochette, A. Lucas, P. Haigron, and A. Combescure. Finite element simulation of the insertion of guidewires during an EVAR procedure: Example of a complex patient case, a first step toward patient-specific parameterized models. *International Journal for Numerical Methods in Biomedical Engineering*, 31:e02716, 2015. doi: 10.1002/cnm.2716.

[82] S. Glagov and H. Wolinsky. Aortic wall as a 'two-phase' material. *Nature*, 199: 606–608, 1963. doi: 10.1038/199606a0.

[83] M. Goudarzi and A. Simone. Discrete inclusion models for reinforced composites: Comparative performance analysis and modeling challenges. *Computer Methods in Applied Mechanics and Engineering*, 355:535–557, 2019. doi: 10.1016/j.cma.2019.06.026.

[84] R. A. Gould, K. Chin, T. P. Santisakultarm, A. Dropkin, J. M. Richards, C. B. Schaffer, and J. T. Butcher. Cyclic strain anisotropy regulates valvular interstitial cell phenotype and tissue remodeling in three-dimensional culture. *Acta Biomaterialia*, 8:1710–1719, 2012. doi: 10.1016/j.actbio.2012.01.006.

[85] N. Grootenboer, J. L. Bosch, J. M. Hendriks, and M. R. H. M. van Sambeek. Epidemiology, aetiology, risk of rupture and treatment of abdominal aortic aneurysms: Does sex matter? *European Journal of Vascular and Endovascular Surgery*, 38: 278–284, 2009. doi: 10.1016/j.ejvs.2009.05.004.

[86] J. H. Haga, Y.-S. J. Li, and S. Chien. Molecular basis of the effects of mechanical stretch on vascular smooth muscle cells. *Journal of Biomechanics*, 40:947–960, 2007. doi: 10.1016/j.jbiomech.2006.04.011.

[87] Y. Han, K. Huang, Q.-P. Yao, and Z.-L. Jiang. Mechanobiology in vascular remodeling. *National Science Review*, 5:933–946, 2018. doi: 10.1093/nsr/nwx153.

[88] D. Hanein and A. R. Horwitz. The structure of cell–matrix adhesions: The new frontier. *Current Opinion in Cell Biology*, 24:134–140, 2012. doi: 10.1016/j.ceb.2011.12.001.

[89] S. S. Hans, O. Jareunpoon, M. Balasubramaniam, and G. B. Zelenock. Size and location of thrombus in intact and ruptured abdominal aortic aneurysms. *Journal of Vascular Surgery*, 41:584–588, 2005. doi: 10.1016/j.jvs.2005.01.004.

[90] H. Hartl. *Development of a continuum-mechanics-based tool for 3D finite element analysis of reinforced concrete structures and application to problems of soil-structure interaction*. Doctoral thesis, Graz University of Technology, AT, 2002.

[91] H. W. Haslach, L. N. Leahy, P. Fathi, J. M. Barrett, A. E. Heyes, T. A. Dumsha, and E. L. McMahon. Crack propagation and its shear mechanisms in the bovine descending aorta. *Cardiovascular Engineering and Technology*, 6:501–518, dec 2015. doi: 10.1007/s13239-015-0245-7.

[92] D. C. Haspinger and G. A. Holzapfel. On the descriptive and predictive capabilities of two model approaches considering the collagen fiber dispersion in healthy and aneurysmal arteries. *European Journal of Mechanics - A/Solids*, 101:105052, 2023. doi: 10.1016/j.euromechsol.2023.105052.

[93] M. Haurani and P. Pagano. Adventitial fibroblast reactive oxygen species as autacrine and paracrine mediators of remodeling: Bellwether for vascular disease? *Cardiovascular Research*, 75:679–689, 2007. doi: 10.1016/j.cardiores.2007.06.016.

[94] E. L. Henderson, Y.-J. Geng, G. K. Sukhova, A. D. Whittemore, J. Knox, and P. Libby. Death of smooth muscle cells and expression of mediators of apoptosis by T lymphocytes in human abdominal aortic aneurysms. *Circulation*, 99:96–104, 1999. doi: 10.1161/01.CIR.99.1.96.

[95] J. A. Hernández, J. Oliver, A. E. Huespe, M. A. Caicedo, and J. C. Cante. High-performance model reduction techniques in computational multiscale homogenization. *Computer Methods in Applied Mechanics and Engineering*, 276:149–189, 2014. doi: 10.1016/j.cma.2014.03.011.

[96] M. R. Hill, X. Duan, G. A. Gibson, S. Watkins, and A. M. Robertson. A theoretical and non-destructive experimental approach for direct inclusion of measured collagen orientation and recruitment into mechanical models of the artery wall. *Journal of Biomechanics*, 45:762–771, 2012. doi: 10.1016/j.jbiomech.2011.11.016.

[97] R. Hill. Elastic properties of reinforced solids: Some theoretical principles. *Journal of the Mechanics and Physics of Solids*, 11:357–372, 1963. doi: 10.1016/0022-5096(63)90036-X.

[98] R. Hill. Continuum micro-mechanics of elastoplastic polycrystals. *Journal of the Mechanics and Physics of Solids*, 13:89–101, 1965. doi: 10.1016/0022-5096(65)90023-2.

[99] R. Hill. A self-consistent mechanics of composite materials. *Journal of the Mechanics and Physics of Solids*, 13:213–222, 1965. doi: 10.1016/0022-5096(65)90010-4.

[100] R. Hill. On constitutive macro-variables for heterogeneous solids at finite strain. *Proceedings of the Royal Society of London. A. Mathematical and Physical Sciences*, 326:131–147, 1972. doi: 10.1098/rspa.1972.0001.

[101] A. T. Hirsch, Z. J. Haskal, N. R. Hertzer, C. W. Bakal, M. A. Creager, J. L. Halperin, L. F. Hiratzka, W. R. C. Murphy, J. W. Olin, J. B. Puschett, K. A. Rosenfield, D. Sacks, J. C. Stanley, L. M. Taylor, C. J. White, J. White, R. A. White, E. M. Antman, S. C. Smith, C. D. Adams, J. L. Anderson, D. P. Faxon, V. Fuster, R. J. Gibbons, J. L. Halperin, L. F. Hiratzka, S. A. Hunt, A. K. Jacobs, R. Nishimura, J. P. Ornato, R. L. Page, and B. Riegel. ACC/AHA guidelines for the management of patients with peripheral arterial disease (lower extremity, renal, mesenteric, and abdominal aortic). *Journal of Vascular and Interventional Radiology*, 17:1383–1398, 2006. doi: 10.1097/01.RVI.0000240426.53079.46.

[102] G. A. Holzapfel. *Nonlinear Solid Mechanics - A Continuum Approach for Engineering*. John Wiley & Sons, Chichester, UK, 2000. ISBN 978-0471823193.

[103] G. A. Holzapfel. Collagen in arterial walls: Biomechanical aspects. In P. Fratzl, editor, *Collagen*, chapter 11, pages 285–324. Springer, Boston, US, 2008. doi: 10.1007/978-0-387-73906-9_11.

[104] G. A. Holzapfel and R. W. Ogden. Constitutive modelling of arteries. *Proceedings of the Royal Society A: Mathematical, Physical and Engineering Sciences*, 466: 1551–1597, 2010. doi: 10.1098/rspa.2010.0058.

[105] G. A. Holzapfel and R. W. Ogden. Biomechanical relevance of the microstructure in artery walls with a focus on passive and active components. *American Journal of Physiology-Heart and Circulatory Physiology*, 315:H540–H549, 2018. doi: 10.1152/ajpheart.00117.2018.

[106] G. A. Holzapfel and R. W. Ogden. A damage model for collagen fibres with an application to collagenous soft tissues. *Proceedings of the Royal Society A: Mathematical, Physical and Engineering Sciences*, 476:20190821, 2020. doi: 10.1098/rspa.2019.0821.

[107] G. A. Holzapfel and R. W. Ogden. An arterial constitutive model accounting for collagen content and cross-linking. *Journal of the Mechanics and Physics of Solids*, 136:103682, 2020. doi: 10.1016/j.jmps.2019.103682.

[108] G. A. Holzapfel and H. W. Weizsäcker. Biomechanical behavior of the arterial wall and its numerical characterization. *Computers in Biology and Medicine*, 28:377–392, 1998. doi: 10.1016/S0010-4825(98)00022-5.

[109] G. A. Holzapfel, T. C. Gasser, and R. W. Ogden. A new constitutive framework for arterial wall mechanics and a comparative study of material models. *Journal of Elasticity*, 61:1–48, 2000. doi: 10.1023/A:1010835316564.

[110] G. A. Holzapfel, T. C. Gasser, and M. Stadler. A structural model for the viscoelastic behavior of arterial walls: Continuum formulation and finite element analysis. *European Journal of Mechanics - A/Solids*, 21:441–463, 2002. doi: 10.1016/S0997-7538(01)01206-2.

[111] G. A. Holzapfel, G. Sommer, and P. Regitnig. Anisotropic mechanical properties of tissue components in human atherosclerotic plaques. *Journal of Biomechanical Engineering*, 126:657–665, 2004. doi: 10.1115/1.1800557.

[112] G. A. Holzapfel, G. Sommer, M. Auer, P. Regitnig, and R. W. Ogden. Layer-specific 3D residual deformations of human aortas with non-atherosclerotic intimal thickening. *Annals of Biomedical Engineering*, 35:530–545, 2007. doi: 10.1007/s10439-006-9252-z.

[113] G. A. Holzapfel, J. A. Niestrawska, R. W. Ogden, A. J. Reinisch, and A. J. Schriefl. Modelling non-symmetric collagen fibre dispersion in arterial walls. *Journal of The Royal Society Interface*, 12:20150188, 2015. doi: 10.1098/rsif.2015.0188.

[114] G. A. Holzapfel, R. W. Ogden, and S. Sherifova. On fibre dispersion modelling of soft biological tissues: A review. *Proceedings of the Royal Society A: Mathematical, Physical and Engineering Sciences*, 475:20180736, 2019. doi: 10.1098/rspa.2018.0736.

[115] L. Horný, T. Adámek, E. Gultova, R. Zitny, J. Vesely, H. Chlup, and S. Konvickova. Correlations between age, prestrain, diameter and atherosclerosis in the male abdominal aorta. *Journal of the Mechanical Behavior of Biomedical Materials*, 4:2128–2132, 2011. doi: 10.1016/j.jmbbm.2011.07.011.

[116] L. Horný, M. Netušil, and T. Voňavková. Axial prestretch and circumferential distensibility in biomechanics of abdominal aorta. *Biomechanics and Modeling in Mechanobiology*, 13:783–799, 2014. doi: 10.1007/s10237-013-0534-8.

[117] J.-J. Hu, J. D. Humphrey, and A. T. Yeh. Characterization of engineered tissue development under biaxial stretch using nonlinear optical microscopy. *Tissue Engineering Part A*, 15:1553–1564, 2009. doi: 10.1089/ten.tea.2008.0287.

[118] J. D. Humphrey. Stress, strain, and mechanotransduction in cells. *Journal of Biomechanical Engineering*, 123:638–641, 2001. doi: 10.1115/1.1406131.

[119] J. D. Humphrey. *Cardiovascular Solid Mechanics*. Springer, New York, US, 2002. ISBN 978-0-387-95168-3.

[120] J. D. Humphrey. Possible mechanical roles of glycosaminoglycans in thoracic aortic dissection and associations with dysregulated transforming growth factor-\beta. *Journal of Vascular Research*, 50:1–10, 2013. doi: 10.1159/000342436.

[121] J. D. Humphrey. Mechanisms of vascular remodeling in hypertension. *American Journal of Hypertension*, 34:432–441, 2021. doi: 10.1093/ajh/hpaa195.

[122] J. D. Humphrey and G. A. Holzapfel. Mechanics, mechanobiology, and modeling of human abdominal aorta and aneurysms. *Journal of Biomechanics*, 45:805–814, 2012. doi: 10.1016/j.jbiomech.2011.11.021.

[123] J. D. Humphrey and K. R. Rajagopal. A constrained mixture model for arterial adaptations to a sustained step change in blood flow. *Biomechanics and Modeling in Mechanobiology*, 2:109–126, 2003. doi: 10.1007/s10237-003-0033-4.

[124] J. D. Humphrey and C. A. Taylor. Intracranial and abdominal aortic aneurysms: Similarities, differences, and need for a new class of computational models. *Annual Review of Biomedical Engineering*, 10:221–246, 2008. doi: 10.1146/annurev.bioeng.10.061807.160439.

[125] J. D. Humphrey, J. F. Eberth, W. W. Dye, and R. L. Gleason. Fundamental role of axial stress in compensatory adaptations by arteries. *Journal of Biomechanics*, 42: 1–8, 2009. doi: 10.1016/j.jbiomech.2008.11.011.

[126] J. D. Humphrey, E. R. Dufresne, and M. A. Schwartz. Mechanotransduction and extracellular matrix homeostasis. *Nature Reviews Molecular Cell Biology*, 15:802–812, 2014. doi: 10.1038/nrm3896.

[127] C. Hurschler, P. P. Provenzano, and R. Vanderby. Application of a probabilistic microstructural model to determine reference length and toe-to-linear region transition in fibrous connective tissue. *Journal of Biomechanical Engineering*, 125:415–422, 2003. doi: 10.1115/1.1579046.

[128] P. A. Iaizzo. General features of the cardiovascular system. In P. A. Iaizzo, editor, *Handbook of Cardiac Anatomy, Physiology, and Devices*, pages 3–12. Humana Press, Totowa, US, 2009. ISBN 978-1-60327-371-8. doi: 10.1007/978-1-60327-372-5_1.

[129] T. Imura, K. Yamamoto, T. Satoh, K. Kanamori, T. Mikami, and H. Yasuda. In vivo viscoelastic behavior in the human aorta. *Circulation Research*, 66:1413–1419, 1990. doi: 10.1161/01.RES.66.5.1413.

[130] B. C. Isenberg, P. A. DiMilla, M. Walker, S. Kim, and J. Y. Wong. Vascular smooth muscle cell durotaxis depends on substrate stiffness gradient strength. *Biophysical Journal*, 97:1313–1322, 2009. doi: 10.1016/j.bpj.2009.06.021.

[131] K. Ivancev and R. Vogelzang. A 35 year history of stent grafting, and how EVAR conquered the world. *European Journal of Vascular and Endovascular Surgery*, 59: 685–694, 2020. doi: 10.1016/j.ejvs.2020.03.017.

[132] M. Jadidi, M. Habibnezhad, E. Anttila, K. Maleckis, A. Desyatova, J. MacTaggart, and A. Kamenskiy. Mechanical and structural changes in human thoracic aortas with age. *Acta Biomaterialia*, 103:172–188, 2020. doi: 10.1016/j.actbio.2019.12.024.

[133] M. Jadidi, S. A. Razian, M. Habibnezhad, E. Anttila, and A. Kamenskiy. Mechanical, structural, and physiologic differences in human elastic and muscular arteries of different ages: Comparison of the descending thoracic aorta to the superficial femoral artery. *Acta Biomaterialia*, 119:268–283, 2021. doi: 10.1016/j.actbio.2020.10.035.

[134] M. Jadidi, S. Sherifova, G. Sommer, A. Kamenskiy, and G. A. Holzapfel. Constitutive modeling using structural information on collagen fiber direction and dispersion in human superficial femoral artery specimens of different ages. *Acta Biomaterialia*, 121:461–474, 2021. doi: 10.1016/j.actbio.2020.11.046.

[135] G. Jain, A. J. Ford, and P. Rajagopalan. Opposing rigidity-protein gradients reverse fibroblast durotaxis. *ACS Biomaterials Science and Engineering*, 1:621–631, 2015. doi: 10.1021/acsbiomaterials.5b00229.

[136] C. Jayyosi, J.-S. Affagard, G. Ducourthial, C. Bonod-Bidaud, B. Lynch, S. Bancelin, F. Ruggiero, M.-C. Schanne-Klein, J.-M. Allain, K. Bruyère-Garnier, and M. Coret. Affine kinematics in planar fibrous connective tissues: An experimental investigation. *Biomechanics and Modeling in Mechanobiology*, 16:1459–1473, 2017. doi: 10.1007/s10237-017-0899-1.

[137] N. S. Kalson, Y. Lu, S. H. Taylor, T. Starborg, D. F. Holmes, and K. E. Kadler. A structure-based extracellular matrix expansion mechanism of fibrous tissue growth. *eLife*, 4:1–22, 2015. doi: 10.7554/eLife.05958.

[138] A. V. Kamenskiy, I. I. Pipinos, Y. A. Dzenis, N. Y. Phillips, A. S. Desyatova, J. Kitson, R. Bowen, and J. N. MacTaggart. Effects of age on the physiological and mechanical characteristics of human femoropopliteal arteries. *Acta Biomaterialia*, 11:304–313, 2015. doi: 10.1016/j.actbio.2014.09.050.

[139] V. A. Kas'yanov and A. I. Rachev. Deformation of blood vessels upon stretching, internal pressure, and torsion. *Mechanics of Composite Materials*, 16:76–80, 1980. doi: 10.1007/BF00618816.

[140] H. Kaul and Y. Ventikos. Dynamic reciprocity revisited. *Journal of Theoretical Biology*, 370:205–208, 2015. doi: 10.1016/j.jtbi.2015.01.016.

[141] M. Kazi, J. Thyberg, P. Religa, J. Roy, P. Eriksson, U. Hedin, and J. Swedenborg. Influence of intraluminal thrombus on structural and cellular composition of abdominal aortic aneurysm wall. *Journal of Vascular Surgery*, 38:1283–1292, 2003. doi: 10.1016/S0741-5214(03)00791-2.

[142] B.-S. Kim, J. Nikolovski, J. Bonadio, and D. J. Mooney. Cyclic mechanical strain regulates the development of engineered smooth muscle tissue. *Nature Biotechnology*, 17:979–983, 1999. doi: 10.1038/13671.

[143] C. E. Korenczuk, R. Y. Dhume, K. K. Liao, and V. H. Barocas. Ex vivo mechanical tests and multiscale computational modeling highlight the importance of intramural shear stress in ascending thoracic aortic aneurysms. *Journal of Biomechanical Engineering*, 141:1–11, 2019. doi: 10.1115/1.4045270.

[144] W. Krasny, C. Morin, H. Magoariec, and S. Avril. A comprehensive study of layer-specific morphological changes in the microstructure of carotid arteries under uniaxial load. *Acta Biomaterialia*, 57:342–351, 2017. doi: 10.1016/j.actbio.2017.04.033.

[145] W. Krasny, H. Magoariec, C. Morin, and S. Avril. Kinematics of collagen fibers in carotid arteries under tension-inflation loading. *Journal of the Mechanical Behavior of Biomedical Materials*, 77:718–726, 2018. doi: 10.1016/j.jmbbm.2017.08.014.

[146] D. Krievins, S. Thora, and C. K. Zarins. Gigantic 25-cm abdominal aortic aneurysm. *Journal of Vascular Surgery*, 61:1067, 2015. doi: 10.1016/j.jvs.2014.09.005.

[147] H. Kuivaniemi, E. J. Ryer, J. R. Elmore, and G. Tromp. Understanding the pathogenesis of abdominal aortic aneurysms. *Expert Review of Cardiovascular Therapy*, 13:975–987, 2015. doi: 10.1586/14779072.2015.1074861.

[148] Y. Lanir. A structural theory for the homogeneous biaxial stress-strain relationships in flat collagenous tissues. *Journal of Biomechanics*, 12:423–436, 1979. doi: 10.1016/0021-9290(79)90027-7.

[149] Y. Lanir. Constitutive equations for fibrous connective tissues. *Journal of Biomechanics*, 16:1–12, 1983. doi: 10.1016/0021-9290(83)90041-6.

[150] Y. Lanir. Multi-scale structural modeling of soft tissues mechanics and mechanobiology. *Journal of Elasticity*, 129:7–48, 2017. doi: 10.1007/s10659-016-9607-0.

[151] B. M. Learoyd and M. G. Taylor. Alterations with age in the viscoelastic properties of human arterial walls. *Circulation Research*, 18:278–292, 1966. doi: 10.1161/01.RES.18.3.278.

[152] F. A. Lederle, S. E. Wilson, G. R. Johnson, D. B. Reinke, F. N. Littooy, C. W. Acher, D. J. Ballard, L. M. Messina, I. L. Gordon, E. P. Chute, W. C. Krupski, S. J. Busuttil, G. W. Barone, S. Sparks, L. M. Graham, J. H. Rapp, M. S. Makaroun, G. L. Moneta, R. A. Cambria, R. G. Makhoul, D. Eton, H. J. Ansel, J. A. Freischlag, and D. Bandyk. Immediate repair compared with surveillance of small abdominal aortic aneurysms. *New England Journal of Medicine*, 346:1437–1444, 2002. doi: 10.1056/NEJMoa012573.

[153] E. J. Lee, J. W. Holmes, and K. D. Costa. Remodeling of engineered tissue anisotropy in response to altered loading conditions. *Annals of Biomedical Engineering*, 36:1322–1334, 2008. doi: 10.1007/s10439-008-9509-9.

[154] P.-Y. Lee, Y.-C. Liu, M.-X. Wang, and J.-J. Hu. Fibroblast-seeded collagen gels in response to dynamic equibiaxial mechanical stimuli: A biomechanical study. *Journal of Biomechanics*, 78:134–142, 2018. doi: 10.1016/j.jbiomech.2018.07.030.

[155] D. Y. M. Leung, S. Glagov, and M. B. Mathews. Cyclic stretching stimulates synthesis of matrix components by arterial smooth muscle cells in vitro. *Science*, 191:475–477, 1976. doi: 10.1126/science.128820.

[156] Z.-Y. Li, J. U-King-Im, T. Y. Tang, E. Soh, T. C. See, and J. H. Gillard. Impact of calcification and intraluminal thrombus on the computed wall stresses of abdominal aortic aneurysm. *Journal of Vascular Surgery*, 47:928–935, 2008. doi: 10.1016/j.jvs.2008.01.006.

[157] J. H. N. Lindeman, B. A. Ashcroft, J.-W. M. Beenakker, M. van Es, N. B. R. Koekkoek, F. A. Prins, J. F. Tielemans, H. Abdul-Hussien, R. A. Bank, and T. H. Oosterkamp. Distinct defects in collagen microarchitecture underlie vessel-wall failure in advanced abdominal aneurysms and aneurysms in Marfan syndrome. *Proceedings of the National Academy of Sciences*, 107:862–865, 2010. doi: 10.1073/pnas.0910312107.

[158] J. Liu, W. Yu, Y. Liu, S. Chen, Y. Huang, X. Li, C. Liu, Y. Zhang, Z. Li, J. Du, C. Tang, J. Du, and H. Jin. Mechanical stretching stimulates collagen synthesis via down-regulating SO2/AAT1 pathway. *Scientific Reports*, 6:21112, 2016. doi: 10.1038/srep21112.

[159] C.-M. Lo, H.-B. Wang, M. Dembo, and Y.-l. Wang. Cell movement is guided by the rigidity of the substrate. *Biophysical Journal*, 79:144–152, 2000. doi: 10.1016/S0006-3495(00)76279-5.

[160] E. O. Lopez, B. D. Ballard, and A. Jan. Cardiovascular Disease. In *StatPearls [Internet]*. StatPearls Publishing, Treasure Island, US, 2023.

[161] T. Luo, H. Chen, and G. S. Kassab. 3D reconstruction of coronary artery vascular smooth muscle cells. *PLOS ONE*, 11:e0147272, 2016. doi: 10.1371/journal.pone.0147272.

[162] R. R. Mahutga and V. H. Barocas. Investigation of pathophysiological aspects of aortic growth, remodeling, and failure using a discrete-fiber microstructural model. *Journal of Biomechanical Engineering*, 142:111007, 2020. doi: 10.1115/1.4048031.

[163] A. Maier, M. W. Gee, C. Reeps, J. Pongratz, H.-H. Eckstein, and W. A. Wall. A comparison of diameter, wall stress, and rupture potential index for abdominal aortic aneurysm rupture risk prediction. *Annals of Biomedical Engineering*, 38:3124–3134, 2010. doi: 10.1007/s10439-010-0067-6.

[164] S. Maiti, J. R. Thunes, R. N. Fortunato, T. G. Gleason, and D. A. Vorp. Computational modeling of the strength of the ascending thoracic aortic media tissue under physiologic biaxial loading conditions. *Journal of Biomechanics*, 108:109884, 2020. doi: 10.1016/j.jbiomech.2020.109884.

[165] A. M. Malek, S. L. Alper, and S. Izumo. Hemodynamic shear stress and its role in atherosclerosis. *JAMA*, 282:2035, 1999. ISSN 0098-7484. doi: 10.1001/jama.282.21.2035.

[166] J. Mandel. Plasticité classique et viscoplasticité. In *CISM Lecture Notes n. 97*. Springer-Verlag, Vienna, AT, 1972.

[167] M. Marino, M. I. Converse, K. L. Monson, and P. Wriggers. Molecular-level collagen damage explains softening and failure of arterial tissues: A quantitative interpretation of CHP data with a novel elasto-damage model. *Journal of the Mechanical Behavior of Biomedical Materials*, 97:254–271, 2019. doi: 10.1016/j.jmbbm.2019.04.022.

[168] J.-L. Martiel, G. Finet, G. A. Holzapfel, M. Stuber, T. Matsumoto, R. I. Pettigrew, and J. Ohayon. Importance of residual stress and basal tone in healthy and pathological human coronary arteries. In J. Ohayon, G. Finet, and R. I. Pettigrew, editors, *Biomechanics of Coronary Atherosclerotic Plaque*, chapter 19, pages 433–461. Academic Press, Cambridge, US, 2020. ISBN 9780128171950. doi: 10.1016/B978-0-12-817195-0.00019-6.

[169] T. Matsumoto, S. Sugita, and K. Nagayama. Tensile properties of smooth muscle cells, elastin, and collagen fibers. In K. Tanishita and K. Yamamoto, editors, *Vascular Engineering*, pages 127–140. Springer Japan, Tokyo, 2016. doi: 10.1007/978-4-431-54801-0_7.

[170] L. McIntosh, J. M. Cordell, and A. J. W. Johnson. Impact of bone geometry on effective properties of bone scaffolds. *Acta Biomaterialia*, 5:680–692, 2009. doi: 10.1016/j.actbio.2008.09.010.

[171] G. Melissano, M. R. L. Moura, Y. Tshomba, E. M. Marone, and R. Chiesa. Small ruptured abdominal aortic aneurysm with renal failure: Endovascular treatment. *Vascular and Endovascular Surgery*, 37:283–287, 2003. doi: 10.1177/153857440303700408.

[172] C. Miehe. Computational micro-to-macro transitions for discretized microstructures of heterogeneous materials at finite strains based on the minimization of averaged incremental energy. *Computer Methods in Applied Mechanics and Engineering*, 192:559–591, 2003. doi: 10.1016/S0045-7825(02)00564-9.

[173] J. Miller and J. Miller. Small ruptured abdominal aneurysm diagnosed by emergency physician ultrasound. *The American Journal of Emergency Medicine*, 17: 174–175, 1999. doi: 10.1016/S0735-6757(99)90055-4.

[174] H. Miyazaki and K. Hayashi. Tensile tests of collagen fibers obtained from the rabbit patellar tendon. *Biomedical Microdevices*, 2:151–157, 1999. doi: 10.1023/A:1009953805658.

[175] J. A. T. Monteiro, E. S. da Silva, M. L. Raghavan, P. Puech-Leão, M. L. Higuchi, and J. P. Otoch. Histologic, histochemical, and biomechanical properties of fragments isolated from the anterior wall of abdominal aortic aneurysms. *Journal of Vascular Surgery*, 59:1393–1401, 2014. doi: 10.1016/j.jvs.2013.04.064.

[176] C. Morin, W. Krasny, and S. Avril. Multiscale mechanical behavior of large arteries. In R. Narayan, editor, *Encyclopedia of Biomedical Engineering*, volume 2, pages 180–202. Elsevier, Oxford, UK, 2019. doi: 10.1016/B978-0-12-801238-3.99934-3.

[177] H. Z. Movat, R. H. More, and M. D. Haust. The diffuse intimal thickening of the human aorta with aging. *The American Journal of Pathology*, 34:1023–31, 1958.

[178] H. Mozafari, L. Wang, Y. Lei, and L. Gu. Multi-scale modeling of the lamellar unit of arterial media. *Nanotechnology Reviews*, 8:539–547, 2019. doi: 10.1515/ntrev-2019-0048.

[179] J. D. Murray, P. K. Maini, and R. T. Tranquillo. Mechanochemical models for generating biological pattern and form in development. *Physics Reports*, 171:59–84, 1988. doi: 10.1016/0370-1573(88)90003-8.

[180] S.-I. Murtada, J. D. Humphrey, and G. A. Holzapfel. Multiscale and multiaxial mechanics of vascular smooth muscle. *Biophysical Journal*, 113:714–727, 2017. doi: 10.1016/j.bpj.2017.06.017.

[181] K. Nagayama and T. Matsumoto. Mechanical anisotropy of rat aortic smooth muscle cells decreases with their contraction (Possible effect of actin filament orientation). *JSME International Journal, Series C: Mechanical Systems, Machine Elements and Manufacturing*, 47:985–991, 2004. doi: 10.1299/jsmec.47.985.

[182] D. Newby, R. Forsythe, O. McBride, J. Robson, A. Vesey, R. Chalmers, P. Burns, O. J. Garden, S. Semple, M. Dweck, C. Gray, T. MacGillivray, C. Wang, Y. G. Koutraki, N. Mitchard, A. Cooper, E. van Beek, G. McKillop, W. Ho, L. Fraser, H. Cuthbert, P. Hoskins, B. Doyle, N. Conlisk, W. Stuart, C. Berry, G. Roditi, L. Murdoch, R. Holdsworth, E. Scott, L. Milne, F. Strachan, F. Wee, K. Oatey, C. Graham, G. Murray, G. Milne, M. Bucukoglu, K. Goodman, J. Kaczynski, A. Shah, A. Tambyraja, J. Brittenden, G. Houston, R. Lambie, and J. Norrie. Aortic wall inflammation predicts abdominal aortic aneurysm expansion, rupture, and need for surgical repair. *Circulation*, 136:787–797, 2017. doi: 10.1161/CIRCULATIONAHA.117.028433.

[183] J. A. Niestrawska, C. Viertler, P. Regitnig, T. U. Cohnert, G. Sommer, and G. A. Holzapfel. Microstructure and mechanics of healthy and aneurysmatic abdominal aortas: Experimental analysis and modelling. *Journal of The Royal Society Interface*, 13:20160620, 2016. doi: 10.1098/rsif.2016.0620.

[184] J. A. Niestrawska, D. C. Haspinger, and G. A. Holzapfel. The influence of fiber dispersion on the mechanical response of aortic tissues in health and disease: A computational study. *Computer Methods in Biomechanics and Biomedical Engineering*, 21:99–112, 2018. doi: 10.1080/10255842.2017.1418862.

[185] J. A. Niestrawska, P. Regitnig, C. Viertler, T. U. Cohnert, A. R. Babu, and G. A. Holzapfel. The role of tissue remodeling in mechanics and pathogenesis of abdominal aortic aneurysms. *Acta Biomaterialia*, 88:149–161, 2019. doi: 10.1016/j.actbio.2019.01.070.

[186] J. A. Niestrawska, A. Pukaluk, A. R. Babu, and G. A. Holzapfel. Differences in collagen fiber diameter and waviness between healthy and aneurysmal abdominal aortas. *Microscopy and Microanalysis*, 28:1649–1663, 2022. doi: 10.1017/S1431927622000629.

[187] L. E. Niklason, J. Gao, W. M. Abbott, K. K. Hirschi, S. Houser, R. Marini, and R. Langer. Functional arteries grown in vitro. *Science*, 284:489–493, 1999. doi: 10.1126/science.284.5413.489.

[188] M. K. O'Connell, S. Murthy, S. Phan, C. Xu, J. Buchanan, R. Spilker, R. L. Dalman, C. K. Zarins, W. Denk, and C. A. Taylor. The three-dimensional micro- and nanostructure of the aortic medial lamellar unit measured using 3D confocal and electron microscopy imaging. *Matrix Biology*, 27:171–181, 2008. doi: 10.1016/j.matbio.2007.10.008.

[189] D. K. Owens, K. W. Davidson, A. H. Krist, M. J. Barry, M. Cabana, A. B. Caughey, C. A. Doubeni, J. W. Epling, M. Kubik, C. S. Landefeld, C.M. Mangione, L. Pbert, M. Silverstein, M. A. Simon, C.-W. Tseng, and J. B. Wong. Screening for abdominal aortic aneurysm: US Preventive Services Task Force recommendation statement. *JAMA - Journal of the American Medical Association*, 322:2211–2218, 2019. doi: 10.1001/jama.2019.18928.

[190] F. R. Packard. Marcello Malpighi. *Annals of Medical History*, 10:209–210, 1928.

[191] A. Pandolfi and M. Vasta. Fiber distributed hyperelastic modeling of biological tissues. *Mechanics of Materials*, 44:151–162, 2012. doi: 10.1016/j.mechmat.2011.06.004.

[192] N. J. Petterson, E. M. J. van Disseldorp, M. R. H. M. van Sambeek, F. N. van de Vosse, and R. G. P. Lopata. Including surrounding tissue improves ultrasound-based 3D mechanical characterization of abdominal aortic aneurysms. *Journal of Biomechanics*, 85:126–133, 2019. doi: 10.1016/j.jbiomech.2019.01.024.

[193] D. V. Phillips and O. C. Zienkiewicz. Finite element non-linear analysis of concrete structures. *Proceedings of the Institution of Civil Engineers*, 61:59–88, 1976. doi: 10.1680/iicep.1976.3503.

[194] A. Pukaluk, A.-S. Wittgenstein, G. Leitinger, D. Kolb, D. Pernitsch, S. A. Schneider, P. Knöbelreiter, V. Horak, K. Bredies, G. A. Holzapfel, T. Pock, and G. Sommer. An ultrastructural 3D reconstruction method for observing the arrangement of collagen

fibrils and proteoglycans in the human aortic wall under mechanical load. *Acta Biomaterialia*, 141:300–314, 2022. doi: 10.1016/j.actbio.2022.01.036.

[195] A. Pukaluk, H. Wolinski, C. Viertler, P. Regitnig, G. A. Holzapfel, and G. Sommer. Changes in the microstructure of the human aortic adventitia under biaxial loading investigated by multi-photon microscopy. *Acta Biomaterialia*, 161:154–169, 2023. doi: 10.1016/j.actbio.2023.02.027.

[196] Y.-X. Qi, J. Jiang, X.-H. Jiang, X.-D. Wang, S.-Y. Ji, Y. Han, D.-K. Long, B.-R. Shen, Z. Q. Yan, S. Chien, and Z.-L. Jiang. PDGF-BB and TGF-β1 on cross-talk between endothelial and smooth muscle cells in vascular remodeling induced by low shear stress. *Proceedings of the National Academy of Sciences*, 108:1908–1913, 2011. doi: 10.1073/pnas.1019219108.

[197] U. Raaz, A. M. Zöllner, I. N. Schellinger, R. Toh, F. Nakagami, M. Brandt, F. C. Emrich, Y. Kayama, S. Eken, M. Adam, L. Maegdefessel, T. Hertel, A. Deng, A. Jagger, M. Buerke, R. L. Dalman, J. M. Spin, E. Kuhl, and P. S. Tsao. Segmental aortic stiffening contributes to experimental abdominal aortic aneurysm development. *Circulation*, 131:1783–1795, 2015. doi: 10.1161/CIRCULATIONAHA.114.012377.

[198] R. Rezakhaniha, A. Agianniotis, J. T. C. Schrauwen, A. Griffa, D. Sage, C. V. C. Bouten, F. N. van de Vosse, M. Unser, and N. Stergiopulos. Experimental investigation of collagen waviness and orientation in the arterial adventitia using confocal laser scanning microscopy. *Biomechanics and Modeling in Mechanobiology*, 11: 461–473, 2012. doi: 10.1007/s10237-011-0325-z.

[199] M. R. Roach and A. C. Burton. The reason for the shape of the distensibility curves of arteries. *Canadian Journal of Biochemistry and Physiology*, 35:681–690, 1957. doi: 10.1139/o57-080.

[200] A. M. Robertson and P. N. Watton. Mechanobiology of the arterial wall. In S. M. Becker and A. V. Kuznetsov, editors, *Transport in Biological Media*, pages 275–347. Elsevier, Boston, US, 2013. doi: 10.1016/B978-0-12-415824-5.00008-4.

[201] P. Roca-Cusachs, V. Conte, and X. Trepat. Quantifying forces in cell biology. *Nature Cell Biology*, 19:742–751, 2017. doi: 10.1038/ncb3564.

[202] F. F. Rocha, P. J. Blanco, P. J. Sánchez, and R. A. Feijóo. Multi-scale modelling of arterial tissue: Linking networks of fibres to continua. *Computer Methods in Applied Mechanics and Engineering*, 341:740–787, 2018. doi: 10.1016/j.cma.2018.06.031.

[203] F. F. Rocha, P. J. Blanco, P. J. Sánchez, E. A. de Souza Neto, and R. A. Feijóo. Damage-driven strain localisation in networks of fibres: A computational homogenisation approach. *Computers & Structures*, 255:106635, 2021. doi: 10.1016/j.compstruc.2021.106635.

[204] E. K. Rodriguez, A. Hoger, and A. D. McCulloch. Stress-dependent finite growth in soft elastic tissues. *Journal of Biomechanics*, 27:455–467, 1994. doi: 10.1016/0021-9290(94)90021-3.

[205] J. F. Rodríguez, C. Ruiz, M. Doblaré, and G. A. Holzapfel. Mechanical stresses in abdominal aortic aneurysms: Influence of diameter, asymmetry, and material anisotropy. *Journal of Biomechanical Engineering*, 130:1–10, 2008. doi: 10.1115/1.2898830.

[206] T. Rothermel, I. Franczek, and P. Alford. Anisotropic mechanics of vascular smooth muscle cells exposed to dynamic loads. *Journal of Biomechanical Engineering*, 143:121007, 2021. doi: 10.1115/1.4052224.

[207] C. S. Roy. The elastic properties of the arterial wall. *The Journal of Physiology*, 3: 125–159, jan 1881. doi: 10.1113/jphysiol.1881.sp000088.

[208] S. Saeb, P. Steinmann, and A. Javili. Aspects of computational homogenization at finite deformations: A unifying review from Reuss' to Voigt's bound. *Applied Mechanics Reviews*, 68:050801–1–33, 2016. doi: 10.1115/1.4034024.

[209] S. Saeidi, M. P. Kainz, M. Dalbosco, M. Terzano, and G. A. Holzapfel. Histology-informed multiscale modeling of human brain white matter. *Scientific Reports*, 13: 19641, 2023. doi: 10.1038/s41598-023-46600-3.

[210] N. Sakalihasan, A. Heyeres, B. V. Nusgens, R. Limet, and C. M. Lapiére. Modifications of the extracellular matrix of aneurysmal abdominal aortas as a function of their size. *European Journal of Vascular Surgery*, 7:633–637, 1993. doi: 10.1016/S0950-821X(05)80708-X.

[211] N. Sakalihasan, R. Limet, and O. D. Defawe. Abdominal aortic aneurysm. *The Lancet*, 365:1577–1589, 2005. doi: 10.1016/S0140-6736(05)66459-8.

[212] N. Sakalihasan, J.-B. Michel, A. Katsargyris, H. Kuivaniemi, J.-O. Defraigne, A. Nchimi, J. T. Powell, K. Yoshimura, and R. Hultgren. Abdominal aortic aneurysms. *Nature Reviews Disease Primers*, 4:34, 2018. doi: 10.1038/s41572-018-0030-7.

[213] S. Sartore, A. Chiavegato, E. Faggin, R. Franch, M. Puato, S. Ausoni, and P. Pauletto. Contribution of adventitial fibroblasts to neointima formation and vascular remodeling. *Circulation Research*, 89:1111–1121, 2001. doi: 10.1161/hh2401.100844.

[214] E. L. Schiffrin. Vascular remodeling in hypertension. *Hypertension*, 59:367–374, 2012. doi: 10.1161/HYPERTENSIONAHA.111.187021.

[215] J. T. C. Schrauwen, A. Vilanova, R. Rezakhaniha, N. Stergiopulos, F. N. van de Vosse, and P. H. M. Bovendeerd. A method for the quantification of the pressure dependent 3D collagen configuration in the arterial adventitia. *Journal of Structural Biology*, 180:335–342, 2012. doi: 10.1016/j.jsb.2012.06.007.

[216] A. J. Schriefl, G. Zeindlinger, D. M. Pierce, P. Regitnig, and G. A. Holzapfel. Determination of the layer-specific distributed collagen fibre orientations in human thoracic and abdominal aortas and common iliac arteries. *Journal of The Royal Society Interface*, 9:1275–1286, 2012. doi: 10.1098/rsif.2011.0727.

[217] A. J. Schriefl, T. Schmidt, D. Balzani, G. Sommer, and G. A. Holzapfel. Selective enzymatic removal of elastin and collagen from human abdominal aortas: Uniaxial mechanical response and constitutive modeling. *Acta Biomaterialia*, 17:125–136, 2015. ISSN . doi: 10.1016/j.actbio.2015.01.003.

[218] C. A. J. Schulze-Bauer, P. Regitnig, and G. A. Holzapfel. Mechanics of the human femoral adventitia including the high-pressure response. *American Journal of Physiology-Heart and Circulatory Physiology*, 282:H2427–H2440, 2002. doi: 10.1152/ajpheart.00397.2001.

[219] B. R. Seo, X. Chen, L. Ling, Y. H. Song, A. A. Shimpi, S. Choi, J. Gonzalez, J. Sapudom, K. Wang, R. C. A. Eguiluz, D. Gourdon, V. B. Shenoy, and C. Fischbach. Collagen microarchitecture mechanically controls myofibroblast differentiation. *Proceedings of the National Academy of Sciences*, 117:11387–11398, 2020. doi: 10.1073/pnas.1919394117.

[220] S. B. Shah, C. Witzenburg, M. F. Hadi, H. P. Wagner, J. M. Goodrich, P. W. Alford, and V. H. Barocas. Prefailure and failure mechanics of the porcine ascending thoracic aorta: Experiments and a multiscale model. *Journal of Biomechanical Engineering*, 136:021028–1–7, 2014. doi: 10.1115/1.4026443.

[221] S. Sharifpoor, C. A. Simmons, R. S. Labow, and J. P. Santerre. A study of vascular smooth muscle cell function under cyclic mechanical loading in a polyurethane scaffold with optimized porosity. *Acta Biomaterialia*, 6:4218–4228, 2010. doi: 10.1016/j.actbio.2010.06.018.

[222] A. Shellard and R. Mayor. Durotaxis: The hard path from in vitro to in vivo. *Developmental Cell*, 56:227–239, 2021. doi: 10.1016/j.devcel.2020.11.019.

[223] S. Sherifova, G. Sommer, C. Viertler, P. Regitnig, T. Caranasos, M. A. Smith, B. E. Griffith, R. W. Ogden, and G. A. Holzapfel. Failure properties and microstructure of healthy and aneurysmatic human thoracic aortas subjected to uniaxial extension with a focus on the media. *Acta Biomaterialia*, 99:443–456, 2019. doi: 10.1016/j.actbio.2019.08.038.

[224] E. S. Silva, A. J. Rodrigues, E. M. C. Tolosa, C. J. Rodrigues, G. V. B. Prado, and J. C. Nakamoto. Morphology and diameter of infrarenal aortic aneurysms: A prospective autopsy study. *Cardiovascular Surgery*, 8:526–532, 2000. doi: 10.1016/S0967-2109(00)00060-0.

[225] A. Solan, S. L. M. Dahl, and L. E. Niklason. Effects of mechanical stretch on collagen and cross-linking in engineered blood vessels. *Cell Transplantation*, 18: 915–921, 2009. doi: 10.3727/096368909X471161.

[226] G. Sommer, C. Benedikt, J. A. Niestrawska, G. Hohenberger, C. Viertler, P. Regitnig, T. U. Cohnert, and G. A. Holzapfel. Mechanical response of human subclavian and iliac arteries to extension, inflation and torsion. *Acta Biomaterialia*, 75:235–252, 2018. doi: 10.1016/j.actbio.2018.05.043.

[227] K. Spanos, H.-H. Eckstein, and A. D. Giannoukas. Small abdominal aortic aneurysms are not all the same. *Angiology*, 71:205–207, 2020. doi: 10.1177/0003319719862965.

[228] D. C. D. Speirs, E. A. de Souza Neto, and D. Perić. An approach to the mechanical constitutive modelling of arterial tissue based on homogenization and optimization. *Journal of Biomechanics*, 41:2673–2680, 2008. doi: 10.1016/j.jbiomech.2008.06.020.

[229] T. Starborg, N. S. Kalson, Y. Lu, A. Mironov, T. F. Cootes, D. F. Holmes, and K. E. Kadler. Using transmission electron microscopy and 3View to determine collagen fibril size and three-dimensional organization. *Nature Protocols*, 8:1433–1448, 2013. doi: 10.1038/nprot.2013.086.

[230] H. C. Stary, D. H. Blankenhorn, A. B. Chandler, S. Glagov, W. Insull, M. Richardson, M. E. Rosenfeld, S. A. Schaffer, C. J. Schwartz, and W. D. Wagner. A definition of the intima of human arteries and of its atherosclerosis-prone regions. A report from the Committee on Vascular Lesions of the Council on Arteriosclerosis, American Heart Association. *Circulation*, 85:391–405, 1992. doi: 10.1161/01.CIR.85.1.391.

[231] A. Stracuzzi, B. R. Britt, E. Mazza, and A. E. Ehret. Risky interpretations across the length scales: Continuum vs. discrete models for soft tissue mechanobiology. *Biomechanics and Modeling in Mechanobiology*, 21:433–454, 2022. doi: 10.1007/s10237-021-01543-4.

[232] T. Stylianopoulos and V. H. Barocas. Multiscale, structure-based modeling for the elastic mechanical behavior of arterial walls. *Journal of Biomechanical Engineering*, 129:611–618, 2007. doi: 10.1115/1.2746387.

[233] P. Sucosky, J. A. Shar, and J. Barrientos. Cardiovascular mechanics and disease. In G. L. Niebur, editor, *Mechanobiology*, chapter 1.2, pages 23–45. Elsevier, New York, US, 2020. doi: 10.1016/B978-0-12-817931-4.00002-9.

[234] S. Sugita and T. Matsumoto. Multiphoton microscopy observations of 3D elastin and collagen fiber microstructure changes during pressurization in aortic media. *Biomechanics and Modeling in Mechanobiology*, 16:763–773, 2017. doi: 10.1007/s10237-016-0851-9.

[235] K. Takamizawa and K. Hayashi. Strain energy density function and uniform strain hypothesis for arterial mechanics. *Journal of Biomechanics*, 20:7–17, 1987. doi: 10.1016/0021-9290(87)90262-4.

[236] T. T. Tanaka and Y.-C. Fung. Elastic and inelastic properties of the canine aorta and their variation along the aortic tree. *Journal of Biomechanics*, 7:357–370, 1974. doi: 10.1016/0021-9290(74)90031-1.

[237] D. W. Thompson. *On Growth and Form*. Cambridge University Press, Cambridge, UK, 1917.

[238] J. R. Thunes, S. Pal, R. N. Fortunato, J. A. Phillippi, T. G. Gleason, D. A. Vorp, and S. Maiti. A structural finite element model for lamellar unit of aortic media indicates heterogeneous stress field after collagen recruitment. *Journal of Biomechanics*, 49:1562–1569, 2016. doi: 10.1016/j.jbiomech.2016.03.034.

[239] J. R. Thunes, J. A. Phillippi, T. G. Gleason, D. A. Vorp, and S. Maiti. Structural modeling reveals microstructure-strength relationship for human ascending thoracic aorta. *Journal of Biomechanics*, 71:84–93, 2018. doi: 10.1016/j.jbiomech.2018.01.037.

[240] K. Tillman, O. D. Lee, and K. Whitty. Abdominal aortic aneurysm: An often asymptomatic and fatal men's health issue. *American Journal of Men's Health*, 7:163–168, 2013. doi: 10.1177/1557988312464195.

[241] J. Tong, T. Cohnert, P. Regitnig, and G. A. Holzapfel. Effects of age on the elastic properties of the intraluminal thrombus and the thrombus-covered wall in abdominal aortic aneurysms: Biaxial extension behaviour and material modelling. *European Journal of Vascular and Endovascular Surgery*, 42:207–219, 2011. doi: 10.1016/j.ejvs.2011.02.017.

[242] J. Tong, T. Cohnert, and G. A. Holzapfel. Diameter-related variations of geometrical, mechanical, and mass fraction data in the anterior portion of abdominal aortic aneurysms. *European Journal of Vascular and Endovascular Surgery*, 49:262–270, 2015. doi: 10.1016/j.ejvs.2014.12.009.

[243] W. D. Tucker, Y. Arora, and K. Mahajan. Anatomy, Blood Vessels. In *StatPearls [Internet]*. StatPearls Publishing, Treasure Island, US, 2023.

[244] E. Tzima, M. Irani-Tehrani, W. B. Kiosses, E. Dejana, D. A. Schultz, B. Engelhardt, G. Cao, H. DeLisser, and M. A. Schwartz. A mechanosensory complex that mediates the endothelial cell response to fluid shear stress. *Nature*, 437:426–431, 2005. doi: 10.1038/nature03952.

[245] G. Urabe, K. Hoshina, T. Shimanuki, Y. Nishimori, T. Miyata, and J. Deguchi. Structural analysis of adventitial collagen to feature aging and aneurysm formation in human aorta. *Journal of Vascular Surgery*, 63:1341–1350, 2016. doi: 10.1016/j.jvs.2014.12.057.

[246] L. Vaccaro. Galileo Galilei. *Annals of Medical History*, 7:372–384, 1935.

[247] R. N. Vaishnav, J. T. Young, and D. J. Patel. Distribution of stresses and of strain-energy density through the wall thickness in a canine aortic segment. *Circulation Research*, 32:577–583, 1973. doi: 10.1161/01.RES.32.5.577.

[248] M. C. H. van der Meulen and R. Huiskes. Why mechanobiology? *Journal of Biomechanics*, 35:401–414, 2002. doi: 10.1016/S0021-9290(01)00184-1.

[249] J. A. van der Vliet and A. P. M. Boll. Abdominal aortic aneurysm. *The Lancet*, 349:863–866, 1997. doi: 10.1016/S0140-6736(96)07282-0.

[250] E. M. J. van Disseldorp, N. J. Petterson, M. C. M. Rutten, F. N. van de Vosse, M. R. H. M. van Sambeek, and R. G. P. Lopata. Patient specific wall stress analysis and mechanical characterization of abdominal aortic aneurysms using 4D ultrasound. *European Journal of Vascular and Endovascular Surgery*, 52:635–642, 2016. doi: 10.1016/j.ejvs.2016.07.088.

[251] J. P. Vande Geest, E. S. Di Martino, A. Bohra, M. S. Makaroun, and D. A. Vorp. A biomechanics-based rupture potential index for abdominal aortic aneurysm risk assessment: Demonstrative application. *Annals of the New York Academy of Sciences*, 1085:11–21, 2006. doi: 10.1196/annals.1383.046.

[252] J. P. Vande Geest, M. S. Sacks, and D. A. Vorp. The effects of aneurysm on the biaxial mechanical behavior of human abdominal aorta. *Journal of Biomechanics*, 39:1324–1334, 2006. doi: 10.1016/j.jbiomech.2005.03.003.

[253] J. S. VanEpps and D. A. Vorp. Mechanopathobiology of atherogenesis: A review. *Journal of Surgical Research*, 142:202–217, 2007. doi: 10.1016/j.jss.2006.11.001.

[254] T. J. Vaughan, C. T. McCarthy, and L. M. McNamara. A three-scale finite element investigation into the effects of tissue mineralisation and lamellar organisation in human cortical and trabecular bone. *Journal of the Mechanical Behavior of Biomedical Materials*, 12:50–62, 2012. doi: 10.1016/j.jmbbm.2012.03.003.

[255] A. K. Venkatasubramaniam, M. J. Fagan, T. Mehta, K. J. Mylankal, B. Ray, G. Kuhan, I. C. Chetter, and P. T. McCollum. A comparative study of aortic wall stress using finite element analysis for ruptured and non-ruptured abdominal aortic aneurysms. *European Journal of Vascular and Endovascular Surgery*, 28:168–176, 2004. doi: 10.1016/j.ejvs.2004.03.029.

[256] G. Vergaro, A. Del Corso, M. Franzini, and M. Emdin. Biomarkers for growth prediction of abdominal aortic aneurysm: A step forward(?). *European Journal of Preventive Cardiology*, 27:130–131, 2020. doi: 10.1177/2047487319888973.

[257] L. Virag, N. Horvat, and I. Karšaj. A computational study of bio-chemo-mechanics of thrombus-laden aneurysms. *Journal of the Mechanics and Physics of Solids*, 171: 105140, 2023. doi: 10.1016/j.jmps.2022.105140.

[258] D. A. Vorp. Biomechanics of abdominal aortic aneurysm. *Journal of Biomechanics*, 40:1887–1902, 2007. doi: 10.1016/j.jbiomech.2006.09.003.

[259] D. A. Vorp, D. H. J. Wang, M. W. Webster, and W. J. Federspiel. Effect of intraluminal thrombus thickness and bulge diameter on the oxygen diffusion in abdominal aortic aneurysm. *Journal of Biomechanical Engineering*, 120:579–583, 1998. doi: 10.1115/1.2834747.

[260] D. A. Vorp, P. C. Lee, D. H. J. Wang, M. S. Makaroun, E. M. Nemoto, S. Ogawa, and M. W. Webster. Association of intraluminal thrombus in abdominal aortic aneurysm with local hypoxia and wall weakening. *Journal of Vascular Surgery*, 34:291–299, 2001. doi: 10.1067/mva.2001.114813.

[261] D. H. J. Wang, M. S. Makaroun, M. W. Webster, and D. A. Vorp. Effect of intraluminal thrombus on wall stress in patient-specific models of abdominal aortic aneurysm. *Journal of Vascular Surgery*, 36:598–604, 2002. doi: 10.1067/mva.2002.126087.

[262] S. R. Watson and S. M. Lessner. (Second) Harmonic disharmony: Nonlinear microscopy shines new light on the pathology of atherosclerosis. *Microscopy and Microanalysis*, 22:589–598, 2016. doi: 10.1017/S1431927616000842.

[263] P. N. Watton, N. A. Hill, and M. Heil. A mathematical model for the growth of the abdominal aortic aneurysm. *Biomechanics and Modeling in Mechanobiology*, 3:98–113, 2004. doi: 10.1007/s10237-004-0052-9.

[264] H. Weisbecker, D. M. Pierce, P. Regitnig, and G. A. Holzapfel. Layer-specific damage experiments and modeling of human thoracic and abdominal aortas with non-atherosclerotic intimal thickening. *Journal of the Mechanical Behavior of Biomedical Materials*, 12:93–106, 2012. doi: 10.1016/j.jmbbm.2012.03.012.

[265] H. Weisbecker, C. Viertler, D. M. Pierce, and G. A. Holzapfel. The role of elastin and collagen in the softening behavior of the human thoracic aortic media. *Journal of Biomechanics*, 46:1859–1865, 2013. doi: 10.1016/j.jbiomech.2013.04.025.

[266] H. Weisbecker, D. M. Pierce, and G. A. Holzapfel. A generalized prestressing algorithm for finite element simulations of preloaded geometries with application to the aorta. *International Journal for Numerical Methods in Biomedical Engineering*, 30:857–872, 2014. doi: 10.1002/cnm.2632.

[267] H. Weisbecker, M. J. Unterberger, and G. A. Holzapfel. Constitutive modelling of arteries considering fibre recruitment and three-dimensional fibre distribution. *Journal of The Royal Society Interface*, 12:20150111, 2015. doi: 10.1098/rsif.2015.0111.

[268] D. Weiss, M. Latorre, B. V. Rego, C. Cavinato, B. J. Tanski, A. G. Berman, C. J. Goergen, and J. D. Humphrey. Biomechanical consequences of compromised elastic fiber integrity and matrix cross-linking on abdominal aortic aneurysmal enlargement. *Acta Biomaterialia*, 134:422–434, 2021. doi: 10.1016/j.actbio.2021.07.059.

[269] WHO. The top 10 causes of death, 2020. URL `https://www.who.int/news-room/fact-sheets/detail/the-top-10-causes-of-death`.

[270] Z. Win, J. M. Buksa, and P. W. Alford. Architecture-dependent anisotropic hysteresis in smooth muscle cells. *Biophysical Journal*, 115:2044–2054, 2018. doi: 10.1016/j.bpj.2018.09.027.

[271] C. M. Witzenburg, R. Y. Dhume, S. B. Shah, C. E. Korenczuk, H. P. Wagner, P. W. Alford, and V. H. Barocas. Failure of the porcine ascending aorta: Multidirectional experiments and a unifying microstructural model. *Journal of Biomechanical Engineering*, 139:031005–1–14, 2017. doi: 10.1115/1.4035264.

[272] H. Wolinsky and S. Glagov. Structural basis for the static mechanical properties of the aortic media. *Circulation Research*, 14:400–413, 1964. doi: 10.1161/01.RES.14.5.400.

[273] H. Wolinsky and S. Glagov. A lamellar unit of aortic medial structure and function in mammals. *Circulation Research*, 20:99–111, 1967. doi: 10.1161/01.RES.20.1.99.

[274] J. Y. Wong, A. Velasco, P. Rajagopalan, and Q. Pham. Directed movement of vascular smooth muscle cells on gradient-compliant hydrogels. *Langmuir*, 19:1908–1913, 2003. doi: 10.1021/la026403p.

[275] J. Wu, K. R. C. Montaniel, M. A. Saleh, L. Xiao, W. Chen, G. K. Owens, J. D. Humphrey, M. W. Majesky, D. T. Paik, A. K. Hatzopoulos, M. S. Madhur, and D. G. Harrison. Origin of matrix-producing cells that contribute to aortic fibrosis in hypertension. *Hypertension*, 67:461–468, 2016. doi: 10.1161/HYPERTENSIONAHA.115.06123.

[276] B. Young, P. Woodford, and G. O'Dowd. *Wheater's Functional Histology - a Text and Color Atlas*. Elsevier, Philadelphia, US, 6th edition, 2013. ISBN 0702054887.

[277] X. Yu and Y. Zhang. A discrete fiber network finite element model of arterial elastin network considering inter-fiber crosslinking property and density. *Journal of the Mechanical Behavior of Biomedical Materials*, 134:105396, 2022. doi: 10.1016/j.jmbbm.2022.105396.

[278] F. Yuan, S. R. Stock, D. R. Haeffner, J. D. Almer, D. C. Dunand, and L. C. Brinson. A new model to simulate the elastic properties of mineralized collagen fibril. *Biomechanics and Modeling in Mechanobiology*, 10:147–160, 2011. doi: 10.1007/s10237-010-0223-9.

[279] J. Yvonnet and Q.-C. He. The reduced model multiscale method (R3M) for the non-linear homogenization of hyperelastic media at finite strains. *Journal of Computational Physics*, 223:341–368, 2007. doi: 10.1016/j.jcp.2006.09.019.

[280] W. Zhang, M. Jadidi, S. A. Razian, G. A. Holzapfel, A. Kamenskiy, and D. A. Nordsletten. A viscoelastic constitutive model for human femoropopliteal arteries. *Acta Biomaterialia*, 170:68–85, 2023. doi: 10.1016/j.actbio.2023.09.007.